Applications of the PGPE Formalism to a Trapped Bose Gas

Alice Bezett

A thesis submitted for the degree of

Doctor of Philosophy at the University of Otago,

Dunedin, New Zealand.

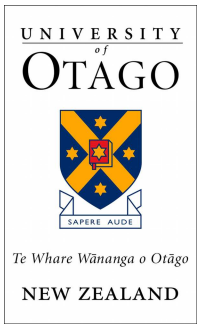

December 2008

Abstract

In this thesis we develop formalism based on the Projected Gross-Pitaevskii equation (PGPE) to describe experimentally realistic systems of finite temperature Bose-Einstein condensation. The PGPE formalism we use has been developed for the harmonically trapped system, and includes nonperturbatively all the interactions within the low energy, highly occupied modes, and is valid in the critical regime. In this thesis we extend the PGPE to study two challenging problems: (i) Modeling the finite temperature collective mode experiment of JILA (ii) The correlation properties of a trapped Bose gas and the emergence of critical physics at the condensation transition. Our work is extensively computational in nature, and a large number of results in experimentally realistic regimes are presented.

We make a quantitative comparison of the PGPE formalism to experimental results by modeling the JILA experiment that studied the quadrupolar collective excitations of a finite temperature Bose gas [PRL **78**, 764 (1997)]. We undertake a comprehensive study of the experimental regime by analysing the condensate and noncondensate excitation frequencies and damping rates as a function of temperature. These simulations allow us to compare the PGPE directly with the experimental results, and also with a large body of theoretical work that has been applied to this problem. We analyse the dependence of our cutoff in energy space to the equilibrium and dynamic properties of our system; this is the first such study of this dependence for the PGPE formalism, and yields new validity conditions for the study of dynamical regimes.

We study the coherence and correlations within a trapped Bose gas by developing formalism for calculating the first and second order correlation functions. We investigate the role of the condensate and thermal components of the system in the temperature range $(0.5 - 1.0)T_c$. We then extend this work to study the onset of coherence in the system at the critical temperature. We study the variation of the correlation length across the phase transition, and so are able to make a prediction for a critical exponent of the transition. We observe finite size effects and identify relevant length scales for the onset of finite size effects. We identify experimentally measurable quantities that can be compared with our theoretical work.

Acknowledgements

I would like to thank my supervisor, Dr Blair Blakie, for his unfailing guidance and support throughout my PhD studies. Blair was always brimming with ideas of how to further our work, and full of enthusiasm for the underlying physics. I think a little of this rubbed off - for which I am truly grateful.

To Prof. Rob Ballagh, for all his encouragement, and for being able to always see the bigger picture.

I would like to thank all the Jack Dodd members, past and present, for all the helpful discussions, and for broadening my physics outlook. On a more personal note, I'd like to thank all the members of 524 over the years, who were always full of support when the going was tough, and could be counted on to humour me when all I really wanted was a distraction.

In the wider physics community I'd like to thank Dr Craig Rodger for his friendship and perspective, and Dr Inga Smith for all her helpful advice, and for providing a new area of interest. I'd also like to thank the IT staff at the physics department, who always managed to fix the things I broke, and the technicians who taught me how to turn equipment on if I ever found myself in a lab, and just generally made the common room a fun place. Thanks also to Sandy, for all her support.

Thanks to my friends and family, who were always there when I needed them most, and especially my parents, for all the love and support. To George, who has always been there for me, patient and thoughtful, thankyou sweetheart, for just being you.

This work was supported by financial assistance from the Tertiary Education Commission, and the Jack Dodd Center. I would also like to thank the University of Otago, and my supervisors, for additional travel funding.

Contents

Chapter 1

Introduction

Bose-Einstein condensate (BEC) is the state of matter characterised by the macroscopic occupation of the ground state of a system of bosons, particles with integer spin (in units $\hbar$). This phenomenon is due purely to quantum statistical effects, rather than interactions, which drive the phase transitions of the states seen in everyday experience. The idea of BEC first emerged theoretically from the work of Bose and Einstein in 1924, but was not experimentally realised until 1995 in the group at JILA [1]. We show their absorptive images of the expanded cloud in Fig. 1.1. This image shows the Bose cloud at three different temperatures, spanning the phase transition. There has been an extraordinary amount of interest in BEC, both theoretically and experimentally, as this fluid allows quantum effects to be seen on the macroscopic scale. The physical situation of a pure condensate (see Fig. 1.1(c)) is well understood and a simple, and widely used theory has emerged that provides a comprehensive description of this regime - the Gross-Pitaevskii equation (GPE). For the cases of mixed condensate and noncondensate (see Fig. 1.1(b)) several theories have been developed, but tend to be much more complicated than the GPE to use, and are often limited to near equilibrium systems. Furthermore, none of those theories are valid for the critical regime (lying at a temperature between Fig. 1.1(a) and (b)), except for a few quantum Monte Carlo predictions. The transitional cases in Fig. 1.1(a) and (b) are significantly more complex due to interactions between condensed and noncondensed components of the cloud. It is the subject of this thesis to develop formalism applicable to recent experimental developments in these regimes.

1.1 Finite Temperature Investigations

The formalism we will develop in this thesis is applicable to the degenerate, harmonically trapped interacting Bose gas at finite temperature. While original experiments probing

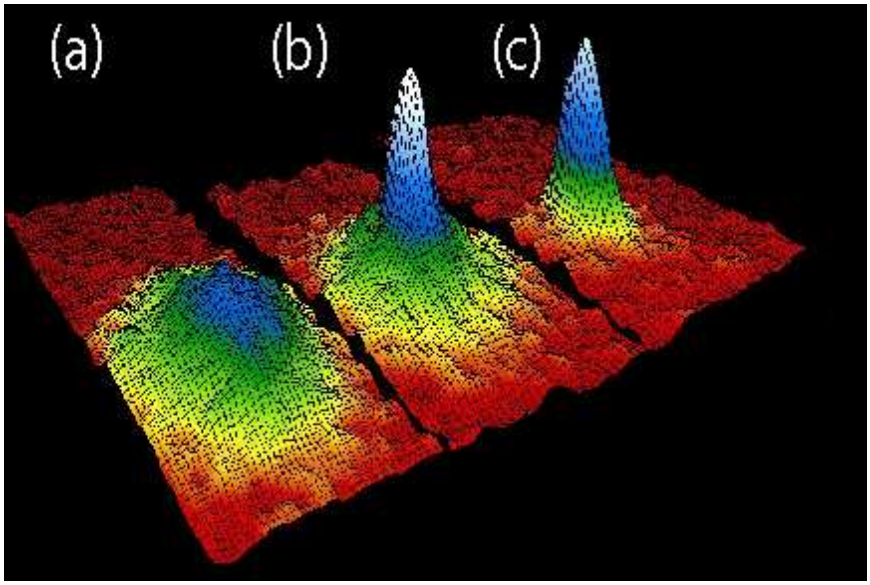

Figure 1.1: Absorption images of the BEC of the experiment of [1]. A dilute gas of ^{87}Rb atoms at (a) 400nK, (b) 200nK, and (c) 50nK, showing the progression of the gas from an uncondensed phase (a) to an almost pure condensate (c). (a) shows an ultra-cold Bose gas which is just above the phase transition where it is not condensed, (b) shows the partially condensed system, and (c) corresponds to a temperature well below the critical temperature, where there is a pure BEC. Reproduced from [1] Copyright 1995 American Association for the Advancement of Science.

this novel quantum fluid were done in the zero-temperature limit, efforts quickly turned to investigating the finite temperature gas, where the BEC interacts strongly with an uncondensed component, which we will refer to from here on as the thermal cloud or noncondensate. In the following, we will give a broad overview of two very important areas of research, that will be the foci of this thesis:

1. The low energy collective excitations of the partially condensed Bose gas.
2. The investigation of correlations within the finite temperature trapped Bose gas, and the critical behaviour of these correlations near T_c.

Below follows a review of the experimental developments in these fields, and of the theoretical results that are applicable to these experiments.

1.1.1 Excitation spectra of an Ultra Cold Bose Gas

The response of a manybody system to an external perturbation, particularly its collective mode response, forms an important method of analysis in condensed matter physics. The BEC is usually confined within a magnetic field. Perturbations of this confining

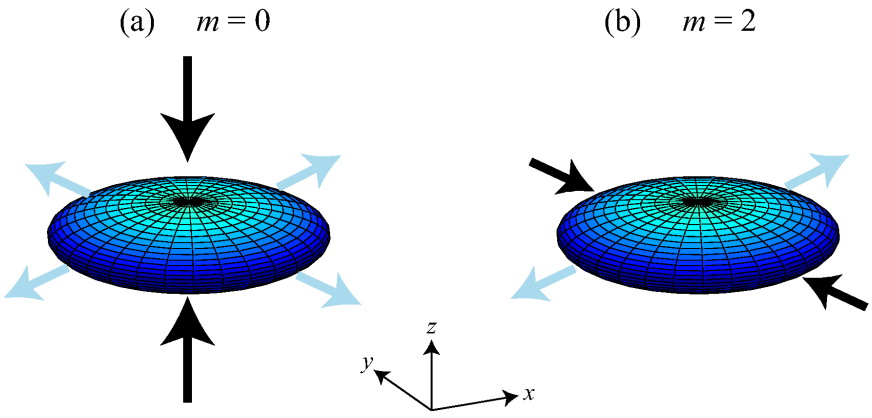

Figure 1.2: Schematic view of the symmetries of the collective modes studied in the experiment of Jin *et al.* [3].

potential can excite the collective modes of the system, and this was the method used in several collective mode experiments [2–6]. The first of these, by Jin *et al.* [2] and Mewes *et al.* [4] investigated various excitation modes in the low temperature limit, where the system was mainly condensate. The results of these investigations could be well described by simple meanfield theory (see [7–9] and results within [4]). We are interested mainly in the extension of this work to study the excitations as a function of temperature, as done by Jin *et al.* in Ref. [3].

In that work, a sinusoidal perturbation was applied to the harmonic trapping potential, in order to excite the $m = 0$ and $m = 2$ excitation modes, where m is the projection of the angular momentum on the z-axis. In Fig. 1.2(a) and (b) we show a schematic representation of the two quadrupolar modes excited in the JILA experiment, for their "pancake" shaped cloud. We see that the $m = 0$ mode corresponds to a "breathing" mode symmetrical in the x and y directions, with out of phase motion in the z direction, while the $m = 2$ mode corresponds to an out of phase motion in the x and y directions, with approximately zero motion in the z direction.

After the sinusoidal perturbation of the appropriate symmetry was applied, the system was allowed to evolve in trap for a variable time, and was then released and imaged using absorptive imaging. Fits to the fluctuating size of the image revealed the frequencies of oscillation and damping rates of the excitations of the thermal and condensate fractions of the system, and we reproduce these results in Fig. 1.3.

In Fig. 1.3(a) we see the temperature dependence of the $m = 0$ and $m = 2$ collective modes. The frequency of the $m = 2$ excitation decreases with increasing temperature, while the $m = 0$ mode frequency increases sharply to the noninteracting limit. The damping rate, in Fig. 1.3(b), increases with increasing temperature for both modes. Results for the thermal cloud are indicated on both graphs, and show the expected

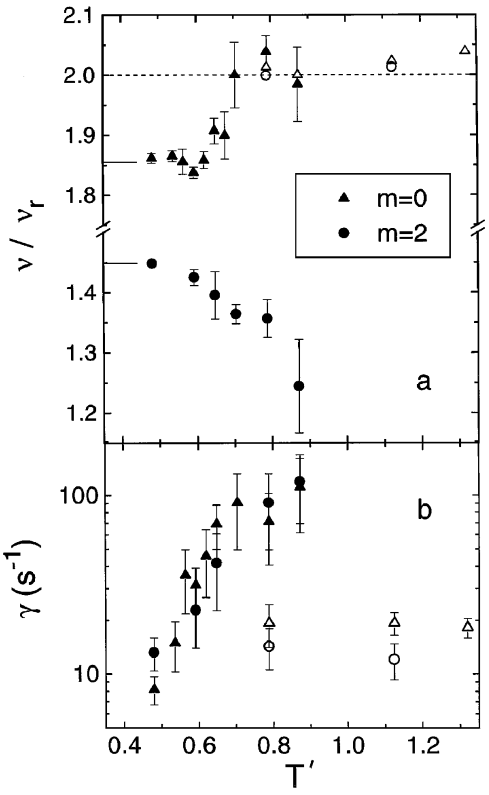

Figure 1.3: Temperature-dependent excitation spectrum: (a) Frequencies (normalised by the radial trap frequency) for $m = 0$ (triangles) and $m = 2$ (circles) collective excitation symmetries are shown as a function of normalised temperature T'. Oscillations of both the condensate (solid symbols) and noncondensate (open symbols) clouds are observed. Short lines extending from the left side of the plot mark the mean-field theoretical predictions in the $T = 0$ limit (for 6000 atoms). (b) Damping rates for the condensate and thermal components as a function of temperature. Reproduced from [3]. Copyright 1997 The American Physical Society

behaviour for a noninteracting gas.

A large body of theoretical work has been conducted on the subject of the JILA experiments [10–24] and is nicely summarised in a recent review by Proukakis and Jackson [25]. The temperature dependence of the $m = 2$ mode was accounted for by gapless Hartree-Fock Bogoliubov (HFB) theory calculations in 1998 [11], which included anomalous average and manybody effects in the system description (also see Refs. [26–29]). However, gapless HFB failed to account for the rather sudden upward shift in the $m = 0$ mode frequency observed in experiments at $T \approx 0.65T_c$.

The experiment of Ref. [5] comprehensively investigated the role of the thermal cloud in collective mode oscillations, and their findings that the thermal cloud was dynamical and interacted strongly with the condensate were in direct contrast with the theory used at the time, which assumed a static thermal cloud. This suggested that more comprehensive theory, inclusive of the dynamics of the thermal cloud would be needed to fully account for experimental findings.

An explanation for the behaviour of the $m = 0$ mode was first provided by Stoof and coworkers [18, 30] (also see [31]), who suggested that it arose from the coupling of in-phase and out-of-phase oscillations of the condensate and thermal cloud. This hypothesis suggested that an adequate theoretical description would require a dynamic treatment of both the condensate and noncondensate parts of the system. The first such formalism was the Zaremba-Nikuni-Griffin (ZNG) finite temperature theory [32–34] in which the system description takes the form of a Gross-Pitaevksii equation for the condensate, coupled to a Boltzmann equation for the noncondensate. Jackson and Zaremba [20] applied the ZNG theory to model the JILA experiment and found relatively good agreement with the experimental results. The following year, Morgan *et al.* [14] reported the results of a second order theory that were also in good agreement with the experimental results. That theory, the culmination of seven years of work by Burnett, Hutchinson, Morgan, Proukakis and coworkers [10–17, 22, 35], consistently included the dynamical interactions between the condensate and noncondensate atoms. To date, the only fully quantitative theoretical descriptions of these results have been provided by the ZNG formalism calculations of Jackson *et al.* [20] in 2002 and the second order theory of Morgan *et al.* [14] in 2003.

In Fig. 1.4 we show a summary of the results of these competing theories, as compiled in Ref. [25]. The wealth of theoretical data on this experiment makes it a highly desirable system to model. In fact, the description of these experiments has become the *de facto* standard for testing finite temperature quantum field theories of BEC. It is for this reason that we find it a valuable test of our finite temperature formalism.

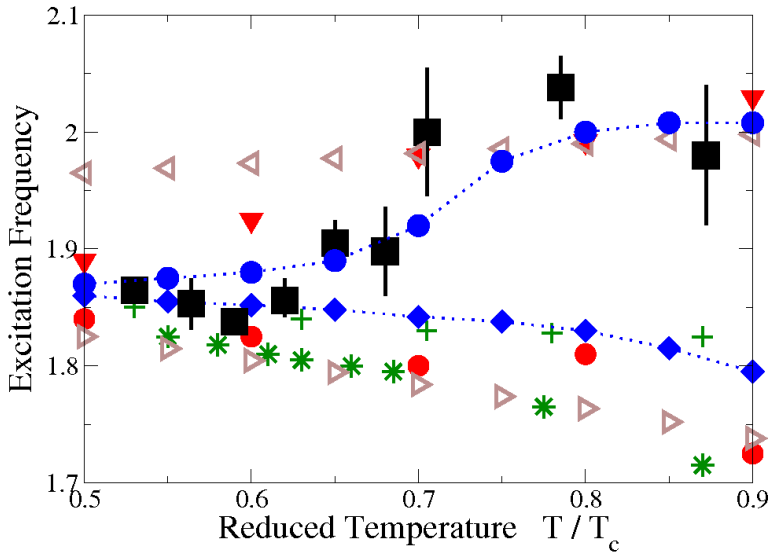

Figure 1.4: Comparison of the predictions for the temperature dependence of the excitation frequency of the $m = 0$ mode measured at JILA [3] (shown by black squares) based on different theoretical models, plotted for the region of the anomalous behaviour of the excitation frequency. Blue (filled) points joined by dotted lines: number-conserving formalism with (upper circles) or without (diamonds) direct excitation of the thermal cloud from the probe [14]. Green: static thermal cloud theories with (*, generalised HFB with $g_t = g(r)$ [11]) or without (+, HFBPopov [16]) inclusion of the anomalous average. Red (filled): predictions of ZNG approach for different excitation probe frequencies aimed at exciting primarily the condensate (lower circles, $\omega = 1.75\omega_z$) or the thermal cloud (inverted triangles, $\omega = 2\omega_z$) [20]. Brown: in-phase (left triangles, top) and out of phase (right triangles, bottom) modes of excitation between condensate and thermal cloud [18, 30]. Reproduced from [25] Copyright 2008 Institute of Physics and IOP Publishing Limited.

1.1.2 Correlations of Bose gas

In this section we will break our discussion of the correlations present in a Bose gas into two sections:

1. The development of experimental techniques for measuring correlations in ultra-cold atom experiments, and relevant theory.
2. The application of these developments to characterising the critical phenomena in the BEC phase transition.

Correlations in the Bose gas

Photon correlations were observed first in the landmark experiment of Hanbury-Brown and Twiss [36]. In that experiment, the second order correlation function (intensity correlations) of light was measured, revealing that photons from a thermal light source are bunched. Since then, there has been significant interest in making these measurements with an atomic source due to interaction effects and that both Bose and Fermi particles can be investigated.

The first experiments with atoms by Yasuda *et al.* [37] used a neutral (bosonic) atomic beam and confirmed atom bunching. Using ultra-cold Bose gases local high order correlations have been inferred from 3-body decay rates [38, 39], and first order coherence has been studied using matter wave interference [40, 41] and Bragg spectroscopy [42, 43].

More recently there has been spectacular experimental progress in the spatially resolved measurement of second order correlations in both bosonic and fermionic ultra-cold gases [44–49]. These experiments can be divided into two broad groups, based on the manner in which the measurements are made. One approach involves directly counting the atoms [44–46], while the other uses absorption imaging to measure density fluctuations [47–49].

The collaboration of the Orsay and Vrije University groups has produced a comparative study of the correlations in Bose and Fermi gases, using two different isotopes of metastable Helium. A schematic showing their method [44] is reproduced in Fig. 1.5. Briefly, an ultracold gas of metastable Helium is prepared in a harmonic trap, then is released and falls under gravity to the microchannel plate, which enables single atom detection. Every event is recorded, and this data is then analysed to study density correlations in the sample. In Fig. 1.6 we reproduce their results comparing second order correlations of the bosonic and fermionic samples.

We can clearly see that for the bosonic source, there is an enhancement in the correlation

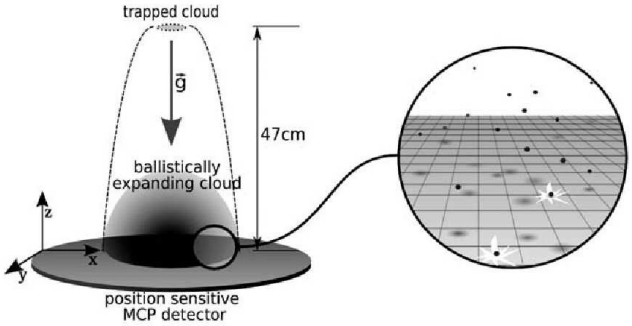

Figure 1.5: Schematic of the apparatus used in the experiments of [44, 46]. During its free fall toward the detector, a thermal cloud acquires a spherical shape. Single particle detection of the neutral atoms is possible because of each atoms 20eV internal energy that is released at contact with the MCP. Position sensitivity is obtained through a delay-line anode at the rear side of the MCP. Reproduced from [44]. Copyright 2005 American Association for the Advancement of Science.

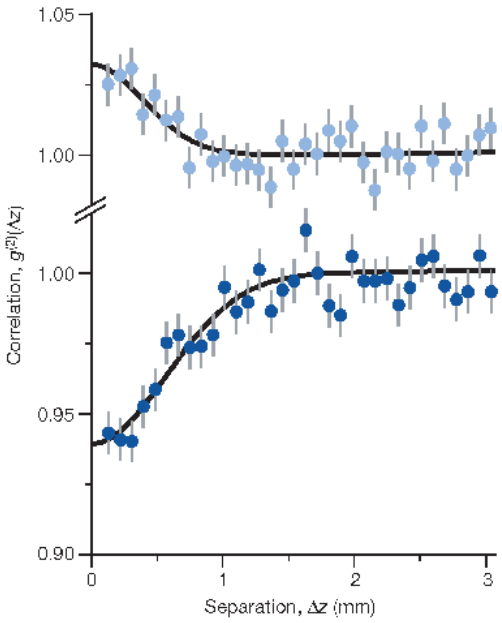

Figure 1.6: Normalised correlation functions for ^{4}He* (bosons) in the upper plot, and ^{3}He* (fermions) in the lower plot. Both functions are measured at the same cloud temperature (0.5 mK), and with identical trap parameters. The bosons show a bunching effect, and the fermions show antibunching. The correlation length for ^{3}He* is expected to be 33% larger than that for ^{4}He* owing to the smaller mass. Reproduced from [46]. Copyright 2007 Nature Publishing Group.

function over short distances (over the uncorrelated value of 1). This confirms bunching in the atomic source, i.e. the tendency of the bosons to cluster. For the fermionic case, we see a suppressed correlation function at small distances, revealing atomic antibunching. The distance scales over which this effect is seen is indicative of the correlation length of the system. This bunching (or antibunching) is caused by the constructive (or destructive) interference of the wavefunction describing the particles, and is ultimately linked to the fundamental properties of the two types of particle. While the bunching effect can be explained in both the quantum and classical pictures, the antibunching can only be explained in the quantum mechanical picture, and so the demonstration of this effect is very important.

Another very important result, which will be of particular interest in this thesis, is the comparison of correlation measurements for a pure BEC, and for a thermal cloud with no BEC present. This effect was first measured in the original Orsay experiment, [44], and also in the atom laser measurements of Ref. [45]. The ETH Zurich group has an alternative method for single particle detection, as shown in Fig. 1.7. Atoms from two regions in the cloud are output coupled, and fall under gravity to the cavity below. A single atom in the cavity reduces the transmission of photons through the cavity, and so single events can be measured. The time between atom transmissions reveals bunching in the atomic cloud, and the contrast of matter wave interference in the cavity reveals the first order coherence between the output coupled points in the BEC. This method of measurement has been applied to the critical behaviour in the Bose system [50], which we discuss further below.

The atom laser measurements showed that while bunching was present for an ultra-cold thermal gas, for the Bose condensed atom laser, no bunching occurred. This showed that the condensate was in fact able to be described as a fully coherent source, and able to be represented with a single, macroscopic wavefunction. The difference between condensate and thermal behaviour in interacting systems of finite temperature, and the emergence of this long-range order, will be aspects of focus in this work.

Correlations can also be measured from analysing the shot noise in absorption images. In Fig. 1.8 we show the experimental setup of Fölling *et al.* [47]. In this experiment, laser light is shone through the Bose cloud, and is absorbed by the atoms. While the average of many of these images gives the average density, it can be shown that a single image reveals atom shot noise, i.e. departures from the average density result, and this noise can be related to the correlations in the sample, e.g. see [47]. In Fig. 1.9 we present the results of [47], which study the correlations in a cloud of bosons released from an optical lattice. A single absorption image of the expanded cloud is shown in Fig. 1.9(a). In Fig. 1.9(c), the results of their analysis is shown: by analysing several

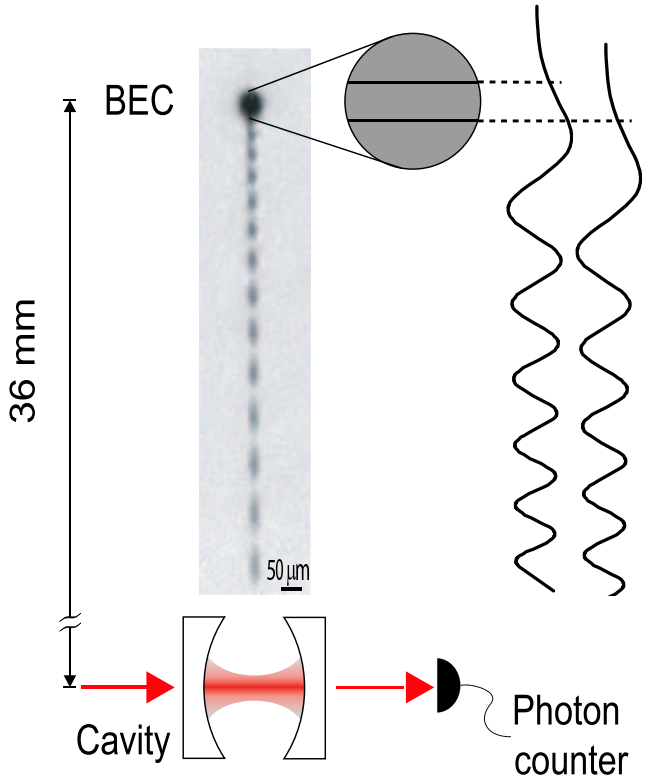

Figure 1.7: Schematic of the experimental setup. From two well defined regions in a Bose-Einstein condensate , atoms are uncoupled to an untrapped state. The real parts of the resulting atom laser wave functions are sketched on the right-hand side. The absorption image shows an interference pattern corresponding to $f = 1$ kHz and an atom flux 106 times larger than in the actual single atom interference experiment. Monitoring the transmission of a probe laser through a high-finesse optical cavity with a photon counter, single atom transits are detected. Reproduced from [51]. Copyright 2006 The American Physical Society.

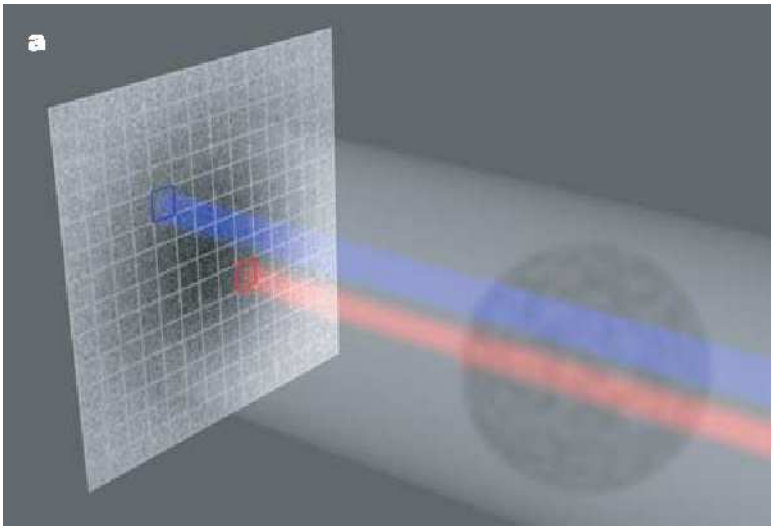

Figure 1.8: Illustration of the atom detection scheme. The cloud of atoms is imaged to a detector plane and sampled by the pixels of a CCD camera. Two pixels P1 and P2 are highlighted, each of which registers the atoms in a column along its line of sight. Depending on their spatial separation d, their signals show correlated quantum fluctuations. Reproduced from [47]. Copyright 2005 Nature Publishing Group.

images, they find density correlations revealing the lattice ordering of the system shown in the noise fluctuations of the images like that shown in Fig. 1.9(a).

There is a body of theoretical work that has been done with regard to correlations in Bose gases. This has included the extension of optical definitions of coherence to atomic samples [52, 53], and examining how correlation measurements made after the sample has expanded from its confinement potential relate to those of the original *in situ* system [54, 55]. Theoretical predictions for correlations functions of the trapped Bose gas has included studies of the ideal case [52, 55, 56] and interacting gases within mean-field descriptions [52].

There are several papers of relevance to the work done in this thesis on correlations. To date, the most comprehensive calculations of second order correlations in the interacting system used the Hartree-Fock Bogoliubov formalism [57], and we reproduce the main results of their paper in Fig. 1.10. These results show the local correlations within a Bose system for a variety of temperatures. We can see that for low fractions of the critical temperature, the second order correlation takes the value 1, as expected for a largely coherent system. As the temperature is increased, the spatial region over which the correlation function increases from the condensate value of 1 to the thermal cloud value of 2 decreases. This shows the decreasing coherence in the system as the condensate reduces in size, and the noncondensate dominates.

Calculations of similar nature were carried out by Holzmann *et al.* [58], using Path

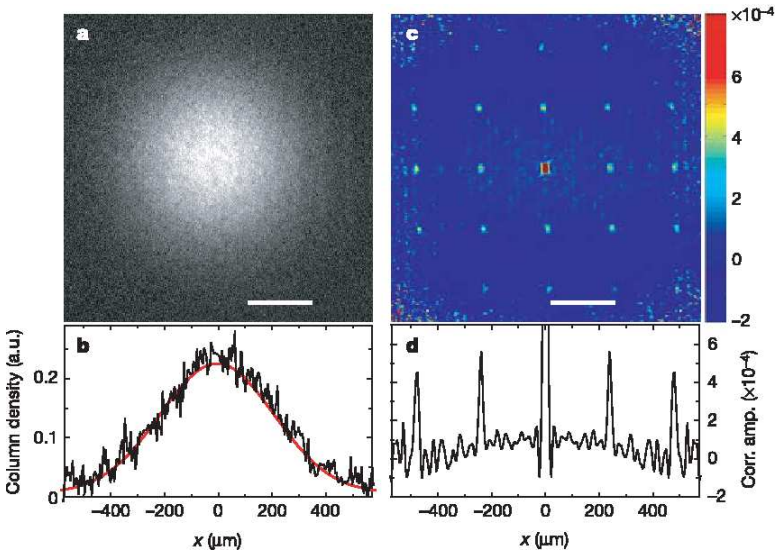

Figure 1.9: Single shot absorption image including quantum fluctuations and the associated spatial correlation function. (a), Two-dimensional column density distribution of a Mott insulating atomic cloud, released from a three-dimensional optical lattice potential. The white bars indicate the reciprocal lattice scale l. (b), Horizontal section (black line) through the center of the image in (a), and Gaussian fit (red line) to the average over 43 independent images, each one similar to (a). (c), Spatial noise correlation function obtained by analysing the same set of images, which shows a regular pattern revealing the lattice order of the particles in the trap. (d), Horizontal profile through the center of the pattern, containing the peaks separated by integer multiples of l. Reproduced from [47]. Copyright 2005 Nature Publishing Group.

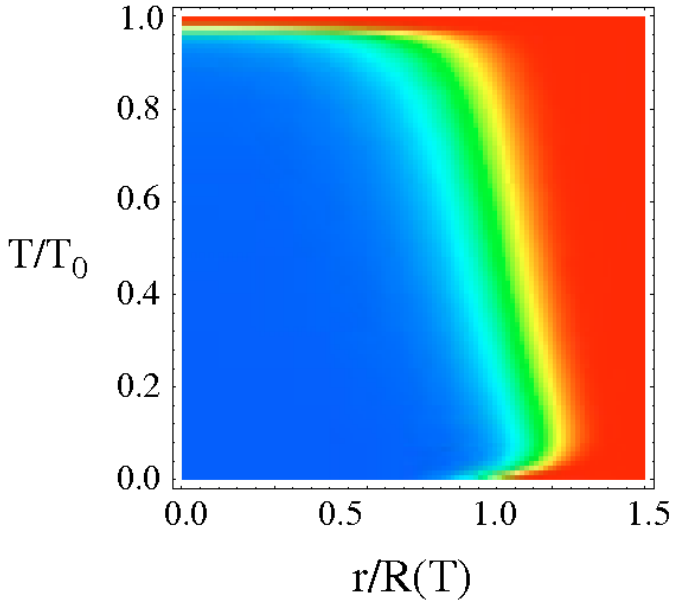

Figure 1.10: A false-colour plot of $g^2(r)$ vs. reduced temperature, T/T_0, and radial trap coordinate r, for atoms in a spherical trap. Blue corresponds to $g^2 = 1$ viz. coherence characteristic of a laser source; red to $g^2 = 2$ viz. coherence characteristic of a thermal source Here, T_0 is the condensation temperature. Reproduced from [57]. Copyright 1997 OSA.

Integral Quantum Monte-Carlo methods. These results showed the two point second order correlation function at a variety of temperatures, taking into account the hardcore repulsion of the interacting bosons. Steel *et al.* [59] measured the first order temporal correlation function for a harmonically trapped BEC, comparing two different phase space techniques, the positive P and Wigner representations (the Wigner formalism is equivalent to the zero temperature extension of our PGPE formalism). A non-local (two point) extension of the formalism of [57] was used to calculate the first order correlation function of the quasi-2D Bose gas [60]. Since our primary interest here is in the 3D Bose gas so we do not consider the rather extensive literature on quasi-1D and 2D gases (e.g. see [61]).

Generally speaking, it is a considerable challenge to calculate correlation functions in a manner that consistently includes the effect of interactions and harmonic confinement. Near the critical point, where a mean-field analysis is no longer valid, there are currently no reliable calculations that have been applied to realistic experimental systems. In this thesis we will develop methods to calculate correlation functions for experimentally realisable conditions, and will also consider the extension of these methods to the phase transition region.

Critical phenomena

The onset of the condensed phase in a Bose gas is a second order transition, and is driven solely by quantum statistical effects. The concept of universality states that the properties of a system in the critical region are independent of the microscopic details of the system, and depend only on a few general system features such as its dimensionality and the symmetry of the order parameter that emerges at the transition. In this context, the critical behaviour of a weakly interacting 3D Bose gas should be identical to that of ^{4}He at the superfluid transition, or to other systems of the same universality class (usually referred to as the 3D XY universality class). Accordingly, high precision experimental measurements of critical ^{4}He (e.g. see [62]) are usually compared against theoretical calculations using idealised XY or ϕ^4 models [63–65], rather than a microscopic description of the system.

The availability of experimental techniques for measuring correlations [66–71] is an important feature of the ultra-cold atom systems that has received extensive theoretical attention, particularly in relation to (zero temperature) quantum phase transitions (e.g. see [72–80]). Another area of interest is the effect of critical fluctuations on correlations in the system at the finite temperature transition, particularly as other quantities usually examined in condensed matter (e.g. susceptibilities and heat capacity) are not easy to measure in atomic gases. While the critical fluctuations of weakly interacting 1D and 2D Bose gases are dominant over a wide temperature range (e.g. see [41, 81]), it was previously thought that the width of the critical region about condensation temperature, T_c, would be far too narrow to permit experimental investigation in the 3D system. However, in extraordinary recent experiments Donner *et al.* [50] have made such measurements of a trapped 3D Bose gas, and were able to determine the critical exponent for the divergence of the correlation length to be $\nu = 0.67 \pm 0.13$. The main results of their work are shown in Fig. 1.11.

In the experiment of Donner *et al.* [50], atoms were output coupled from two points symmetric about the center of a Bose cloud using an RF probe, and the resulting atoms falling under gravity were detected with high precision using a cavity, as shown in Fig. 1.7. This measurement allowed them to calculate the second order correlations between particles, and thus infer the correlation length. It is known that the correlation length present in a system is proportional to the temperature as $\xi \propto |T - T_c|^{-\nu}$, where ν is the critical exponent of the transition. In Fig. 1.11 we show their results for the divergence of the correlation length as the critical temperature is approached from above, from which they measure ν. In its own right this result is an impressive demonstration that universality applies to a mesoscopic system with of order 10^5 atoms. Additionally, this direct measurement of two-point correlations is of interest because it has not been

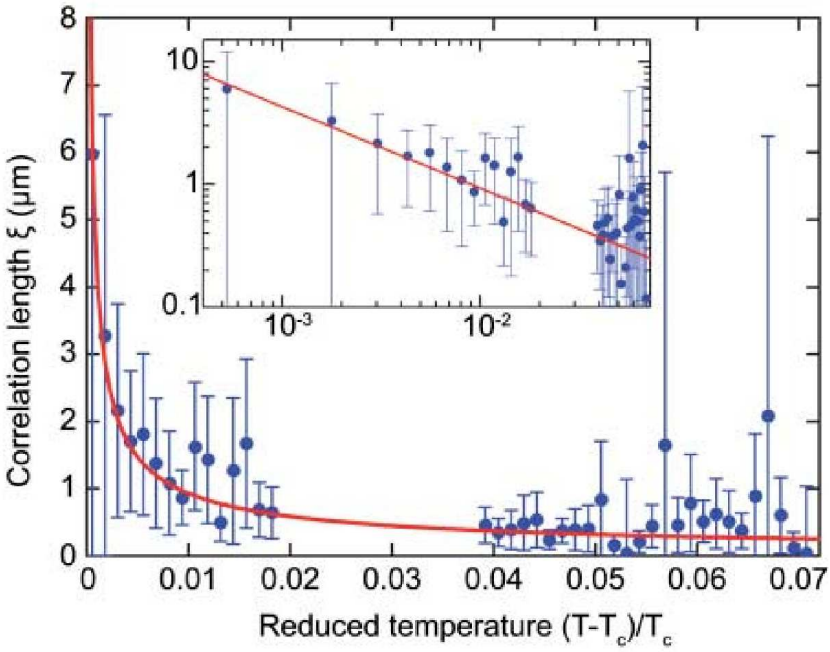

Figure 1.11: Divergence of the correlation length as a function of temperature. The red line is a fit of $|T - T_c|^{-\nu}$ to the data, with ν and T_c as free parameters. Inset: Double logarithmic plot of the same data. Reproduced from [50]. Copyright 2007 American Association for the Advancement of Science.

possible to do this in helium, although a value for the correlation length critical exponent of helium ($\nu = 0.67056 \pm 0.0006$) is inferred from the heat capacity exponent using Josephson scaling relation, $\alpha = 2 - 3\nu$.

This measurement of the correlation length in the trapped Bose gas would be a natural extension to the formalism we will develop to calculate correlation functions in the Bose system and poses the formidable challenge for the PGPE to reveal critical physics. We also note that we are able (through the finite size of our system) to probe finite size effects. Finite-size effects have a profound influence on the critical properties of a system, and have been extensively studied to understand the cross-over of helium critical behaviour during dimensional reduction [82]. Such systems, confined to a finite region of size L, are well described by finite-size scaling theory [83, 84]. This theory shows that there is a universal scaling function that relates physical quantities of the finite to infinite systems depending on the quantity, the ratio of the correlation length to the system size, and the nature of the boundary conditions. In this context the scenario occurring in the harmonic trap is rather interesting (see Fig. 1.12), and was first considered by Damle *et al.* in 1996 [85]. The effect of the trapping potential is to slowly vary the local value of the chemical potential. If the gas is critical at the trap center, then moving out radially, the system gradually becomes normal. Thus the finite-size boundary conditions

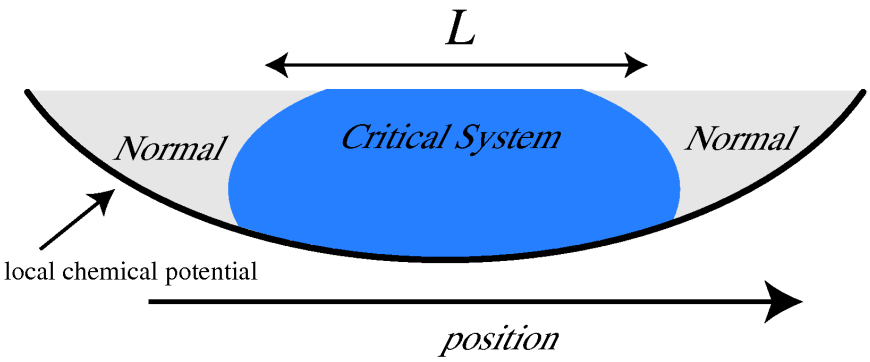

Figure 1.12: Schematic view of the critical regime of a trapped Bose gas. The local chemical potential varies across the system due to the harmonic trap potential. When the system is critical at the center, the criticality extends over the finite spatial range L with a normal cloud boundary condition.

are rather difficult to describe, as they require an understanding of the (non-universal) normal system. The experiment by Donner *et al.* [50] did not observe finite-size effects: their two-point measurements were made over a region much smaller than the spatial extent of the critical region, and yielded a value of the critical exponent in line with the uniform system. The finite temperature formalism we will develop to describe this system is applicable to both the normal system, and the critical system. Thus it is able to be easily applied to the system which is a mixture of those two states. This will allow us to make steps toward formalism which can be accurately used in the phase transition regime of the trapped interacting Bose gas.

1.2 C-field Theory - the PGPE

The experimental developments outlined in Sec. 1.1 show that there has been a great deal of interest in non-equilibrium dynamics and finite temperature properties of Bose systems. These experiments are all conducted where there is a large fraction of the system that is not condensed, and interactions between the condensate and thermal cloud play an important role in determining the properties of the system. In general, it is difficult to make a theoretical description of the finite temperature Bose system which includes the effect of interactions, and the harmonic trapping potential. There has been a class of theoretical methods developed to deal with this regime, which are referred to as the classical field (or c-field) methods, and include the truncated Wigner, the Projected Gross-Pitaevskii equation (PGPE), and the Stochastic Gross-Pitaevskii equation (SGPE) [86]. In this thesis, our focus is on the PGPE, and the development of this formalism to describe current systems of interest. The PGPE is non-perturbative, and includes the dynamics of the low-energy modes of the system exactly. We outline

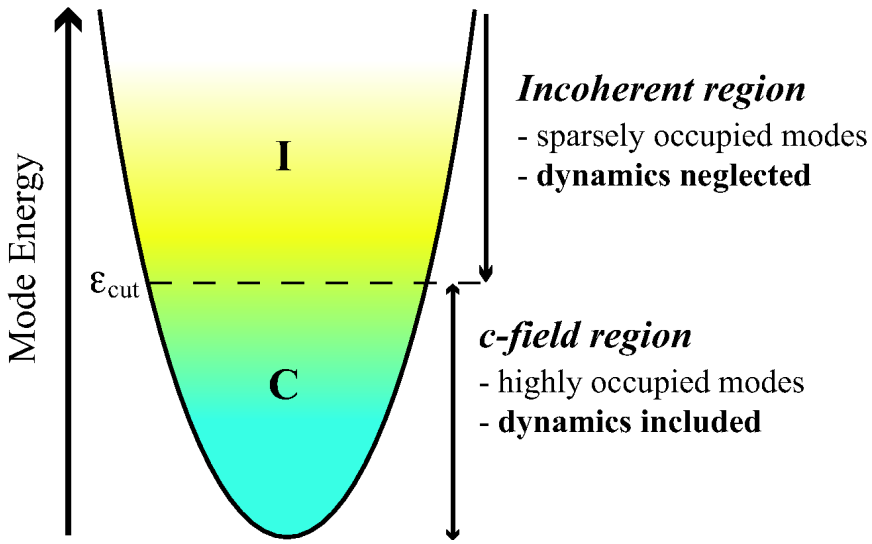

Figure 1.13: Schematic view of the c-field and the incoherent regions for a Bose gas in a harmonic trap potential, and the approximations we employ in our treatment of the collective mode dynamics.

the historical developments of this theory below.

It was first argued that the Gross-Pitaevskii equation (GPE) could be used to describe a finite temperature Bose gas by Svistunov [87] and Kagan *et al.* [88–90]. They argued that at finite temperature, highly occupied modes can be described classically by neglecting the quantum fluctuations, analogous to the highly occupied modes of a laser being well described using classical equations. Early calculations were performed by Damle *et al.* [91], who studied the approach to equilibrium of a Bose gas to a superfluid state, and by Marshall *et al.* [92], who investigated evaporative cooling in the Bose cloud. Both of these works used the GPE to investigate finite temperature clouds.

The projection operator was first introduced by Davis *et al.* [93]. The purpose of this projector was to consistently split the system modes into two separate parts: the c-field region, which contains all of the low-energy modes with high occupation, and the incoherent region, which contains the high energy modes which are sparsely occupied. The energy cutoff $\epsilon_{\rm cut}$ between the two regions is chosen so that all of the c-field region modes contain at least one particle. Occupations of this order justify the classical description of these modes. The modes of the incoherent region cannot be treated classically due to the low mode occupation, and so we assume that the incoherent region is in thermal and diffusive equilibrium with the c-field region, and that the incoherent region can be well described using a meanfield description. In Fig. 1.13 we show a schematic view of the c-field and incoherent regions, and the position of our cutoff, $\epsilon_{\rm cut}$.

In Fig. 1.14 we reproduce the results of Davis *et al.* [94], who compared PGPE predic-

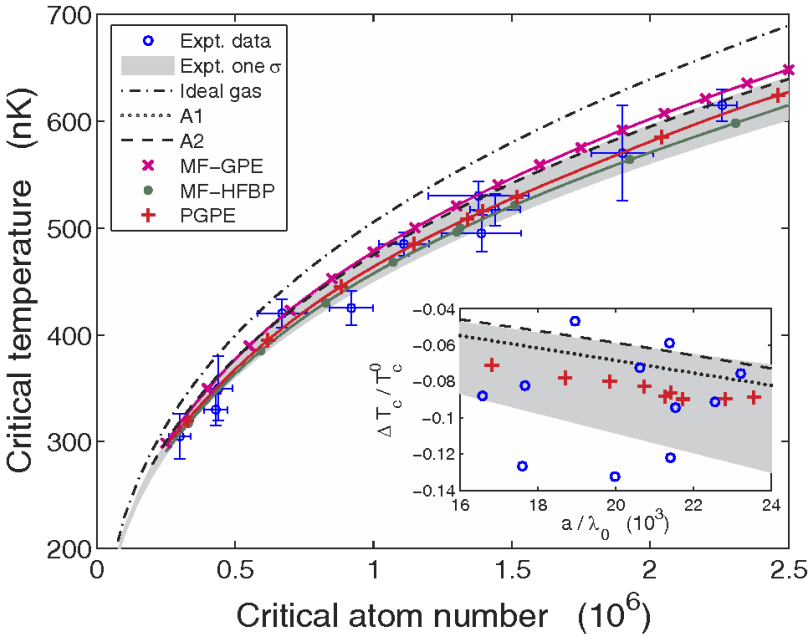

Figure 1.14: Comparison of theoretical calculations with experiment. The main figure plots T_c vs N_c , whereas the inset plots the shift of T_c against the scattering length over the de Broglie wavelength, a/λ_0 . Experimental results: data (open circles), one σ fit (gray area). Theoretical results for Tc : PGPE (pluses), against analytic and mean-field theories. Solid lines through the data points are polynomial fits. Reproduced from [94]. Copyright 2006 The American Physical Society.

tions for the change in critical temperature with that of experiment [95], and with other theoretical treatments. The results show excellent agreements with experiment. We note that improved accuracy would be required in experiment to distinguish between the theories. In Fig. 1.15 we show recent results of the PGPE predictions of the irrotational and superfluid oscillation frequencies for the scissors mode of a 2D Bose gas which has yet to be investigated experimentally. In related work those authors also used the PGPE to explain the emergence of phase defects in the 2D system [96] as observed by the ENS group [97]. The PGPE has been shown to be applicable to the critical region also, e.g. see [96,98–100]. We note also that other c-field methods have had a great deal of success in comparison with finite temperature experiments. In Fig. 1.16 we show results of the SGPE simulations for the formation of the BEC [101], after a temperature quench. We can see spontaneous formation of vortices in the BEC, the statics of which were in good agreement with experiment [101]. The truncated Wigner formalism (applicable to the $T = 0$ case where quantum noise dominates) has been used by Norrie *et al.* [102] to study the collisional halo of two colliding BECs. The main results are reproduced in Fig. 1.17. The modeling of this scenario was a significant achievement, as this was the first analysis of the condensate collision that treated the full dynamics of the field, and so could be applied to systems in which a substantial fraction of the

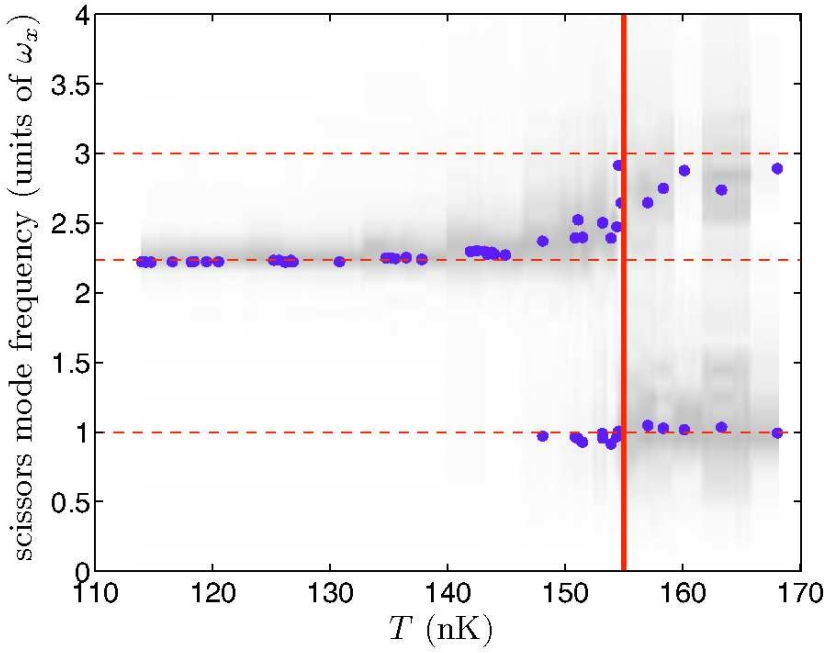

Figure 1.15: Scissors mode frequencies as a function of temperature. The horizontal dashed lines are the analytical predictions of the irrotational and superfluid component oscillation frequencies and the solid vertical line is our estimate of the superfluid transition temperature. Reproduced from [100]. Copyright 2008 The American Physical Society.

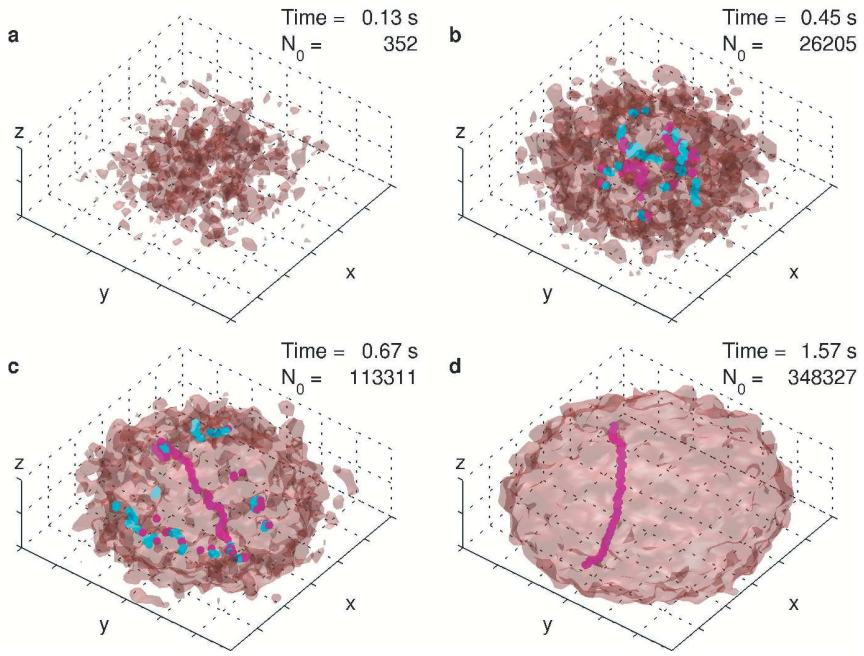

Figure 1.16: BEC growth dynamics. Four snapshots during the simulated growth of a BEC showing isodensity surfaces (in light red) in a three- dimensional rendering. Vortex cores of opposite charges about the z axis are indicated as magenta and cyan lines. The corresponding times are 0.13s (a), 0.45s (b), 0.67s (c), 1.57s (d). Reproduced from [101]. Copyright 2008 Nature Publishing Group.

initial condensate particles were scattered into the halo.

The new experimental developments outlined in this chapter pose a challenge for theory and motivate the continued development of theories of Bose systems. In this thesis we will address this need, by developing and applying the PGPE formalism to explore these areas of interest.

1.3 This work

1.3.1 Thesis overview

In this thesis we describe and develop the PGPE for use in comparison with finite temperature experiments. The layout of the thesis is as follows. In Chapter 2 we outline the formalism of the PGPE, and discuss methods for measuring system parameters. We go on to discuss the numerical implementation of the PGPE in Chapter 3. In Chapter 4 we present results for a comprehensive study of the finite temperature excitations of a Bose gas, modelling the experiment of Jin *et al.* [3]. In Chapter 5 we develop formalism to calculate correlations in the Bose gas at finite temperature, and present results for

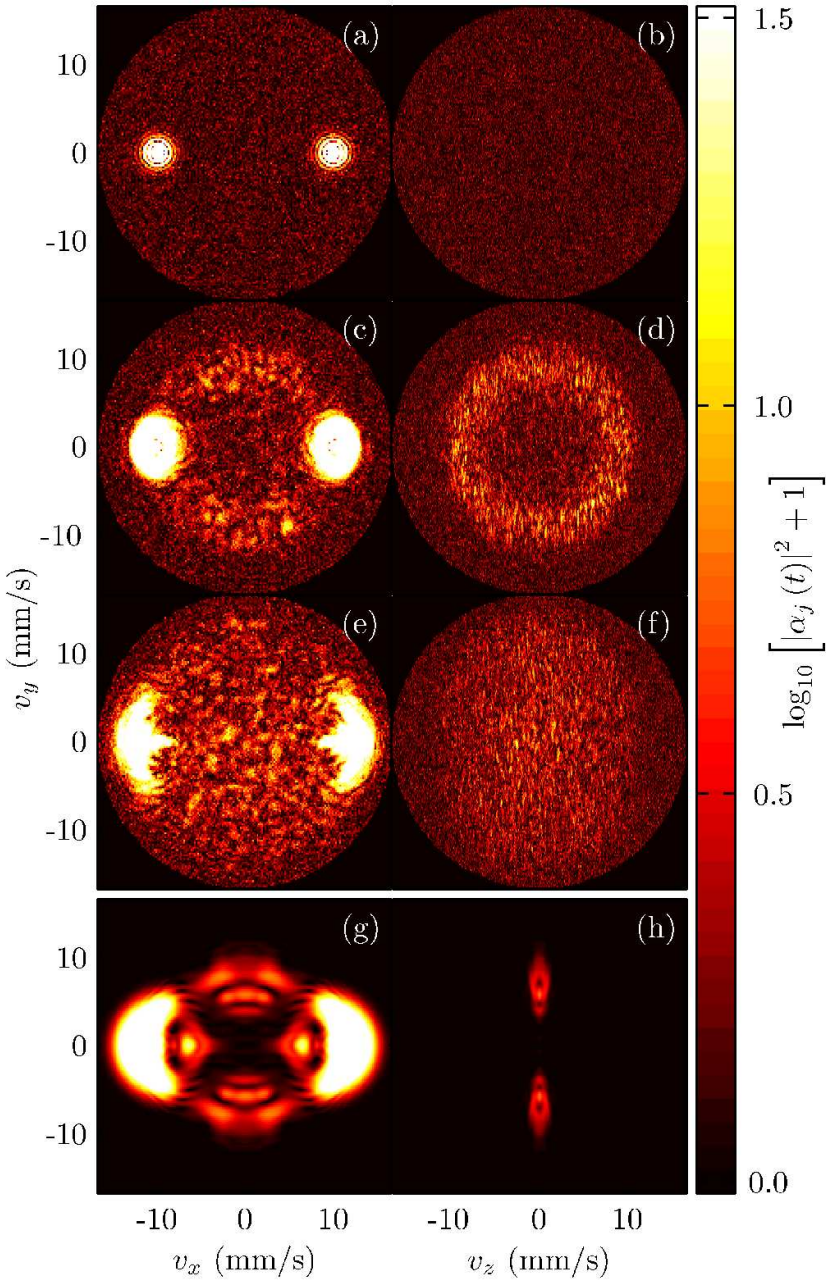

Figure 1.17: (a) (f) Velocity mode populations on the planes $v_z = 0$ (left) and $v_x = 0$ (right) for the condensate collision described in the text at $t = 0$ (top), $t = 0.5$ ms (middle), and $t = 2.0$ ms (bottom). The spherical momentum cutoff is clearly visible in the upper plots due to the presence of quantum fluctuations. (g)(h) Mode populations at $t = 2.0$ ms for an identical collision excluding vacuum noise. Reproduced from [102]. Copyright 2005 The American Physical Society.

an experimentally feasible system. We also extend this formalism to the critical region, and present results on the critical phenomena of a BEC, following the methodology of Donner *et al.* [50] in Chapter 6. We conclude in Chapter 7.

1.3.2 Peer-reviewed Publications

We note that the main results of this thesis have been submitted for publication. The excitation study of Chapter 4 has been submitted for publication to Physical Review A in November 2008, and since the submission of ths thesis has been published, see Ref. [103]. The two point correlation study of Chapter 5 has been published [99], and the phase transition study of Chapter 6 has been submitted for publication to Physical Review A in December 2008, and later published [104].

Additional collaborative work during this PhD has been devoted to optical lattices, and is not included in the main part of this thesis. So that this thesis might serve as a complete record of the work undertaken papers resulting from this are reproduced in Appendix C.

Chapter 2

Formalism

2.1 Introduction

Here we give details of the PGPE formalism which we will use to describe the finite temperature systems of interest in this thesis. The PGPE for a harmonically trapped system was first developed in [105]; a more recent review of this and other classical field techniques can be found in Ref. [86]

2.2 System Hamiltonian

We wish to describe a dilute gas of cold atoms. When describing a low energy system, it is appropriate to use an effective field theory, which is restricted to a low energy subspace (i.e. the L-region indicated in Fig. 2.1) Our system is then described by the second quantised Hamiltonian

$$\hat{H} = \int d\mathbf{r} \left\{ \hat{\Psi}^\dagger(\mathbf{r}) \left(-\frac{\hbar^2}{2m}\nabla^2 + V(\mathbf{r},t) \right) \hat{\Psi}(\mathbf{r}) + \frac{1}{2} U_0 \hat{\Psi}^\dagger(\mathbf{r}) \hat{\Psi}^\dagger(\mathbf{r}) \hat{\Psi}(\mathbf{r}) \hat{\Psi}(\mathbf{r}) \right\}, \quad (2.1)$$

where $\hat{\Psi}(\mathbf{r},t)$ is the Bose field operator for the full field. The Bose field operator annihilates a particle from position $\mathbf{r}$ at time t and obeys the equal time commutation relations

$$\left[\hat{\Psi}^\dagger(\mathbf{r},t), \hat{\Psi}^\dagger(\mathbf{r}',t) \right] = \left[\hat{\Psi}(\mathbf{r},t), \hat{\Psi}(\mathbf{r}',t) \right] = 0, \quad (2.2)$$

$$\left[\hat{\Psi}(\mathbf{r},t), \hat{\Psi}^\dagger(\mathbf{r}',t) \right] = \delta(\mathbf{r}-\mathbf{r}'). \quad (2.3)$$

In forming this Hamiltonian we have made the assumption that the interaction term between particles is well approximated by the contact potential $U_0 = 4\pi\hbar^2 a/m$, where a is the s-wave scattering length. This *pseudopotential* was first introduced in [106] as an approximation to the interaction potential, and is valid in the limit of only low energy collisions occurring, so will be appropriate for our work here. In principle the value of a appearing in the coupling constant may need to be renormalised appropriate to the energy cutoff in the theory. However, for the typical cutoffs we use in applications this renormalisation is of order the uncertainty in the scattering length itself. We refer the reader to [107] for a fuller discussion of the limitations of this approximation. Our potential term $V(\mathbf{r}, t)$ is defined as follows:

$$V(\mathbf{r}, t) = V_0(\mathbf{r}) + \delta V(\mathbf{r}, t), \tag{2.4}$$

where

$$V_0(\mathbf{r}) = \frac{1}{2} m(\omega_x^2 x^2 + \omega_y^2 y^2 + \omega_z^2 z^2), \tag{2.5}$$

is the harmonic trapping potential, and $\delta V(\mathbf{r}, t)$ is some small time-dependent perturbation to the system. We include this perturbation here as it is necessary to develop formalism to study the excitations of the trapped interacting Bose gas, which we explore later in this work. For future reference, we also define

$$H_0 = -\frac{\hbar^2}{2m}\nabla^2 + V_0(\mathbf{r}), \tag{2.6}$$

which we refer to as the single particle Hamiltonian. The Heisenberg equation of motion of $\hat{\Psi}(\mathbf{r}, t)$ is

$$i\hbar\frac{\partial\hat{\Psi}(\mathbf{r}, t)}{\partial t} = \left(-\frac{\hbar^2}{2m}\nabla^2 + V_0(\mathbf{r}) + \delta V(\mathbf{r}, t)\right)\hat{\Psi}(\mathbf{r}, t) + U_0|\hat{\Psi}(\mathbf{r}, t)|^2\hat{\Psi}(\mathbf{r}, t), \tag{2.7}$$

which gives the full dynamics of the system. This equation is impossible to solve in the regime of 3D BEC experiments without considerable use of approximation. In the next section we explain our approach to obtain a practical method for simulating this equation.

2.3 The Projected Gross-Pitaevskii Equation

Here we outline the PGPE formalism. The key feature of this formalism is the formal separation of the modes of the system, as performed by the projection operator. The projection operator was first introduced by Davis [93] for the case of the homogeneous 3D Bose gas. This projector separates the modes of the system into two regions, and at

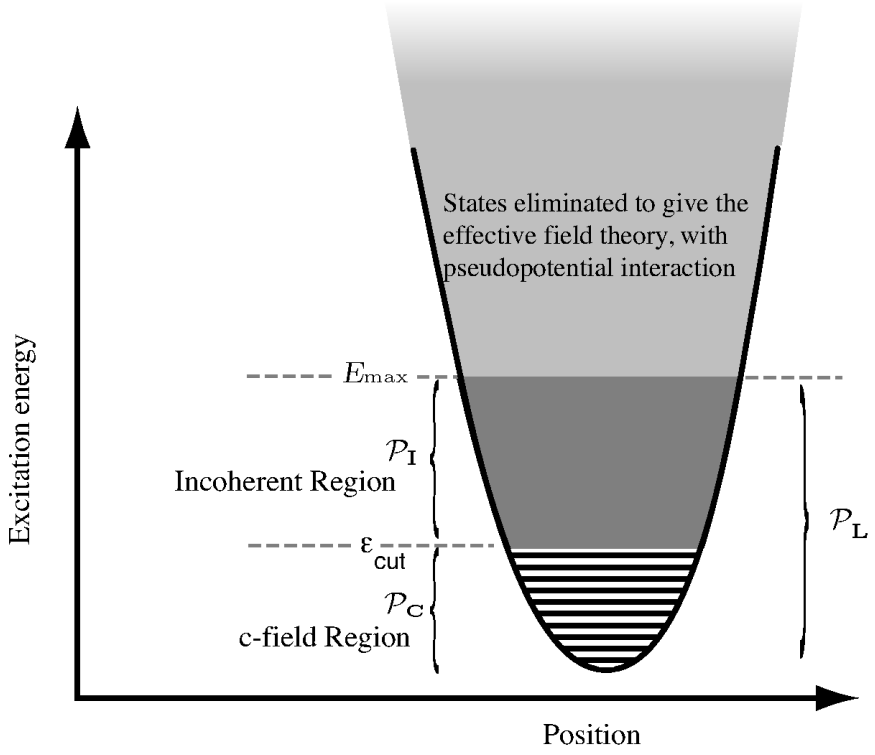

Figure 2.1: Schematic view of the classical region, the incoherent region, and the states eliminated to give the effective field theory for an harmonic trap

finite temperatures we can choose this energy cutoff $\epsilon_{\rm cut}$ to define these regions as:

Classical Region, **C**. This region contains the low energy modes of the system, which are highly occupied, and can be described using a classical description. Note, here we use the term classical in the sense of "classical matter waves" in which the effect of adding/removing a quantum from each mode is negligible.

Incoherent region, **I**. This region contains the high energy modes, which are sparsely occupied. These must be treated with a separate formalism as the inclusion of these modes in the classical description will lead to a UV catastrophe.

We outline the application of this projection operator to a harmonically trapped system below, as detailed in [105].

2.3.1 Projection Operators

We define the projectors which formalise the cutoff in our system, as follows:

$$P_{\mathbf{C}}\{F(\mathbf{x})\} \equiv \sum_{n\in\mathbf{C}} \phi_n(\mathbf{x}) \int d^3\mathbf{x}' \phi_n^*(\mathbf{x}') F(\mathbf{x}'), \tag{2.8}$$

$$P_{\mathbf{I}}\{F(\mathbf{x})\} \equiv \sum_{n\in\mathbf{I}} \phi_n(\mathbf{x}) \int d^3\mathbf{x}' \phi_n^*(\mathbf{x}') F(\mathbf{x}'), \tag{2.9}$$

which define the **C** and **I** region projections of a function F, respectively. In the above we have taken $\phi_n(\mathbf{x})$ to be the harmonic oscillator basis that diagonalises the single particle Hamiltonian, i.e.,

$$H_0\phi_n(\mathbf{x}) = \epsilon_n\phi_n(\mathbf{x}), \tag{2.10}$$

and this forms the appropriate basis for implementing an energy cutoff. We now define $n \in \mathbf{C}$ as the modes, n, below this energy cutoff and included within the classical region **C**, and $n \in \mathbf{I}$ as the modes above the energy cutoff and included within the incoherent region **I**. We can expand the field operator in this basis,

$$\Psi(\mathbf{x}) = \sum_n \hat{a}_n \phi_n(\mathbf{x}), \tag{2.11}$$

making the implementation of this energy cutoff trivial. The mode operator $\hat{a}_n$ annihilates a particle from mode n, and obeys the equal time commutation relations

$$[\hat{a}_i, \hat{a}_j] = \left[\hat{a}_i^\dagger, \hat{a}_j^\dagger\right] = 0, \tag{2.12}$$

$$\left[\hat{a}_i, \hat{a}_j^\dagger\right] = \delta_{ij}. \tag{2.13}$$

We can then define the field operators on the classical and incoherent regions in terms of this energy ϵ_n as follows:

$$\hat{\psi}_{\mathbf{C}}(\mathbf{x}) = P_{\mathbf{C}}\{\hat{\Psi}(\mathbf{x})\}, \tag{2.14}$$

$$\hat{\psi}_{\mathbf{I}}(\mathbf{x}) = P_{\mathbf{I}}\{\hat{\Psi}(\mathbf{x})\}, \tag{2.15}$$

where we note that

$$\hat{\Psi}(\mathbf{x}) = \hat{\psi}_{\mathbf{C}}(\mathbf{x}) + \hat{\psi}_{\mathbf{I}}(\mathbf{x}). \tag{2.16}$$

We choose the cutoff between the two regions $\epsilon_{\rm cut}$ as the energy in the single particle basis where the occupation of the mode is ≈ 1. There has been a significant body of work on applications of the classical field methods to zero and finite temperature properties of Bose gases [59, 92–94, 96, 98, 102, 108–119]. These studies show that this splitting of the field operator can be done in a consistent manner and provides a quantitative

description of experiment (in particular see Ref. [94]). In this thesis we present results in Sec. 4.3.5 showing the effect of varying the cutoff on physical predictions of the theory.

2.3.2 C-field Equation of Motion (PGPE)

We can use the decomposition of Eq. (2.16) to find an equation of motion for the classical field operator. We substitute Eq. (2.16) into the Hamiltonian of Eq. (2.1), from which we can derive the Heisenberg equation of motion for the operator $\hat{\psi}_{\mathbf{C}}(\mathbf{x})$. It is now appropriate to introduce the first significant approximation: to neglect the quantum fluctuations in the classical field operator, and replace it by a classical field, i.e.

$$\hat{\psi}_{\mathbf{C}}(\mathbf{x}) \rightarrow \psi_{\mathbf{C}}(\mathbf{x}), \tag{2.17}$$

The condition that the modes in the coherent region are appreciably occupied justifies this approximation. Formally,

$$\psi_{\mathbf{C}}(\mathbf{x}) = \sum_{n \in \mathbf{C}} c_n \phi_n(\mathbf{x}), \tag{2.18}$$

where the c_n are complex numbers. Taking the average value of the Heisenberg equation for the field $\psi_{\mathbf{C}}(\mathbf{x})$ yields [93]

$$\begin{aligned} i\hbar\frac{\partial\psi_{\mathbf{C}}(\mathbf{x})}{\partial t} &= (H_0 + \delta V)\psi_{\mathbf{C}}(\mathbf{x}) + U_0 P_{\mathbf{C}}\{|\psi_{\mathbf{C}}(\mathbf{x})|^2\psi_{\mathbf{C}}(\mathbf{x})\} \\ &+ U_0 P_{\mathbf{C}}\{2|\psi_{\mathbf{C}}(\mathbf{x})|^2\langle\hat{\psi}_{\mathbf{I}}(\mathbf{x})\rangle + \psi_{\mathbf{C}}(\mathbf{x})^2\langle\hat{\psi}^\dagger_{\mathbf{I}}(\mathbf{x})\rangle\} \\ &+ U_0 P_{\mathbf{C}}\{\psi^*_{\mathbf{C}}(\mathbf{x})\langle\hat{\psi}_{\mathbf{I}}(\mathbf{x})\hat{\psi}_{\mathbf{I}}(\mathbf{x})\rangle + 2\psi_{\mathbf{C}}(\mathbf{x})\langle\hat{\psi}^\dagger_{\mathbf{I}}(\mathbf{x})\hat{\psi}_{\mathbf{I}}(\mathbf{x})\rangle\} \\ &+ U_0 P_{\mathbf{C}}\{\langle\hat{\psi}^\dagger_{\mathbf{I}}(\mathbf{x})\hat{\psi}_{\mathbf{I}}(\mathbf{x})\hat{\psi}_{\mathbf{I}}(\mathbf{x})\rangle\}. \end{aligned} \tag{2.19}$$

To arrive at the PGPE we neglect all couplings between the coherent and incoherent regions. In this manner, we treat the incoherent region as a thermal bath at equilibrium. For equilibrium clouds, this should be a good approximation. The PGPE is as follows

$$\begin{aligned} i\hbar\frac{\partial\psi_{\mathbf{C}}(\mathbf{r},t)}{\partial t} &= \left(-\frac{\hbar^2}{2m}\nabla^2 + V_0(\mathbf{r}) + \delta V(\mathbf{r},t)\right)\psi_{\mathbf{C}}(\mathbf{r},t) \\ &+\mathcal{P}\left\{U_0|\psi_{\mathbf{C}}(\mathbf{r},t)|^2\psi_{\mathbf{C}}(\mathbf{r},t)\right\}, \end{aligned} \tag{2.20}$$

2.3.3 Ergodicity and Time Averaging

We will now consider the PGPE for cases where $\delta V(\mathbf{r},t) = 0$, i.e. the system Hamiltonian (Eq. (2.1)) is time independent. The energy functional for this system is given

as

$$H_{\mathbf{C}}[\psi_{\mathbf{C}}] = \int d\mathbf{r}\, \psi^*_{\mathbf{C}} \left(-\frac{\hbar^2}{2m}\nabla^2 + V_{trap}(\mathbf{r}) + \frac{U_0}{2}|\psi_{\mathbf{C}}|^2 \right) \psi_{\mathbf{C}}, \tag{2.21}$$

and the number functional as

$$\mathcal{N}_{\mathbf{C}}[\psi_{\mathbf{C}}] = \int d\mathbf{r}\, |\psi_{\mathbf{C}}(\mathbf{r})|^2, \tag{2.22}$$

where we will use the notation

$$E_{\mathbf{C}} = H_{\mathbf{C}}[\psi_{\mathbf{C}}], \tag{2.23}$$

$$N_{\mathbf{C}} = \mathcal{N}_{\mathbf{C}}[\psi_{\mathbf{C}}], \tag{2.24}$$

to give the values of the energy and number of particles in the classical region, respectively. These are constants of motion, i.e. under evolution according to Eq. (2.20), $E_{\mathbf{C}}$ and $N_{\mathbf{C}}$ are constant. These quantities are therefore important in characterising the equilibrium states the system thermalises to. Indeed, the PGPE (Eq. (2.20)) is a microcanonical system, and due to the presence of the nonlinear interactions it's evolution is expected to be ergodic for the 3D trapped gas with sufficiently large U_0. This means that the system will move through a series of microstates as it evolves in time, and sampling these microstates is equivalent to taking an ensemble average, for a long enough evolution, i.e.

$$\langle \mathcal{O} \rangle_{ensemble} = \lim_{\theta\to\infty} \frac{1}{\theta} \int dt \langle \mathcal{O} \rangle, \tag{2.25}$$

where $\mathcal{O}$ is some observable. In this work we extensively use time averaging to calculate equilibrium properties. It is not practical for us to evolve the PGPE over extremely long periods of time to sample a large portion of the accessible microstates. Some care needs to be taken when performing finite time averaging. e.g. over ~ 100 trap periods. Usually the initial state is some non-equilibrium configuration we have generated with the desired constants of motion. The initial evolution of this state is strongly nonequilibrium and passes through many microstates not typical of the equilibrium state. Thus to avoid biasing our averages we do not sample until the system has "thermalised", which usually takes of order a few trap periods of evolution (e.g. see Ref. [120])

2.3.4 Common Observables

We can calculate the density of the system by time-averaging the classical field, i.e.

$$n_{\mathbf{C}}(\mathbf{r}) = \langle \psi^*_{\mathbf{C}}(\mathbf{r}) \psi_{\mathbf{C}}(\mathbf{r}) \rangle \approx \frac{1}{M_S} \sum_{S=1}^{M_S} |\psi_{\mathbf{C}}(\mathbf{r}, t_S)|^2, \tag{2.26}$$

where M_S is the number of samples taken of the classical field, and t_S is the time at which they are taken. Typically we would use 500 samples at equilibrium, taken over a time period of the order of 100 trap periods. The momentum space field operator can be defined as

$$\phi_{\mathbf{C}}(\mathbf{p}) = \frac{1}{(2\pi)^{3/2}} \int d\mathbf{r} \psi_{\mathbf{C}}(\mathbf{r}) e^{-i\mathbf{p}\cdot\mathbf{r}/\hbar} \tag{2.27}$$

and the corresponding momentum density is given as

$$n_{\mathbf{C}}(\mathbf{p}) \approx \frac{1}{M_S} \sum_S |\phi_{\mathbf{C}}(\mathbf{p}, t_S)|^2 \tag{2.28}$$

We give examples of the time-averaged and instantaneous position and momentum densities in later sections of this work.

To find the condensate fraction of our system, we use the Penrose Onsager definition [121], that the condensate N_0 is the largest eigenvalue of the one body density matrix

$$G^{1B}(\mathbf{x}, \mathbf{x}') = \langle \psi^*_{\mathbf{C}}(\mathbf{x}) \psi_{\mathbf{C}}(\mathbf{x}) \rangle, \tag{2.29}$$

which is easily evaluated with time averaging. We use the eigenvector $\psi_{\rm cond}$ associated with this

$$\int d\mathbf{x}' G^{1B}(\mathbf{x}, \mathbf{x}') \psi_{\rm cond}(\mathbf{x}') = N_{\rm cond} \psi_{\rm cond}(\mathbf{x}) \tag{2.30}$$

to define the condensate mode of the system with condensate number $N_{\rm cond}$. We emphasise here that this condensate mode is not the bare ground state of our basis, rather, a mixture of the modes of the classical region. We note another definition of the condensate "order parameter" used in symmetry-breaking formalisms is the mean value of the field operator, which in our case would correspond to $\langle \psi_{\mathbf{C}} \rangle$. However, we note that this average in our case is generally zero, and so this definition is of no practical use in our formalism.

2.3.5 Temperature

To calculate the temperature and chemical temperature of the classical region we use the method derived by Rugh [122]. These ideas were first developed for the PGPE theory by Davis and Morgan [98], and were adapted to the harmonically trapped case by Davis and Blakie [109]. In Rugh's formalism, the Hamiltonian is written as $H_{\mathbf{C}} = H_{\mathbf{C}}(\Gamma)$, where

$\Gamma = \{Q_i, P_i\}$, consists of the canonically-conjugate coordinates Q_n and P_n, defined as

$$\begin{aligned} Q_n &= \frac{1}{\sqrt{2\epsilon_n}}(c_n^* + c_n), \\ P_n &= i\sqrt{\frac{\epsilon_n}{2}}(c_n^* - c_n). \end{aligned} \tag{2.31}$$

In Rugh's notation, the Hamiltonian may have a number of independent first integrals, that are invariant under the dynamics of $H_{\mathbf{C}}$ (in addition to $E_{\mathbf{C}}$). In the PGPE formalism, we have that the normalisation of the classical field, $N_{\mathbf{C}}$ is constant. This can also be written as a function of the canonical position and momentum coordinates $\{Q_i, P_i\}$, i.e. $N_{\mathbf{C}} = \mathcal{N}_{\mathbf{C}}(\Gamma)$.

The expression for the temperature of a system in the microcanonical ensemble is

$$\frac{1}{T} = \left(\frac{\partial S}{\partial E_{\mathbf{C}}}\right)_{N_{\mathbf{C}}}, \tag{2.32}$$

where the entropy S is defined as

$$S = k_B \ln\left\{\int d\Gamma \delta[E_{\mathbf{C}} - H_{\mathbf{C}}(\Gamma)]\delta[N_{\mathbf{C}} - \mathcal{N}_{\mathbf{C}}(\Gamma)]\right\}, \tag{2.33}$$

Using Rugh's methods, the temperature of the system can be written as

$$\frac{1}{k_B T} = \langle D \cdot \mathbf{X}_T(\Gamma)\rangle, \tag{2.34}$$

where the angled brackets indicate an ensemble average over all possible states in the microcanonical ensemble. In our formalism, since the ergodic theorem is applicable, this can easily be interpreted as a time average. The components of D are

$$D_i = e_i \frac{\partial}{\partial \Gamma_i} \tag{2.35}$$

where e_i can be chosen to be any scalar value, including zero. We make two particular choices in our calculations, $D_P = \{0, \partial/\partial P_i\}$ and $D_Q = \{\partial/\partial Q_i, 0\}$. This leads to two different calculations for the temperature which will only agree if the system is in thermal equilibrium. The vector $\mathbf{X}_T$ can be freely chosen within the constraints

$$DH_{\mathbf{C}} \cdot \mathbf{X}_T = 1, \tag{2.36}$$

$$D\mathcal{N}_{\mathbf{C}} \cdot \mathbf{X}_T = 0. \tag{2.37}$$

The vector

$$\mathbf{X}_T = \frac{DH_{\mathbf{C}} - \lambda_N D\mathcal{N}_{\mathbf{C}}}{|DH_{\mathbf{C}}|^2 - \lambda_N(D\mathcal{N}_{\mathbf{C}} \cdot DH_{\mathbf{C}})} \tag{2.38}$$

satisfies these constraints, where we introduce the parameter

$$\lambda_N = \frac{D\mathcal{N}_{\mathbf{C}} \cdot DH_{\mathbf{C}}}{|D\mathcal{N}_{\mathbf{C}}|^2}. \tag{2.39}$$

The chemical potential can be calculated in a similar manner to the temperature, according to

$$\begin{aligned} \frac{\mu}{k_B T} &= -\left(\frac{\partial S}{\partial \mathcal{N}_{\mathbf{C}}}\right)_{E_{\mathbf{C}}} \\ &= \langle D \cdot \mathbf{X}_\mu(\Gamma) \rangle \end{aligned} \tag{2.40}$$

where the constraints on $\mathbf{X}_\mu$ are

$$\begin{aligned} DH_{\mathbf{C}} \cdot \mathbf{X}_\mu &= 0 \\ D\mathcal{N}_{\mathbf{C}} \cdot \mathbf{X}_\mu &= 1. \end{aligned} \tag{2.41}$$

The appropriate vector field has the same form as that given in Eq.(2.38) but with $H_{\mathbf{C}}$ and $\mathcal{N}_{\mathbf{C}}$ interchanged, i.e.

$$\mathbf{X}_T = \frac{D\mathcal{N}_{\mathbf{C}} - \lambda_N DH_{\mathbf{C}}}{|D\mathcal{N}_{\mathbf{C}}|^2 - \lambda_N (DH_{\mathbf{C}} \cdot D\mathcal{N}_{\mathbf{C}})}. \tag{2.42}$$

2.3.6 Ground state and Thomas-Fermi Approximation

While our interest lies in finite temperature properties of the system it is of use to characterise aspects of the zero temperature state. This can be found by minimising the PGPE energy functional, $H_{\mathbf{C}}$, subject to the constraint of fixed particle number [123].

The ground state orbital, ψ_g, satisfies the time-independent Gross-Pitaevksii equation

$$\mu_g \psi_g = H_0 \psi_g + U_0 |\psi_g|^2 \psi_g, \tag{2.43}$$

where μ_g is known as the condensate chemical potential. In this case

$$N_{\mathbf{C}} = \int d\mathbf{r} |\psi_g|^2, \tag{2.44}$$

and the system is a pure condensate. In the physical system the condensate is slightly depleted due to interactions, which can be realised by the inclusion of truncated Wigner noise. However, as our interest is at finite temperatures we will not concern ourselves with this small correction.

We also note that we have chosen the notation ψ_g here for the $T = 0$ condensate

to distinguish from the finite temperature condensate mode, $\psi_{\rm cond}$, determined by the Penrose Onsager condition (see Eq. (2.30). For a given number of atoms $N_{\mathbf{C}}$ in the classical region the $T = 0$ condensate mode gives us a minimum value for the classical region energy i.e.

$$E_{\mathbf{C}} \geq E_g, \tag{2.45}$$

where

$$E_g = \int d\mathbf{r}\psi_g^* \left(H_0 + \frac{U_0}{2}|\psi_g|^2 \right) \psi_g. \tag{2.46}$$

Thus E_g forms an effective zero point energy. Since our interest is in finite temperature cases, the complexity involved in solving for ψ_g is unnecessary, and instead an approximate solution, termed the Thomas-Fermi approximation, is appropriate.

The Thomas-Fermi approximation provides a solution for the condensate mode by neglecting the contribution of the kinetic energy term in the time independent GPE Eq. (2.43). This approximation is well justified when the condensate is large, and is least accurate on the edges of the condensate, where kinetic energy is significant. This approximation leads to an algebraic expression for the ground state mode ψ_{TF}, i.e.

$$\hbar\mu\psi_{TF}(\mathbf{r}) = [V_0(\mathbf{r}) + N_{\rm cond}U_0|\psi_{TF}(\mathbf{r})|^2]\psi_{TF}(\mathbf{r}). \tag{2.47}$$

This expression may be rearranged to give the wavefunction:

$$\psi_{TF}(\mathbf{r}) = \sqrt{\frac{\hbar\mu_{TF} - V_0(\mathbf{r})}{N_{\rm cond}U_0}}\theta(\mu_{TF} - V_0(\mathbf{r})) \tag{2.48}$$

where μ_{TF} is chosen so that the Thomas-Fermi density is normalised to the condensate number, $N_{\rm cond}$, i.e.

$$\mu_{TF} = \frac{1}{2}(15a\hbar^2\sqrt{m}\omega_x\omega_y\omega_z N_{\rm cond})^{2/5}, \tag{2.49}$$

and θ is the Heaviside step function

$$\theta(z) = \begin{cases} 0 & z < 0, \\ 1 & z \geq 0. \end{cases} \tag{2.50}$$

The energy of the ground state given by the Thomas-Fermi approximation is

$$E_{TF} = \frac{5}{7}\mu_{TF}N_{\rm cond}. \tag{2.51}$$

We will use the Thomas-Fermi approximation later in this thesis as a means of obtaining a low energy initial state for the PGPE.

2.4 Incoherent Region

In this thesis we include the incoherent region at a meanfield level of description. We assume that the classical and incoherent regions are weakly coupled and are in thermal and diffusive equilibrium, i.e. we assume the incoherent region has a temperature and chemical potential equal to that determined by the Rugh method for the classical region. The incoherent region can be described using the one-particle Wigner function

$$W_{\mathbf{I}}(\mathbf{r},\mathbf{p}) = \frac{1}{h^3}\frac{1}{e^{\beta(E(\mathbf{r},\mathbf{p})-\mu)}-1}, \tag{2.52}$$

where $\beta = 1/k_B T$. The variables $\mathbf{r}$ and $\mathbf{p}$ are treated as classical commuting variables in the semiclassical limit. This should be a good approximation, as the incoherent region consists of modes that have energy $E > \epsilon_{cut} \gg \hbar\omega$, for which the semiclassical approximation is well justified. The energy states for the incoherent region are given by the Hartree-Fock expression

$$E(\mathbf{r},\mathbf{p}) = \frac{\mathbf{p}^2}{2m} + V_0(\mathbf{r}) + 2U_0(n_{\mathbf{C}}(\mathbf{r}) + n_{\mathbf{I}}(\mathbf{r})), \tag{2.53}$$

and the incoherent density is evaluated as

$$n_{\mathbf{I}}(\mathbf{r}) = \int_{\Omega_{\mathbf{I}}} d\mathbf{p}\, W_{\mathbf{I}}(\mathbf{r},\mathbf{p}) \tag{2.54}$$

The incoherent region density is found self consistently, and we note that the total number of particles in the incoherent region is

$$N_{\mathbf{I}} = \int d\mathbf{r} n_{\mathbf{I}}(\mathbf{r}). \tag{2.55}$$

It follows that the total number of particles in the system is

$$N = N_{\mathbf{C}} + N_{\mathbf{I}}. \tag{2.56}$$

It is necessary to restrict the region of phase space we integrate over to find the incoherent region density, and in that respect the $\Omega_{\mathbf{I}}$ on the integral details this restriction; we only integrate over energy states that have not been included in the classical region, i.e.

$$\Omega_{\mathbf{I}} = \{\mathbf{r},\mathbf{p} : \frac{\mathbf{p}^2}{2m} + V_{trap}(\mathbf{r}) > \epsilon_{\text{cut}}\}. \tag{2.57}$$

2.5 Truncated Wigner formalism

Earlier in this chapter we presented a phenomenological derivation of the PGPE. For completeness we note that the formal justification for the PGPE (and other c-field techniques) can be made using a Wigner distribution methodology, and briefly present the theoretical basis for that treatment here. The Wigner distribution and other phase space techniques have been widely used in quantum optics (e.g. see [124, 125]). The theoretical formulation of the Wigner approach for Bose gas dynamics was first made by the group of Dan Walls in 1998 [59], where it was applied to simulating the time evolution of a trapped one dimensional Bose gas.

Wigner representation of a many-body quantum system

For a bosonic many-body system with **C**-region density operator $\hat{\rho}_{\mathbf{C}}$, the *symmetrically ordered* characteristic function is defined as

$$\chi_W(\boldsymbol{\lambda}, \boldsymbol{\lambda}^*) = \mathrm{tr}\left\{ \hat{\rho}_{\mathbf{C}} \prod_{n\in\mathbf{C}} e^{\lambda_n \hat{a}_n^\dagger - \lambda_n^* \hat{a}_n} \right\}, \tag{2.58}$$

where $\boldsymbol{\lambda} = [\lambda_0, \lambda_1, \ldots, \lambda_{M-1}]^T$ is a vector of complex variables, with M the number of modes in **C**. The symmetrically ordered moments are given by derivatives of χ_W at $\boldsymbol{\lambda} = \mathbf{0}$, e.g.

$$\left\langle \left\{ \hat{a}_i^s \left(\hat{a}_j^\dagger\right)^r \right\}_{\mathrm{sym}} \right\rangle = \left(\frac{\partial}{\partial \lambda_j}\right)^r \left(-\frac{\partial}{\partial \lambda_i^*}\right)^s \chi_W(\boldsymbol{\lambda}, \boldsymbol{\lambda}^*)\big|_{\boldsymbol{\lambda}=\mathbf{0}}, \tag{2.59}$$

where $\{\}_{\mathrm{sym}}$ means a symmetrical product of the operators.

The Wigner function, introduced by Wigner in 1932 [126], is the Fourier transform of the quantum characteristic function

$$W_{\mathbf{C}}(\boldsymbol{\alpha}, \boldsymbol{\alpha}^*) \;=\; \int \frac{d\boldsymbol{\lambda}}{\pi^{2M}} \exp\left(\boldsymbol{\lambda}^\dagger \boldsymbol{\alpha} - \boldsymbol{\alpha}^\dagger \boldsymbol{\lambda}\right) \chi_W(\boldsymbol{\lambda}, \boldsymbol{\lambda}^*). \tag{2.60}$$

The Wigner function exists for any density matrix [124], and analytic expressions are know for the Wigner function of many standard quantum states (e.g see Sec. 2.5).

Integrating Eq. (2.60) by parts we see that

$$\int d\boldsymbol{\alpha}\; \alpha_i^s (\alpha_j^*)^r W_{\mathbf{C}}(\boldsymbol{\alpha}, \boldsymbol{\alpha}^*) = \left(\frac{\partial}{\partial \lambda_j}\right)^r \left(-\frac{\partial}{\partial \lambda_i^*}\right)^s \chi_W(\boldsymbol{\lambda}, \boldsymbol{\lambda}^*)\big|_{\boldsymbol{\lambda}=\mathbf{0}}. \tag{2.61}$$

Thus (from Eq. (2.59)) the moments of the Wigner function give symmetrically ordered

operator averages

$$\langle\{\hat{a}^s(\hat{a}^\dagger)^r\}_{\rm sym}\rangle = \overline{\alpha^s(\alpha^*)^r} \equiv \int d\boldsymbol{\alpha}\; \alpha^s(\alpha^*)^r W(\alpha,\alpha^*), \tag{2.62}$$

where $\overline{F(\alpha,\alpha^*)}$ indicates "averaging" the function $F(\alpha,\alpha^*)$ over the Wigner distribution. This suggests that the Wigner function acts like a probability distribution, indeed $W(\alpha,\alpha^*)$ is commonly referred to as a *quasi-probability* since it need not be positive. However, for many important classes of quantum states the Wigner function is either positive (or is well-approximated by a positive function) and can be interpreted as a probability distribution. In these cases the average $\overline{F(\alpha,\alpha^*)}$ is equivalently calculated by statistically sampling α as a random variable from this distribution and calculating the average of $F(\alpha,\alpha^*)$ over many such samples.

Operator correspondences and equations of motion

The equation of motion for the many-particle density operator evolving according to the effective cold atom Hamiltonian is

$$i\hbar\frac{\partial\hat{\rho}_{\mathbf{C}}}{\partial t} = \left[\hat{H},\hat{\rho}_{\mathbf{C}}\right]. \tag{2.63}$$

The right hand side of Eq. (2.63) involves products of operators and the density operator, and which can be equivalently mapped onto a differential operator acting on the Wigner function according to the correspondences [124]

$$\hat{\psi}_{\mathbf{C}}(\mathbf{r})\hat{\rho}_{\mathbf{C}} \;\longleftrightarrow\; \left(\psi_{\mathbf{C}}(\mathbf{r}) + \frac{1}{2}\frac{\bar{\delta}}{\bar{\delta}\psi^*_{\mathbf{C}}(\mathbf{r})}\right) W_{\mathbf{C}}, \tag{2.64}$$

$$\hat{\psi}^\dagger_{\mathbf{C}}(\mathbf{r})\hat{\rho}_{\mathbf{C}} \;\longleftrightarrow\; \left(\psi^*_{\mathbf{C}}(\mathbf{r}) - \frac{1}{2}\frac{\bar{\delta}}{\bar{\delta}\psi_{\mathbf{C}}(\mathbf{r})}\right) W_{\mathbf{C}}, \tag{2.65}$$

$$\hat{\rho}_{\mathbf{C}}\hat{\psi}_{\mathbf{C}}(\mathbf{r}) \;\longleftrightarrow\; \left(\psi_{\mathbf{C}}(\mathbf{r}) - \frac{1}{2}\frac{\bar{\delta}}{\bar{\delta}\psi^*_{\mathbf{C}}(\mathbf{r})}\right) W_{\mathbf{C}}, \tag{2.66}$$

$$\hat{\rho}_{\mathbf{C}}\hat{\psi}^\dagger_{\mathbf{C}}(\mathbf{r}) \;\longleftrightarrow\; \left(\psi^*_{\mathbf{C}}(\mathbf{r}) + \frac{1}{2}\frac{\bar{\delta}}{\bar{\delta}\psi_{\mathbf{C}}(\mathbf{r})}\right) W_{\mathbf{C}}, \tag{2.67}$$

which are used to map the equation of motion for the density operator onto an equation of motion for $W_{\mathbf{C}}$, and where we have defined the functional derivative

$$\frac{\bar{\delta}}{\bar{\delta}\psi_{\mathbf{C}}(\mathbf{r})} \;\equiv\; \sum_{n\in\mathbf{C}}\phi^*_n(\mathbf{r})\frac{\partial}{\partial\alpha_n}. \tag{2.68}$$

Using these correspondences we find that the Wigner distribution evolution equation

for the cold-atom case is

$$\left.\frac{\partial W_{\mathbf{C}}}{\partial t}\right|_{\hat{H}_{\mathbf{C}}} = \int d\mathbf{r}\Bigg\{\frac{iU_0}{4\hbar}\frac{\bar{\delta}^2}{\bar{\delta}\psi_{\mathbf{C}}(\mathbf{r})\bar{\delta}\psi^*_{\mathbf{C}}(\mathbf{r})}\psi^*_{\mathbf{C}}(\mathbf{r})\frac{\bar{\delta}}{\bar{\delta}\psi^*_{\mathbf{C}}(\mathbf{r})} + \text{h.c.} \\ \frac{i}{\hbar}\frac{\bar{\delta}}{\bar{\delta}\psi_{\mathbf{C}}(\mathbf{r})}\Big(\left[H_{sp}+\delta V\right]+U_0|\psi_{\mathbf{C}}(\mathbf{r})|^2\Big)\psi_{\mathbf{C}}(\mathbf{r}) + \text{h.c.}\Bigg\}W_{\mathbf{C}}, \tag{2.69}$$

where h.c. represents the Hermitian conjugate. Equation (2.69) as it stands is as difficult to solve as the full Heisenberg equation of motion for $\hat{\psi}_{\mathbf{C}}$. However, by neglecting the first line of right hand side terms containing third order derivatives, which is referred to as the *truncated Wigner approximation* (TWA), an approximate solution can be found. In particular, since the Wigner function evolution takes the form of a Fokker-Planck equation with drift but no diffusion terms, i.e.,

$$\left.\frac{\partial W_{\mathbf{C}}}{\partial t}\right|_{\hat{H}_{\mathbf{C}}} \approx \int d\mathbf{r}\Bigg\{\frac{i}{\hbar}\frac{\bar{\delta}}{\bar{\delta}\psi_{\mathbf{C}}(\mathbf{r})}\Big(\left[H_{sp}+\delta V\right]+U_0|\psi_{\mathbf{C}}(\mathbf{r})|^2\Big)\psi_{\mathbf{C}}(\mathbf{r}) + \text{h.c.}\Bigg\}W_{\mathbf{C}}. \tag{2.70}$$

The Fokker-Planck evolution can be equivalently mapped to a stochastic partial differential equation [127] that describes the trajectory of a single realisation of the field $\psi_{\mathbf{C}}(\mathbf{r})$, i.e.

$$i\hbar\frac{\partial\psi_{\mathbf{C}}(\mathbf{r})}{\partial t} = \mathcal{P}_{\mathbf{C}}\left\{\Big(H_{sp}+\delta V+U_0|\psi_{\mathbf{C}}(\mathbf{r})|^2\Big)\psi_{\mathbf{C}}(\mathbf{r})\right\}. \tag{2.71}$$

The lack of a diffusion term in (2.70) means that no explicit noise term appears in the TWPGPE, however the initial conditions are stochastic and need to be appropriately sampled from the initial Wigner function.

Sampling the Wigner distribution

Some simple examples of (single mode) Wigner distributions are:

1. Single mode **coherent state** (i.e. pure state with $\hat{a}|\psi\rangle = \alpha_0|\psi\rangle$):

$$W_{coh}(\alpha,\alpha^*) = \frac{2}{\pi}\exp\left(-2|\alpha-\alpha_0|^2\right), \tag{2.72}$$

2. Single mode **thermalised state** (i.e. mixed state defined as $\rho = \exp(-\epsilon\hat{a}^\dagger\hat{a}/k_BT)/Z$ with $Z = \text{tr}\{\exp(-\epsilon\hat{\text{a}}^\dagger\hat{\text{a}}/\text{k}_\text{B}\text{T})\}$):

$$W_{th}(\alpha,\alpha^*) \;=\; \frac{2}{\pi}\tanh\left(\frac{\epsilon}{k_BT}\right)\exp\left[-2|\alpha|^2\tanh\left(\frac{\epsilon}{k_BT}\right)\right]. \tag{2.73}$$

Both of the above states are positive valued Wigner functions that can be sampled stochastically (the number state is an example of a state that is negative and cannot be sampled exactly). A multitude of uncorrelated many-body states can be constructed as trivial outer products of such simple states, however the ground and finite temperature states of the cold-atom Hamiltonian have a considerable amount of correlation between the modes and require elaborate procedures to sample precisely (e.g. the number conserving Bogoliubov procedure developed by Sinatra *et al.* [117]).

Relationship to the PGPE

While the truncated Wigner formalism provides a formal justification for the PGPE as a means to calculate moments of full quantum system, several important properties of the finite temperature regime make use of the PGPE more convenient.

1. High mode occupancy. In the PGPE description all modes in the **C**-region are highly-occupied, meaning that the distinction between symmetric and non-symmetrically ordered moments can be neglected (effectively, we can ignore the commutation relations for the highly occupied modes).

2. The ergodicity in the PGPE means that we do not need to concern ourselves with elaborate procedures for approximately sampling the initial states of the Wigner function. By fixing constants of motion we can allow the system to evolve to equilibrium and sample the space of equilibrium states using time evolution (see Sec. 2.3.3).

Chapter 3

Numerics

In this chapter we give details of the numerical method used to implement the PGPE formalism [105]. We detail the computational units used in Sec. 3.1. In Sec. 3.2 we define our basis and expand our classical field in this. We then show how to find an appropriate initial state in Sec. 3.3. We detail our method of evolving the PGPE in Sec. 3.4, noting the similarities with previous methods [128, 129] of the Otago theory group. In Sec. 3.5 we give details of the quadrature method to evaluate matrix elements of the nonlinear term in the PGPE, basing our discussion on that found in [120].

3.1 Computational Units

It is useful to transform the PGPE into computational units, and we detail this here. We choose a convenient reference frequency ω_0 to define units of time $t_0 = 1/\omega_0$ and distance $x_0 = \sqrt{\frac{\hbar}{m\omega_0}}$. We can then define our dimensionless units of $\tilde{x} = x/x_0$ for position and $\tilde{t} = t/t_0$ for time. This gives us an expression for the classical field in dimensionless units, $\tilde{\psi}_{\mathbf{C}} = \psi_{\mathbf{C}} x_0^{3/2}$, and we also define our nonlinear constant, $N_{\mathbf{C}}U_0$, as $C = N_{\mathbf{C}}U_0 t_0/\hbar x_0^3$. We note that this means we explicitly normalise our field to unity for numerical simulations, and $N_{\mathbf{C}}$ is explicitly included in the nonlinearity. We can now write the PGPE in our dimensionless units as

$$i\frac{\partial\tilde{\psi}_{\mathbf{C}}}{\partial\tilde{t}} = -\frac{1}{2}\tilde{\nabla}^2\tilde{\psi}_{\mathbf{C}} + \frac{1}{2}(\lambda_x^2\tilde{x}^2 + \lambda_y^2\tilde{y}^2 + \lambda_z^2\tilde{z}^2)\tilde{\psi}_{\mathbf{C}} + C|\tilde{\psi}|^2\tilde{\psi} \tag{3.1}$$

where $\lambda_x = \frac{\omega_x}{\omega_0}$, $\lambda_y = \frac{\omega_y}{\omega_0}$, and $\lambda_z = \frac{\omega_z}{\omega_0}$. For the rest of this chapter we will consider the isotropic case, with $\omega_x = \omega_y = \omega_z$, and will also take $\omega_0 = 1$, to simplify our notation.

3.2 Basis

Most commonly, grid FFT methods are used to implement GPE methods. For the harmonically trapped PGPE formalism we use a harmonic oscillator basis set representation, for two reasons:

1. This makes the projection trivial to implement.
2. That our high mode occupation requires that all modes are propagated accurately.

To this end it is convenient to use the harmonic oscillator basis, which was used to formally define $\psi_{\mathbf{C}}(\mathbf{r})$ in Sec. 2.3.1. In dimensionless units we expand

$$\tilde{\psi}_{\mathbf{C}}(\tilde{\mathbf{r}}) = \sum_{n\in\mathbf{C}} c_n \tilde{\phi}_n(\tilde{\mathbf{r}}) \tag{3.2}$$

where

$$\left(\frac{1}{2}\tilde{\nabla}^2 + \frac{1}{2}|\tilde{\mathbf{r}}|^2\right)\tilde{\phi}_n(\tilde{\mathbf{r}}) = \tilde{\epsilon}_n\tilde{\phi}_n(\tilde{\mathbf{r}}), \tag{3.3}$$

and $\tilde{\epsilon}_n$ is the 3D harmonic oscillator eigenvalue. In the rest of this chapter we detail the numerical process to simulate the PGPE. We break this into three parts: finding an initial input state, evolving the PGPE, and evaluation of the nonlinear term in the PGPE.

3.3 Initial State

We need to prepare an initial input state for evolution in the PGPE. The specific form of this state is irrelevant, and we require only that it has the appropriate constants of motion energy and number of atoms in the classical region, given in Eqs. (2.21) and (2.22). We have three parameters to characterise our initial state vector:

(i) The energy cutoff, $\epsilon_{\rm cut}$. This sets the cutoff between the two regions, classical and incoherent. This parameter sets the number of modes in the classical region, since only states with energy below this are allowed.

(ii) The number of classical region atoms, $N_{\mathbf{C}}$ (or equivalently the nonlinear constant C). Being the coefficient of the nonlinear term this parameter is responsible for mode mixing and ergodicity.

(iii) Energy $E_{\mathbf{C}}$, defined as in Eq. (2.21). This is a constant of the motion. To set the energy of a given state vector, we mix a low energy state (formed within the

Thomas-Fermi approximation) with a high energy state (a vector of random input values).

3.3.1 Thomas-Fermi approximation in Computational Units

To use the Thomas-Fermi formalism to make an initial input we will require its form in computational units, which we give here. The Thomas-Fermi chemical potential can be written as

$$\tilde{\mu}_{TF} = \left(\frac{15\lambda_x\lambda_y\lambda_z C}{2^{9/2}\pi} \right)^{2/5}, \tag{3.4}$$

and the potential given by the harmonic trap as

$$\tilde{V}_0(\tilde{\mathbf{r}}) = \frac{1}{2}(\tilde{x}^2 + \tilde{y}^2 + \tilde{z}^2), \tag{3.5}$$

We can then form the Thomas-Fermi wavefunction as

$$\tilde{\psi}_{TF}(\tilde{\mathbf{r}}) = \sqrt{\frac{\tilde{\mu}_{TF} - \tilde{V}_0(\tilde{\mathbf{r}})}{C}}\theta(\tilde{\mu}_{TF} - \tilde{V}_0(\tilde{\mathbf{r}})). \tag{3.6}$$

3.3.2 Initial State Preparation

We form the Thomas-Fermi wavefunction on an appropriate spatial grid and then transform it using quadrature methods back to a c-vector representation (i.e. to obtain the $\{c_n\}$ coefficients for this state). We can generate a state $\eta_E(\tilde{\mathbf{r}})$ of desired energy by superimposing the Thomas-Fermi state with a (high energy) randomised state, $\eta_{\rm ran}(\tilde{\mathbf{r}})$ (normalised to $N_{\mathbf{C}}$), according to

$$\eta_E(\tilde{\mathbf{r}}) = p_0\tilde{\psi}_{TF}(\tilde{\mathbf{r}}) + p_1\eta_{\rm ran}(\tilde{\mathbf{r}}), \tag{3.7}$$

where the variables p_0 and p_1 are adjusted to obtain the desired energy. In practice, $\eta_{\rm ran}$ is approximately orthogonal to $\eta_{\rm TF}$ and we can take $p_1 = \sqrt{1 - |p_0|^2}$.

3.4 Evolution of the PGPE

To evolve the PGPE, we use an adaptive stepsize Runge-Kutta (RK) method. The RK method is based on the midpoint method of solving ordinary differential equations, and the solution is propagated by evaluating derivatives between timesteps to arrive at a solution at the new time. To evolve the PGPE we will use the adaptive stepsize RK

method [105], which is an extension of earlier methods developed at Otago, in particular the RK4IP method, see for example [128, 129] . We will compare and contrast the two methods where appropriate in the current section. For the remainder of this chapter we dispense with the tilde notation and all quantities are taken to be in computational units.

3.4.1 Formal algorithm in Position Space Representation

In this subsection we give an overview of the algorithm in position space, before discussing the equivalent, but more convenient, basis set form of the algorithm that is the basis of our numerical implementations.

Interaction picture

The PGPE can be written in the form

$$\frac{\partial \psi_{\mathbf{C}}}{\partial t} = -i[H_0 + K]\psi_{\mathbf{C}}, \tag{3.8}$$

where

$$H_0 = -\frac{1}{2}\nabla^2 + \frac{1}{2}(x^2 + y^2 + z^2), \tag{3.9}$$

$$K = C|\psi_{\mathbf{C}}(\mathbf{r})|^2 + \delta V(\mathbf{r}, t). \tag{3.10}$$

We accordingly define an interaction picture for the field evolution as

$$\psi^{\mathrm{I}}_{\mathbf{C}}(\mathbf{r}, t) = e^{iH_0(t-t')}\psi_{\mathbf{C}}(\mathbf{r}, t), \tag{3.11}$$

where t' is the time origin for the interaction picture that we discuss later. Such transformation removes the explicit dependence of the field's evolution on H_0, i.e., the system now evolves according to

$$\frac{\partial \psi^{\mathrm{I}}_{\mathbf{C}}}{\partial t} = -iK^{\mathrm{I}}\psi^{\mathrm{I}}_{\mathbf{C}}, \tag{3.12}$$

where

$$K^{\mathrm{I}} \equiv e^{iH_0(t-t')}Ke^{-iH_0(t-t')}, \tag{3.13}$$

$$= C|\psi^{\mathrm{I}}_{\mathbf{C}}(\mathbf{r}, t)|^2 + \delta V^{\mathrm{I}}(\mathbf{r}, t), \tag{3.14}$$

is the *interaction* operator in the interaction picture, with

$$\delta V^{\mathrm{I}}(\mathbf{r}, t) \equiv e^{iH_0(t-t')}\delta V(\mathbf{r}, t)e^{-iH_0(t-t')}. \tag{3.15}$$

Since $\left(\psi_{\mathbf{C}}^{\mathrm{I}}(\mathbf{r},t)\right)^* = \psi_{\mathbf{C}}(\mathbf{r},t)^* e^{-iH_0(t-t')}$, we have that $|\psi_{\mathbf{C}}^{\mathrm{I}}(\mathbf{r},t)|^2 = |\psi_{\mathbf{C}}(\mathbf{r},t)|^2$, and so either the interaction or the Schrödinger picture field can be used to evaluate the nonlinear density term.

Adaptive step evolution algorithm

Our aim is to obtain an efficient and accurate algorithm for propagating the PGPE forward in time from an initial state $\psi_{\mathbf{C}}(\mathbf{r},t_0)$. To do this we will need to recast the partial differential equation (Eq. (3.12)) as a system of ordinary differential equations (see Sec. 3.4.2), and then we make use of a Runge-Kutta algorithm to propagate this system of equations forward in time. In this procedure the field is evaluated at a discrete set of times

$$t_j \in \{t_0, t_1, t_2, \ldots, t_F\}, \quad j \in [0, F], \tag{3.16}$$

where t_F is the final time and F is the number of steps used to complete the simulation. We use an adaptive step algorithm and the time steps,

$$\Delta t_j = t_j - t_{j-1}, \quad j \in [1, F], \tag{3.17}$$

are in general not equally sized.

We can now focus on the irreducible element of this procedure, the single step, i.e. the scheme for obtaining $\psi_{\mathbf{C}}^{\mathrm{I}}(\mathbf{r},t_{j+1})$ given $\psi_{\mathbf{C}}^{\mathrm{I}}(\mathbf{r},t_j)$. For simplicity it is convenient to choose the origin of the interaction picture to be the start time of each time step, i.e.

$$\psi_{\mathbf{C}}^{\mathrm{I(j)}}(\mathbf{r},t) \equiv e^{iH_0(t-t_j)}\psi_{\mathbf{C}}(\mathbf{r},t).$$

We use the adaptive stepsize Runge-Kutta method, which provides a fourth and fifth order accurate approximations to $\psi_{\mathbf{C}}^{\mathrm{I(j+1)}}(\mathbf{r},t_{j+1})$ (see Sec. 3.4.2). By comparing these two estimates we can control the relative error of the solution by adjusting the time step size.

Comparison to RK4IP

This choice of interaction picture differs from that usually made for the Runge-Kutta 4th order interaction picture (RK4IP) algorithm developed in the Otago theory group by Ballagh and coworkers [128, 129] over the past decade.

- In RK4IP the interaction picture is defined by the operator $H_0 = -\frac{1}{2}\nabla^2$, and the harmonic trapping potential is thus left with the interaction term K. This choice

was made because the RK4IP method is based on a planewave/FFT representation in which $-\frac{1}{2}\nabla^2$ is diagonal. Since we work in the harmonic oscillator basis of the full single particle Hamiltonian (excluding the perturbation potential) we can exponentiate both kinetic and trap potential terms.

- In RK4IP the propagation is done using a 4th order Runge-Kutta algorithm and the time origin is taken to be the mid-point between t_j and t_{j+1}. This time origin choice leads to certain efficiencies in the detailed implementation since the time step sizes are fixed. However, we have instead focused on implementing an algorithm that is higher order and controls the error accumulated, although at greater computational cost per time step.

3.4.2 Basis Set Algorithm

The previous position space representation of the PGPE can be converted to the basis set representation by projecting the equations onto the oscillator basis of Sec. 3.2. In particular, taking

$$\psi_{\mathbf{C}}^{\mathrm{I(j)}}(\mathbf{r},t) = \sum_n c_n^{\mathrm{I(j)}}\phi_n(\mathbf{r}), \tag{3.18}$$

(c.f. Eq. (3.2)), we observe that the interaction picture transformation is trivial since H_0 is diagonal in the $\phi_n(\mathbf{r})$ basis, i.e.

$$\begin{aligned} c_n^{\mathrm{I(j)}} &= \int d\mathbf{r}\,\phi_n^*(\mathbf{r})e^{iH_0(t-t_j)}\psi_{\mathbf{C}}(\mathbf{r},t), &(3.19)\\ &= e^{i\epsilon_n(t-t_j)}c_n(t). &(3.20)\end{aligned}$$

The interaction picture PGPE takes the form

$$\frac{\partial c_n^{\mathrm{I(j)}}}{\partial t} = -iK_n^{\mathrm{I}}[\{c_n^{\mathrm{I(j)}}\},t], \tag{3.21}$$

where

$$\begin{aligned} K_n^{\mathrm{I}}[\{c_n^{\mathrm{I(j)}}\},t] &= F_n^{\mathrm{I}}[\{c_n^{\mathrm{I(j)}}\}] + \sum_m G_{nm}^{\mathrm{I}}(t)c_m^{\mathrm{I(j)}}, &(3.22)\\ F_n^{\mathrm{I}}[\{c_m^{\mathrm{I(j)}}\}] &= C\int d\mathbf{r}\,\phi_n^*(\mathbf{r})|\psi_{\mathbf{C}}^{\mathrm{I(j)}}(\mathbf{r},t)|^2\psi_{\mathbf{C}}^{\mathrm{I(j)}}(\mathbf{r},t), &(3.23)\\ G_{nm}^{\mathrm{I}}(t) &= \int d\mathbf{r}\,\phi_n^*(\mathbf{r})\delta V^{\mathrm{I}}(\mathbf{r},t)\phi_m(\mathbf{r}), &(3.24)\end{aligned}$$

and we have introduced the nonlinear ($F_n^{\mathrm{I}}[\{c_m^{\mathrm{I(j)}}\}]$) and perturbation potential (G_{nm}^{I}) matrix elements. The notation $F_n^{\mathrm{I}}[\{c_m^{\mathrm{I(j)}}\}]$ emphasises that the nonlinear matrix element

depends on the field $\psi^{\rm I}_{\mathbf{C}}$, i.e. all the coefficients $\{c_n^{\rm I(j)}\}$. In Sec. 3.5 we show that both $F_n^{\rm I}[\{c_m^{\rm I(j)}\}]$ and $G^{\rm I}_{nm}$ can be evaluated accurately and efficiently.

For the remainder of this section we explain our propagation algorithm assuming that we can evaluate these two quantities. For the purposes of efficient notation we shall use a vector notation, i.e.

$$c_n^{\rm I(j)} \leftrightarrow \mathbf{c}^{\rm I}, \tag{3.25}$$

$$K_n^{\rm I(j)}[\{c_n^{\rm I(j)}\},t] \leftrightarrow \mathbf{K}^{\rm I}[\mathbf{c}^{\rm I},t], \tag{3.26}$$

$$\epsilon_n \leftrightarrow \mathbf{e}, \tag{3.27}$$

and so on, where we have suppressed indicating the interaction picture time origin.

The Runge-Kutta method for propagating Eq. (3.21) is

$$\mathbf{k}_1^{\rm I} = -i\mathbf{K}^{\rm I}[\mathbf{c}^{\rm I}(t_j),t_j], \tag{3.28}$$

$$\mathbf{k}_2^{\rm I} = -i\mathbf{K}^{\rm I}[\mathbf{c}^{\rm I}(t_j)+b_{21}\mathbf{k}_1^{\rm I},t_j+a_2\Delta t_j], \tag{3.29}$$

$$\mathbf{k}_3^{\rm I} = -i\mathbf{K}^{\rm I}[\mathbf{c}^{\rm I}(t_j)+b_{31}\mathbf{k}_1^{\rm I}+b_{32}\mathbf{k}_2^{\rm I},t_j+a_3\Delta t_j], \tag{3.30}$$

$$\mathbf{k}_4^{\rm I} = -i\mathbf{K}^{\rm I}[\mathbf{c}^{\rm I}(t_j)+b_{41}\mathbf{k}_1^{\rm I}+b_{42}\mathbf{k}_2^{\rm I}+b_{43}\mathbf{k}_3^{\rm I},t_j+a_4\Delta t_j], \tag{3.31}$$

$$\mathbf{k}_5^{\rm I} = -i\mathbf{K}^{\rm I}[\mathbf{c}^{\rm I}(t_j)+b_{51}\mathbf{k}_1^{\rm I}+b_{52}\mathbf{k}_2^{\rm I}+b_{53}\mathbf{k}_3^{\rm I}+b_{54}\mathbf{k}_4^{\rm I},t_j+a_5\Delta t_j], \tag{3.32}$$

$$\mathbf{k}_6^{\rm I} = -i\mathbf{K}^{\rm I}[\mathbf{c}^{\rm I}(t_j)+b_{61}\mathbf{k}_1^{\rm I}+b_{62}\mathbf{k}_2^{\rm I}+b_{63}\mathbf{k}_3^{\rm I}+b_{64}\mathbf{k}_4^{\rm I}+b_{65}\mathbf{k}_5^{\rm I},t_j+a_6\Delta t_j]., \tag{3.33}$$

Together all these $\mathbf{k}_j^{\rm I}$ values give us the approximate solution at time t_{j+1} as

$$\mathbf{c}^{\rm I}(t_{j+1}) = \mathbf{c}^{\rm I}(t_j) + \sum_{k=1}^{6} c_k \mathbf{k}_k^{\rm I}, \tag{3.34}$$

which is 5th order accurate in the time step Δt_j, where the coefficients $\{a_k, b_k, c_k\}$ are the Cash-Karp coefficients (e.g. see [130]) given in Table 3.1.

i	a_i	b_{ij}					c_i	$\bar{c}_i$
1							$\frac{37}{378}$	$\frac{2825}{27648}$
2	$\frac{1}{5}$	$\frac{1}{5}$					0	0
3	$\frac{3}{10}$	$\frac{3}{40}$	$\frac{9}{40}$				$\frac{250}{621}$	$\frac{18575}{48384}$
4	$\frac{3}{5}$	$\frac{3}{10}$	$-\frac{9}{10}$	$\frac{6}{5}$			$\frac{125}{594}$	$\frac{13525}{55296}$
5	1	$-\frac{11}{54}$	$\frac{5}{2}$	$-\frac{70}{27}$	$\frac{35}{27}$		0	$\frac{277}{14336}$
6	$\frac{7}{8}$	$\frac{1631}{55296}$	$\frac{175}{512}$	$\frac{575}{13824}$	$\frac{44275}{110592}$	$\frac{253}{4096}$	$\frac{512}{1771}$	$\frac{1}{4}$
j		1	2	3	4	5		

Table 3.1: The Cash-Karp coefficients for Embedded Runge-Kutta Method

We can also obtain a 4th order accurate estimate for the solution, i.e.

$$\bar{\mathbf{c}}^{\mathrm{I}}(t_{j+1}) = \mathbf{c}^{\mathrm{I}}(t_j) + \sum_{k=1}^{6} \bar{c}_k \mathbf{k}_k^{\mathrm{I}}, \tag{3.35}$$

with coefficients $\bar{c}_k$ in Table 3.1. We can then obtain the maximum relative error as

$$\delta X_{\mathrm{rel}} = \max \left\{ \frac{|c_n^{\mathrm{I(j)}}(t_{j+1}) - \bar{c}_n^{\mathrm{I(j)}}(t_{j+1})|^2}{|c_n^{\mathrm{I(j)}}(t_{j+1})|^2} \right\}, \tag{3.36}$$

where we only include non-negligibly occupied modes (i.e. those satisfying $|c_n|^2 > 10^{-3} \max\{|c_n|^2\}$) to avoid the pathological behaviour of the relative error measure on modes of vanishingly small occupation.

We can use δX_{rel} to decide if a step was sufficiently accurate. Indeed, generally we require a relative tolerance of our time propagation of TOL $= 10^{-6}$, meaning that $\delta X_{\mathrm{rel}} <$ TOL for each time step. At the conclusion of a time step δX_{rel} is analysed and the algorithm makes the following decision:

Successful step ($\delta X_{\mathrm{rel}} <$ TOL): We accept the solution and choose a step size for the next time step of

$$\Delta t_{j+1} = 0.92 \Delta t_j \left(\frac{\mathrm{TOL}}{\delta X_{\mathrm{rel}}} \right)^{1/5}. \tag{3.37}$$

Failed step ($\delta X_{\mathrm{rel}} \geq$ TOL): We reject the current solution and repeat the calculations for the current time interval with a smaller time step given by

$$\Delta t_j^{\mathrm{new}} = 0.92 \Delta t_j \left(\frac{\mathrm{TOL}}{\delta X_{\mathrm{rel}}} \right)^{1/4}. \tag{3.38}$$

We note that the factor of 0.92 is a "safety factor" designed to give a greater likelihood of success for the next step, as is the exponent of 1/4 in the failed step adjustment (the method should be fifth order accurate, hence the normal use of an exponent of 1/5 for adjusting the step size to obtain the desired tolerance, see e.g. [130]).

To provide a complete description of the code, we note that we have chosen to implement the algorithm in Eqs. (3.28)-(3.33) transformed back into the Schrödinger picture for

the purpose of simplifying the operator evaluation, i.e.

$$\mathbf{k}_1^{\mathrm{I}} = -i\mathbf{K}[\mathbf{c}^{\mathrm{I}}(t_j), t_j], \tag{3.39}$$

$$\mathbf{k}_2^{\mathrm{I}} = -ie^{i\mathbf{e}a_2\Delta t_j}\mathbf{K}[e^{-i\mathbf{e}a_2\Delta t_j}(\mathbf{c}^{\mathrm{I}}(t_j) + b_{21}\mathbf{k}_1^{\mathrm{I}}), t_j + a_2\Delta t_j], \tag{3.40}$$

$$\mathbf{k}_3^{\mathrm{I}} = -ie^{i\mathbf{e}a_3\Delta t_j}\mathbf{K}[e^{-i\mathbf{e}a_3\Delta t_j}(\mathbf{c}(t_j) + b_{31}\mathbf{k}_1^{\mathrm{I}} + b_{32}\mathbf{k}_2^{\mathrm{I}}), t_j + a_3\Delta t_j], \tag{3.41}$$

$$\mathbf{k}_4^{\mathrm{I}} = -ie^{i\mathbf{e}a_4\Delta t_j}\mathbf{K}[e^{-i\mathbf{e}a_4\Delta t_j}(\mathbf{c}^{\mathrm{I}}(t_j) + b_{41}\mathbf{k}_1^{\mathrm{I}} + b_{42}\mathbf{k}_2^{\mathrm{I}} + b_{43}\mathbf{k}_3^{\mathrm{I}}), t_j + a_4\Delta t_j], \tag{3.42}$$

$$\mathbf{k}_5^{\mathrm{I}} = -ie^{i\mathbf{e}a_5\Delta t_j}\mathbf{K}[e^{-i\mathbf{e}a_5\Delta t_j}(\mathbf{c}^{\mathrm{I}}(t_j) + \sum_{k=1}^{4} b_{5k}\mathbf{k}_k^{\mathrm{I}}), t_j + a_5\Delta t_j], \tag{3.43}$$

$$\mathbf{k}_6^{\mathrm{I}} = -ie^{i\mathbf{e}a_6\Delta t_j}\mathbf{K}[e^{-i\mathbf{e}a_6\Delta t_j}(\mathbf{c}^{\mathrm{I}}(t_j) + \sum_{k=1}^{5} b_{6k}\mathbf{k}_k^{\mathrm{I}}), t_j + a_6\Delta t_j], \tag{3.44}$$

where

$$K_n[\{c_n\}, t] = F_n[\{c_n\}] + \sum_m G_{nm}(t)c_m, \tag{3.45}$$

$$F_n[\{c_m\}] = C\int d\mathbf{r}\, \phi_n^*(\mathbf{r})|\psi_{\mathbf{C}}(\mathbf{r}, t)|^2\psi_{\mathbf{C}}(\mathbf{r}, t), \tag{3.46}$$

$$G_{nm}(t) = \int d\mathbf{r}\, \phi_n^*(\mathbf{r})\delta V(\mathbf{r}, t)\phi_m(\mathbf{r}), \tag{3.47}$$

are the Schrödinger form of the operators introduced earlier.

3.5 Quadrature

To evaluate the matrix components of Eqs. (3.23) and (3.24), it is necessary to introduce new notation for our basis, which is separable in the spatial dimensions. We introduce new notation for 1D energy values, so that $\epsilon_n = \varepsilon_\alpha + \varepsilon_\beta + \varepsilon_\gamma$, with the indices $\{\alpha, \beta, \gamma\}$ corresponding to the directions $\{x, y, z\}$. We also introduce the decomposition

$$\psi_{\mathbf{C}}(\mathbf{r}, t) = \sum_{\alpha\beta\gamma\in\mathbf{C}} c_{\alpha\beta\gamma}(t)\varphi_\alpha(x)\varphi_\beta(y)\varphi_\gamma(z) \tag{3.48}$$

The basis functions φ have the form of Hermite polynomials, given by

$$\varphi_\alpha(x) = h_\alpha H_\alpha(x)e^{-x^2/2} \tag{3.49}$$

where H_α is a Hermite polynomial of degree α, and h_α is an appropriate normalisation factor (determined so the wavefunction is normalised to unity). The vector $c_{\alpha\beta\gamma}(t)$ gives the complex number amplitudes of the basis functions outlined above, and we will refer to this from now on as the c-vector. The classical field wavefunction is completely

described just by the c-vector, and determining the time evolution of $c_{\alpha\beta\gamma}(t)$ will allow us to find solutions of the PGPE. We expand the PGPE in our chosen basis, to give the equation of motion of $c_{\alpha\beta\gamma}(t)$:

$$\frac{\partial c_{\alpha\beta\gamma}(t)}{\partial t} = -i[(\varepsilon_\alpha + \varepsilon_\beta + \varepsilon_\gamma)c_{\alpha\beta\gamma}(t) + F_{\alpha\beta\gamma}(\psi_{\mathbf{C}}), \tag{3.50}$$

which is the Schrödinger picture form of Eq. (3.21) where $F_{\alpha\beta\gamma}(\psi_{\mathbf{C}})$ is defined as

$$F_{\alpha\beta\gamma}(\psi_{\mathbf{C}}) = \int d\mathbf{r}\varphi^*_\alpha(x)\varphi^*_\beta(y)\varphi^*_\gamma(z)|\psi_{\mathbf{C}}(\mathbf{r})|^2\psi_{\mathbf{C}}(\mathbf{r}), \tag{3.51}$$

(c.f. Eq. (3.23))

We now write in detail how we calculate the nonlinear term, $F_{\alpha\beta\gamma}$ in the above evolution. The nonlinear term has the form

$$F_{\alpha\beta\gamma} = \int d\mathbf{r}\varphi^*_\alpha(x)\varphi^*_\beta(y)\varphi^*_\gamma(z)|\psi_{\mathbf{C}}(\mathbf{r},t)|^2\psi_{\mathbf{C}}(\mathbf{r},t). \tag{3.52}$$

Let α_{max} be the maximum number of distinctive values that any one of the independent variables can take (i.e. $\alpha \in [0, \alpha_{max} - 1]$ in the **C**-region). Using our Hermite polynomials, we can write the field at any time as

$$\psi_{\mathbf{C}}(\mathbf{r},t) = Q(x,y,z)e^{-(x^2+y^2+z^2)/2}, \tag{3.53}$$

where

$$Q(x,y,z) = \sum_{\alpha\beta\gamma} c_{\alpha\beta\gamma}(t)h_\alpha H_\alpha(x)h_\beta H_\beta(y)h_\gamma H_\gamma(z). \tag{3.54}$$

$Q(x,y,z)$ is a polynomial of maximum order α_{max} in the independent variables. We can now write the nonlinear term as

$$F_{\alpha\beta\gamma} = \int d\mathbf{r}e^{-2(x^2+y^2+z^2)}P(x,y,z), \tag{3.55}$$

with

$$P(x,y,z) = h_\alpha H_\alpha(x)h_\beta H_\beta(y)h_\gamma H_\gamma(z)|Q(x,y,z)|^2Q(x,y,z), \tag{3.56}$$

which is a polynomial of maximum degree $4\alpha_{max}$ in the independent variables. To evaluate $F_{\alpha\beta\gamma}$ it is desirable to use Gaussian quadrature since it can evaluate the matrix elements in Eq. (3.55) exactly. We give some background detail on these here (further details on general Gaussian quadrature is found in [130]). We start with the quadrature expression

$$\int_a^b W(x)f(x)dx \approx \sum_{j=1}^{N} w_j f(x_j), \tag{3.57}$$

where $W(x)$ is the weight function, w_j are the weights, and x_j are the quadrature points Say we form a set of orthonormal, orthogonal polynomials $p_N(x)$, which are mutually orthogonal over the weight function $W(x)$, i.e.

$$\int_a^b W(x)p_i(x)p_j(x)dx = 0 \tag{3.58}$$

for any i, j in our set. It can be shown that $p_N(x)$ has exactly N distinct roots in the interval $[a, b]$. It can also be shown that these roots are the x_j required in the quadrature expression above Eq. (3.57). The weight functions can be found once the roots are known (see Ref. [130] for the general case). This quadrature, with N polynomials, is accurate for polynomials of order $2N - 1$ or less. In our particular case, we recognise that our function $F_{\alpha\beta\gamma}$ takes the form required for Gauss-Hermite quadrature in each direction, with weight function $W(x) = e^{-x^2/2}$. In this case, the appropriate roots and weight functions can be found, and the integral of the $4\alpha_{max}$ polynomial $P(x, y, z)$ will be exact if a quadrature of order $2\alpha_{max}$ is used along each direction (i.e. a 3D grid $\mathbf{r}_{ijk} = (x_i, x_j, x_k)$ of $2\alpha_{max} \times 2\alpha_{max} \times 2\alpha_{max}$ points), which we refer to as our quadrature grid. We note that while the computational cost of this quadrature step is $O(\alpha_{max}^4)$, calculating the nonlinear term directly in the spectral basis takes $O(\alpha_{max}^{12})$, and so a significant saving of computational time has been made.

We can therefore write our nonlinear term as

$$F_{\alpha\beta\gamma} = \sum_{ijk} w_i w_j w_k P_{\alpha\beta\gamma}(x_i, x_j, x_k), \tag{3.59}$$

where x_i and w_i are the $2\alpha_{max}$ roots and weights of the 1D Gauss-Hermite quadrature with weight function $W(x) = e^{-2x^2}$. To calculate our nonlinear term, we undertake the following procedure: We transform the field to spatial representation, on the quadrature grid, i.e.

$$\psi_{\mathbf{C}}(\mathbf{r}_{ijk}, t) = \sum_{\alpha\beta\gamma} U_{i\alpha} U_{j\beta} U_{k\gamma} c_{\alpha\beta\gamma}(t), \tag{3.60}$$

where

$$U_{i\alpha} = \varphi_\alpha(x_i). \tag{3.61}$$

The integrands are then constructed as quadratures by dividing by the weight function and premultiplying by the weights, i.e.

$$f(\mathbf{r}_{ijk}) = w_i w_j w_k e^{2|\mathbf{r}_{ijk}|^2} |\psi_{\mathbf{C}}(\mathbf{r}_{ijk}, t)|^2 \psi_{\mathbf{C}}(\mathbf{r}_{ijk}, t) \tag{3.62}$$

We then inverse transform, to give the desired matrix elements

$$F_{\alpha\beta\gamma} = \sum_{ijk} U^*_{i\alpha} U^*_{j\beta} U^*_{k\gamma} f(\mathbf{r}_{ijk}). \tag{3.63}$$

3.5.1 Time-dependent Perturbation

We wish to discuss evaluation of the perturbation potential term in the PGPE, i.e. of the form

$$G_{\alpha\beta\gamma} = \int d\mathbf{r} \varphi^*_\alpha(x) \varphi^*_\beta(y) \varphi^*_\gamma(z) \delta V(\mathbf{r}, t) \psi_{\mathbf{C}}. \tag{3.64}$$

We will assume that $\delta V(\mathbf{r}, t)$ can be evaluated on the quadrature grid we used for the nonlinear term. In this thesis our interest is in perturbations of the form

$$\delta V(x, t) = A \sin(\omega_x t) \omega_x^2 x^2, \tag{3.65}$$

and similar generalisations for exciting collective modes (e.g. see Chapter 4). We have developed a time-dependent algorithm for evaluating this term. We investigate the accuracy of this algorithm by testing it in the non-interacting limit against an analytical result, and we present this in Appendix B.

3.6 Discussion on Computational Resources

We have made significant use of computational resources to generate the results presented in this thesis.

A single trajectory simulation can take anywhere between 30 minutes and 24 hours to run on a typical workstation and has a very small memory footprint (typically $\sim$ 1MB). The simulation time is very dependent on the number of modes and nonlinearity being simulated due to the adaptive step tolerance control. This large variability in simulation time (i.e. number of steps and step size) indicates the importance of our adaptive stepsize algorithm over the fixed step RK4IP method. To generate the large numbers of trajectories and data sets required here we have made substantial use of the Vulcan cluster made available by the LART research theme. The total CPU time we have used on this cluster is in excess of one year.

We also note that due to the nature of our input state of the PGPE, it can be difficult to determine in advance what the appropriate values of $E_{\mathbf{C}}$, $N_{\mathbf{C}}$, and ϵ_{cut} should be to obtain states with certain desired macroscopic parameters (such as a fixed total number, or temperature). For this reason, it is often necessary to keep refining the input state

and repeating simulations. Several hundred simulations would usually be needed to produce a dozen states within the desired macroscopic parameters, such that it often took weeks of computation and refinement to generate the states used for the studies presented in the following chapters.

Part I

Excitations

Chapter 4

Quadrupolar Excitations of the Bose gas

4.1 Introduction

In this section we undertake a comprehensive study into the excitation spectrum of a finite temperature Bose gas. We model the experiment of Jin *et al.* [3], which has become a benchmark test for finite temperature theory. This is the first time that the PGPE has been applied to a dynamical system which has allowed qualitative comparison with experiment, and we use this opportunity to evaluate the performance of the PGPE formalism in this regime. We begin by outlining the application of the PGPE to the experiment in Sec. 4.2. We then present our results in Sec. 4.3, giving comparison with previous experimental and theoretical findings where appropriate, and giving an analysis of the dependence of our results on the energy cutoff $\epsilon_{\rm cut}$ used to define the c-field region.

4.2 Formalism

Here we outline the formalism for modelling the experiment of [3]. We begin detailing the experimental method in Sec. 4.2.1. We then show how to find appropriate equilibrium states in Sec. 4.2.2, and then give our dynamic modeling formalism in Sec. 4.2.3.

4.2.1 Experimental Procedure

The theory we develop here is relevant to the finite temperature excitation experiment undertaken by Jin *et al.* in Ref. [3]. It is instructive to outline the details of that experiment, and we do that here. In the experiment a degenerate ^{87}Rb Bose gas was prepared in a magnetic trap with frequencies $\omega_r \equiv \omega_{x,y} = 2\pi \times 129$Hz, $\omega_z = 2\pi \times 365$Hz, and initial temperatures ranging from 0.4–1.4T_c. The total number of atoms increased with temperature, varying from about 5×10^3 to 60×10^3 atoms over that temperature range, with a condensate number of about $6 \times 10^3 \pm 2 \times 10^3$ for $T \lesssim 0.9T_c$.

Two different symmetries of perturbation were investigated in experiments, chosen to effectively couple to the lowest energy $m = 0$ and $m = 2$ collective modes. To excite the collective mode the trap was perturbed for 14 ms and then evolved in the static trap for a variable hold time before the cloud was released and imaged after expansion (see Fig. 4.1(a)). The condensate and non-condensate components were determined using bimodal fits to the absorption image, and the widths of each component were extracted as a function of time. These results were analysed to give excitation frequencies and damping rates for both components.

Time-dependent perturbation

The perturbation used to drive the $m = 0$ mode was a weak sinusoidal modulation of the radial trap frequency (see Fig. 4.1(b)). For the $m = 2$ mode the trap frequencies in the x and y directions were modulated sinusoidally with π phase difference (see Fig. 4.1(c)). For calibration, the dipole mode was also measured by center-of-mass excitation (see Fig. 4.1(d)).

Our system is described by the second quantised Hamiltonian given in Eq. (2.1). Here, our trapping potential will be given by

$$V(\mathbf{r}, t) = V_0(\mathbf{r}) + \delta V(\mathbf{r}, t), \tag{4.1}$$

where $V_0(\mathbf{r})$ is the static harmonic trap potential, given in Eq. (2.5), and $\delta V(\mathbf{r}, t)$ is a time-dependent perturbing potential whose form we will change dependent on the cloud perturbation we wish to model. We discuss this further below. In our approach to modeling these collective excitations we explicitly simulate the perturbation procedure used in experiments. To do this we use a perturbation potential of the form

$$\delta V(\mathbf{r}, t) = \frac{m}{2} A(t) \left\{ \omega_x^2 x^2 \cos(\omega_p t + \phi) + \omega_y^2 y^2 \cos(\omega_p t) \right\}, \tag{4.2}$$

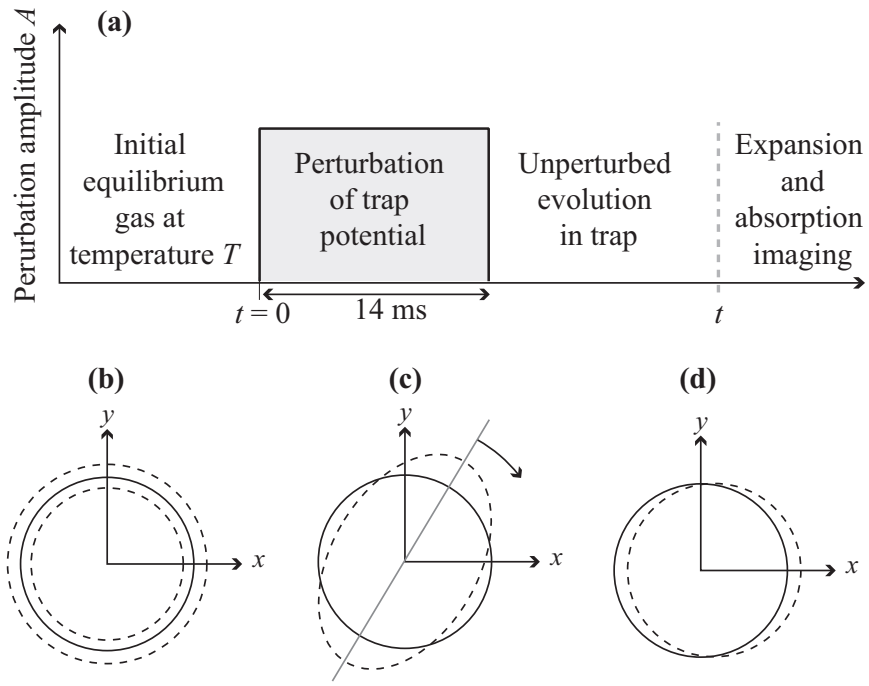

Figure 4.1: Experimental time sequence and form of trap perturbations used to excite the Bose gas. (a) Overview of time sequence used in the experiment to excite and observe collective excitations in the system. (b)-(d) Schematic representations of the various trap perturbations used (see text). Contours of equipotential in the xy-plane are shown for the unperturbed (solid lines) and for the perturbed (dashed lines) traps. (b) Symmetric perturbation used to drive the $m = 0$ mode. (c) The perturbation used to drive the $m = 2$ mode corresponds to a rotating ellipse. (d) Trap center displacement used to drive the dipole mode.

where ω_p is the perturbation frequency, ϕ is a phase factor between the x and y perturbation, and $A(t)$ is the dimensionless time-dependent amplitude of the perturbation (see Fig. 4.1(a)) of the square pulse form

$$A(t) = \begin{cases} A_0, & 0 \leq t \leq 14\,\text{ms}, \\ 0, & \text{otherwise}, \end{cases} \tag{4.3}$$

with $A_0 = 0.015$. The choice of $\phi = 0$ ($\phi = \pi$) in Eq. (4.2) corresponds to the perturbation used in experiment to excite the $m = 0$ ($m = 2$) mode. In the experiment ω_p was chosen "to match the frequency of the excitation being studied", with the motivation that this should cause the system to oscillate at its natural frequency.

To drive the dipole oscillation, we use a perturbation potential of the form

$$\delta V(\mathbf{r}, t) = \frac{1}{2} m\omega_x^2 \{d^2 \sin^2(\omega_x t) - 2xd \sin(\omega_x t)\}, \tag{4.4}$$

where $d = 0.034\mu$m is the amplitude of the sinusoidal motion of the trap in the x

direction.

4.2.2 Equilibrium States

To use the PGPE to model a dynamical system, we first need to form equilibrium states that have the N, $N_{\rm cond}$, and T of the original states in the experiment. This is to ensure that the effects we see from our analysis are due solely to the perturbation applied to the system, as opposed to the thermalisation of states. While the procedure for forming an initial state has been detailed in Sec. 3.3, we need to show how to form states with specified N, $N_{\rm cond}$, and T, as these are not input values to the formation of our initial state.

The overall algorithm for generating equilibrium states within the PGPE formalism is summarised as a three step process:

1. Using selected values of $\{E_{\mathbf{C}},\ N_{\mathbf{C}}, \epsilon_{\rm cut}\}$, an appropriate randomised state is constructed and evolved according to the PGPE. Using time averaging $N_{\rm cond}, n_{\mathbf{C}}(\mathbf{r}), T$, and μ are calculated.

2. Using $n_{\mathbf{C}}(\mathbf{r}), T$, and μ, the incoherent region is analysed, yielding $n_{\mathbf{I}}(\mathbf{r})$, and hence the total atom number
$$N = N_{\mathbf{C}} + N_{\mathbf{I}}. \tag{4.5}$$

3. The values obtained for N, T, and $N_{\rm cond}$ are compared to the desired values from experiment and the values of $\{E_{\mathbf{C}},\ N_{\mathbf{C}}, \epsilon_{\rm cut}\}$ are adjusted before returning to step 1.

Following this procedure, we have sampled equilibrium configurations with condensate occupation $N_{\rm cond} \approx 6000 \pm 2000$ over the temperature range $0.51T_c$ to $0.83T_c$ (see Sec. 4.3.1). These samples of the equilibrium state are used as initial conditions for the collective mode excitation procedure we discuss next. We examine attributes of the initial states, particularly the dependence on $\epsilon_{\rm cut}$, later in this chapter.

4.2.3 Formalism for Dynamical Modeling of Collective Mode Excitation

The fundamental approximation in our treatment of collective mode excitation is to neglect the the dynamics of the **I** region, and their influence on the **C** region. In this

approximation the many-body dynamics are described by the PGPE

$$i\hbar\frac{\partial\psi_{\mathbf{C}}}{\partial t} = H_0\psi_{\mathbf{C}} + \mathcal{P}_{\mathbf{C}}\left\{\left(\delta V(\mathbf{r},t) + U_0|\psi_{\mathbf{C}}|^2\right)\psi_{\mathbf{C}}\right\}, \tag{4.6}$$

which differs from the PGPE used to generate equilibrium states by the inclusion of the perturbation potential. The motivation for considering only the **C** region is that many noncondensate modes and their effect on the collective mode dynamics are included in **C**. We critically examine this approximation later.

Initial conditions

We begin our simulations at $t = 0$ when the perturbation potential is first applied (see Eqs. (4.2) and (4.3)). The perturbation potential, and the ensuring dynamics it generates, break the ergodicity of the PGPE for some period of time after the perturbation has concluded (until the system rethermalised when the collective modes have damped out). Ensemble averages of the dynamical system thus need to be taken as an average over many trajectories. For each trajectory, we take as an initial condition

$$\psi_{\mathbf{C}}^{(j)}(\mathbf{r}, t=0) = \psi_{\mathbf{C}}^{\mathrm{Eq}}(\mathbf{r}, \tau_j), \tag{4.7}$$

where we have used the notation $\psi_{\mathbf{C}}^{\mathrm{Eq}}$ to represent the equilibrium states generated for the time independent potential (i.e. the states $\psi_{\mathbf{C}}(\mathbf{r}, \tau_j)$ appearing in Eq. (2.26)), and $\psi_{\mathbf{C}}^{(j)}$ to represent the j-th trajectory for the simulation of the collective mode dynamics. The subsequent evolution of $\psi_{\mathbf{C}}^{(j)}(\mathbf{r}, t)$ is according to Eq. (4.6), which excites collective modes in the system .

Observations and analysis

In the analysis of the system dynamics we present in the next section we make extensive use of the line density, defined for the j-th trajectory as

$$n_l^{(j)}(x,t) = \int dydz\, |\psi_{\mathbf{C}}^{(j)}(\mathbf{r},t)|^2. \tag{4.8}$$

This quantity, for a single trajectory, is itself of interest as the spatial integration corresponds to a spatial averaging of the system over the many modes in the **C** region, and there is some evidence that single trajectories of the PGPE can be compared to single experimental results. However, we will also be interested in the trajectory average

calculated as

$$n_l(x,t) = \frac{1}{M_t}\sum_{j=1}^{M_t} n_l^{(j)}(x,t), \tag{4.9}$$

where we use $M_t = 20$ for the trajectory averaged results presented in this paper.

We will also be interested in the momentum space equivalent line densities,

$$n_l^{(j)}(p_x,t) = \int dp_y dp_z \, |\phi_{\mathbf{C}}^{(j)}(\mathbf{p},t)|^2, \tag{4.10}$$

$$n_l(p_x,t) = \frac{1}{M_t}\sum_{j=1}^{M_t} n_l^{(j)}(p_x,t). \tag{4.11}$$

We emphasise that these line densities only include contributions from atoms in the **C** region.

We can also use trajectory averaging to obtain other quantities, such as the coherent condensate component of the system. We do this by extending the one-body density matrix to the nonequilibrium case and evaluating it with trajectory averaging, i.e.

$$G^{(1)}(\mathbf{r},\mathbf{r}',t) = \sum_{j=1}^{M_t} \left(\psi_{\mathbf{C}}^{(j)}(\mathbf{r},t)\right)^* \psi_{\mathbf{C}}^{(j)}(\mathbf{r}',t). \tag{4.12}$$

Diagonalising $G^{(1)}(\mathbf{r},\mathbf{r}',t)$ at each time we can obtain the instantaneous condensate (coherent) field $\psi_{\rm cond}(\mathbf{r},t)$, and hence the condensate line density

$$n_l^{\rm cond}(x,t) = \int dydz \, |\psi_{\rm cond}(\mathbf{r},t)|^2. \tag{4.13}$$

4.3 Results

In this section, we present a detailed analysis of the PGPE simulations of the JILA experiment [3]. First, in Sec. 4.3.1, we present the parameters of the equilibrium states we have generated that we use as the basis for our collective excitation modeling. Then in Sec. 4.3.2, we develop convenient observables and examine the density response of the Bose cloud to the perturbative drive. We then use Fourier methods to attempt to examine the density response of the system in Sec. 4.3.3. In Sec. 4.3.4 we formulate a new method of analysis and present results for the frequencies and decay rates of the lowest energy $m = 2$ and $m = 0$ modes. Then, in Sec. 4.3.5, we analyse the effect of the energy cutoff in our formalism, and provide evidence for how it affects the equilibrium and dynamic properties of the Bose cloud. For completeness, we then calculate the frequencies of the dipole mode as a function of temperature in Sec. 4.3.6, and lastly

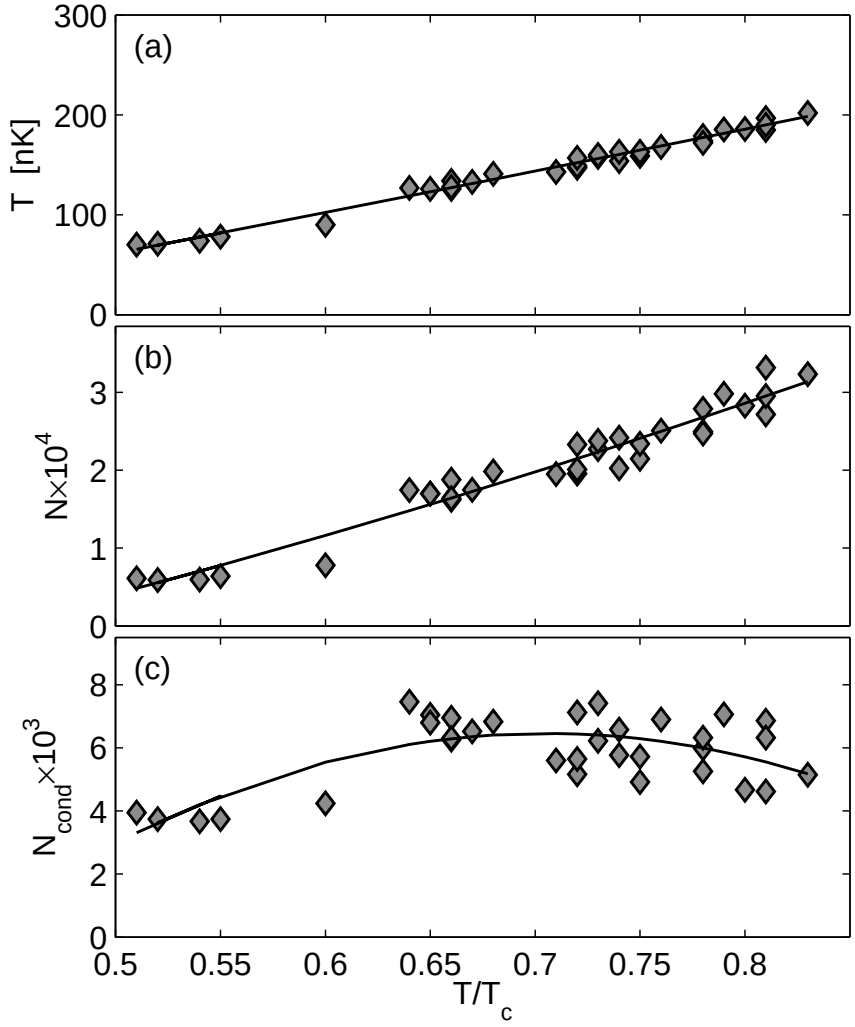

Figure 4.2: Equilibrium state properties. (a) Temperature, (b) total atom number, and (c) condensate number as a function of T/T_c. PGPE results (diamonds) and lines are guides to the eye.

discuss the phase of the noncondensate and condensate oscillations in Sec. 4.3.7.

4.3.1 Equilibrium States

First we present a summary of our results for the equilibrium states generated according to the procedure discussed in Sec. 3.3. The macroscopic parameters of the states we have produced are shown in Fig. 4.2. These states provide initial conditions over the temperature range $0.51T_c - 0.83T_c$ with a condensate number in the range $3.5 \times 10^3 - 7.5 \times 10^3$, which is comparable to the spread in condensate values used in experiment over this temperature range (see. Fig. 1(c) of Ref. [3]). A complete list of the parameters and properties of our initial equilibrium states is given in Table 4.1.

$\epsilon_{\rm cut}$ $[\hbar\omega_x]$	$N_{\mathbf{C}} \times 10^3$	$E_{\mathbf{C}}$ $[\hbar\omega_x]$	$N_{\rm cond} \times 10^3$	$N \times 10^4$	T [nK]	T/T_c	$n_{\rm min}$
17	4.64	7.2	3.95	0.613	70	0.51	0.89
17	4.54	7.25	3.74	0.64	78	0.55	1.12
18	4.54	7.3	3.74	0.591	71	0.52	0.94
19	4.54	7.5	3.67	0.598	74	0.54	0.89
17	5.05	7.5	4.24	0.78	90	0.6	1.26
32	11.9	12.3	7.46	1.75	127	0.64	0.89
32	11.4	12.3	7.05	1.7	126	0.65	0.84
32	11.1	12.3	6.8	1.7	126	0.65	0.79
32	11.9	12.6	6.95	1.88	134	0.66	0.83
32	10.9	12.3	6.26	1.62	126	0.66	0.81
31	10.6	12.1	6.31	1.64	128	0.66	0.86
30	10.6	11.9	6.52	1.75	133	0.67	0.91
32	11.9	12.8	6.83	1.99	141	0.68	0.84
36	11.9	14.4	5.6	1.95	143	0.71	0.81
37	11.9	15	5.16	1.96	147	0.72	0.7
36	11.9	14.6	5.64	2.01	149	0.72	0.85
33	12.4	13.5	7.12	2.33	157	0.72	1.02
35	12.4	14.4	6.22	2.27	158	0.73	0.91
32	12.4	13.2	7.41	2.38	160	0.73	1.09
46	13.1	22	5.77	2.03	154	0.74	0.67
34	12.4	14.1	6.57	2.42	163	0.74	0.99
38	11.9	16	4.92	2.15	159	0.75	0.88
35	12.1	14.6	5.72	2.34	163	0.75	1.02
33	12.4	13.8	6.89	2.51	168	0.76	1.01
36	11.9	15.5	5.26	2.5	174	0.78	1.05
33	12.4	14.1	5.98	2.79	179	0.78	1.15
27	10.1	11.7	6.32	2.47	172	0.78	1.44
32	12.4	13.8	7.06	2.98	186	0.79	1.29
36	11.9	16	4.67	2.83	186	0.8	1.06
37	11.9	16.5	4.62	2.72	185	0.81	1.03
32	12.4	14.1	6.86	3.32	197	0.81	1.32
25	9.59	11.3	6.32	2.96	190	0.81	1.79
36	11.9	16.5	5.14	3.24	202	0.83	1.14

Table 4.1: A summary of the equilibrium state parameters used for the results reported in Fig. 4.2 and used as initial states for the results presented in Sec. 4.3.4. The first three columns give the parameters used to generate the initial states and the remaining columns give the macroscopic parameters determined for these states.

4.3.2 Density Response

In this section, we show examples of the density response of the system after the sinusoidal perturbation has been switched off, and the cloud is evolving *in situ* in a static harmonic potential.

Figures 4.3(a)-(e) and Figs. 4.4(a)-(b) show the evolution of the position and momentum line densities for a Bose gas after the perturbation with $m = 0$ symmetry has been applied, where the time is measured with $t = 0$ corresponding to the beginning of the perturbation (see Fig. 4.1). The timescale of these results corresponds to the period of observation used in experiments. The position line density has a clear width oscillation induced by the perturbation. We have made similar observations of the y and z line densities (defined analogously to Eqs. (4.8) and (4.10)) and have verified that width oscillations also occur. For the $m = 0$ symmetry perturbation we find that the x and y oscillations are in phase, whereas the x and z oscillations are out of phase. Thus we conclude that the perturbation has excited the $m = 0$ mode more strongly than any other mode.

A similar study of the density response of the system to the perturbation with $m = 2$ symmetry reveals expected behaviour: the widths in the x and y directions oscillate out of phase, and the z width remains (approximately) constant.

Figure 4.3(d) shows the momentum line density for a single trajectory of a Bose gas after the perturbation with $m = 0$ symmetry has been applied. Figure 4.3(e) and Fig. 4.4(b) show the trajectory averaged line density. The momentum line density is sharply peaked at $p_x = 0$ due to the presence of a condensate. The peak value of the momentum line density oscillates periodically with minor peaks occurring between major peaks (see Fig. 4.4(b)). The major peak occurs first at $t \approx 16$ ms and then returns each time the condensate width reaches the outer turning point of its oscillation in position space (i.e. the condensate is at its widest, see Fig. 4.3(c)). This connection between the position space width and momentum space peak value for the condensate arises through the Heisenberg relationship, i.e. the position and momentum widths of the condensate mode are inversely related. The intermediate minor peak arises because of the out of phase oscillation of condensate width in the different directions integrated over to obtain the line density. In the case of the $m = 0$ mode the out-of-phase oscillations is along the z direction, whereas for the $m = 2$ mode is it along the y direction (e.g. see Fig. 1.2)

In addition to the dominant condensate peak at $p_x = 0$, a broad background feature is apparent in the momentum density at larger $|p_x|$ values. This feature, which we attribute to the non-condensate portion on the system in the **C** region, is more clearly apparent in momentum line density shown in Figs. 4.5 (a) and (b).

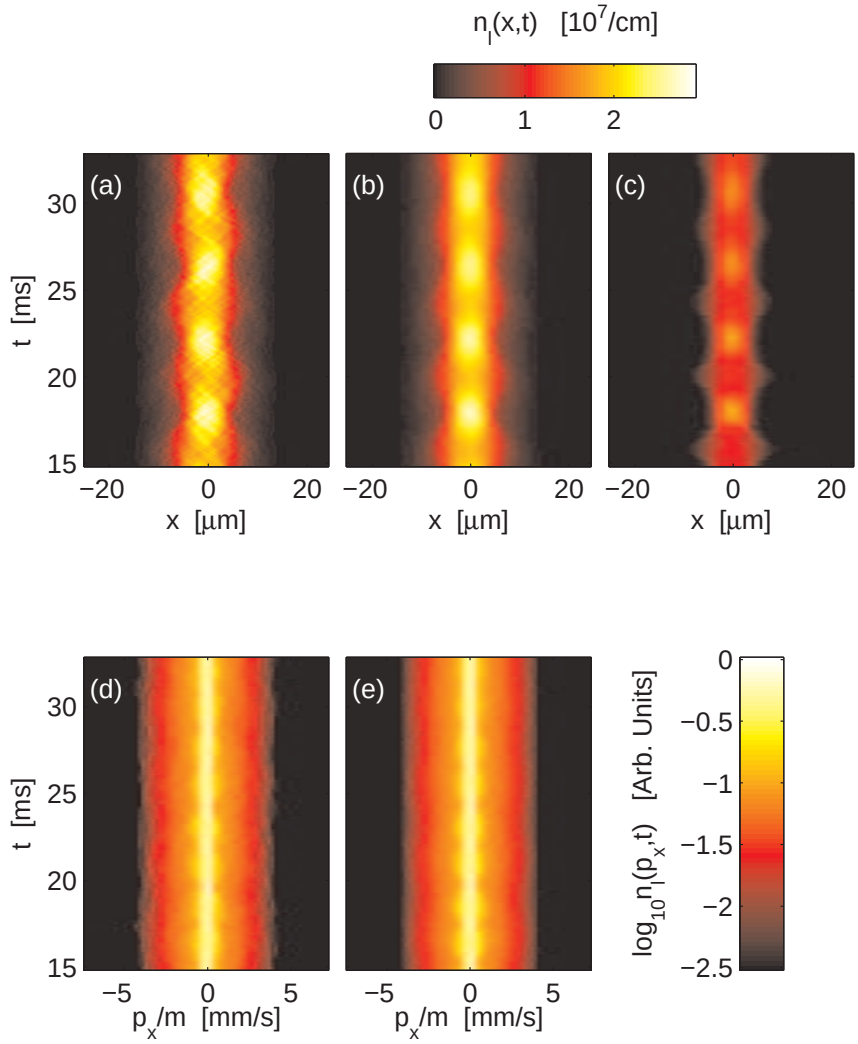

Figure 4.3: Line densities evolution after perturbation. (a) A single trajectory position space line density $n_l^{(j)}(x,t)$. (b) Trajectory averaged position space line density $n_l(x,t)$. (c) Condensate position space line density $n_l^{\rm cond}(x,t)$. (d) A single trajectory momentum space line density $n_l^{(j)}(p_x,t)$. (e) Trajectory averaged momentum space line density $n_l(p_x,t)$. Results for a system with $T = 154$ nK, $N = 2.0 \times 10^4$, $N_{\rm cond} = 5.7 \times 10^3$.

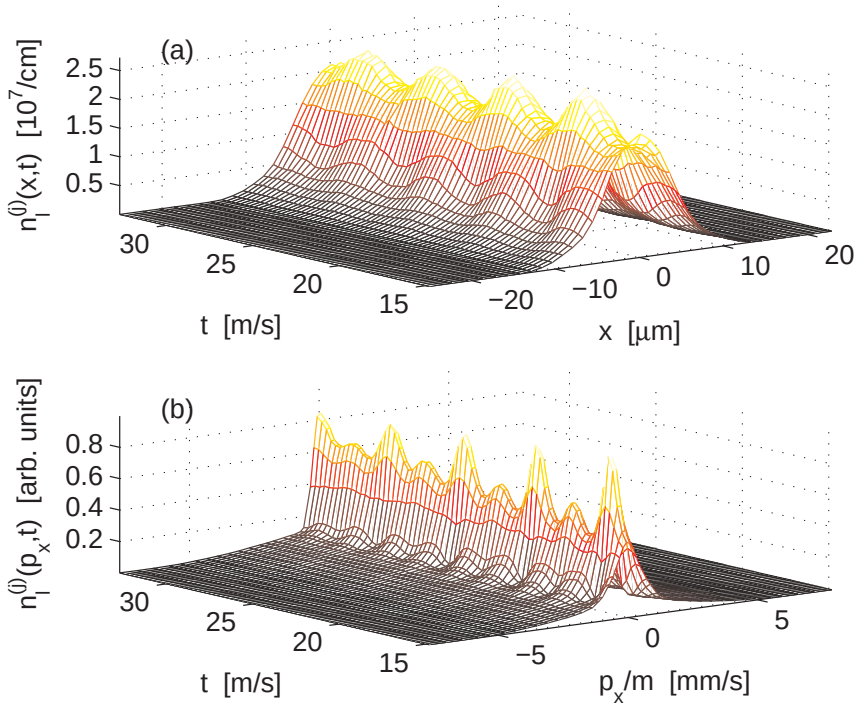

Figure 4.4: Surface plots of trajectory averaged line density plots. (a) Trajectory averaged position space line density $n_l(x,t)$. (b) Trajectory averaged position space line density $n_l(p_x,t)$. Same data as displayed in Fig. 4.3(b) and (e).

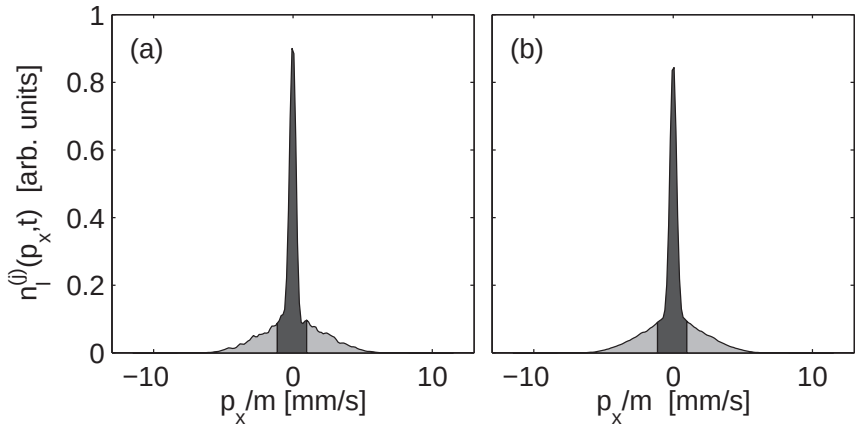

Figure 4.5: (a) Single trajectory and (b) trajectory averaged momentum line density at $t = 32$ ms for the condensate domain (dark shaded region) and the noncondensate domain (light shaded region) are shown (see text). Results for the same parameters given in Fig. 4.3.

4.3.3 Fourier Analysis of Field Moment Dynamics

We wish to study the collective modes excited by either the $m = 0$ or $m = 2$ excitation symmetries, and so look for observables that would be sensitive to oscillations in the width of the system. Experimentally, the width of the condensate and thermal components is probed by fitting a bimodal function to the density distribution of atoms released from the trap. The *in situ* momentum distribution (e.g. see the momentum line density in Fig. 4.5(b)) clearly reveals the distinct character of the condensate and noncondensate components, and (like in experiments) fitting a bimodal distribution to determine the widths of the condensate and thermal components would seem to be an obvious choice for observable. However, the *in situ* condensate momentum peak is extremely narrow and we have found that performing bimodal fits to the momentum line density is ambiguous and noisy. We note that in experiments the expansion procedure gives rise to considerable broadening of the condensate momentum distribution (e.g. see [131]) and thus cannot be compared directly to our *in situ* line density. This motivates us to examine other observables that reveal the collective response of the system. Our first consideration is the x direction position and momentum moments

$$\langle x^m \rangle^j = \int d\mathbf{r} |\psi_{\mathbf{C}}^{(j)}(\mathbf{r}, t)|^2 x^m \tag{4.14}$$

$$\langle p_x^m \rangle^j = \int d\mathbf{p} |\phi_{\mathbf{C}}^{(j)}(\mathbf{p}, t)|^2 p_x^m \tag{4.15}$$

for each timestep t of each trajectory evolution, for $m = 1$ or $m = 2$. The $\langle x \rangle$ moment, for example, shows the fluctuation in the average position of the cloud along the x axis, while the $\langle x^2 \rangle$ moment shows the fluctuations in the width of the cloud, and likewise for the moments in momentum space. Studying the frequency of the fluctuations in these moments gives direct information on the system dynamics caused by various excitations, however does not distinguish between condensate and noncondensate response. To analyse our results, we first calculate the power spectrum of individual trajectories for position and momentum space, defined as

$$F^j_{\langle x^m \rangle^j}(\omega) \equiv |\int dt e^{-i\omega t} \langle x^m(t) \rangle^j|^2 \tag{4.16}$$

$$F^j_{\langle p_x^m \rangle^j}(\omega) \equiv |\int dt e^{-i\omega t} \langle p_x^m(t) \rangle^j|^2. \tag{4.17}$$

We can then calculate the average of the trajectory power spectrums as

$$F_{\langle x^m \rangle}(\omega) = \frac{1}{M_t} \sum_{1}^{M_t} F^j_{\langle x^m \rangle^j} \tag{4.18}$$

$$F_{\langle p_x^m \rangle}(\omega) = \frac{1}{M_t} \sum_{1}^{M_t} F^j_{\langle p_x^m \rangle^j}. \tag{4.19}$$

We evaluate our power spectrums using a discrete Fourier transform (via MatLab FFT function) over the finite time interval $t_{max} = 180$ms, with a total number of steps $N_{steps} = 5550$, this gives us a frequency resolution of

$$\omega_{\rm res} = \frac{1}{\Delta N_{steps}} \tag{4.20}$$

where

$$\Delta = \frac{t_{max}}{N_{steps} - 1} \tag{4.21}$$

this gives $\omega_{\rm res} \approx 0.04\omega_x$ in our units. The Nyquist frequency is given as

$$\omega_{\rm nyq} = \frac{1}{2\Delta} \tag{4.22}$$

which is $\omega_{\rm nyq} \approx 118\omega_x$. We now discuss results of the analysis of each of these moments in turn.

In Fig. 4.6 we show the results for the $\langle x \rangle$ moment for an equilibrium cloud and a cloud where the dipole perturbation (see Eq. (4.4)) is applied, where the cloud has $N = 6131$, $N_{\rm cond} = 3947$, and $T/T_c = 0.51$. These moments show just the center of mass motion of the cloud. For an equilibrium system (no trap perturbation), we see that the cloud has center of mass motion with a frequency of $0.95\omega_x$ (where ω_x is the radial trap frequency). This corresponds to the dipole or Kohn mode, which is associated with a "sloshing" motion of the gas in the trap. These modes have frequencies which are equal to the trap frequency. Our results of $0.95\omega_x$ is below the expected result; we present some ideas at the end of this section as to why this method of analysis could be inaccurate. We make the important note here that since our equilibrium system is at finite temperature, there will be excitations already present. We see this here, through the finite excitation of the dipole mode in an unperturbed cloud, showing that there is some center of mass motion of the cloud already present.

When we drive the cloud with the dipole perturbation of form given in Eq. (4.4) we see a 40% increase in the strength of the signal in the power spectrum of Fig. 4.6. This shows that our trap perturbation has indeed excited the correct mode. We note also that there is no change in the frequency of the excitation. Similar results are found for

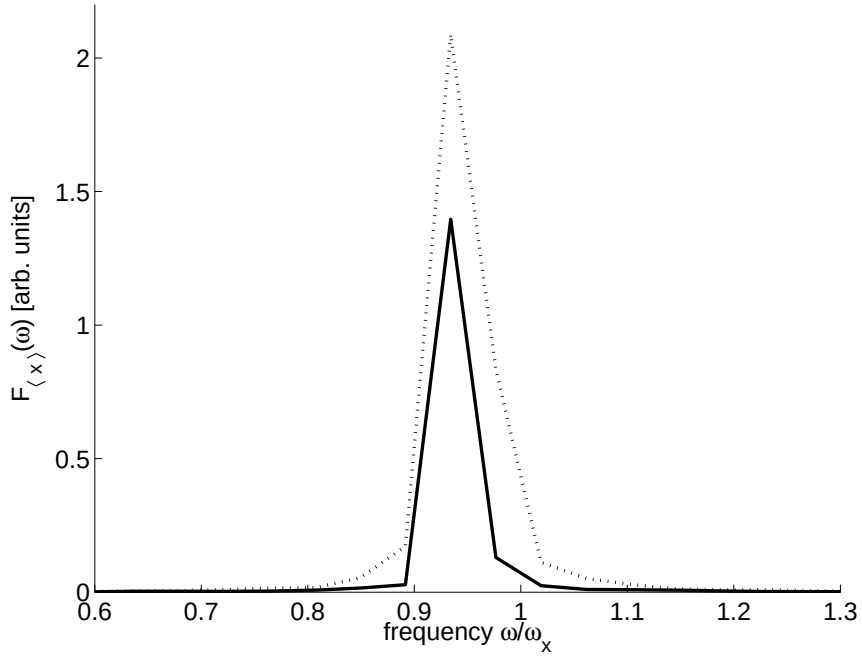

Figure 4.6: Power spectrum of the time evolution of the $\langle x \rangle$ moment for a cloud with the dipole perturbation applied (dotted) and in equilibrium (solid). System $N = 6131$, $N_{\text{cond}} = 3947$, and $T/T_c = 0.51$.

the dipole moment by analysing the power spectrum of the $\langle p \rangle$ moment, and we do not repeat them here.

The power spectrum for the $\langle x^2 \rangle$ moment for an equilibrium system (with the same parameters as above) is shown in Fig. 4.7. This moment most strongly reveals system dynamics related to width fluctuations of the cloud. We see two prominent peaks in Fig. 4.7, which have frequencies of $1.45\omega_x$ and $1.85\omega_x$. These correspond to the $m = 0$ and $m = 2$ modes, respectively, with these frequencies agreeing well with experimentally measured results at this temperature. We note here again, that the presence of these excitations in the equilibrium system is due to there being small amounts of excitation in the finite temperature system. In Fig. 4.8 we show results for the power spectrum of the $\langle x^2 \rangle$ moment at the same temperature, but after the system has been excited with the $m = 0$ symmetry perturbation (i.e. Eq. (4.2) with $\phi = 0$). This should couple most strongly to the $m = 0$ mode, and indeed, we see a 40-fold increase in the peak power at the frequency corresponding to the $m = 0$ mode, showing that our trap perturbation has selectively excited this mode. Similarly, the peak at $\omega \approx 1.45\omega_x$ is enhanced with the $m = 2$ symmetry perturbation.

We have attempted to use the power spectra, as outlined above, to characterise the collective mode frequency as a function of temperature. This analysis led to poor results for the following reasons. First, that the extended timescale needed to obtain good

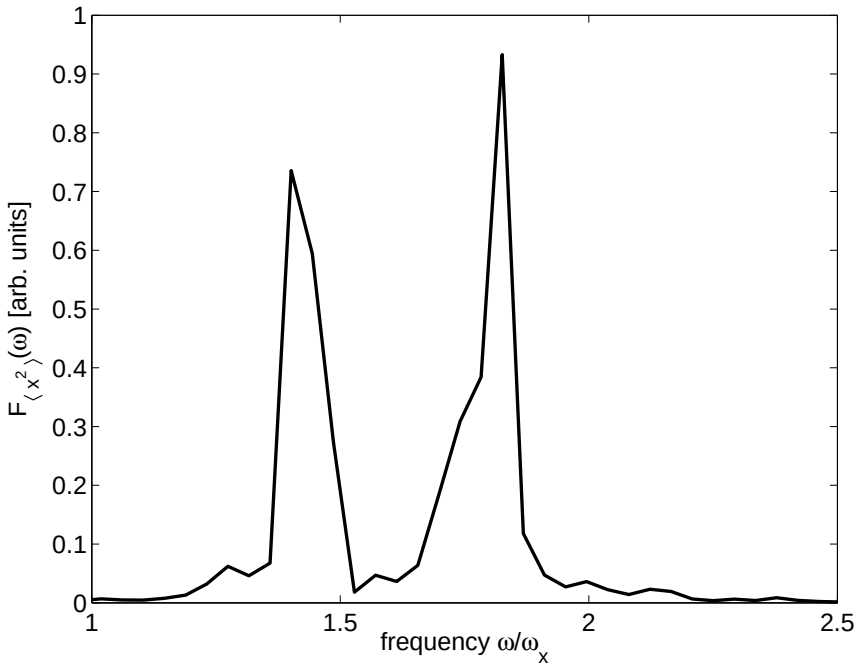

Figure 4.7: Power spectrum of the time evolution of the $\langle x^2 \rangle$ moment for an unperturbed cloud with $N = 6131$, $N_{\rm cond} = 3947$, and $T/T_c = 0.51$.

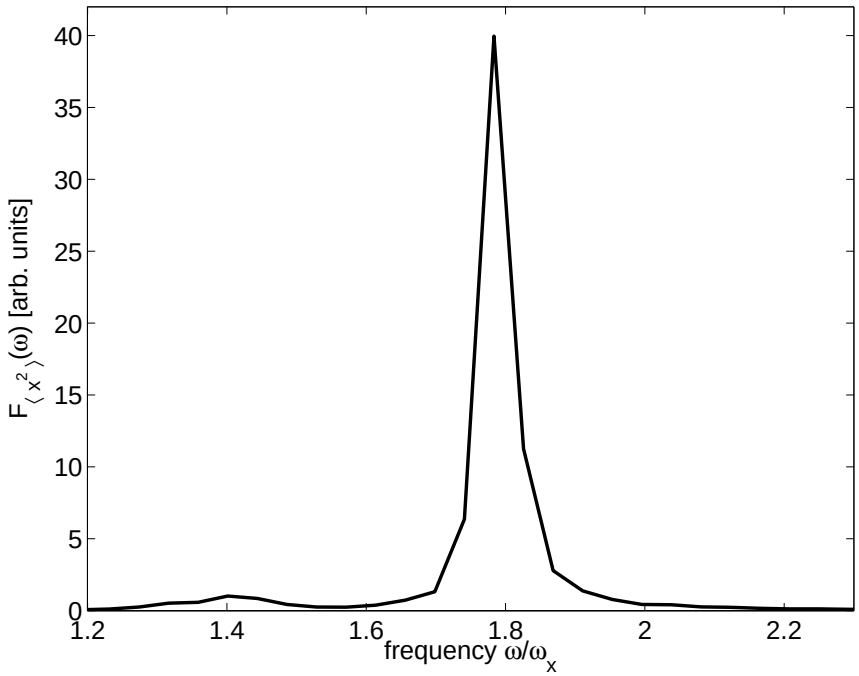

Figure 4.8: Power spectrum of the time evolution of the $\langle x^2 \rangle$ moment for a cloud with the m=0 perturbation applied. System has $N = 6131$, $N_{\rm cond} = 3947$, and $T/T_c = 0.51$.

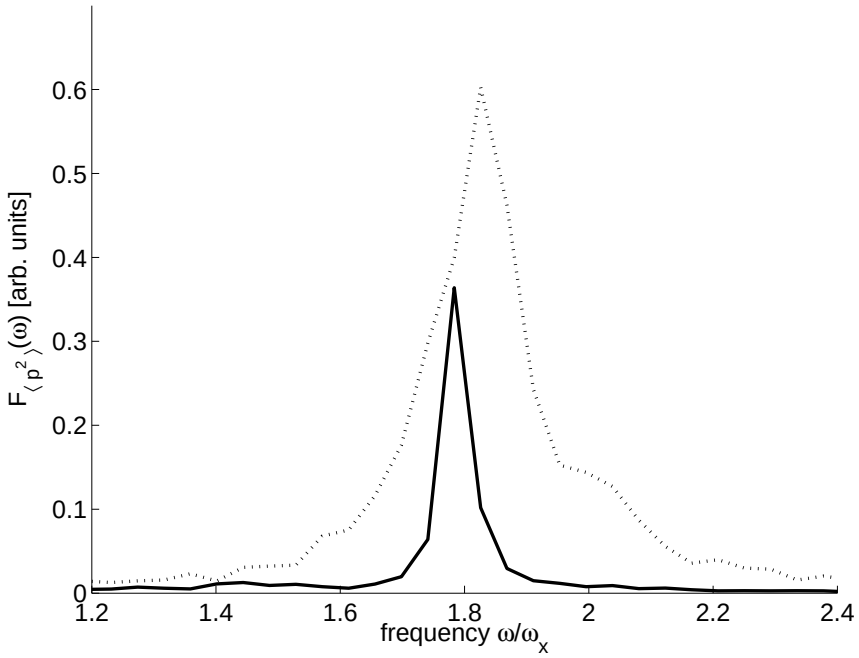

Figure 4.9: Power spectrum of the time evolution of the $\langle p^2 \rangle$ moment for a perturbed cloud with $N = 19862$, $N_{\rm cond} = 3169$, and $T/T_c = 0.73$ (dotted line) compared with power spectrum of the time evolution of the $\langle p^2 \rangle$ moment for a perturbed cloud with $N = 6131$, $N_{\rm cond} = 3947$, and $T/T_c = 0.51$.

frequency resolution means that the original excitations in the system have damped. Second, that the moments being calculated give no means to distinguish the condensate and thermal dynamics. Third, at high temperatures, we would expect to see a strong peak in the excitation spectrum at $2\omega_x$, corresponding to oscillations of just the thermal cloud, for both the $m = 0$ and $m = 2$ perturbations. However, we do not see this in the power spectrum of $\langle x^2 \rangle$ at any temperature. The reason for this can be seen by examining the spectrum of $\langle p^2 \rangle$, which is more sensitive to oscillations in the respective components of the cloud. In Fig. 4.9 we show the power spectrum for $\langle p^2 \rangle$ for a cloud driven with the $m = 0$ symmetry for the parameters given above, and we compare this to the results for a high temperature system, which has $N = 19862$, $N_{\rm cond} = 3169$, and $T/T_c = 0.73$, and is plotted with a dotted line on Fig. 4.9. For the lower temperature system, we see just a peak corresponding to the excitation of the condensate mode, as at this temperature the thermal component is very small, and it leaves no discernible signature in the excitation spectrum. For the higher temperature system, however, we can see that the condensate peak has broadened considerably, and a noncondensate response at $\approx 2\omega_x$ is apparent. We cannot resolve the thermal component by itself, however, and so we conclude that this observable is not appropriate to perform an analysis of the separate behaviour of the condensate and noncondensate fractions as was done in experiment.

4.3.4 Frequencies and Decay Rates of Collective Modes

Observables

In light of the problems associated with analysing the frequencies of the collective modes using Fourier methods, we develop two new observables that avoid both Fourier transforms, and the need to fit to our bimodal distribution. First we observe that the two momentum domains, defined as

$$\mathrm{c} = \{p_x : |p_x| \leq p_0\}, \tag{4.23}$$

$$\mathrm{n} = \{p_x : |p_x| > p_0\}, \tag{4.24}$$

with $p_0 = \sqrt{2\hbar m\omega_x}$, are dominated by the condensate (i.e. narrow peak) and noncondensate (broad background) respectively (see shaded regions in Figs. 4.5 (a) and (b)). We thus refer to these domains as the condensate (i.e. c) and noncondensate (i.e. n) domains respectively. The value of p_0 is in some sense arbitrary as long as it is greater than the condensate momentum width, and much less than the characteristic thermal momentum ($p_{\mathrm{th}} = h/\lambda_{\mathrm{dB}}$, with λ_{dB} the thermal de Broglie wavelength). Our choice, $p_0 = \sqrt{2\hbar m\omega_x}$, satisfies both of these criteria.

We can now define our two observables, as the variance of the momentum line densities on these restricted domains, i.e.

$$P_{\mathrm{c}}(t) = \langle p_x^2\rangle_{\mathrm{c}} - \langle p_x\rangle_{\mathrm{c}}^2, \tag{4.25}$$

$$P_{\mathrm{n}}(t) = \langle p_x^2\rangle_{\mathrm{n}} - \langle p_x\rangle_{\mathrm{n}}^2, \tag{4.26}$$

where

$$\langle p_x^j\rangle_\sigma = \frac{\int_\sigma dp_x n_l(p_x,t)p_x^j}{\int_\sigma dp_x n_l(p_x,t)}, \tag{4.27}$$

with $\sigma = \{\mathrm{c},\mathrm{n}\}$. We note that the denominator of Eq. (4.27) appropriately normalises the moments, and the choice of variance for P_σ, rather than the second moment $\langle p_x^2\rangle_\sigma$, is to remove the effects of any residual center of mass motion of the system.

We note here that our choice of observables is made to coincide with that made in the experiment of [3], in which the condensate and noncondensate components of the cloud were treated separately. It has been argued (see for example [14, 20]) that at high temperatures where the system behaves collectively there is an unclear division between the condensate and noncondensate, but since we aim to adhere to experimental procedure as closely as possible, we will not consider that here.

In Fig. 4.10(a) and (b) we show examples of $P_{\mathrm{c}}(t)$ and $P_{\mathrm{n}}(t)$, evaluated from the PGPE

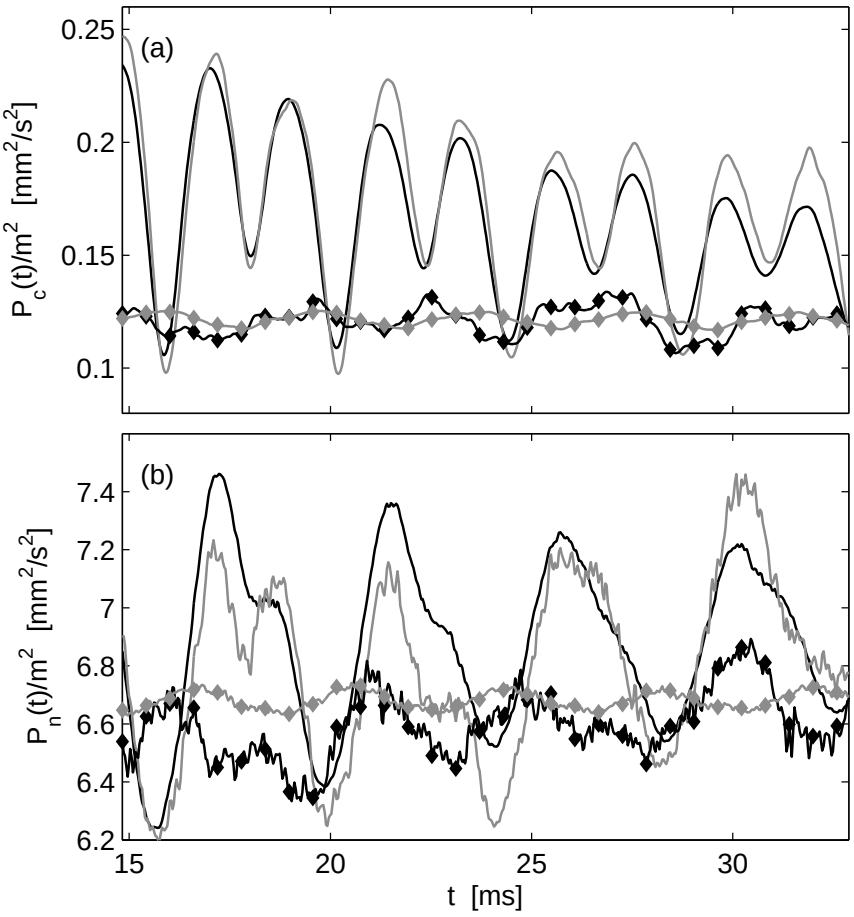

Figure 4.10: (a) Condensate domain observable, $P_{\rm c}(t)$, and (b) noncondensate domain observable, $P_{\rm n}(t)$, as a function of time. For a system excited by the $m = 0$ symmetry perturbation: Trajectory averaged result (black line), and single trajectory result (grey line). For unperturbed equilibrium system: Trajectory averaged result (black diamond line), and single trajectory result (grey diamond line). System parameters: $T = 159$ nK$\approx 0.75T_c$, $N = 2.1 \times 10^4$, $N_{\rm cond} = 4.9 \times 10^3$.

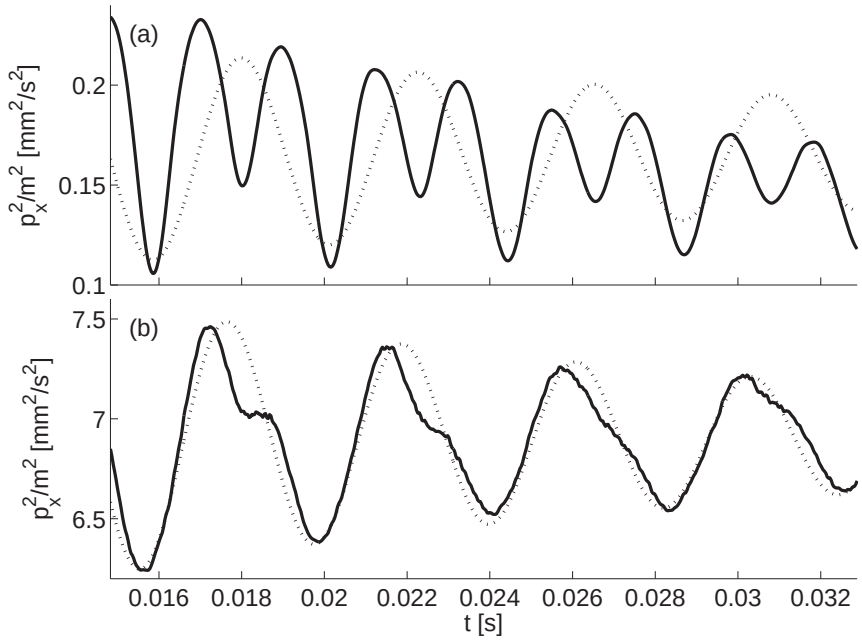

Figure 4.11: Fits to observables: (a) Condensate domain observable, $P_{\rm c}(t)$, (line) and (b) noncondensate domain observable, $P_{\rm c}(t)$, (line) as a function of time for a system excited by the $m = 0$ symmetry perturbation. Fits to observables using Eq. (4.28) shown (dotted lines). System parameters: $T = 159$ nK$\approx 0.75T_c$, $N = 2.1 \times 10^4$, $N_{\rm cond} = 4.9 \times 10^3$.

simulation of an equilibrium system and a system excited by the perturbation with $m = 0$ symmetry. From these results it is clear that the observables reveal the collective mode induced by the perturbation compared to the much smaller thermal fluctuations in the equilibrium states. In the collective mode analysis we always use $P_{\rm c}(t)$ and $P_{\rm n}(t)$ evaluated from the trajectory averaged line density, $n_l(p_x, t)$, however the results in Fig. 4.10 show that if the single trajectory line density, $n_l^{(j)}(p_x, t)$, is used to evaluate these quantities a useful signal is also obtained.

For both $P_{\rm c}(t)$ and $P_{\rm n}(t)$ we notice that considerable damping occurs over the period of observation. In both signals anharmonic features are present, but are most apparent in the condensate observable where a weaker intermediate dip is apparent. The origin of this feature is the same as for the intermediate peak in Fig. 4.4(b) (see discussion in Sec. 4.3.2): integration over the out of phase oscillation of the $m = 0$ mode in the z direction. We have also verified that the observable signal is relatively insensitive to small adjustments of the value of p_0 used to define the c and n domains.

As in the experiment we fit a decaying sinusoid of the form

$$P_{\rm fit}(t) = Ae^{-\gamma t}\sin(\omega t + \vartheta) + B, \tag{4.28}$$

to our results, to obtain the collective mode frequency (ω) and damping rate (γ). Example fits to the observable, shown in Figs. 4.11(a) and (b), indicate that while our combination of observable and fitting function is adequate for accurately determining the mode frequency, it does not provide a good description of the amplitude or damping behaviour of the modes. We do note, however, that for the finite observation time, this method gives better frequency resolution than Fourier transforming, as was carried out in Sec. 4.3.3

Mode frequencies

Our results for the mode frequency variation with temperature are presented in Fig. 4.12, along with the experimental results from Jin *et al.* [3] for comparison. We show results for the $m = 0$ mode and the $m = 2$ mode, and give the frequencies for both the condensate (solid symbols) and noncondensate (open symbol) components.

We first examine the $m = 0$ mode behaviour shown in Fig. 4.12(a). At temperatures below $0.6T_c$ the $m = 0$ mode frequencies of the condensate and noncondensate components are almost the same, indicating that the two components oscillate together. In this temperature range the agreement with the experimental results for the condensate frequency is good. There are no experimental measurements for the noncondensate behaviour in this regime as the noncondensate fraction is too small to measure. At temperatures above $0.6T_c$ our theoretical predictions and the experimental results exhibit markedly different behaviour: As temperature increases above $0.6T_c$ our results (for both the condensate and noncondensate) decrease in frequency, whereas the experimental results show a rather rapid increase in frequency. This feature of the experimental results evaded theoretical description (e.g. see [12]) until the works of Jackson *et al.* [20] in 2002 and Morgan *et al.* [14] in 2003. We discuss the origin of the disagreement between PGPE and the experimental results further in Sec. 4.3.5, and show that it arises from our lack of a dynamical description of the **I** region. We note that the PGPE predictions of a downward trend in the frequency of the $m = 0$ mode is consistent with the results of gapless Hartree-Fock-Bogoliubov calculations (see Fig. 2 of Hutchinson *et al.* [11]), indicating that anomalous average effects are included in our description. Our predictions are also in good agreement with the second order theory of Morgan *et al.* for the mode frequency in the absence of direct thermal driving (see diamond symbols on Fig. 1(a) of Ref. [14]).

In Fig. 4.12(b) the $m = 2$ mode is considered. Here we see reasonable agreement between the PGPE predictions for the condensate oscillation frequency and the experimentally measured values at all temperatures simulated. At high temperatures our predictions lie slightly above the experimentally measured values in a similar manner to the full second

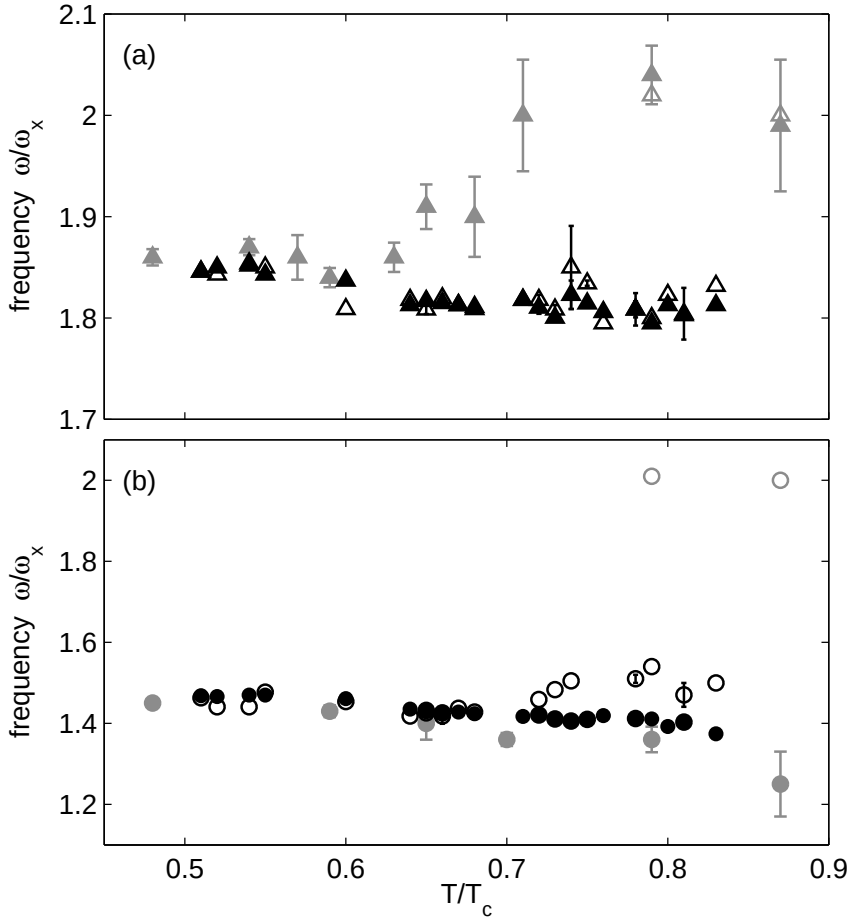

Figure 4.12: Results for the frequency dependence on temperature for PGPE and experimental results of [3]. (a) $m = 0$ mode frequencies. (b) $m = 2$ mode frequencies. Experimental results (grey symbols) and PGPE results (black symbols). Frequency for condensate (solid symbols) and noncondensate (open symbols). Error bars on some PGPE results indicate the spread in values from different calculations at the same temperature.

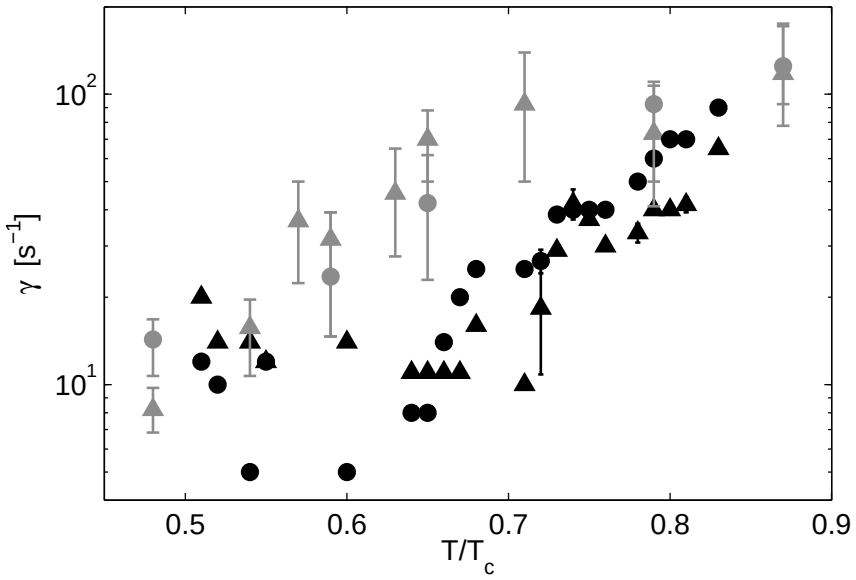

Figure 4.13: Results for the damping rates variation with temperature for PGPE and experimental results. Results are given for the condensate $m = 0$ modes (triangles) and $m = 2$ modes (circles). Experimental results (grey symbols) and PGPE results (black symbols). Error bars on some PGPE results indicate the spread in values from different calculations at the same temperature.

order predictions (i.e. including thermal driving) of Morgan *et al.* (see open circles in Fig. 1(b) of Ref. [14]). For the $m = 2$ mode noncondensate oscillation frequency, we see poor agreement with experimental results. There are no other theoretical predictions for the $m = 2$ thermal modes for us to compare against as neither Ref. [20] or [14] present results for this case. The PGPE predictions for the noncondensate mode at temperatures above $0.70T_c$ show that the noncondensate decouples from the condensate, and that its frequency is well above that of the condensate. This behaviour is qualitatively the same as that seen in experimental results (with experimental results only available at temperatures above $0.78T_c$), however the upward shift of the thermal mode frequency we calculate is much lower than that observed in experiments. We discuss the origin of this quantitative disagreement between the PGPE and experimental results further in Sec. 4.3.5.

Mode damping

In Fig. 4.13 we present the PGPE predictions for the damping rates of the $m = 0$ and $m = 2$ condensate modes, which we compare against the experimental results. Although there is considerable scatter in the PGPE results, they appear to be consistent with the experimental measurements. In particular, we observe that in the temperature range $0.5T_c - 0.6T_c$ the $m = 0$ mode decays most rapidly (i.e. larger γ), while at higher

temperatures the $m = 2$ mode gradually takes over with a larger damping rate, broadly consistent with the experimental findings. We note that our choice of observable is more appropriate for determining mode frequency than decay due to the non-sinusoidal shape of the observable signal (see discussion in Sec. 4.3.4). This will lead to a systematic shift in our predictions for the damping rate and may be responsible for the general downward shift of our results relative to the experimental measurements. Future work should look into other observables to improve the accuracy with which to analyse the mode damping rates.

4.3.5 Cutoff Dependence

In this section we investigate the dependence of equilibrium and dynamic properties of the system on the energy cutoff ($\epsilon_{\rm cut}$) used in our simulations.

Dependence of equilibrium states on $\epsilon_{\rm cut}$

To consider the effect of varying cutoff we follow the procedure discussed in Sec. 4.2.2 to prepare an initial state with a cutoff of $\epsilon_{\rm cut} = 46\hbar\omega_x$, and equilibrium parameters of $T = 154$nK$= 0.74T_c$, $N_{\rm cond} = 5.8 \times 10^3$, and $n_{\rm min} = 0.65$ where $n_{\rm min}$ is the mean occupation of the highest energy mode in the $\mathbf{C}$ region (i.e. the least occupied $\mathbf{C}$ region mode). The quantity $n_{\rm min}$ is an important indicator of the PGPE validity, as it allows us to ensure that all the modes in $\mathbf{C}$ are appreciably occupied.

To investigate the cutoff dependence we *down-project* the equilibrium microstates $\psi_{\mathbf{C}}$ of this system according to

$$\psi_{\mathbf{C}'} = \mathcal{P}'\{\psi_{\mathbf{C}}\}, \tag{4.29}$$

where $\mathcal{P}'$ is the projector for the cutoff $\epsilon'_{\rm cut} < \epsilon_{\rm cut}$. The effect of this projection is to reduce the size of $\mathbf{C}$ to a smaller region, $\mathbf{C}'$, and thus remove the occupation and energy of the modes lying between $\epsilon'_{\rm cut}$ and $\epsilon_{\rm cut}$. Since the constants of the motion, $E_{\mathbf{C}'}$ ($< E_{\mathbf{C}}$) and $N_{\mathbf{C}'}$ ($< N_{\mathbf{C}}$) have changed it is interesting to investigate if the equilibrium properties of the down-projected state differ from the original state. To check this we evolve $\psi_{\mathbf{C}'}$ according to the PGPE (2.20) (on region $\mathbf{C}'$), and analyse the thermal state that $\psi_{\mathbf{C}'}$ describes, after it is given time to thermalise. For the results we present here, we change $\epsilon'_{\rm cut}$ from $45\hbar\omega_x$ to $30\hbar\omega_x$. Over this range the number of $\mathbf{C}$ region modes decreases from 5706 (for the original state with $\epsilon_{\rm cut} = 46\hbar\omega_x$) down to 1575 (for $\epsilon'_{\rm cut} = 30\hbar\omega_x$), i.e. the total number of $\mathbf{C}$ regions modes changes by a factor of 3.6 between the cutoff extremes we consider.

In Fig. 4.14 we present results for the equilibrium properties of our down-projected

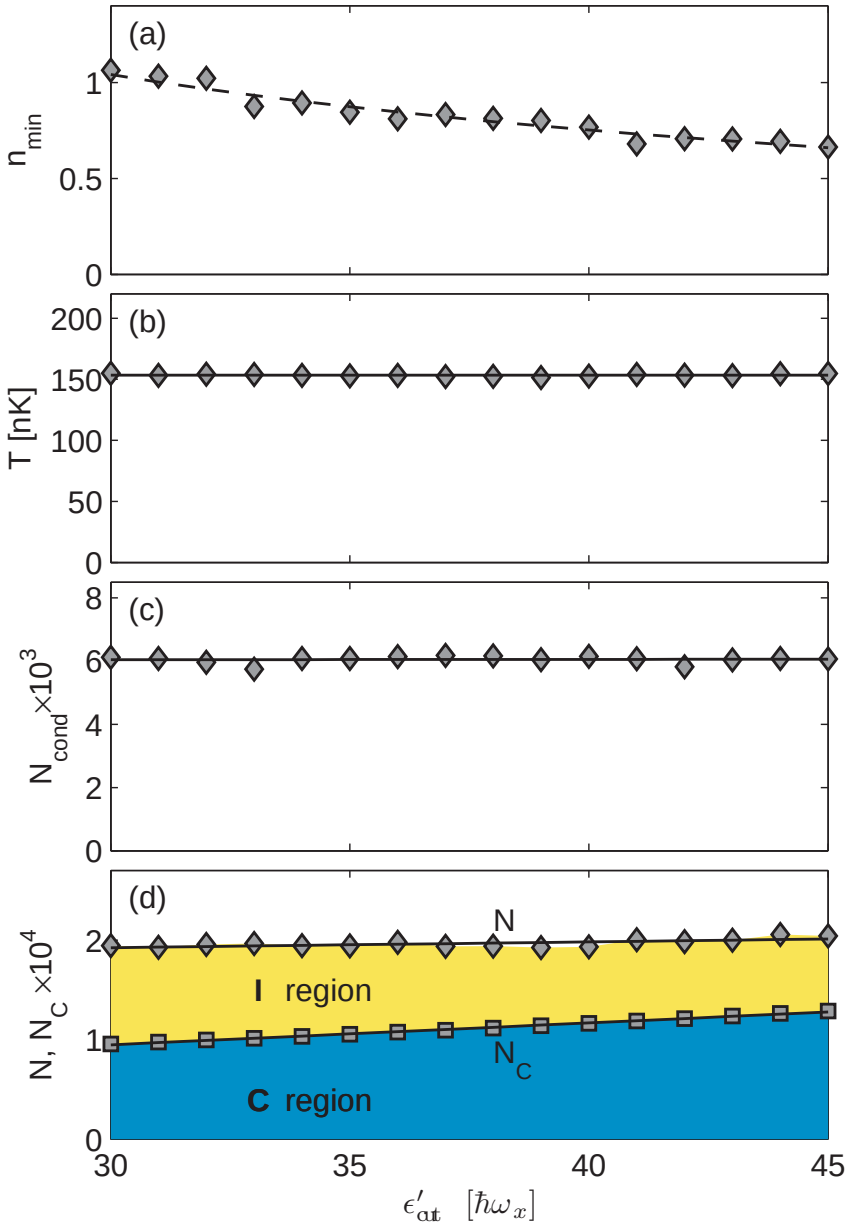

Figure 4.14: Dependence of equilibrium variables of down-projected state on the energy cutoff $\epsilon'_{\rm cut}$. (a) Average occupation of highest energy **C** region mode $n_{\rm min}$ (diamonds), (b) temperature T (diamonds), (c) condensate number $N_{\rm cond}$ (diamonds) and (d) total atom number N (diamonds) and **C** region atom number $N_{\mathbf{C}}$ (squares). Dashed line in (a) is a linear fit to $n_{\rm min}$ in the variable $1/\epsilon'_{\rm cut}$, solid lines in (b)-(d) are linear fits to the data. In (d) the shaded regions indicate the relative number of atoms in the **C** and **I** regions for each value of $\epsilon_{\rm cut}$.

states. Fig. 4.14(a) shows the population ($n_{\rm min}$) of the highest harmonic oscillator state present in the simulation as a function of the energy cutoff. As $\epsilon'_{\rm cut}$ is lowered, we see that the number occupying this highest state increases, in a manner consistent with the equipartition occupation of this mode (i.e. $n_{\rm min} \sim k_B T/\epsilon'_{\rm cut}$).

Figures 4.14(b)-(d) show the results for the macroscopic parameters T, $N_{\rm cond}$, $N_{\mathbf{C}}$, and N, respectively, of the down-projected state. We can see that these parameters (excluding $N_{\mathbf{C}}$) do not vary systematically with $\epsilon'_{\rm cut}$, and conclude that the equilibrium parameters of our PGPE simulations are not dependent on the energy cutoff. These are the first results we are aware of showing the insensitivity of classical field method predictions to cutoff. Of course there are limits to how low we can take $\epsilon'_{\rm cut}$, since our **C** region must represent the condensate mode accurately which requires us to use a cutoff energy greater than the condensate chemical potential.

Collective mode dependence on $\epsilon_{\rm cut}$

Above we have shown that the equilibrium properties are insensitive to the cutoff defining the portion of the system in the **C** and **I** regions. In contrast we would expect that the PGPE theory for simulating collective modes, as developed here, will show dependence on the cutoff. Fundamentally this is because the full dynamics of the **C** region are simulated, while the population of the **I** region is neglected. Thus, in situations where the noncondensate dynamics are important the number of noncondensate modes included in **C** will have a direct effect on the dynamical observables of the system. It would therefore seem desirable to include as much of the noncondensate population in the **C** region as is possible, i.e. increase $\epsilon_{\rm cut}$. However, there is a limit to how high we can set $\epsilon_{\rm cut}$. As discussed in Sec. 2.3, we formally require that all the **C** modes are appreciably occupied for the classical field approximation to be a valid description of the Bose gas. For $\epsilon_{\rm cut} = 46\hbar\omega_x$ we have $n_{\rm min} \approx 0.65$, and so there is limited scope for using higher energy cutoffs.

In the absence of a dynamical theory for the **I** region, adjusting the value of $\epsilon_{\rm cut}$ allows us a mechanism by which to qualitatively investigate the role of the noncondensate dynamics in the collective mode dynamics. As we increase $\epsilon_{\rm cut}$ from $30\hbar\omega_x$ to $46\hbar\omega_x$ the percentage of the total number of atoms in the **C** region increases from approximately 50% to 65% (see Fig. 4.14(d)).

We now investigate the frequency dependence of the $m = 0$ and $m = 2$ modes on the energy cutoff. Our procedure is the same as in Sec. 4.3.4, except that we consider a single temperature of $0.74T_c$ and sample our initial conditions for the PGPE from the equilibrium states of varying $\epsilon'_{\rm cut}$ (i.e. those used to average for the macroscopic

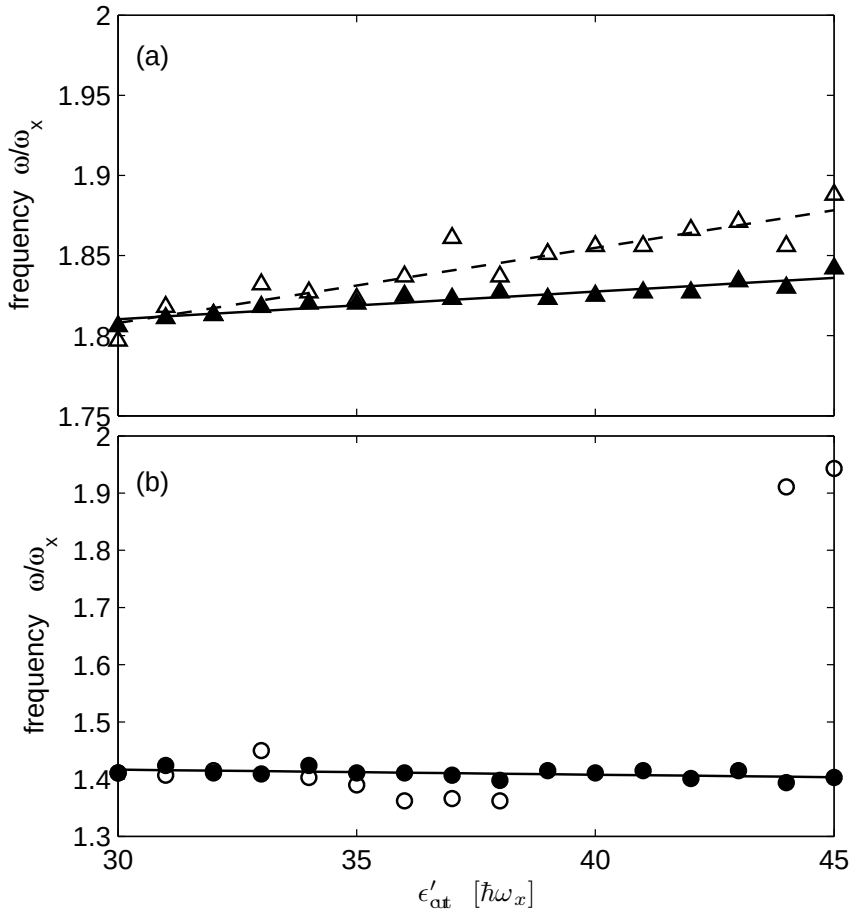

Figure 4.15: Frequency dependence of mode excitation on energy cutoff, for (a) $m = 0$ mode and (b) $m = 2$. Condensate frequency (solid symbols) and noncondensate frequency (open symbols). Solid lines are linear fits to the condensate data, and dashed line in (a) is fit to the noncondensate data.

parameters shown in Fig. 4.14). From these simulations we determine frequencies of oscillation of the condensate and noncondensate components, with the results shown in Fig. 4.15(a) and (b). The frequency of the noncondensate $m = 2$ mode for $\epsilon'_{\rm cut}/\hbar\omega_x \in [38, 44]$ are omitted as a single frequency fit of sufficient quality cannot be found (see discussion below).

The $m = 0$ modes show a dependence on $\epsilon'_{\rm cut}$, with the frequency of oscillation increasing as $\epsilon'_{\rm cut}$ increases. The noncondensate frequency increases at a greater rate than the condensate, which is consistent with the increase in the condensate frequency arising from it being driven by the noncondensate component. Morgan has also seen this effect in his second order treatment by examining the influence of including thermal driving on the condensate mode (see Ref. [17]). Our results clearly indicate that including the dynamics of all noncondensate atoms is crucial to obtain a condensate mode frequency that would be comparable with the experimental results of Jin *et al.* [3].

The $m = 2$ condensate mode shows almost no dependence on the energy cutoff, suggesting that the noncondensate component does not couple strongly to this motion of the condensate. However, the noncondensate $m = 2$ mode does show cutoff dependence: At low $\epsilon'_{\rm cut}$ (small thermal component) the noncondensate oscillates at the same frequency as the condensate, while at high $\epsilon'_{\rm cut}$ (large thermal component) it oscillates at a frequency of $\omega \approx 2\omega_x$ (which the expected value for the noninteracting limit of a thermal cloud). In the intermediate cutoff range, $\epsilon'_{\rm cut}/\hbar\omega_x \in [38, 44]$, a combination of the condensate dominated and noninteracting limit behaviours occur, and we were unable to fit a single frequency to these values. This suggests that there is a cutoff value, $\sim 40\hbar\omega_x$, at which sufficient noncondensate is dynamically simulated for it to oscillate independently of the condensate.

We now make some observations, from comparison of the goodness of the PGPE description of the experimental frequencies in Fig. 4.12 to the cutoff analysis of the modes in this section. For the $m = 0$ modes, both the condensate and noncondensate predictions are in poor agreement with experiment at $0.74T_c$, and both are observed to be cutoff dependent [Fig. 4.15(a)]. For the $m = 2$ mode we find that: (i) The condensate dynamics, which are in good agreement with experiment, are independent of cutoff [Fig. 4.15(b)]. (ii) The noncondensate results, which are in poor agreement with the experiment at high temperatures, are strongly cutoff dependent [Fig. 4.15(b)]. In general, these observations lead us to expect that cutoff independent predictions of the dynamical PGPE theory are likely to be accurate in the absence of a dynamical theory of the **I** region, while cutoff dependent predictions are unreliable. In the latter case a dynamical theory of the **I** region is required.

4.3.6 Dipole Mode

It is rigorously known that a harmonically trapped system will have a center-of-mass motion oscillation mode at the trapping frequency (Kohn mode) [132]. This mode is an important test of theory and was analysed in experiment [3] for the purposes of frequency calibration. Due to the presence of a projector in the PGPE theory the Kohn mode is not a constant of motion (see Ref. [118]) and so for completeness we investigate the dynamics of this mode here. To do this we use the PGPE (2.20) following the same procedure for setting up simulations as was done for the $m = 0$ and $m = 2$ modes, but with the dipole perturbation potential (4.4). To analyse our data, we study the first moments $\langle p_x \rangle_\sigma$ for $\sigma = \{\mathrm{c}, \mathrm{n}\}$ (see Sec. 4.3.4) to provide observables for the condensate and noncondensate behaviour. Our results, shown in Fig.4.16, indicate that the condensate and noncondensate components both oscillate at approximately $1.0\omega_r$, as expected.

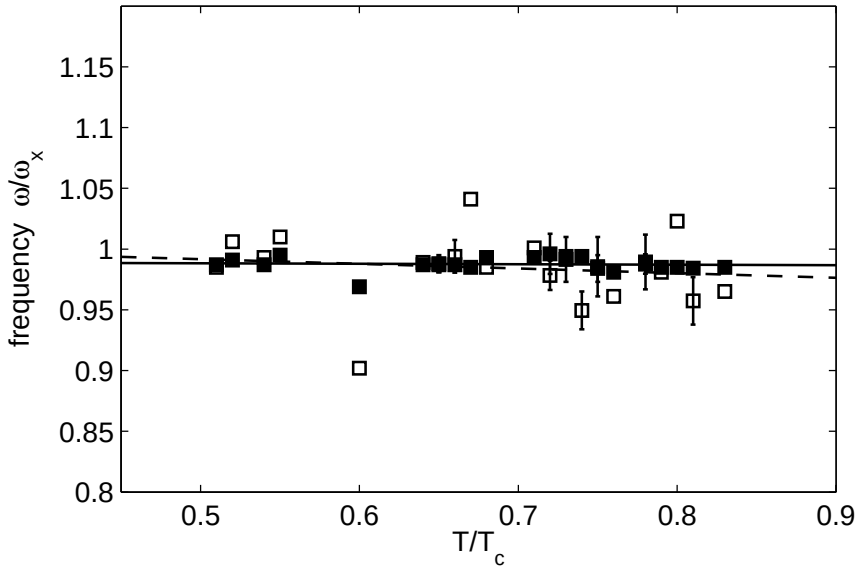

Figure 4.16: Frequency of dipole mode as a function of temperature. Condensate (solid squares) and noncondensate (open squares). Error bars on some results indicate the spread in values from different calculations at the same temperature. Linear fit to the condensate (line) and noncondensate (dashed) results.

4.3.7 Relative Phase of Condensate-Noncondensate Oscillations

The relative phase of the condensate and noncondensate oscillations has played a central part in the explanation of the sharp jump in the frequency spectrum of the $m = 0$ mode. Stoof and coworkers [18,30] argued that the anomalous jump was caused by a transition from out-of-phase to in-phase oscillations of the condensate and noncondensate components at high temperature. Morgan [17] lends support to this theory by calculating the relative phase between the oscillations of the condensate and noncondensate components, and shows that at moderate temperatures ($\sim 0.5T_c$) the components oscillate out of phase, whereas at high temperatures ($\sim 0.8T_c$) they oscillate in phase. This is consistent with the physical picture that a large noncondensate fraction oscillating at the noninteracting frequency $2\omega_x$ couples strongly to the condensate $m = 0$ mode and drives it at this higher frequency. Morgan's results for the $m = 2$ mode show the relative phase between the components increases with increasing temperature up to about $0.85T_c$, at which point a slight decrease is observed to begin.

Here we follow the method of Morgan [17] closely. We calculate the phase difference between the two components using the first oscillation cycle after the perturbation is concluded. We find the relative phase by using the difference in minima of the two observable curves (see Fig. 4.11) as a fraction of the half period of the condensate oscillation, to give a result from zero to π. We present our results in Fig. 4.17. These

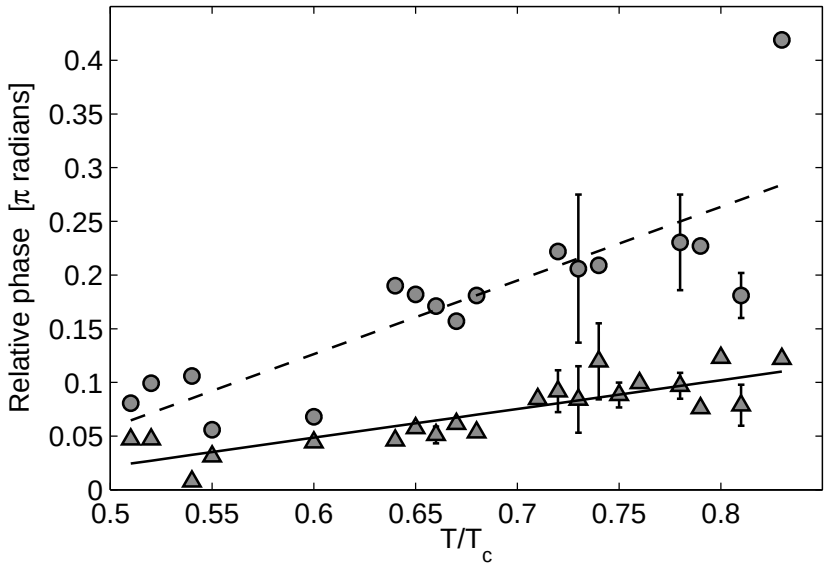

Figure 4.17: Relative phase between the condensate and noncondensate collective modes for the different symmetries studied: $m = 0$ mode (triangles) and $m = 2$ (circles). Error bars on some PGPE results indicate the spread in values from different calculations at the same temperature. Solid line is a linear fit to the $m = 0$ data and dashed line is a linear fit to the $m = 2$ data. Same parameters as in Fig. 4.15.

results are in reasonable qualitative agreement with those of Morgan at low temperatures, where the relative phases of each mode are increasing with temperature, with the $m = 2$ mode having a larger phase angle to the $m = 0$ mode at any given temperature (c.f. Fig. 11 [17]). However, generally our predicted values for the relative phase are less than those calculated by Morgan, and more importantly, we do not see the sudden reduction in phase angle for the $m = 0$ mode as temperatures increases above $\sim 0.7T_c$. The likely explanation for our disagreement is that the fraction of noncondensate being dynamically simulated is not great enough so that: (i) At moderate temperatures ($\sim 0.5T_c$) the noncondensate is being dominated by the condensate oscillation, leading to a smaller than expected relative phase between the components (for both $m = 0$ and $m = 2$ modes). (ii) At higher temperatures ($> 0.7T_c$) the noncondensate component is insufficiently dominant to effectively drive the condensate back in-phase with its natural oscillation (applying only to the resonantly coupled $m = 0$ mode).

To further investigate these effects, in Fig. 4.18 we show the dependence of the relative phase on the energy cutoff $\epsilon'_{\rm cut}$, and hence noncondensate fraction in the **C** region. In particular, we consider a system at temperature $0.74T_c$ for various $\epsilon'_{\rm cut}$ (i.e. the same as was examined in Sec. 4.3.5). At this temperature Morgan predicts a relative phase of 0.25π for the $m = 0$ mode (and that with increasing temperature this phase decreases) and a relative phase of 0.45π for the $m = 2$ mode (which remains approximately constant with increasing temperature, before starting to decrease at about $0.85T_c$). Our results

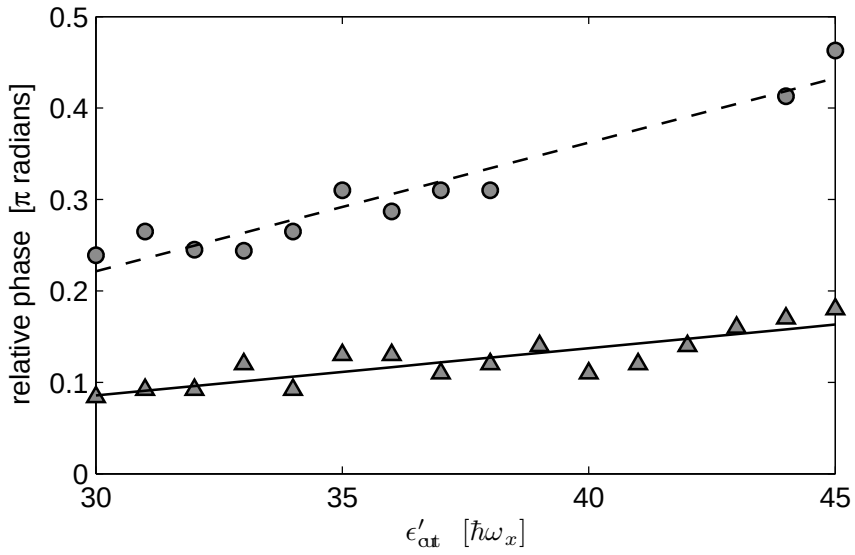

Figure 4.18: Relative phase between the condensate and noncondensate collective modes the $m = 0$ (triangles) and $m = 2$ modes (circles) as a function of the down-projected energy cutoff $\epsilon'_{\rm cut}$. Solid line is a linear fit to the $m = 0$ data and dashed line is a linear fit to the $m = 2$ data. Same parameters as in Fig. 4.15.

for the dependence on $\epsilon'_{\rm cut}$ show that the relative phase of both modes increase with increasing cutoff, although the $m = 0$ mode does so more slowly than the $m = 2$ mode. The $m = 2$ behaviour indicates that as the noncondensate component being simulated increases (i.e. as $\epsilon'_{\rm cut}$ increases) it's phase, relative to the condensate, becomes more independent. We note that while the $m = 2$ condensate mode is cutoff insensitive, the relative phase between the $m = 2$ modes shows a dependence because the noncondensate mode does change character with $\epsilon'_{\rm cut}$ (see Sec. 4.3.5). The slower rate of increase in the the relative phase of the $m = 0$ modes with cutoff (as compared to the $m = 2$ modes, see Fig. 4.18) may be indicative of the resonant coupling between the components.

At our maximum value of cutoff ($\epsilon'_{\rm cut} = 45\hbar\omega_x$), about 50% of the noncondensate atoms are included in the PGPE description, and we speculate that a complete dynamical representation of the noncondensate would lead to this mode driving the condensate and the return to an in phase oscillation.

Part II

Correlations

Chapter 5

Two point Correlations of the Bose Gas

5.1 Introduction

In this chapter we will develop formalism to calculate two-point correlations within a harmonically trapped Bose gas. We will analyse separately the role of the condensate and thermal components in the coherence of a system. We begin in Sec. 5.2 by giving definitions of the correlation functions we use, and showing how these apply in our finite temperature formalism. We give results for these correlation functions in Sec. 5.3.

5.2 Formalism

5.2.1 System and Correlation Functions

We will develop the PGPE formalism to calculate two-point correlations in a finite temperature three dimensional Bose cloud. We begin by defining the correlation functions of interest, and then showing how to apply the methods developed in Chapter 2 to explore the correlations in our system.

Position space correlation functions

The density and unnormalised first and second order correlation functions (e.g. see [52]) are defined as

$$n(\mathbf{r}) = \langle\hat{\Psi}^\dagger(\mathbf{r})\hat{\Psi}(\mathbf{r})\rangle, \tag{5.1}$$

$$G^1(\mathbf{r},\mathbf{r}') = \langle\hat{\Psi}^\dagger(\mathbf{r}')\hat{\Psi}(\mathbf{r})\rangle, \tag{5.2}$$

$$G^2(\mathbf{r},\mathbf{r}') = \langle\hat{\Psi}^\dagger(\mathbf{r}')\hat{\Psi}^\dagger(\mathbf{r})\hat{\Psi}(\mathbf{r})\hat{\Psi}(\mathbf{r}')\rangle, \tag{5.3}$$

where the averages are to be interpreted as thermal averages. We note that local first order correlations are equal to the density, i.e. $n(\mathbf{r}) = G^1(\mathbf{r},\mathbf{r})$. For the purposes of interpreting particle correlations it is convenient to introduce the normalised versions of the correlation functions

$$g^1(\mathbf{r},\mathbf{r}') = \frac{G^1(\mathbf{r},\mathbf{r}')}{\sqrt{n(\mathbf{r}')n(\mathbf{r})}}, \tag{5.4}$$

$$g^2(\mathbf{r},\mathbf{r}') = \frac{G^2(\mathbf{r},\mathbf{r}')}{n(\mathbf{r}')n(\mathbf{r})}. \tag{5.5}$$

The first order correlation function describes phase fluctuations in the system, and as G^1 is the one-body density matrix of the system, off-diagonal long range order in this quantity is the defining characteristic of Bose-Einstein condensation [121]. The second order function is a measure of pair correlations in the system, for instance the atoms tendency to cluster (bunch) or separate (anti-bunch). Recent experiments in a superfluid Fermi gas have revealed non-local pairing through measurements of second order correlations [48]. We note here that the normally ordered second order correlation function that we define can be related to the density correlation function by [52]

$$\langle\hat{\Psi}^\dagger(\mathbf{r})\hat{\Psi}(\mathbf{r})\hat{\Psi}^\dagger(\mathbf{r}')\hat{\Psi}(\mathbf{r}')\rangle = G^2(\mathbf{r},\mathbf{r}') + G^1(\mathbf{r},\mathbf{r})\delta(\mathbf{r}-\mathbf{r}'). \tag{5.6}$$

We will not calculate the density correlation function here, but note that it has been used in other theoretical works (e.g. see Ref. [133]).

Momentum space correlation functions

Often the correlation functions for ultra-cold atom systems are measured after *time of flight* expansion for time $t_{\rm exp}$. In this situation the measured correlations are proportional to the *in situ* momentum correlations, with the relationship between final (observed) position $\mathbf{R}$ and *in situ* momentum given by $\mathbf{R}/t_{\rm exp} = \mathbf{p}/m$. For this reason we also develop our formalism to calculate momentum space correlations, defined in

terms of the momentum field operator $\hat{\Phi}(\mathbf{p})$, as

$$n(\mathbf{p}) = \langle \hat{\Phi}^\dagger(\mathbf{p})\hat{\Phi}(\mathbf{p})\rangle, \tag{5.7}$$
$$G^1(\mathbf{p},\mathbf{p}') = \langle \hat{\Phi}^\dagger(\mathbf{p}')\hat{\Phi}(\mathbf{p})\rangle, \tag{5.8}$$
$$G^2(\mathbf{p},\mathbf{p}') = \langle \hat{\Phi}^\dagger(\mathbf{p}')\hat{\Phi}^\dagger(\mathbf{p})\hat{\Phi}(\mathbf{p})\hat{\Phi}(\mathbf{p}')\rangle. \tag{5.9}$$

Many aspects of the formalism we present for position and momentum space are similar, and in what follows we focus primarily on giving a detailed derivation for the position case, and will only comment on any important differences that arise in the momentum case.

5.2.2 Finite Temperature Formalism

To describe the trapped Bose gas within our finite temperature formalism we split the full field operator as previously noted Eq. (2.16)

$$\hat{\Psi} = \psi_{\mathbf{C}} + \hat{\psi}_{\mathbf{I}} \tag{5.10}$$

We now use this decomposition to find expressions for the full correlation functions using just the incoherent and classical region field operators.

Substituting expression (5.10) into the Eqs. (5.1)-(5.3) gives

$$n(\mathbf{r}) = n_{\mathbf{C}}(\mathbf{r}) + n_{\mathbf{I}}(\mathbf{r}), \tag{5.11}$$
$$G^1(\mathbf{r},\mathbf{r}') = G^1_{\mathbf{C}}(\mathbf{r},\mathbf{r}') + G^1_{\mathbf{I}}(\mathbf{r},\mathbf{r}'), \tag{5.12}$$
$$G^2(\mathbf{r},\mathbf{r}') = G^2_{\mathbf{C}}(\mathbf{r},\mathbf{r}') + G^2_{\mathbf{I}}(\mathbf{r},\mathbf{r}') + 2G^1_{\mathbf{I}}(\mathbf{r},\mathbf{r}')G^1_{\mathbf{C}}(\mathbf{r},\mathbf{r}') + n_{\mathbf{I}}(\mathbf{r})n_{\mathbf{C}}(\mathbf{r}') + n_{\mathbf{I}}(\mathbf{r}')n_{\mathbf{C}}(\mathbf{r}), \tag{5.13}$$

where

$$n_j(\mathbf{r}) = \langle \psi_j^\dagger(\mathbf{r})\psi_j(\mathbf{r})\rangle \tag{5.14}$$
$$G^1_j(\mathbf{r},\mathbf{r}') = \langle \psi_j^\dagger(\mathbf{r}')\psi_j(\mathbf{r})\rangle, \tag{5.15}$$
$$G^2_j(\mathbf{r},\mathbf{r}') = \langle \psi_j^\dagger(\mathbf{r}')\psi_j^\dagger(\mathbf{r})\psi_j(\mathbf{r})\psi_j(\mathbf{r}')\rangle, \tag{5.16}$$

with $j = \{\mathbf{I},\mathbf{C}\}$ for the incoherent and classical regions respectively.

Several approximations have been made in deriving Eqs. (5.11)-(5.13). We assume that:

(i) the classical and incoherent regions are uncorrelated, so that expectations of mixed terms of classical and incoherent operators can be factorised, e.g. $\langle \hat{\psi}^\dagger_{\mathbf{I}}\psi^*_{\mathbf{C}}\psi_{\mathbf{C}}\hat{\psi}_{\mathbf{I}}\rangle =$

$\langle\hat{\psi}^{\dagger}_{\mathbf{I}}\hat{\psi}_{\mathbf{I}}\rangle\langle\psi^{*}_{\mathbf{C}}\psi_{\mathbf{C}}\rangle$. For this to be a good approximation we require that our fields are expanded in a basis that approximately diagonalises the problem at the energy cutoff. For our purposes the single particle basis of the harmonic oscillator potential is satisfactory (also see [111]).

(ii) we can neglect the averages of single fields. We note that in the classical region this is justified because we do not make the symmetry breaking approximation to describe the condensate.

(iii) we can neglect the averages of anomalous fields, e.g. $\langle\psi_{\mathbf{C}}\psi_{\mathbf{C}}\rangle$. The anomalous average of the fields is rigorously zero, and only occurs as a nonzero contribution in symmetry broken formalism such as Hartree-Fock-Bogoliubov. Thus the anomalous average of the classical operator is zero for our classical field approximation, and the anomalous expectation of the incoherent field is also zero within the Hartree-Fock approximation we use here.

5.2.3 Classical Region

The classical region is described with the PGPE formalism.

Taking N_s samples of the coherent field at times $\{t_j\}$ after it has thermalised, we evoke the ergodic hypothesis to evaluate the correlation functions as

$$n_{\mathbf{C}}(\mathbf{r}) = \frac{1}{N_s}\sum_{j=1}^{N_s}\left|\psi_{\mathbf{C}}(\mathbf{r},t_j)\right|^2, \tag{5.17}$$

$$G^1_{\mathbf{C}}(\mathbf{r},\mathbf{r}') = \frac{1}{N_s}\sum_{j=1}^{N_s}\psi^{*}_{\mathbf{C}}(\mathbf{r},t_j)\psi_{\mathbf{C}}(\mathbf{r}',t_j), \tag{5.18}$$

$$G^2_{\mathbf{C}}(\mathbf{r},\mathbf{r}') = \frac{1}{N_s}\sum_{j=1}^{N_s}\left|\psi_{\mathbf{C}}(\mathbf{r}',t_j)\right|^2\left|\psi_{\mathbf{C}}(\mathbf{r},t_j)\right|^2. \tag{5.19}$$

Correlation functions in momentum space can be immediately evaluated using the procedure in (5.17)-(5.19), but using the momentum field as given in Eq. (2.27)

5.2.4 Incoherent Region

The incoherent region is treated using the meanfield treatment detailed in Sec. 2.4, and is thus a Gaussian theory. To calculate correlation functions for the incoherent region we closely follow the work of Glauber [52].

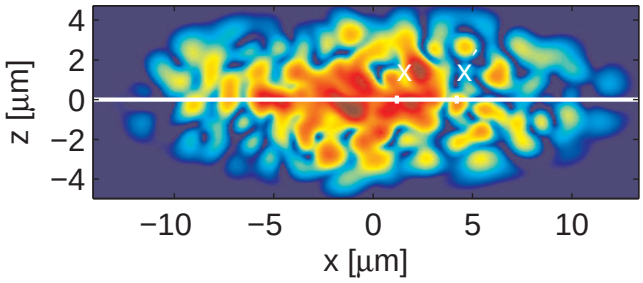

Figure 5.1: Instantaneous density slice of classical field in xz-plane showing the system and correlation measurement geometry. The x-axis is indicated (white line) and two points x and x' are shown. The field and density correlations between these points define $G_c^1(x,x')$ and $G_c^2(x,x')$ respectively. This result is for a system of 3×10^5 ^{87}Rb atoms in the trap described in the text at a temperature of 159 nK.

The Wigner function for the incoherent region is related to the first order correlation function by [52]

$$G_{\mathbf{I}}^1(\mathbf{r},\mathbf{r}') = \int_{\Omega_{\mathbf{I}}} d\mathbf{p}\, e^{-i\mathbf{p}\cdot(\mathbf{r}-\mathbf{r}')/\hbar} W_{\mathbf{I}}\left(\frac{\mathbf{r}+\mathbf{r}'}{2},\mathbf{p}\right). \tag{5.20}$$

Since our Hartree-Fock treatment of the incoherent region is Gaussian, the second order correlation function is

$$G_{\mathbf{I}}^2(\mathbf{r},\mathbf{r}') = G_{\mathbf{I}}^1(\mathbf{r},\mathbf{r})G_{\mathbf{I}}^1(\mathbf{r}',\mathbf{r}') + |G_{\mathbf{I}}^1(\mathbf{r},\mathbf{r}')|^2, \tag{5.21}$$

which can be justified by Wick's theorem.

The momentum space correlation functions for the incoherent region can be obtained in a similar manner to the position space case using the result

$$G_{\mathbf{I}}^1(\mathbf{p},\mathbf{p}') = \int_{\Omega_{\mathbf{I}}} d\mathbf{r}\, e^{-i\mathbf{r}\cdot(\mathbf{p}-\mathbf{p}')/\hbar} W_{\mathbf{I}}\left(\mathbf{r},\frac{\mathbf{p}+\mathbf{p}'}{2}\right). \tag{5.22}$$

Equation (5.21) can also be applied to the momentum space result, and we do not repeat it here.

For our case of a system with external confinement, the two-point correlation functions will depend on all coordinates [1]. Hence a complete characterisation of these correlations in the 3D system requires six-dimensions. The results we present here are for the correlation functions of the full 3D system for the case of both points lying on the x-axis, e.g. $G^1(\mathbf{r}=x\hat{\mathbf{x}},\mathbf{r}'=x'\hat{\mathbf{x}})$, where $\hat{\mathbf{x}}$ is the unit vector in x direction, and this will now be abbreviated to just $G^1(x,x')$. The geometry of this is indicated in Fig. 5.1. Here we detail how to calculate the appropriately integrated Wigner functions needed

[1] This is in contrast to the homogeneous case where translational invariance means that correlation functions only depend on the relative separation of the points e.g. $G^2_{\rm hom}(\mathbf{r},\mathbf{r}') = G^2_{\rm hom}(\mathbf{r}-\mathbf{r}')$.

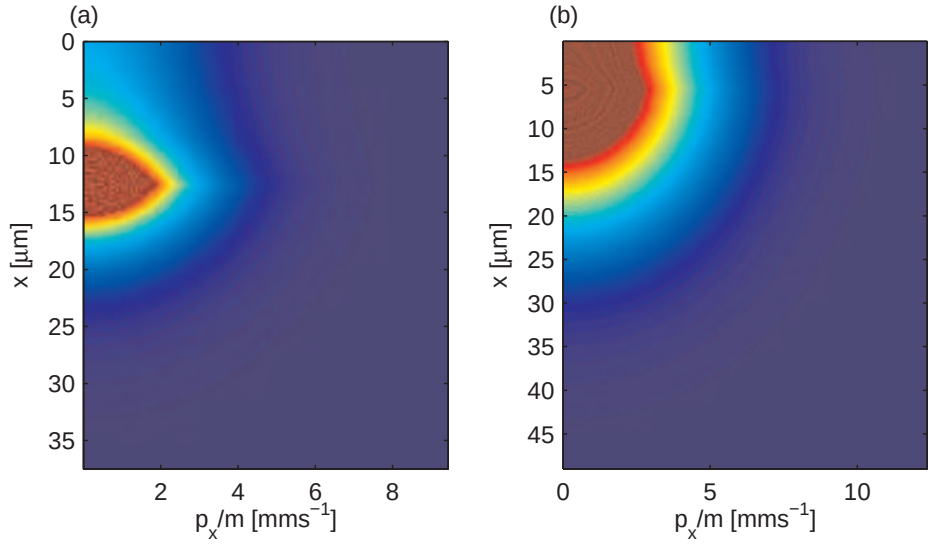

Figure 5.2: Wigner function $W_{\mathbf{I}}^{\mathrm{pos}}(x, p_x)$ (arb. units) for a cloud of 3×10^5 ^{87}Rb atoms in a trap with frequencies $\{\omega_x, \omega_y, \omega_z\} = 2\pi \{1, 1, \sqrt{8}\} \times 40\, s^{-1}$ at 93 nK (a) and 159 nK (b).

to calculate such correlations, and give examples of the form they take for systems of interest.

For the position space correlation function, we wish to calculate

$$G_{\mathbf{I}}^1(x, x') \equiv G_{\mathbf{I}}^1(x\hat{\mathbf{x}}, x'\hat{\mathbf{x}}) = \int_{\Omega_{\mathbf{I}}} d\mathbf{p} e^{-i\mathbf{p}.(x\hat{\mathbf{x}} - x'\hat{\mathbf{x}})/\hbar} W_{\mathbf{I}}(\frac{x\hat{\mathbf{x}} + x'\hat{\mathbf{x}}}{2}, \mathbf{p}) \tag{5.23}$$

This integral is separable in the momentum coordinates, and so our procedure to calculate Eq. (5.23) has two steps. First, we integrate over the p_y and p_z coordinates, as these coordinates are independent of the Fourier transform to be taken. We wish to calculate

$$W_{\mathbf{I}}^{\mathrm{pos}}(x\hat{\mathbf{x}}, p_x\hat{\mathbf{p}}_x) = \int_{\Omega_{\mathbf{I}}} dp_y dp_z W_{\mathbf{I}}(x\hat{\mathbf{x}}, \mathbf{p}). \tag{5.24}$$

We restrict the momentum space to be integrated by

$$\epsilon_{\mathrm{cut}} > \frac{\mathbf{p}^2}{2m} + V_0(\mathbf{r}). \tag{5.25}$$

In Fig. 5.2 we show the Wigner function of Eq. (5.24), for temperatures 93nK (a) and 159nK (b). These Wigner functions will be used in the construction of results shown in the following section. Comparing Fig. 5.2 (a) and (b), we see that at higher

temperatures the meanfield potential arising from the classical region atoms is weaker and the incoherent region atoms are more strongly thermally activated. As such we have higher occupation of phase space in the small x and p_x region. We note that the maximum value of $W_{\mathbf{I}}^{\mathrm{pos}}$ is set by the lower energy bound, not the upper bound on our integration, as we take this high enough that there are no states at that energy.

The second step is now to take the Fourier transform of $W_{\mathbf{I}}^{\mathrm{pos}}$, i.e. calculate

$$G_{\mathbf{I}}^{1}(x,x') = \int_{\Omega_{\mathbf{I}}} dp_x e^{-ip_x(x-x')/\hbar} W_{\mathbf{I}}^{\mathrm{pos}}(\frac{x+x'}{2}, p_x) \tag{5.26}$$

In practice this Fourier transform can be implemented as a discrete Fourier transform, however the discrete spatial and momentum grids (which are reciprocally related) must be chosen carefully to accurately represent the system properties. The details of these choices, and the efficient numerical algorithm for carrying out the transformation of Eq. (5.26) forms an important contribution of our research and are discussed in detail in Appendix A.

The momentum space correlation function, $G_{\mathbf{I}}^{1}(p_x, p_x')$ is found in an analogous way. We first calculate

$$W_{\mathbf{I}}^{\mathrm{mtm}}(x\hat{\mathbf{x}}, p_x\hat{\mathbf{p}}_x) = \int_{\Omega_{\mathbf{I}}} dydz W_{\mathbf{I}}(\mathbf{x}, p_x\hat{\mathbf{p}}_x) \tag{5.27}$$

This is computationally more taxing, since the position space energy values are dependent on not just the trap potential but the meanfield effects of the atoms in the system. This total potential is not isotropic and so this potential in coordinates (y,z) must be integrated for each position in (x,p_x) space.

Figure 5.3 shows the appropriate incoherent region Wigner distribution, $W_{\mathbf{I}}^{\mathrm{mtm}}$ for calculating the momentum space correlation functions. With increasing temperature, we again see an increase in the Wigner function. There is a sharp feature at $p_x = 2$ in both graphs, this corresponds to integration over the y,z components at an energy where there is a potential minimum between the meanfield effect of the coherent region atoms, and the trap potential. The Fourier transform of $W_{\mathbf{I}}^{\mathrm{mtm}}$

$$G_{\mathbf{I}}^{1}(p_x, p_x') = \int_{\Omega_{\mathbf{I}}} dx e^{-ix(p_x-p_x')/\hbar} W_{\mathbf{I}}^{\mathrm{mtm}}(x, \frac{p_x+p_x'}{2}), \tag{5.28}$$

yields the correlation function. A numerical method similar to that for the position case can be used to efficiently implement this transformation (see Appendix A).

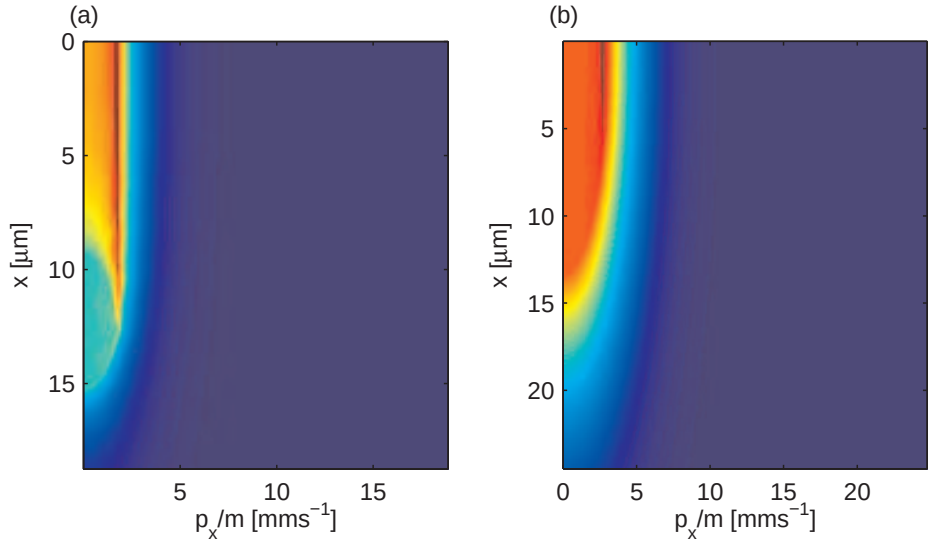

Figure 5.3: Wigner function $W_{\mathbf{I}}^{\mathrm{mtm}}(x, p_x)$ (arb. units) for a cloud of 3×10^5 ^{87}Rb atoms in a trap with frequencies $\{\omega_x, \omega_y, \omega_z\} = 2\pi\,\{1, 1, \sqrt{8}\} \times 40\,s^{-1}$ at 93 nK (a) and 159 nK (b).

5.3 Results

In this section we present results of the application of our formalism to an ultra-cold Bose cloud. The system we consider consists of approximately 3×10^5 ^{87}Rb atoms confined in an anisotropic harmonic trap of frequencies $\{\omega_x, \omega_y, \omega_z\} = 2\pi\,\{1, 1, \sqrt{8}\} \times 40\,s^{-1}$. We explore a temperature range of approximately $0.6T_c$ – $1.0T_c$ to investigate the interplay of the thermal and condensate clouds, and to see how this affects the correlation functions. The analytic estimate of the critical temperature including finite size and mean-field shifts [134] gives $T_c \approx 162$ nK for this system, however our results suggest the actual T_c may be slightly lower, with the system attaining $\sim 1\%$ condensate fraction at about 159 nK. In Fig. 5.4 we present the macroscopic parameters of the states we will analyse in this section. A complete list of the parameters and properties of our equilibrium states is given in Table 5.1.

5.3.1 Position Space Correlations

Figure 5.5 shows the one body density matrix ($G^1(x, x')$) at a temperature of 93 nK calculated for the coherent region (a) and incoherent region (b). In the one body density matrix for the coherent region, (a), two distinct features are clearly apparent. (i) A narrow ridge runs down the diagonal. The peak values of this ridge gives the density of the system (recall $n(x) = G^1(x, x')$). We interpret the width of the ridge as the length scale over which phase coherence decays for the thermal component of the coherent

$\epsilon_{\rm cut}$ $[\hbar\omega_x]$	$N_{\mathbf{C}} \times 10^4$	$E_{\mathbf{C}}$ $[\hbar\omega_x]$	$N_{\rm cond} \times 10^4$	$N \times 10^5$	T [nK]	T/T_c	$n_{\rm min}$
40	7.56	18.1	5.22	3.16	136	0.78	2.64
40	3.64	19	1.59	3.01	149	0.87	2.6
41	6.26	18.3	3.95	3.10	141	0.82	2.41
36	1.83	20.5	0.35	3.10	159	0.92	2.77
38	2.27	20.5	0.57	3.02	155	0.91	2.63
33	7.52	16.4	6.00	2.97	129	0.76	3.24
45	18.3	22	15.4	3.22	99	0.57	1.81
44	18.3	21.8	15.3	3.05	93	0.54	1.79

Table 5.1: A summary of the equilibrium state parameters used for the results reported in Fig. 5.4. The first three columns give the parameters used to generate the initial states and the remaining columns give the macroscopic parameters determined for these states.

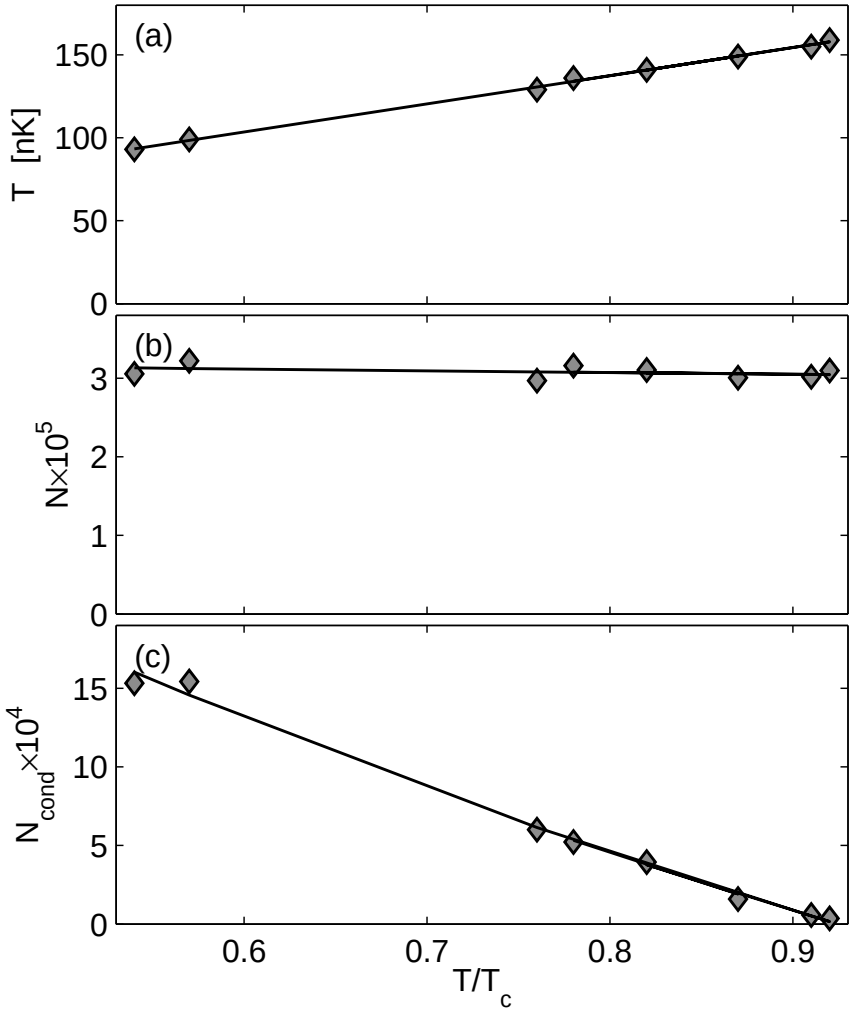

Figure 5.4: Equilibrium state properties. (a) Temperature, (b) total atom number, and (c) condensate number as a function of T/T_c. PGPE results (diamonds) and lines are guides to the eye.

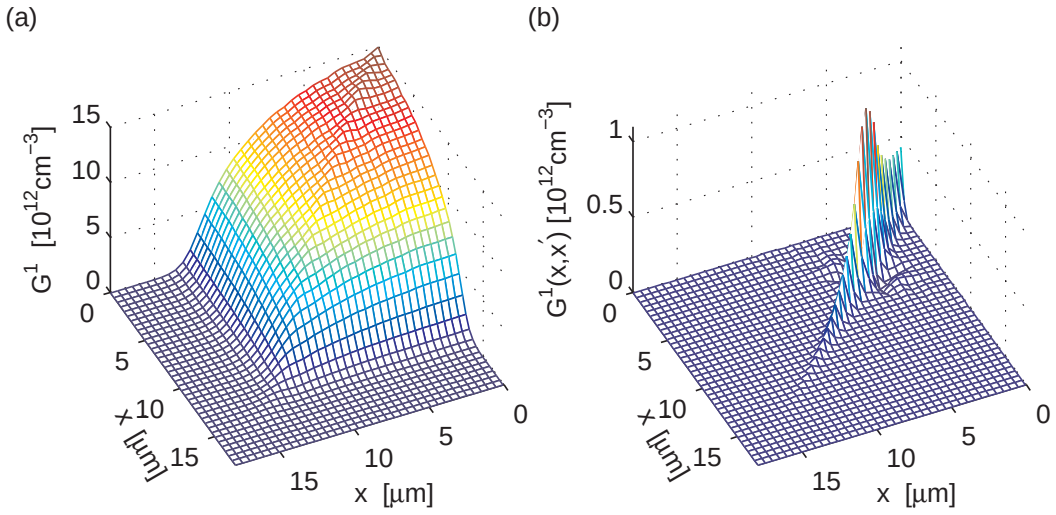

Figure 5.5: The one body density matrix $G^1(x, x')$ for the coherent (a) and incoherent (b) regions, for a cloud of 3×10^5 ^{87}Rb atoms in a trap described in the text $T = 93$ nK

region (note that the coherent region is made up of not just the condensate mode but all low energy highly occupied modes of the system). (ii) The broad background feature represents the off-diagonal long range order in the system. According to Penrose and Onsager [121], this off-diagonal long range order is a signature of the presence of a condensate in a system, with the condensate number corresponding to the largest eigenvalue of the one body density matrix, as detailed in Sec. 2.3.4. Using the PGPE formalism, we can directly calculate and study this quantity, and so have an advantage over symmetry breaking methods [135].

The one body density matrix for the incoherent region (b), by contrast, shows only a ridge down the diagonal. This shows that in the incoherent region the only phase coherence present is over short distance scales consistent with near neighbour interactions. The peak height of $G^1_{\mathbf{I}}(x, x')$ is a factor of 10 smaller than $G^1_{\mathbf{C}}(x, x')$. This shows that at this temperature, the majority of atoms are contained within the coherent region. Another feature of this graph is the dip in the ridge height near the center of the trap. We see here that the thermal atoms of the incoherent region are repelled by the large potential caused by the meanfield of the condensate. This can be seen clearly in Fig. 5.6, where we show the densities $G^1_{\rm cond}(x, x)$, $G^1_{\mathbf{C}}(x, x)$, and $G^1_{\mathbf{I}}(x, x)$. In this figure, the top line gives $G^1_{\mathbf{C}}(x, x)$, the middle line $G^1_{\rm cond}(x, x)$, and the lowest $G^1_{\mathbf{I}}(x, x)$. From $G^1_{\mathbf{C}}(x, x) - G^1_{\rm cond}(x, x)$ we see, in fact, that there is a large amount of thermal cloud at the center of the trap, accounted for in the PGPE formalism. We interpret the repulsion of $G^1_{\mathbf{I}}(x, x)$ from the center to be largely due to the meanfield treatment of this region.

Figure 5.7 shows the one body density matrix ($G^1(x, x')$) and the normalised first and second order correlation functions for temperatures 93 nK [(a)-(c)] and 159 nK [(d)-(f)].

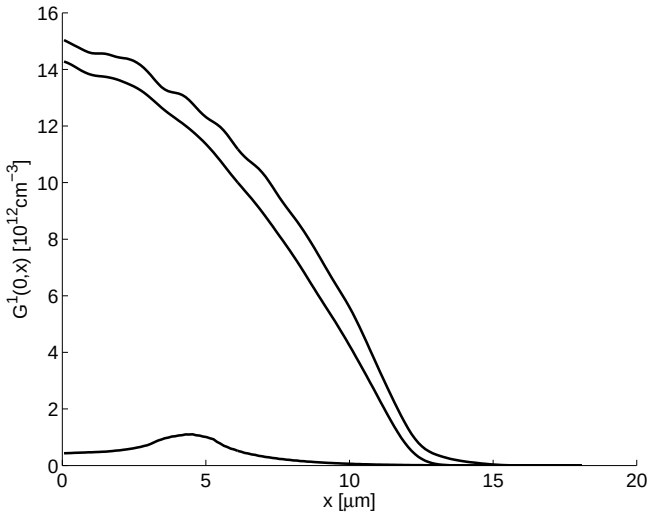

Figure 5.6: Density for a cloud of 3×10^5 ^{87}Rb atoms in a trap described in the text t 93 nK, showing (top to bottom) $G^1_{\mathbf{C}}(x,x)$, $G^1_{\mathrm{cond}}(x,x)$, and $G^1_{\mathbf{I}}(x,x)$ contributions.

In the one body density matrix for the full system we see the two separate features, the off-diagonal long range order and the thermal ridge, that were described separately above. For the lower temperature result [Fig. 5.7 (a)] the long range order dominates due to the large condensate fraction. In contrast, in the higher temperature case [Fig. 5.7 (d)] the thermal component is much more significant compared to the condensate, which is smaller in peak density and spatial extent. This result is close to the critical point and the thermal component has a substantial density even at the trap center.

We note that while the background feature arises entirely from the coherent region, the ridge has contributions from both coherent and incoherent regions.

In the normalised first order correlations [Fig. 5.7 (b) and (e)], the background and ridge features are still apparent. However, normalisation emphasises the thermal component's contribution at large distances from the trap center. The ridge peak value is now unity, as is clear from Eq. (5.4).

The broadened feature seen in the ridge at large x ($x \approx x' \approx 15\mu m$) is an artefact that arises from the limitations of our semiclassical description for the incoherent region. The position where this occurs corresponds to the classical turning point for the energy cutoff used to define the coherent region [2]. Beyond this point all the modes of the coherent region are evanescent, and in examination of $G^1_{\mathbf{C}}(x,x')$ this manifests as an apparent long range order. The local nature of the semiclassical approximation means that $G^1_{\mathbf{I}}(x,x')$ does not cancel this feature, as we would expect in a more complete (wave) treatment of the incoherent region. With reference to Fig. 5.7(a) and (d) we note that

[2]The classical turning point for the harmonic trapping is defined as $V_0(\mathbf{r}) = \epsilon_{\mathrm{cut}}$.

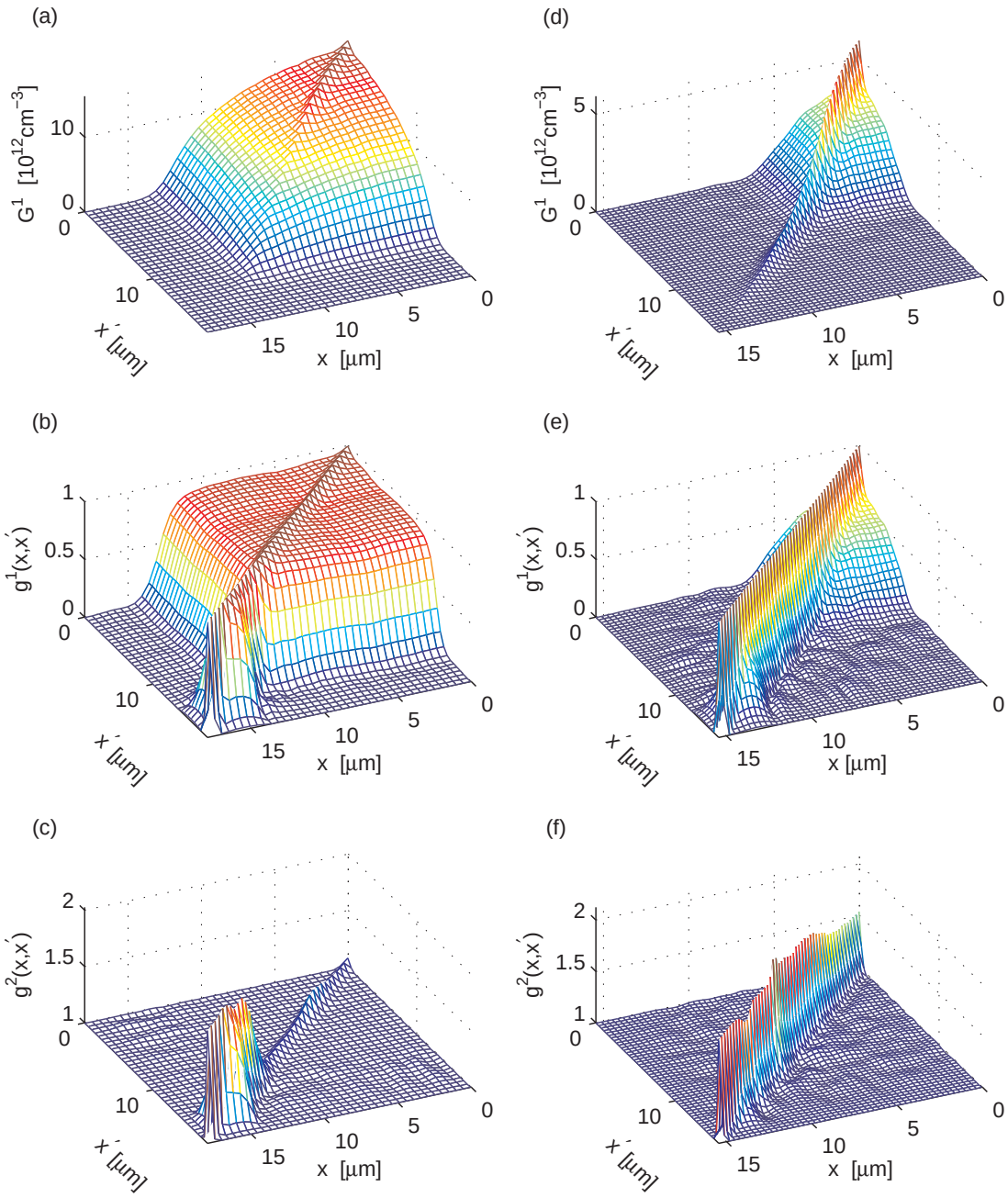

Figure 5.7: Position space correlation functions of a harmonically trapped Bose gas. (a)-(c) at $93nK$ and (d)-(f) $159nK$. Other parameters: (a)-(c) $N_{\rm cond} = 153{\times}10^3$ (condensate number), $N_{\mathbf{C}} = 1.8 \times 10^5$, $N_{\mathbf{I}} = 1.2 \times 10^5$, $\epsilon_{\rm cut} = 44\hbar\omega_z$, $E_{\mathbf{C}} = N_{\mathbf{C}} \times 21.8\hbar\omega_z$; (d)-(f) $N_{\rm cond} = 3540$, $N_{\mathbf{C}} = 1.8 \times 10^4$, $N_{\mathbf{I}} = 2.9 \times 10^5$, $\epsilon_{\rm cut} = 36\hbar\omega_z$, $E_{\mathbf{C}} = N_{\mathbf{C}} \times 20.5\hbar\omega_z$.

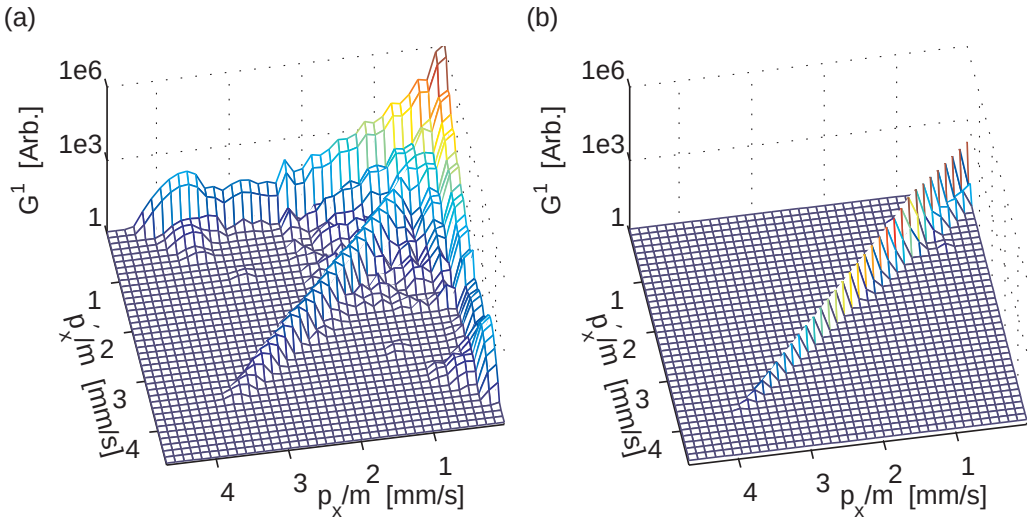

Figure 5.8: The one body density matrix $G^1(p_x, p'_x)$ for the coherent (a) and incoherent (b) regions, for a cloud of 3×10^5 ^{87}Rb atoms in a trap described in the text $T = 93$ nK.

this artefact occurs in a low density region and should have a minor effect when results are averaged over the whole system.

We now consider the second order correlations shown in Fig. 5.7 (c) and (f), which show a ridge, but no background feature. The height of the ridge varies from a value of slightly above one up to two. Comparing the second order results with the respective first order results, we see that in locations where the density is dominated by the condensate, the value of g^2 is suppressed from the maximum value of two.

These observations are consistent with the well known behaviour of g^2 for photons. For the case of an ideal laser $g^2(x, x') = 1$, whereas for a thermal light source photon bunching occurs with $g^2(x, x) = 2$.

We note that the artefact seen in Fig. 5.7 (b) and (e), and discussed above, is also seen in these results.

5.3.2 Results of Correlation Functions in Momentum Space

Figure 5.8 shows the one body density matrix ($G^1_{\mathbf{C}}(p_x, p'_x)$) at 93 nK for the coherent (a) and incoherent (b) regions of our system. The dominant feature in $G^1_{\mathbf{C}}(p_x, p'_x)$ is a sharp spike in momentum which is a signature of condensation. Indeed, we enhance the appearance of the thermal component in Fig 5.8 (a) by using a logarithmic scale in which the density varies by six orders of magnitude. In contrast, the position case Fig 5.5 (a) has a clearly discernible thermal component on a linear scale. The cross-like

structure extending along the p_x and p'_x axes in Fig 5.8 (a) is due to the enhancement that the large condensate momentum space peak provides (this feature is negligible after normalisation, see Fig 5.9 (b) below).

The one body density matrix for the incoherent region (Fig 5.8 (b)) has just the ridge down the diagonal, where the width of the ridge shows the range over which one would expect to see phase coherence, analogous to the position space results. We see here as well the effect of the condensate excluding the thermal cloud from the zero momentum states.

Figure 5.9 shows the one body density matrix ($G^1(p_x, p'_x)$) and the normalised first and second order correlation functions in momentum space for temperatures 93 nK [(a)-(c)] and 159 nK [(d)-(f)].

We see that Fig 5.9 (a) is almost identical to Fig 5.8 (a), even though the latter shows the one body density matrix for the full system. This can be understood by observing that the peak density of the incoherent region is four orders of magnitude smaller than that for the incoherent region, and so it makes only very little contribution to the final result.

Comparing the low and high temperature results in Figures 5.9(a) and (d) respectively, we observe the peak density of the condensate spike to vary by approximately two orders of magnitude, whereas for the same temperature change the position space density is observed to only change by a factor of around two. This observation emphasises that condensation is in some sense a momentum space phenomenon, but also marks a rather important difference between the position and momentum space correlation functions.

The normalised versions of the correlation functions more clearly reveals the non-condensed modes in the system. Due to the massive contrast between condensate and non-condensate modes in momentum space, experimental measurement of these correlations will likely prove challenging. Indeed, in Ref. [44] results were restricted to above T_c due to saturation issues with the detector when a condensate was present.

5.3.3 Coherence length

In this section we wish to study the long range order present in our system at varying temperatures. We first explore this by analysing our results for the one body density matrix for a greater number of temperatures. In later sections we calculate the coherence length, first with the PGPE formalism, and then using a self-consistent meanfield approach.

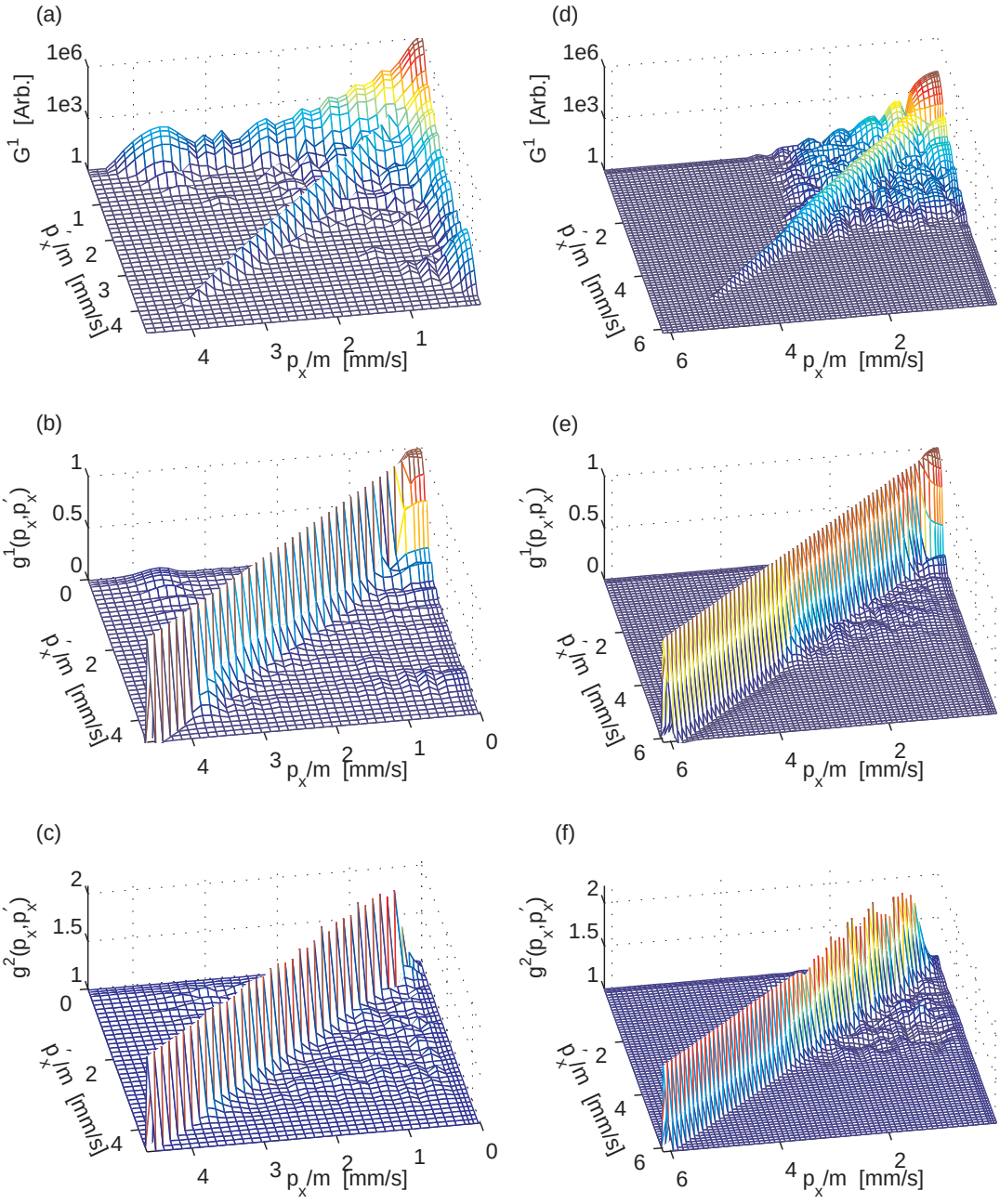

Figure 5.9: Momentum space correlation functions of a harmonically trapped Bose gas. (a)-(c) at $93nK$ and (d)-(f) $159nK$. Other parameters: (a)-(c) $N_{\rm cond} = 153 \times 10^3$, $N_{\mathbf{C}} = 1.8 \times 10^5$, $N_{\mathbf{I}} = 1.2 \times 10^5$, $\epsilon_{\rm cut} = 44\hbar\omega_z$, $E_{\mathbf{C}} = N_{\mathbf{C}} \times 21.8\hbar\omega_z$; (d)-(f) $N_{\rm cond} = 3540$, $N_{\mathbf{C}} = 1.8 \times 10^4$, $N_{\mathbf{I}} = 2.9 \times 10^5$, $\epsilon_{\rm cut} = 36\hbar\omega_z$, $E_{\mathbf{C}} = N_{\mathbf{C}} \times 20.5\hbar\omega_z$.

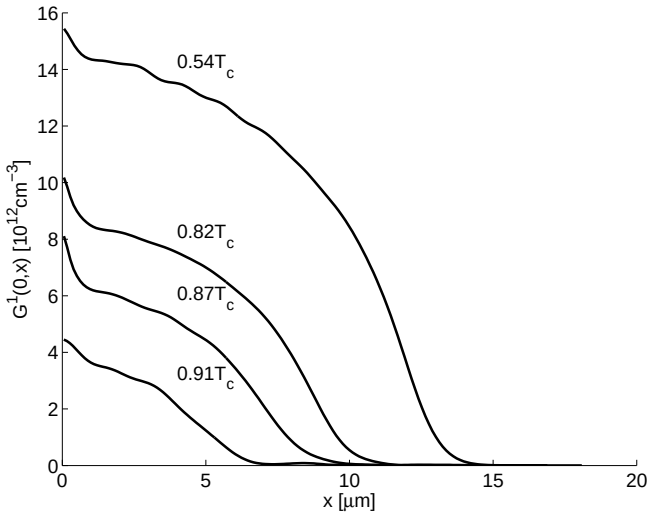

Figure 5.10: One body density matrix cross-section $G^1(0, x)$ for systems with various temperatures. Systems have 3×10^5 ^{87}Rb atoms in a trap described in the text.

Emergence of Long Range Order

In Figure 5.10 we plot $G^1(0, x)$ for a range of temperatures $\{0.54, 0.82, 0.87, 0.91\}T_c$, where T_c is the critical temperature calculated with finite size and mean-field shifts. The highest temperature data set we have, at $0.97T_c$, is not plotted here because it is not clearly visible on the same scale.

We start by discussing the three lowest temperature results, $\{0.54, 0.82, 0.87\}T_c$. In these lines, there are two features present. (i) A small spike which starts at $x = 0\mu m$. The width of this spike is $\sim \lambda_{dB}$, corresponding to the length scale over which phase coherence occurs for the thermal component of the system. As the temperature increases, this spike accounts for a larger proportion of the curve, corresponding to an increased thermal component of the system. (ii) A broad curve decaying down to the x axis. This curve shows the off-diagonal long range order present in the system. This feature reduces in width and relative contribution as temperature is increased, and the condensate responsible for it diminishes. We note also that the decay in this long range order is quite sharp at low temperature, and much more gradual at high temperature, showing increasing coherence in the system.

The curve at highest temperature here, $0.91T_c$, doesn't show the two aforementioned features, showing a distinctly flattened or more linear looking curve. This change in behaviour signals the beginning of the Bose-Einstein condensate phase transition regime, further changes of the correlation function across this parameter regime will be the subject of the next chapter.

Coherence Length

The coherence length is a measure of first order correlations that specifies the typical length scale over which reproducible interference fringes might be expected. Recent experiments [50] have made detailed measurements of the coherence between atoms at different spatial locations within a trapped Bose gas using RF-fields to output couple the atoms. This approach has the advantage that it avoids volume averaging which tends to smear features of the correlation functions (e.g. see [52]). This motivates us to consider an *on-axis* coherence length defined as

$$L_x^2 = \frac{\int dx\, dx'\, |G^1(x,x')|^2 (x-x')^2}{2\int dx\, dx'\, |G^1(x,x')|^2} \tag{5.29}$$

which will be used to compare results at different temperatures. This expression is similar in form to the coherence length defined by Barnett *et al.* [56] (also see Ref. [136]), but without volume averaging over the whole system, and should be more appropriate for the aforementioned experiments. For reference, the uniform Boltzmann gas with $G^1(x,x') \sim \exp\left(-\pi|x-x'|^2/\lambda_{dB}^2\right)$, gives $L_x = \lambda_{dB}/\sqrt{8\pi}$ where $\lambda_{dB} = h/\sqrt{2\pi mkT}$ is the thermal de Broglie wavelength. We calculate the coherence length using two different methods, as detailed below.

PGPE

The coherence length is calculated using the one body density matrix for the total system, as previously calculated. We note that the expression for the coherence length is dominated by the condensate mode. In Figure 5.11 we compare $G^1(0,x)$ and $G^1_{\rm cond}(0,x)$ to show this effect, where

$$G^1_{\rm cond}(0,x) = \psi^*_{\rm cond}(0)\psi_{\rm cond}(x), \tag{5.30}$$

and the condensate wavefunction $\psi_{\rm cond}$ is found as specified in the method of Sec. 2.3.4.

The functions $G^1(x,x')$ and $G^1_{\rm cond}(x,x')$ give nearly identical results when used to calculate the coherence length, and so we present just the full system results in the results section below.

Meanfield approach

As a comparison we also calculate the coherence length using a self consistent meanfield approach. This approach describes the condensate (for $T < T_c$) using the Thomas-Fermi

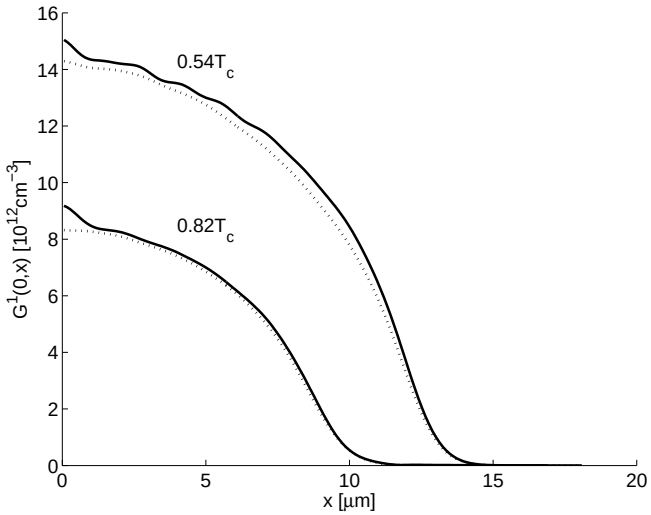

Figure 5.11: One body density matrix cross-section calculated using the coherent region (solid line) and just condensate mode (dotted), for systems as described in the text.

approximation and the non-condensate using Hartree-Fock Bogoliubov Popov (HFBP) theory in the semiclassical limit (e.g. see Ref. [134]).

We use the Thomas-Fermi approximation as detailed in Sec. 2.3.6, and choose μ_{TF} so that the Thomas-Fermi density is normalised to the condensate number, $N_{\rm cond}$. We construct the Wigner function for the distribution, as given in Eq. (2.52), using energy as in Eq. (2.53). The thermal density is now calculated as Eq. (2.54), but our integral is restricted differently, we integrate over all states except the ground state (i.e. $\epsilon_{\rm cut} \to 0$). We find our Wigner function self consistently - i.e. we iterate with the thermal density until we have reached an equilibrium state. We then use this Wigner function to find the first order correlation function for the thermal component as detailed in Section 5.2.4.

The first order coherence function is then constructed as $G^1_{\rm HFBP}(x,x') = G^1_{\rm cond}(x,x') + G^1_{\rm th}(x,x')$.

Results

Figure 5.12 shows the behaviour of the on-axis coherence length for the same system considered in the previous section. Our results using the PGPE formalism show the coherence length decreases steadily as the critical temperature is approached from below.

The results of Figure 5.12 indicate that the value of L_x calculated using meanfield theory is always greater than the value obtained from the PGPE simulations for the temperatures considered. This primarily occurs because the equilibrium condensate

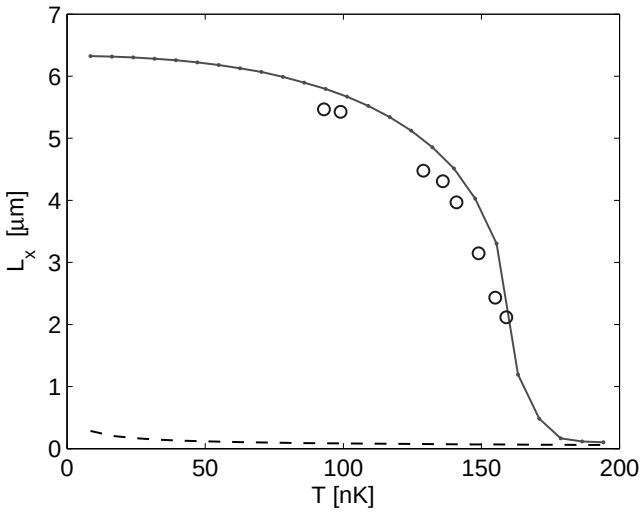

Figure 5.12: Coherence length L_x calculated using classical field approach (circles), and semiclassical HFBP theory (line with dots). For reference $\lambda_{dB}/\sqrt{8\pi}$ is shown as the dashed line. System parameters as in Fig. 5.7

fraction in the meanfield results is greater than the PGPE case at the same temperature[3]. Nevertheless, while there is reasonable agreement between these theories for $T < T_c$, as $T \to T_c$ their behaviour appears to be rather different, with the classical field prediction for L_x decreasing much less rapidly on the approach to the critical point. We note that for the highest temperature classical field result (i.e. $T = 159$ nK) the condensate fraction is $\sim 1\%$ and the many other low-lying modes will necessarily play an important role in the coherence properties of the system in this regime. A complete investigation of this behaviour is probably best done via the correlation length, ξ, defined such that $G^1(x, 0) \propto x^{-1} \exp(-x/\xi)$, valid for $x \gtrsim \lambda_{dB}$, and we detail investigations of this nature in the following chapter.

[3]Discrepancies between the HFBP and PGPE calculations for the system equilibrium properties, in particular condensate fraction, may be due to limitations of the semiclassical approximation in addition to beyond meanfield effects.

Chapter 6

Critical Region of the Trapped Bose Gas

In this chapter we extend the formalism of the previous chapter to study the onset of coherence in the Bose system around the transition region. We give details of how we will extend our formalism to the critical region in Sec. 6.1, and give the results of our investigations in Sec. 6.2.

6.1 Critical Region Methods

We wish to study the onset of critical behaviour of a BEC. Studies in this regime pose new problems. Because of the strong fluctuations expected, we will be required to take our time averages over increased time periods, so that a true representation of the system can be found. In the following section, we typically use ~ 7000 samples over the 140 trap periods of our simulation to perform averages to find the macroscopic parameters of the system, and to calculate the appropriate correlation functions.

Our investigations will be centered around the analysis of the first order correlation function, as given in Eq. (5.2). However, we note that for our purposes in this region it is appropriate to use just the first order correlation function for the classical region, as this will contain all of the critical fluctuations we wish to study, and to disregard any contribution from the incoherent region. This is because we take $\epsilon_{\rm cut} > U_0 n$, and so $G^1_{\mathbf{I}}(\mathbf{r},\mathbf{r}')$ contains only normal system correlations that decay on the length scale of the thermal de Broglie wavelength, $\lambda_{\rm dB} = h/\sqrt{2\pi m k_B T}$, so that the contribution of $G^1_{\mathbf{I}}(\mathbf{r},\mathbf{r}')$ is negligible for $|\mathbf{r}-\mathbf{r}'| \gtrsim \lambda_{\rm dB}$.

For the remainder of this section, we will use the notation $\langle N_{\rm cond}\rangle$ for the mean conden-

sate number we find as in Eq. (2.30), i.e.

$$\int d\mathbf{r}'\, G^1_{\mathbf{C}}(\mathbf{r},\mathbf{r}')\psi_{\rm cond}(\mathbf{r}') = \langle N_{\rm cond}\rangle \psi_{\rm cond}(\mathbf{r}). \tag{6.1}$$

This will distinguish it from the equilibrium distribution of $N_{\rm cond}$ we consider in Sec. 6.2.3.

6.2 Results

6.2.1 Sampling Equilibrium States across the Transition Region

We now discuss our procedure for generating equilibrium states spanning the condensation transition. We fix the variables $N_{\mathbf{C}}$ and $\epsilon_{\rm cut}$ to define our system and the generate equilibrium states with various energy values ($E_{\mathbf{C}}$) finely spaced over a range where the thermalised condensate fraction is of order 1%. Varying $E_{\mathbf{C}}$ in this way causes T to vary (as is desired), but also causes the total number of atoms to vary (see Fig. 6.1).

For each simulation we calculate the temperature and total atom number using the methods described in the previous section. The results for these quantities for the case of a ^{87}Rb system with $\omega_{x,y} = 2\pi\times 129$Hz, $\omega_z = 2\pi\times 364$Hz, $\epsilon_{\rm cut} = 32\hbar\omega_x$ and $N_{\mathbf{C}} = 7573$ are shown in Figs. 6.1(a) and (b). We have chosen to use these parameters rather than those of the ETH experiment [50] which was carried out in a weaker trap. This is because we need to take more care in choosing the classical region $\mathbf{C}$ when we study the phase transition. Typically strong fluctuations occur in the infra-red modes up to the energy scale $U_0 n$ where n is the density. Above this energy scale the modes are well-described by mean-field theory (e.g. see the discussion in [137, 138]). We choose our trap so that

$$\epsilon_{\rm cut} \sim k_B T > U_0 n. \tag{6.2}$$

For each energy we perform 20 simulations (using different random initial states) and the spread in results seen in Figs. 6.1(a) and (b) for each energy is indicative of the typical uncertainties in the thermal parameters. These results also show that as we change $E_{\mathbf{C}}$ the total number of atoms in the system changes quite appreciably. It is therefore convenient to work in terms of the reduced temperature, $T' = T/T_{c1}$, where

$$T_{c1} \;=\; T_{c0} - \left(0.73\frac{\bar{\omega}}{\omega}N^{-\frac{1}{3}} + 1.33\frac{a}{a_{\rm ho}}N^{\frac{1}{6}}\right)T_{c0}, \tag{6.3}$$

with

$$k_B T_{c0} = 0.94 \hbar \omega N^{1/3}, \tag{6.4}$$

$\omega = (\omega_x \omega_y \omega_z)^{1/3}$, $\bar{\omega} = (\omega_x + \omega_y + \omega_z)/3$, and $a_{\rm ho} = \sqrt{\hbar/m\omega}$, see [134]. The two terms in brackets in Eq. (6.3) correspond to the finite-size ($\propto N^{-1/3}$) and meanfield interaction ($\propto N^{1/6}$) shifts of the critical temperature, respectively.

In Fig. 6.1(c) we show the condensate fraction from these simulations as a function of T'. We note that $T' = 1$ does not identify the transition precisely enough for understanding critical properties, as the above expression for T_{c1} excludes meanfield effects beyond first order and does not account for any critical fluctuation effects.

6.2.2 Spatial Correlations and the Correlation Length

In this section we consider the behaviour of spatial correlations and the correlation length across the transition region. The spatial inhomogeneity of the trapped system requires explicit consideration. Unlike the homogeneous system, where spatial fluctuations are only a function of the separation between coordinates, in the trapped case both coordinates are separately important. So to study the development of order in the trapped system, we choose to examine correlations symmetrically about the trap center to minimise inhomogeneous effects [1]. We do this by defining the normalised correlation function

$$g_{\mathbf{C}}(\Delta x) \equiv \frac{G^1_{\mathbf{C}}\left(\frac{1}{2}\Delta x\,\hat{\mathbf{x}}, -\frac{1}{2}\Delta x\,\hat{\mathbf{x}}\right)}{n_{\mathbf{C}}(\mathbf{0})}, \tag{6.5}$$

where $\hat{\mathbf{x}}$ is the unit vector in the x direction, and $n_{\mathbf{C}}(\mathbf{0})$ is the $\mathbf{C}$ region density at trap center. As discussed in Sec. 6.1, the spatial correlations over distances exceeding $\lambda_{\rm dB}$ are described completely by the $\mathbf{C}$ region one-body density matrix.

We evaluate $G^1_{\mathbf{C}}(\mathbf{r}, \mathbf{r}')$ by time-averaging (see Eq. (5.18)), but due to our system's symmetry in the xy-plane, we can improve the quality of our results for $g_{\mathbf{C}}(\Delta x)$ by making use of radial averaging. Examples of $g_{\mathbf{C}}(\Delta x)$ are shown in Fig. 6.2. In the region of the phase transition the first order correlation function is expected to take the form

$$g_{\mathbf{C}}(\Delta x) \propto \frac{1}{\Delta x} e^{-\Delta x/\xi} \tag{6.6}$$

for $\Delta x > \lambda_{\rm dB}$, where ξ is the correlation length of the system. The variation in the correlation length as the temperature approaches the critical value is given by

$$\xi \propto |T' - T'_c|^{-\nu}, \tag{6.7}$$

[1] In the experiments of Donner *et al.* correlations were also measured at points symmetrically placed about the trap center.

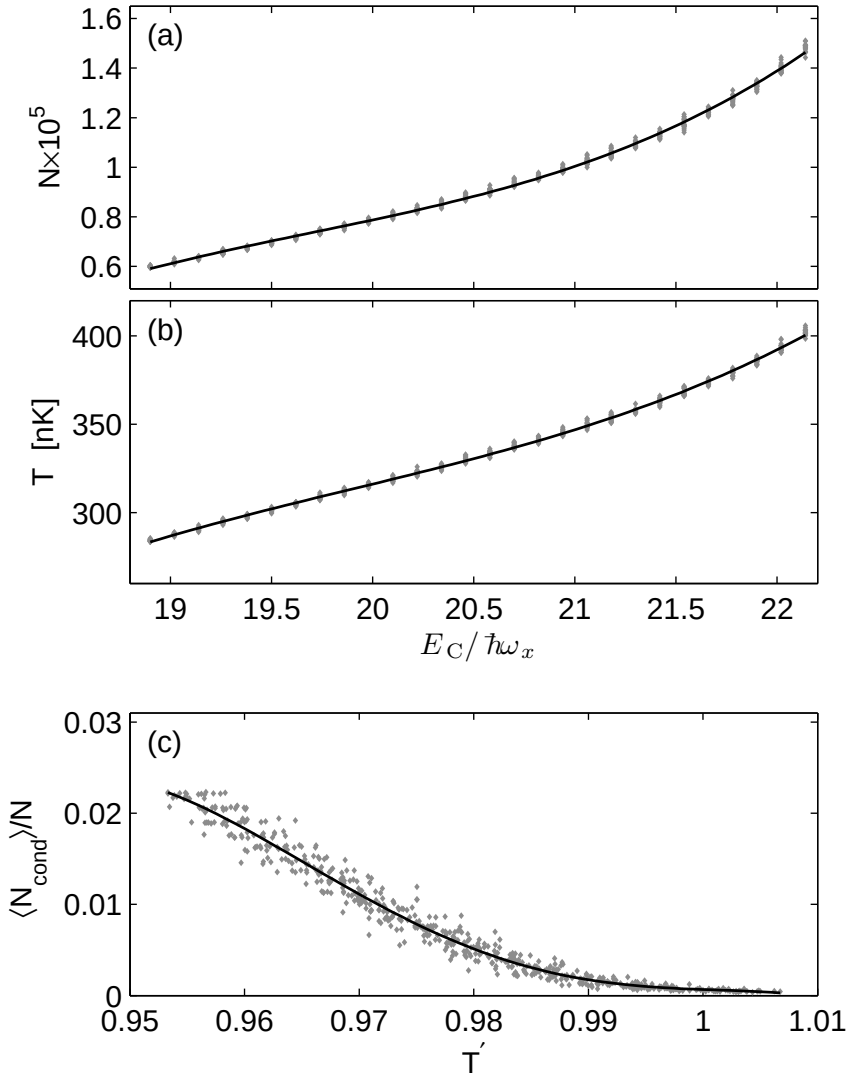

Figure 6.1: Macroscopic parameters for a critical trapped Bose gas. (a) Total number of atoms and (b) temperature as the PGPE energy $E_{\mathbf{C}}$ is changed. (c) Condensate fraction as a function of the reduced temperature $T/T_{c1}(N)$. Parameters: ^{87}Rb system with $\omega_{x,y} = 2\pi \times 129$ Hz, $\omega_z = 2\pi \times 364$ Hz, $\epsilon_{\rm cut} = 18.9\hbar\omega_x$ and $N_{\mathbf{C}} = 7573$.

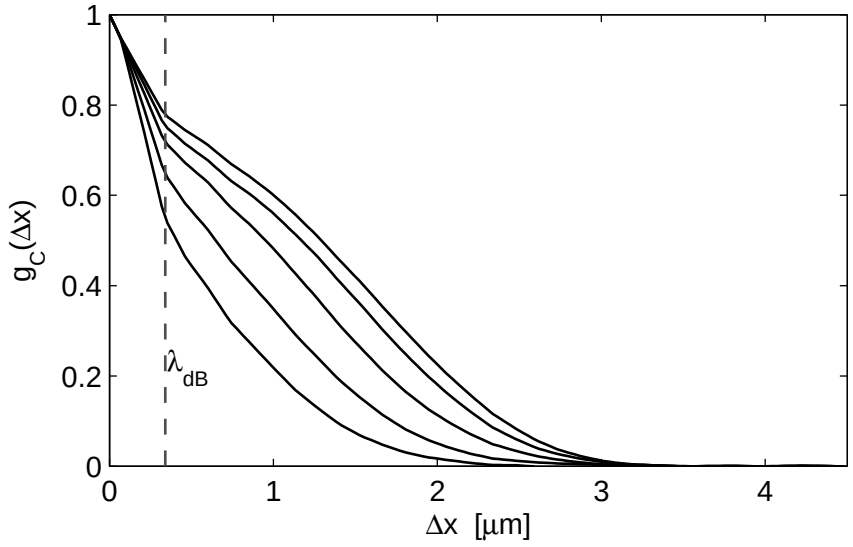

Figure 6.2: First order correlation function $g_{\mathbf{C}}(\Delta x)$ for, from highest to lowest curves, $T' = \{0.957, 0.962, 0.969, 0.981, 0.990\}$. Parameters for calculations as in Fig. 6.1. Thermal de Broglie wavelength distance scale indicated for reference.

for the uniform system, where ν is the relevant critical exponent.

To determine ξ we fit (6.6) to our numerical results for $g_{\mathbf{C}}(\Delta x)$ on the spatial range $0.5\mu\text{m} \leq \Delta x \leq 2.2\mu\text{m}$ (i.e. $1.5\lambda_{\text{dB}} \leq \Delta x \leq 6.4\lambda_{\text{dB}}$). This range matches that used by Donner *et al.* [50], and ensures that we avoid having to deal with normal correlations at small separations, and inhomogeneous/finite-size effects at larger separations (also see Sec. 6.2.2). The values of ξ we obtain are shown in Fig. 6.3, where we see ξ growing rapidly as T' approaches ~ 0.96 from above. At temperatures below this the quality of the fits used to determine ξ is quite poor and there is appreciable scatter in the data points for ξ. This poor fit arises from the development of appreciable condensate in the system (e.g. see the coldest results shown in Fig. 6.2). In the uniform system the condensate is spatially uniform and is easily neglected in correlation functions, however in the trapped system it appears at the transition point in a spatially localised mode with a size of order the oscillator length, which is difficult to distinguish from the non-condensate correlations. We interpret the data for $T' \lesssim 0.963$ as being below the transition point and our ξ values extracted using fits to (6.6) in this regime as being unreliable.

We then fit expression (6.7) to the correlation length results with T'_c, ν, and an overall constant of proportionality as fitting parameters. The fit for our data is shown in Fig. 6.3, with a value of $\nu = 0.8 \pm 0.12$ and $T'_c = 0.963$. We notice that while the fit is reasonable, there appears to be a certain degree of *rounding off* in the divergence of ξ near the critical point. While our data has appreciable scatter (mainly due to uncertainty

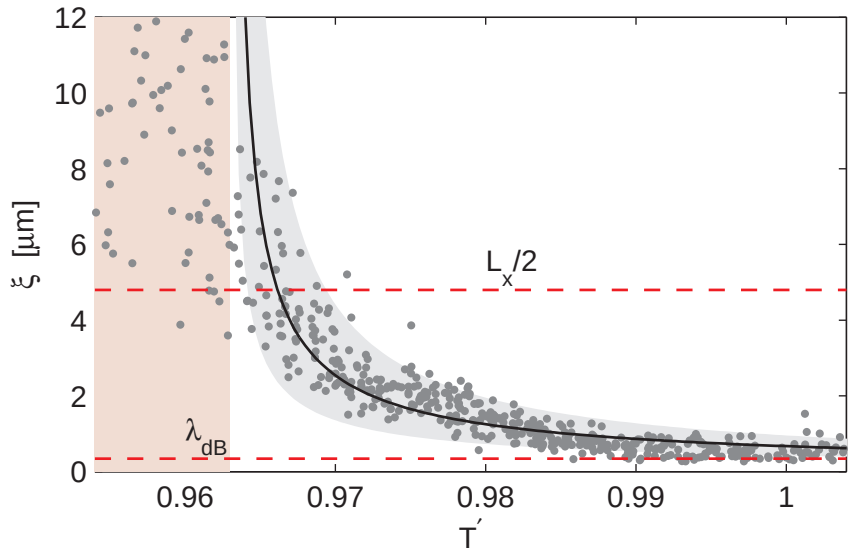

Figure 6.3: The behaviour of the correlation length across the condensation transition. Solid line is a fit using (6.7) with $\nu = 0.8$ and $T_c' = 0.963$. Other parameters as in Fig. 6.1. Shaded region around the solid line indicates fits within the error bar range ($\nu = 0.8 \pm 0.12$). Rectangular shaded region indicates points excluded as being below T_c'. Dashed lines show values of quantities discussed in the text.

in T), we expect that this rounding off is primarily due to finite-size effects. Additionally, our large uncertainty in the critical exponent arises because of the difficulty in locating the precise value of T_c for our system. In principle the divergence of ξ marks T_c, however the rounding off of this divergence and the scatter in our results adds uncertainties to the precise value of T_c that is difficult to quantify without a theory for the finite-size behaviour of ξ.

Our fit value for ν differs from that for the 3D XY model (i.e. $\nu \approx 0.67$) which is expected to be of the same universality class, but is within the error bars of the Donner *et al.* experiment, which reported $\nu = 0.67 \pm 0.13$. The critical temperature identified by our fit (i.e. $T_c' \approx 0.963$) is also shifted downward from the prediction of (6.6). A similar downward shift in T_c was found by Davis *et al.* [94] in their analysis of the trapped Bose gas, arising because meanfield effects are typically underestimated by the analytic expression (6.3).

Finite-size effects

As our above results motivate, an important issue to consider in the trapped system is the role of finite-size effects [85]. At fixed temperature, the Ginzburg criterion for the dominance of critical fluctuations requires that the chemical potential (μ) differs from

the critical value (μ_c) by no more than

$$\delta\mu = |\mu - \mu_c| \leq \frac{16\pi^2 m a^2 k_B^2 T_{c0}^2}{\hbar^2}, \tag{6.8}$$

e.g. see [134]. In the trapped system the effective system chemical potential varies spatially according to $\mu(\mathbf{r}) = \mu - V_0(\mathbf{r})$ and, taking $\mu(\mathbf{r} = \mathbf{0}) = \mu_c$, we can map the Ginzburg condition to a spatial length scale over which the system is critical. This length scale (diameter), along direction $x_j = \{x, y, z\}$, is

$$L_j = 8\sqrt{2}\pi a \frac{k_B T_{c0}}{\hbar\omega_j}, \tag{6.9}$$

which we shall refer to as the Ginzburg length. This sets the maximum correlation length that can occur in the system, thus defining the relevant parameter for assessing finite-size effects, and takes this (its largest) value when the center of the system is at the critical point. For the case of two-point correlations (measured along the x-direction for definiteness) another important length scale in the trapped system is $\Delta x_{\max}$, the maximum point separation (about trap center) used to measure the correlation length (i.e. the fit of $\exp(-\Delta x/\xi)/\Delta x$ is made over the range $\lambda_{\rm dB} < \Delta x < \Delta x_{\max}$).

System	$\lambda_{\rm dB}(T_c)$	$\Delta x_{\max}$	L_x	ν
Expt.	$0.5\,\mu$m	$2.2\,\mu$m	$20\,\mu$m	0.67 ± 0.13
Th. 1	$0.34\,\mu$m	$2.2\,\mu$m	$9\,\mu$m	0.8 ± 0.12
Th. 2	$0.42\,\mu$m	$2.2\,\mu$m	$6\,\mu$m	$0.8 \pm 0.12^{\dagger}$

Table 6.1: A summary of the parameters for critical property measurements. Expt. values refer to those of Donner *et al.* [50]. Th. 1 refer to the values for the main theoretical results presented in this Chapter. Th. 2 refer to the results presented in Sec. 6.2.2, where we investigate a smaller system size. † These numbers are not fit, see text for additional discussion.

The following conditions are required to accurately measure critical properties and minimise finite-size effects

$$\lambda_{\rm dB} \ll \Delta x_{\max} \ll L_j. \tag{6.10}$$

The first inequality ensures that there is a reasonable distance scale over which correlation measurements can be made to accurately determine the correlation length. The second inequality ensures that finite-size effects are minimised. Obviously, finite-size effects cannot be completely avoided, since the correlation length can never diverge in the finite system, and L_j sets the maximum value we might expect for ξ. The values of these various quantities for experiments and our results are shown in Table 6.1.

To examine the influence of finite-size effects, we have performed calculations for a system with the same trap parameters considered for the main results presented in this

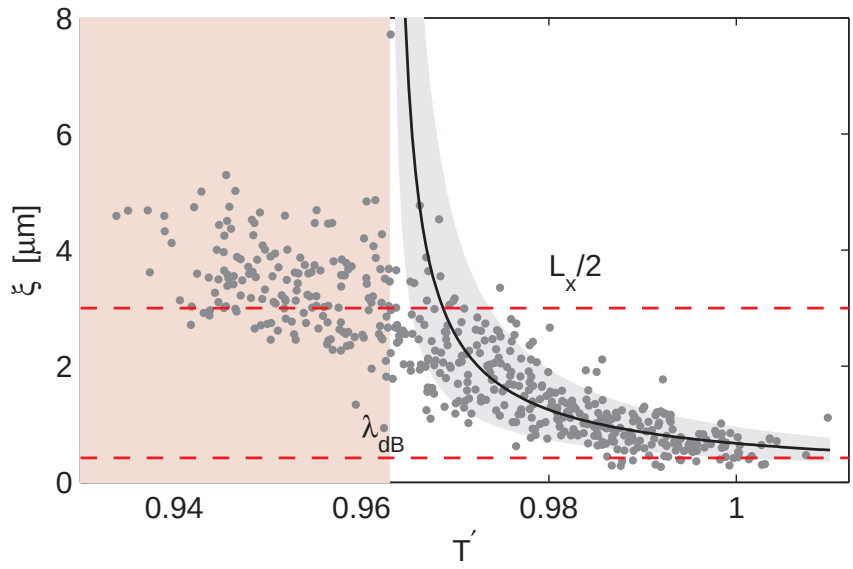

Figure 6.4: The correlation length for a smaller system with $N_{\mathbf{C}} = 3.03 \times 10^3$ and $\epsilon_{\rm cut} = 23\hbar\omega_x$, with other parameters as described in Sec. 6.2.1. Solid line and surrounding shaded region are not fits to the data, but are precisely the same as those used in Fig. 6.3 (see text). Rectangular shaded region indicates points excluded as being below T_c'. Dashed lines show values of quantities discussed in the text.

paper, but with fewer atoms. In this case the critical physics occurs at a temperature of $T_c \approx 200$ nK and a lower $\epsilon_{\rm cut}$ value of $23\hbar\omega_x$ is used. The relevant parameters for this system are summarised as "Th. 2" in Table 6.1, revealing that for this system all three length scales in (6.10) are similar. Our results for the correlation length behaviour of this system are given in Fig. 6.4 and show a rather striking broadening of the critical behaviour, as compared to the previous case displayed in Fig. 6.3. As a result, this data is difficult to fit to the infinite system result (6.7) for the purposes of extracting the critical exponent. Instead of fitting, we simply place the same curves used in Fig. 6.3 (i.e. same ν, T_c', and error bars) on the data and observe that it provides an acceptable characterisation of these results also. For both cases (Figs. 6.3 and 6.4) we see that fits to the normal divergent expression (6.7) are good for $\xi \lesssim L_x/2$, but significantly depart from this fit for larger values of ξ. Since the values of L_x differ by roughly a factor of two between these calculations, this suggests that L_x is indeed the correct length scale for assessing finite-size effects.

6.2.3 Condensate Number Fluctuations and the Generalised Binder Cumulant

An important issue to deal with in the trapped system is the identification of the critical point, as this will be needed for a better understanding of the critical region and

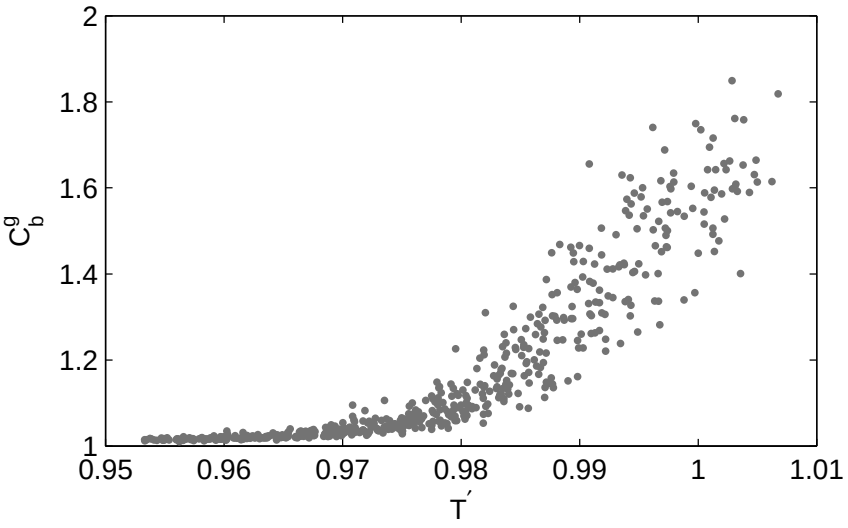

Figure 6.5: Binder cumulant behaviour across the condensation transition. Parameters same as in Fig. 6.1.

the future development of higher precision calculations. For the uniform Bose gas the transition point is conveniently identified using a Binder cumulant, defined as

$$C_b = \frac{\langle N_0^2 \rangle}{\langle N_0 \rangle^2}, \tag{6.11}$$

where N_0 the population of the zero-momentum (condensate) mode. This Binder cumulant characterises condensate number fluctuations, and takes the universal value of $C_b^{\rm crit} = 1.2430$ at the transition (see [98]).

Here we propose a generalisation of the Binder cumulant to the trapped system of the form

$$C_b^g \equiv \frac{\langle N_{\rm cond}^2 \rangle}{\langle N_{\rm cond} \rangle^2}, \tag{6.12}$$

with $N_{\rm cond}$ the condensate mode occupation. Our procedure to analyse the condensate number fluctuations is as follows. The condensate (lowest energy normal mode), $\psi_{\rm cond}(\mathbf{r})$, is determined according to the Penrose-Onsager method described in Sec. 2.3.4 using the time-averaged density matrix. We then use this mode to determine the instantaneous condensate amplitude by evaluating the inner product

$$\alpha_{\rm cond}(t_j) = \int d\mathbf{r}\, \psi_{\rm cond}^*(\mathbf{r}) \psi_{\mathbf{C}}(\mathbf{r}, t_j), \tag{6.13}$$

on every microstate used to sample system properties. We identify $N_{\rm cond} = |\alpha_{\rm cond}(t_j)|^2$ as the condensate number in this microstate, and by sampling over long times, we can obtain histograms of the condensate fluctuations.

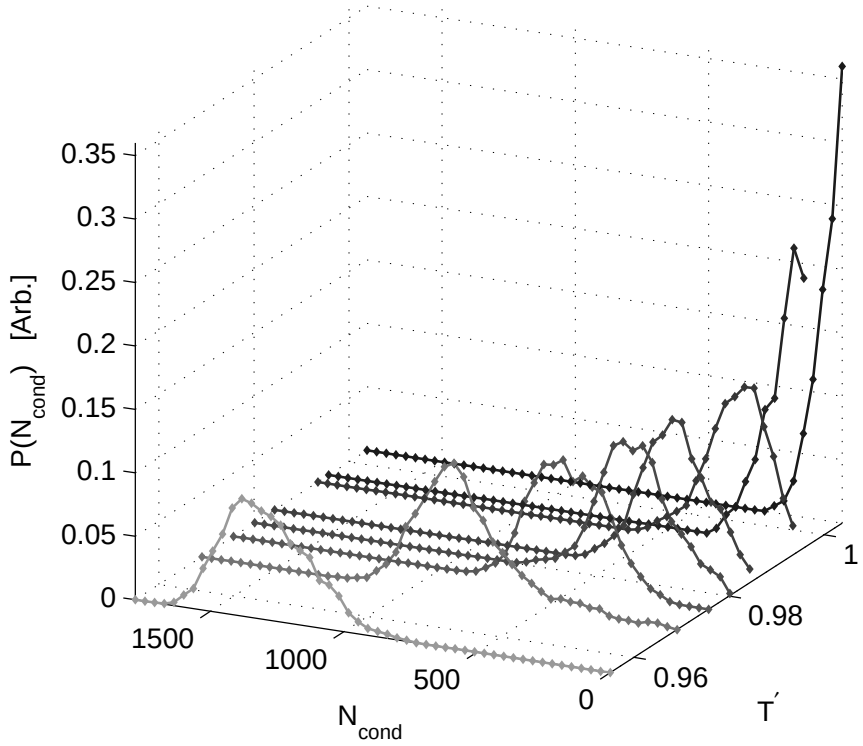

Figure 6.6: Histograms of condensate/ground mode number fluctuations across the critical point.

In Fig. 6.5 we show our results for C_b^g across the critical region. These exhibit a rather dramatic reduction in the number fluctuations from values approaching $C_b^g = 2$ (expected for the normal system) at temperatures slightly above the transition point, to values of $C_b^g \approx 1$ below the transition. At our transition temperature of $T_c' \approx 0.963$ (as determined from fitting the critical exponent) we find a mean value of $C_b^g \approx 1.03$, a value well-below the expected for the uniform system in the thermodynamic limit. This suggests that if the Binder cumulant is a useful quantity for characterising the condensation transition in the trapped case, the critical value of C_b^g is much lower than the uniform system.

Investigations of the number fluctuations of the condensate across the transition are of interest in their own right, and may be suitable to the techniques available in ultra-cold atom experiments. The subject of condensate number fluctuations has been extensively discussed in the dilute gas BEC literature (e.g. see the review of [139] and references therein), particularly the unphysical large fluctuations for the ideal gas predicted within the grand canonical ensemble.

In Fig. 6.6 we show histograms of the the condensate (lowest mode) number distribution across the transition. We see the development of coherence in the system as the shape of the distribution changes from being maximum at $N_{\rm cond} = 0$ above the transition,

to having a maximum at finite $N_{\rm cond}$ below the transition. We also find that as the temperature decreases the condensate number fluctuations are suppressed, i.e.

$$\frac{\langle (N_{\rm cond} - \langle N_{\rm cond}\rangle)^2\rangle}{\langle N_{\rm cond}\rangle^2} \to 0, \tag{6.14}$$

(as was implicit in the behaviour of C_b^g observed above) and that the distribution has negative skew.

Given the phenomenal recent interest in measuring spatial correlations in ultra-cold atom systems [66–71], it would be of great interest to develop analogous techniques for observing these condensate number distribution in experiments. It is difficult to devise an experimental procedure which could be used to measure $\alpha_{\rm cond}$ (or $N_{\rm cond}$) in a manner equivalent to (6.13), which requires complete phase and amplitude information about the field. So here we propose a quantity that can be directly measured in experiments and used to reveal the transition from incoherent to coherent number statistics of the condensate mode. In particular, we consider the central momentum column density

$$n_{p=0} \equiv \left[\int dp_z\, n(\mathbf{p})\right]_{p_x=p_y=0}, \tag{6.15}$$

as an observable, since it is proportional to the peak density measured in the usual absorption images taken of ultra-cold systems [140]. The motivation for choosing this quantity is that the long range coherence of the condensate is clearly revealed as a peak in momentum space, thus the central momentum value is correlated with the condensate occupation. The detailed relationship between $n_{p=0}$ and $N_{\rm cond}$ is not unique, due to the contribution of the noncondensate to $n_{p=0}$. So measurements of $n_{p=0}$ cannot be considered equivalent to the condensate yet, as we show below, there is clear qualitative similarities between the distributions of both quantities.

In Fig. 6.7 we compare the distributions for $n_{p=0}$ and $N_{\rm cond}$ obtained from analysis of data sets from the same PGPE calculations. Qualitatively, the behaviour of these distributions appears to be quite similar. The $n_{p=0}$ distribution is clearly seen to be offset from zero at high temperatures as compared to the $N_{\rm cond}$ distribution (see Figs. 6.7(e) and (j)). This offset is related to the average momentum column density of the noncondensate component.

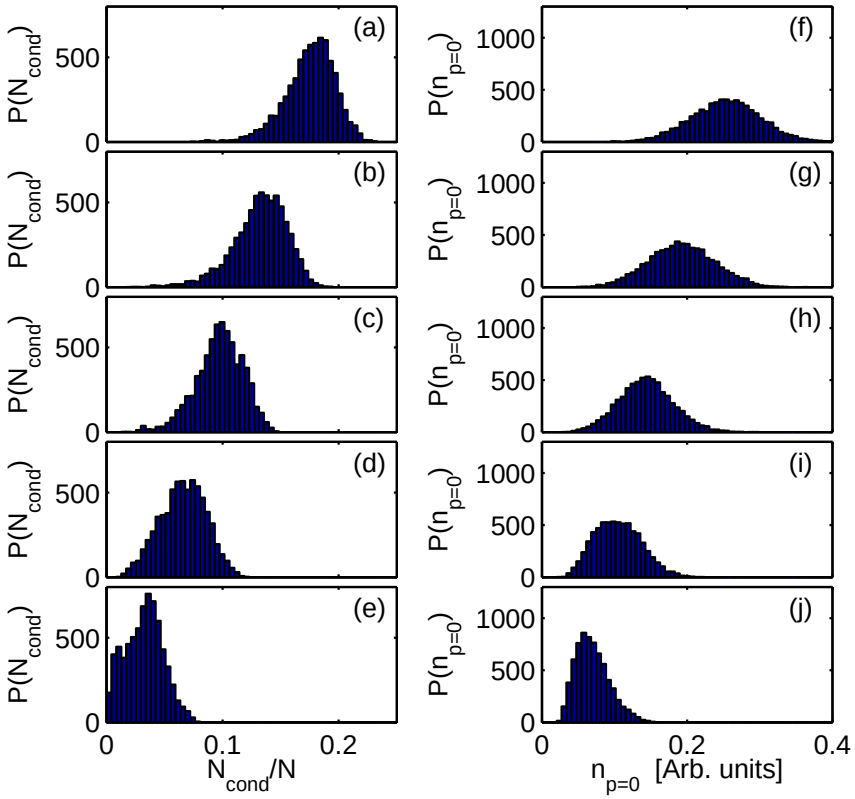

Figure 6.7: Comparison of (a-e) histograms of condensate/ground mode number distribution and (f-j) the the central momentum column density distribution across the critical point. Results (a-e) and (f-j) correspond to the temperatures $T' = \{0.957, 0.962, 0.969, 0.981, 0.990\}$ respectively.

Chapter 7

Conclusions

We have developed the PGPE formalism to study finite temperature experiments currently of interest in the field. We have made a quantitative comparison of the PGPE predictions of quadrupolar excitation frequencies with experiment [3], and an assessment of the validity of the PGPE formalism for describing dynamical systems. We have studied the correlations in the finite temperature Bose gas, and study critical phenomena in the gas.

Excitations

We have presented a comprehensive study of the excitation spectrum of a Bose cloud at finite temperature by modelling the experiment of Jin *et al.* [3] with the PGPE formalism. Our results for the frequency of the $m = 2$ mode is in good agreement with experiment. We found that our formalism failed to predict the anomalous jump in frequency of the $m = 0$ mode that occurs around $0.65T_c$. We have demonstrated that the origin of this failure in the current formalism is that we only provide a dynamical description for the portion of the noncondensate in the **C** region.

We are able to show that the frequency of the $m = 0$ mode oscillation relies on the inclusion of the noncondensate dynamics, through a study of the cutoff dependence. While the equilibrium properties of the system are insensitive to the energy cutoff, we found that certain dynamic properties weren't. The study of cutoff dependence in the collective mode results clearly reveals the importance of the interplay between condensate and noncondensate components in the mode behaviour, and suggests a new practical validity check for the PGPE theory: Dynamical predictions (in the absence of a dynamical theory for the **I** region) should be verified to be independent of the cutoff energy.

We suggest that future work should be directed towards developing a fully dynamical description of the incoherent region **I**, coupled to the coherent region **C**. We believe that in cases where there is cutoff dependence, this method would allow correct prediction of system properties. Such a method has been implemented for the ZNG theory, but for the case where all the noncodensate atoms are described as a classical "billiard ball" gas. A challenge for our case would be to implement this description only for atoms with energy exceeding $\epsilon_{\rm cut}$.

We also note that other types of collective excitations have been studied experimentally, e.g. scissor modes. These studies would be another avenue for comparison with our theory.

Correlations

We have presented the theoretical development of an efficient, computationally tractable method for calculating correlation functions of the finite temperature trapped Bose gas in position and momentum space. Our results show the generic characteristics of these functions, emphasise the striking differences between their behaviour in position and momentum space, and reveal the interplay between condensate and thermal components of the system. We study the dependence of the coherence length on the temperature of the system, for temperatures up to T_c.

We then focused this formalism to study the critical fluctuations in the Bose system motivated by the recent theoretical work by the ETH group [50]. For numerical convenience we have studied a trapped Bose gas with different parameters to the experimental system, yet obtain a critical exponent that agrees to within the error bars of both results. We have discussed finite-size effects and show that they can significantly alter the critical physics for systems with a small Ginzburg length. Finally, we considered fluctuations of the condensate mode occupation across the transition region, and have shown that measurements of the central momentum column density can be used to experimentally reveal the emergence of coherent statistics in the system.

Our study here represents the first quantitative theoretical calculations for this system beyond meanfield level. However, there are numerous avenues for improvement of our approach that could be used to obtain higher precision results, which we believe will be needed to develop a better understanding of the trapped system critical physics, and stimulate more experiments in this fascinating new area for ultra-cold atomic gases. For instance, it would be interesting to apply the SPPE formalism [111] to the critical regime, as both the chemical potential and temperature are control parameters in this

approach. This may allow more precise measurement of critical exponents and would make direct comparisons with the fixed N experiment of Donner *et al.* [50] more easy to achieve. Another avenue of investigation would be to build on our formalism a more efficient method of sampling, e.g. using Monte Carlo algorithms (e.g. see [137]). With additional improvements in precision we believe our formalism will be able to provide a detailed characterisation of the finite-size cross over functions for the trapped Bose gas. Knowledge of these functions would be useful for several problems of current interest in the ultra-cold atomic physics, such as better understanding of the quasi-2D behaviour and the emergence of phase defects in quenches across the critical regime [141].

Appendix A

Fourier Methods

We want to calculate

$$G^1(x,x') = \int dk W\left(\frac{x+x'}{2},k\right) e^{ik(x-x')}, \tag{A.1}$$

where certain physical requirements dictate that the appropriate x-grid is given by

$$-\frac{L}{2} \leq x_j \leq \frac{L}{2}, \quad 1 \leq j \leq M, \tag{A.2}$$

with spacing δx. The Fourier related momentum grid is given by

$$-\frac{K}{2} \leq k_j \leq \frac{K}{2}, \quad 1 \leq j \leq M, \tag{A.3}$$

where $K = 2\pi/\delta x$, and $\delta k = 2\pi/L$.

To efficiently evaluate this function it is useful to change variables to center of mass ($R = (x+x')/2$) and relative ($r = (x-x')$) coordinates, defined as

$$R_\alpha \equiv \frac{1}{2}(x_i + x_j), \tag{A.4}$$

$$r_\alpha \equiv (x_i - x_j), \tag{A.5}$$

where $\alpha = i + j$ is an index that goes from 1 to $2M$, with $-\frac{L}{2} \leq R \leq \frac{L}{2}$, $\delta R = \frac{1}{2}\delta x$, and $-L \leq r \leq L$, $\delta r = \delta x$.

The problem is now (for $G(r,R)$)

$$G_{\alpha\beta} = \delta\tilde{k} \sum_J e^{-i\tilde{k}_J r_\alpha} W(R_\beta, \tilde{k}_J), \tag{A.6}$$

where $\tilde{k}_J$ is the appropriate momentum grid to transform the r-coordinate. Now, because

the r-coordinate grid has the same spacing as the x-grid, yet twice the range, the $\tilde{k}$-grid has the same range as the k-grid yet half the spacing. We then get back $G^1(x, x')$ by choosing the appropriate pairs of $G_{\alpha\beta}$.

A.1 Scaling

We can make a simple analysis of the harmonically trapped system. Let f be a term used to set the energy cutoff for thermal description of the system, i.e. we include all contributions up to energy scale $E = fk_BT$. This is important because it sets constraints on the coordinate and momentum grids we must use in our description, i.e. for the case of a harmonically trapped system we use a position grid of extent L (i.e. $L/2 \leq x \leq L/2$) so where we choose L according to $\frac{1}{2}m\omega^2(L/2)^2 = fk_BT$, i.e.

$$L = \sqrt{\frac{8fk_BT}{m\omega^2}}. \tag{A.7}$$

Similarly for momentum we choose K (with $K/2 \leq k \leq K/2$) so that $\hbar^2(K/2)^2/2m = fk_BT$, i.e.

$$K = \sqrt{\frac{8mfk_BT}{\hbar^2}}. \tag{A.8}$$

the momentum and spatial extents are related as reciprocal (Fourier) grids, thus the spacing of points on one grid relates to the extent of its reciprocal grid as $\delta k = 2\pi/L$, $\delta x = 2\pi/K$. Thus the number of grid points is given by

$$M = \frac{KL}{2\pi} = \frac{8fk_BT}{\hbar\omega}. \tag{A.9}$$

To understand how this scales for typical problems, we note the typical temperature scale of interest is the critical temperature, given by

$$T_c = \frac{\hbar\omega}{k_B}\left(\frac{N}{1.202}\right)^{1/3}, \tag{A.10}$$

for the trapped system. Thus we have

$$M \sim 8fN^{1/3}, \tag{A.11}$$

and so for typical f values ($f \sim 10$) and numbers of atoms ($N \sim 10^6$) we will need grids of order 10^4 points. Note that the size of these grids need to double when we transform to the r and R grid, so in general this procedure is quite demanding numerically, and efficient techniques are necessary.

Appendix B

TDPT comparison with PGPE

We will consider a perturbation of the form

$$\delta V(x,t) = A\sin(\omega_x t)\omega_x^2 x^2, \tag{B.1}$$

We apply this only in the x direction. We can evaluate the applicability of using the quadrature grids used to calculate $F_{\alpha\beta\gamma}$ to calculate $G_{\alpha\beta\gamma}$ by comparing the results from a PGPE calculation with an analytical result, and we do this for the case of the noninteracting gas. In this case we will use time-dependent perturbation theory (TDPT) to make this comparison.

Using TDPT, we know that for a noninteracting harmonically trapped Bose gas, the probability of a transition from an initial state (ϕ_i) to an excited state (ϕ_f) is given by

$$\langle\phi_f|\hat{U}_I(t)|\phi_i\rangle = \frac{V_{fi}}{2\hbar}\left(\frac{1-\exp(i(\omega_{fi}+\omega)t)}{\omega_{fi}+\omega} + \frac{1-\exp(i(\omega_{fi}-\omega)t)}{\omega_{fi}-\omega}\right) \tag{B.2}$$

where

$$V_{fi} = \langle\phi_f|\hat{V}|\phi_i\rangle \tag{B.3}$$

and

$$\omega_{fi} = \frac{\epsilon_f - \epsilon_i}{\hbar}. \tag{B.4}$$

In this case we will take the perturbation to be of the form

$$\hat{V} = \sin(\omega t)\hat{x}^2. \tag{B.5}$$

We calculate the probability of a transition from the ground state to the first excited state in the x direction for a three dimensional system. We compare this to the population of the first excited state found using the PGPE, when the initial state is a c-vector with all the amplitude in the ground harmonic oscillator state, and interactions between

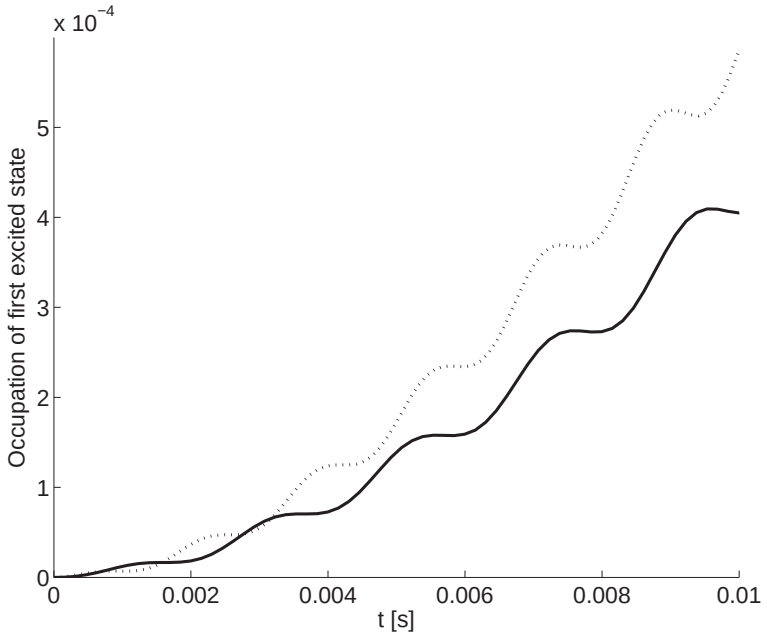

Figure B.1: Comparison of TDPT (dots) with PGPE(line) for a sinusoidal perturbation of the form given in Eq. (B.1)

particles are zero (i.e. $C = 0$). The form of our perturbation means that only the x oscillator states will couple to it.

The results for the two different methods are shown in Fig. B.1. We see reasonable agreement between the two, and conclude that this approximation is adequate for the extra perturbation potentials that we will explore later in this work.

Appendix C

Optical Lattice papers

PHYSICAL REVIEW A **71**, 033616 (2005)

Adiabatic cooling of fermions in an optical lattice

P. B. Blakie and A. Bezett
Department of Physics, University of Otago, P.O. Box 56, Dunedin, New Zealand
(Received 5 October 2004; published 11 March 2005)

The entropy-temperature curves are calculated for noninteracting fermions in a three-dimensional optical lattice. These curves facilitate understanding of how adiabatic changes in the lattice depth affect the temperature, and we demonstrate regimes in which the atomic sample can be significantly heated or cooled. When the Fermi energy of the system is near the location of a band gap, the cooling regimes disappear for all temperatures and the system can be heated by only lattice loading. For samples with greater than one fermion per site, we find that lattice loading can lead to a large increase in the degeneracy of the system. We study the scaling properties of the system in the degenerate regimes and assess the effects of nonadiabatic loading.

DOI: 10.1103/PhysRevA.71.033616 PACS number(s): 03.75.Ss, 32.80.Pj, 05.30.−d

I. INTRODUCTION

Tremendous progress has been made in the preparation, control, and manipulation of Fermi gases in the degenerate regime [1–7]. Such systems have many potential applications in the controlled study of fermionic superfluidity and the production of ultracold molecules. Another area of developing theoretical interest is in the physics of fermions in optical lattices [8–11], and initial experiments have already begun to examine the properties of Fermi gases (prepared as boson-fermion mixtures) in one-dimensional optical lattices [12,13]. For Bose gases, optical lattices have been used to demonstrate an impressive array of experiments, such as quantum matter-wave engineering [14,15]; the Mott-insulator quantum-phase transition [16]; quantum entanglement [17]; and coherent molecule production [18]. It seems likely that a similar range of rich physics lies ahead for fermions in optical lattices.

Many of the physical phenomena that are suitable to experimental investigation in optical lattices are sensitive to temperature, and it is therefore of great interest to understand how the temperature of a quantum degenerate gas changes with lattice depth. Experimental results by Kastberg *et al*. [19] in 1995 showed that loading laser-cooled atoms into a three-dimensional (3D) optical lattice caused the atoms to increase their temperature [20]. Recently, one of us conducted a detailed thermodynamic study of bosonic atoms in optical lattices [21]. In that work we showed that for sufficiently low initial temperatures, a new regime would be entered in which adiabatically ramping up the lattice depth would have the desirable effect of cooling the system. The typical temperatures at which Bose-Einstein condensates are produced lie well within this cooling regime, and thus benefit from reduced thermal fluctuations when adiabatically loaded into an optical lattice. In this paper we examine how degenerate fermions are affected by adiabatic loading into an optical lattice. In Fermi gases, the lowest temperatures obtained in experiments tend to be much higher than in Bose gas experiments. It is therefore important to understand to what extent the introduction of an optical lattice might affect the temperature; in particular, to determine in what regimes additional cooling can occur during lattice loading.

The quintessential difference in the properties of degenerate fermions and bosons is embodied by the Fermi energy: the energy that marks the top of the Fermi sea of occupied states (at $T=0$). The Fermi energy sets a new energy scale that has no analog in boson systems and plays a crucial role in determining the effect that lattice loading has upon the system. We find that as the Fermi energy approaches a band gap, the cooling regime vanishes and the system can heat only with increasing lattice depth. However, we also find that when the Fermi energy lies in the second band (when the average number of fermions per site is greater than 1), a cooling regime is re-established. This cooling regime for the second band is accompanied by a large amplification of degeneracy; i.e., adiabatically loading into the lattice causes both T and the ratio T/T_F to decrease.

The results we present in this paper are obtained from a numerical study of the thermodynamic properties of an ideal gas of fermions in a 3D cubic lattice. We work with the grand canonical ensemble and use the exact single-particle eigenstates of the lattice to determine the entropy-temperature curves for the system for various lattice depths and filling factors. We develop analytic expressions for the plateaus that develop in the entropy-temperature curves and characterize a scaling relationship that holds for low temperatures and in deep lattices. A *fast-loading* procedure is considered to ascertain how robust our results are to nonadiabatic effects. The physics we explore here will be relevant to current experiments, and many of the predictions we make should be easily seen.

II. FORMALISM

A. Single-particle eigenstates

We consider a cubic 3D optical lattice made from three independent (i.e., noninterfering) sets of counterpropagating laser fields of wavelength λ, giving rise to a potential of the form

$$V_{\mathrm{Latt}}(\mathbf{r}) = \frac{V}{2}[\cos(2kx) + \cos(2ky) + \cos(2kz)], \qquad (1)$$

where $k=2\pi/\lambda$ is the single-photon wave vector, and V is the lattice depth. We take the lattice to be of finite extent with a total of N_s sites, consisting of an equal number of sites along

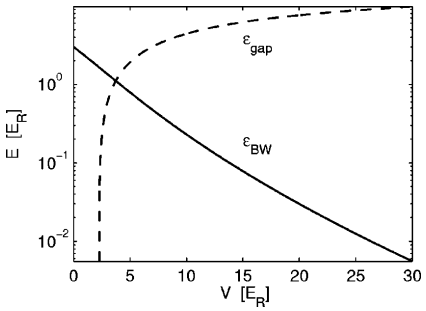

FIG. 1. The dependence of the energy gap (ϵ_{gap}, dashed line) and ground band width (ϵ_{BW}, solid line) on the lattice depth (see the text).

each of the spatial directions with periodic boundary conditions. The single-particle energies $\epsilon_{\mathbf{q}}$ are determined by solving the Schrödinger equation

$$\epsilon_{\mathbf{q}}\psi_{\mathbf{q}}(\mathbf{r}) = \frac{\mathbf{p}^2}{2m}\psi_{\mathbf{q}}(\mathbf{r}) + V_{\text{Latt}}(\mathbf{r})\psi_{\mathbf{q}}(\mathbf{r}), \tag{2}$$

for the Bloch states $[\psi_{\mathbf{q}}(\mathbf{r})]$ of the lattice. For notational simplicity, we choose to work in the extended zone scheme where $\mathbf{q}$ specifies both the quasimomentum and band index of the state under consideration [22]. By using the single-photon recoil energy $E_R=\hbar^2k^2/2m$ as our unit of energy, the energy states of the system are completely specified by the lattice depth V and the number of lattice sites N_s (i.e., in recoil units $\epsilon_{\mathbf{q}}$ is independent of k).

For completeness, we briefly review some important features of the band structure of Eq. (2) relevant to the thermodynamic properties of the system. For sufficiently deep lattices, an energy gap (ϵ_{gap}) will separate the ground and first excited bands (see Fig. 1). For the cubic lattice we consider here, a finite gap appears at a lattice depth of $V\approx 2E_R$ [23] (marked by the vertical asymptote of the dashed line in Fig. 1). For lattice depths greater than this, the gap increases with lattice depth. In forming the gap, higher-energy bands are shifted upwards in energy, and the ground band becomes compressed — a feature characteristic of the reduced tunneling between lattice sites. We refer to the energy range over which the ground band extends as the (ground) band width ϵ_{BW}. As is apparent in Fig. 1, the ground band width decreases exponentially with V, causing the ground band to have an extremely high density of states for deep lattices.

B. Equilibrium properties

Our primary interest lies in understanding the process of adiabatically loading a system of N_p fermions into a lattice. Under the assumption of adiabaticity, the entropy remains constant throughout this process, and the most useful information can be obtained from knowing how the entropy depends on the other parameters of the system. In the thermodynamic limit, where $N_s\to\infty$ and $N_p\to\infty$ while the filling factor $n\equiv N_p/N_s$ remains constant, the entropy per particle is completely specified by the intensive parameters T, V, and n. The calculations we present in this paper are for finite-sized systems that are sufficiently large to approximate the thermodynamic limit. We would like to emphasize at this point the remarkable fact that V is an adjustable parameter in optical lattice experiments, in contrast to solid state systems in which the lattice parameters are immutable.

The entropy is determined as follows: The single-particle spectrum $\{\epsilon_{\mathbf{q}}\}$ of the lattice is calculated for given values of N_s and V. We then determine the thermodynamic properties of the lattice with N_p fermions in the grand canonical ensemble, for which we calculate the partition function $\mathcal{Z}$ as

$$\log \mathcal{Z} = \sum_{\mathbf{q}} \log(1 + e^{-\beta(\epsilon_{\mathbf{q}}-\mu)}), \tag{3}$$

where μ is found by ensuring particle conservation. The entropy of the system can then be expressed as

$$S = k_B(\log \mathcal{Z} + \beta E - \mu\beta N_p), \tag{4}$$

where $\beta=1/k_BT$, and $E=-\partial \ln \mathcal{Z}/\partial\beta$ is the mean energy.

Multiple components

In most current experiments, mixtures of Fermi gases in different internal states are studied. This is required because s-wave elastic collisions, needed for re-equilibration, are prohibited by the Pauli principle for spin-polarized samples [24]. The theory we present here is for the spin-polarized case, but is trivially extensible to multiple components if the lattice potential is spin independent and the number of atoms in each component is the same: in this case all extensive parameters are doubled (e.g., $\{E,S\}$) and intensive parameters (e.g., $\{T,\mu\}$) remain the same. The inclusion of interaction effects, which will be important in the multiple-component case, is beyond the scope of this paper.

III. RESULTS

A. Effect of lattice loading on Fermi-gas temperature

In Fig. 2 we show entropy-temperature curves for various lattice depths and filling factors n. These curves have been calculated for a lattice with 31 lattice sites along each spatial dimension; i.e., $N_s\approx 3\times 10^4$.

A general feature of these curves is the distinct separation of regions where adiabatic loading causes the temperature of the sample to increase or decrease, which we will refer to as the regions of heating and cooling, respectively. These regions are separated by a value of entropy at which the curves plateau — a feature that is more prominent in the curves for larger lattice depths. This plateau entropy is indicated by a horizontal dashed line and is discussed below. For the case of unit filling factor shown in Fig. 2(c), this plateau occurs at $S=0$, and only a heating region is observed.

We now explicitly demonstrate the temperature changes that occur during adiabatic loading using two possible adiabatic processes labeled A and B, and marked as dotted lines in Fig. 2(a). Process A begins with a gas of free particles in a state with an entropy value lying above the plateau entropy. As the gas is loaded into the lattice, the process line indicates

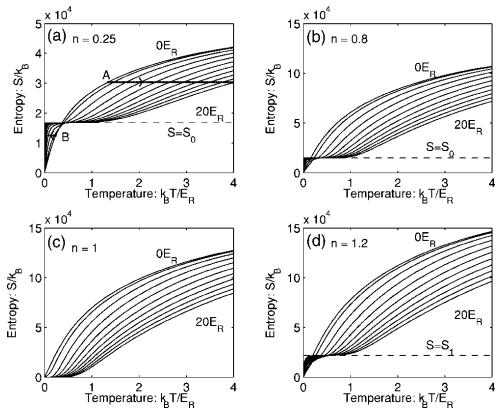

FIG. 2. Entropy versus temperature curves for a $N_s \approx 3\times 10^4$ site cubic lattice, at various depths $V=0$ to $20E_R$ (with a spacing of $2E_R$ between each curve). Filling factors used are (a) $n=0.25$, (b) $n=0.8$, (c) $n=1.0$, and (d) $n=1.2$. The entropy plateau is shown as a dashed line. Dotted line marked *A* shows a path along which adiabatic loading into the lattice causes the temperature to increase. Dotted line marked *B* shows a path along which adiabatic loading into the lattice causes the temperature to decrease.

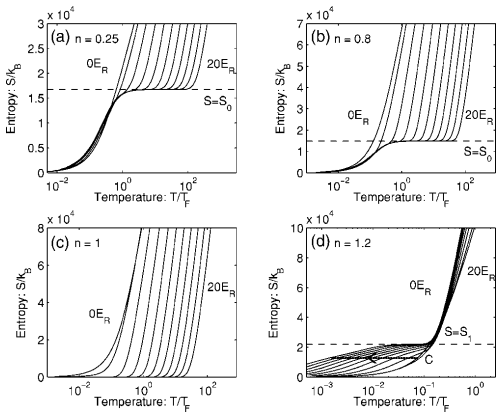

FIG. 3. Entropy versus temperature over Fermi temperature curves for the same cases considered in Fig. 2 (see that figure for details of parameters used). The entropy plateau is shown as a dashed line. The dotted line marked *C* shows a path along which adiabatic loading into the lattice causes the ratio of the temperature to the Fermi temperature to decrease.

that the temperature increases rapidly with the lattice depth. Conversely, process *B* begins with a gas of free particles in a state with entropy below the plateau. For this case, adiabatic lattice loading causes a rapid decrease in temperature. This behavior can be qualitatively understood in terms of the modifications the lattice makes to the energy states of the system. As is apparent in Fig. 1, the ground band rapidly flattens for increasing lattice depth, causing the density of states to be more densely compressed at lower energies. Thus, in the lattice, all these states can be occupied at a much lower temperature than for the free particle case. As we discuss below, S_0 is the maximum entropy available from accessing states of only the lowest band. If $S<S_0$, the temperature of the system must decrease with increasing lattice depth to remain at constant entropy. Alternatively, for $S>S_0$, the occupation of states in higher bands is important, and as the lattice depth and hence $\epsilon_{\rm gap}$ increase, the temperature must increase for these excited states to remain accessible.

B. Fermi-gas degeneracy

In addition to the effect that lattice loading has on the temperature of a Fermi gas, it is of considerable interest to understand how the ratio of temperature to the Fermi temperature (T_F) [25] changes. Indeed, the ratio T/T_F is the standard figure of merit used to quantify the degeneracy of dilute Fermi gases. In Fig. 3 we show how T/T_F changes with adiabatic lattice loading for the same parameters used in Fig. 2. In Figs. 3(a) and 3(b) the same general behavior is seen: Below the entropy plateau where cooling is observed [see Figs. 2(a) and 2(b)], the ratio of T/T_F remains approximately constant, so that there is little change in the degeneracy of the gas. Above the entropy plateau where heating was observed, the ratio of T/T_F rapidly increases, so that in this regime the gas will rapidly become nondegenerate as it is loaded into the lattice. For the unit filling case [Fig. 3(c)], there is no cooling regime, and heating is accompanied by a rapid increase in T/T_F for all initial conditions of the gas. In Fig. 3(d), where the filling factor is $n=1.2$, rather different behavior is seen: In the cooling regime, the ratio of T/T_F is rapidly suppressed as the temperature decreases; see, e.g., the dotted line marked *C* in Fig. 3(d). This most desirable behavior could be used, for example, to prepare a Fermi gas into a highly degenerate state where the BCS transition might be observable. We also note that for the same parameters, but in the heating regime, the ratio T/T_F remains relatively constant.

We can give a simple explanation for the behavior of T/T_F. For the three cases considered in Fig. 3(a)–3(c), the Fermi energy lies within or at the top of the first band of energy states. As shown in Fig. 1, the width of the ground band ($\epsilon_{\rm BW}$) decreases rapidly with lattice depth. Because the number of states contained in each band is constant (given by the number of lattice sites), both the Fermi energy and T_F scale identically to $\epsilon_{\rm BW}$, and thus will rapidly decrease with lattice depth. In the cooling regime, the temperature scales in the same manner as $\epsilon_{\rm BW}$ (see Sec. III D and Fig. 4), and thus the ratio T/T_F remains approximately constant. In the heating regime T increases slowly, while the ratio T/T_F increases rapidly with lattice depth (due to T_F becoming small).

For the case considered in Fig. 3(d), the filling factor satisfies $n>1$ and the Fermi energy lies in the second band. As the lattice depth increases, the Fermi energy and T_F now scale like $\epsilon_{\rm gap}$; i.e.. slowly increase with lattice depth (see Fig. 1). Thus, in the regime wherein the temperature decreases, the ratio T/T_F must become smaller. We note that

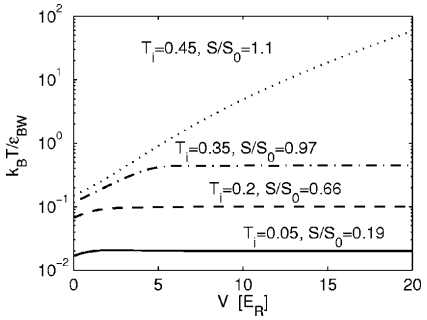

FIG. 4. Scaled temperature change during adiabatic lattice loading. Ratio of temperature to bandwidth for various lattice depths along adiabatic contours for several values of entropy. Initial temperature (at $V=0$) and ratio of entropy to the plateau entropy is indicated for each curve. Results are indicated for the case of filling factor $n=0.25$.

the temperature reduction occurs because the width of the second band decreases with lattice depth.

C. Entropy plateau

In Figs. 2(a) and 2(b) a horizontal plateau (at the level marked by the dashed lines) is common to the entropy-temperature curves for larger lattice depths ($V \gtrsim 8E_R$). This occurs because for these lattices, the energy range over which the ground band extends is small compared to the energy gap to the excited band, and there is a large temperature range over which states in the excited bands are inaccessible; yet all the ground band states are uniformly occupied. The entropy value indicated by the dashed line in Figs. 2(a) and 2(b) corresponds to the total number of N_p-particle states in the ground band. Since the number of single-particle energy states in the ground band is equal to the number of lattice sites, the total number of available N_p-particle states (Ω_0) is given by $\Omega_0 = N_s!/[N_p!(N_s-N_p)!]$ (valid for $N_p \leqslant N_s$). The associated entropy $S_0 = k_B \log \Omega_0$, which we shall refer to as the plateau entropy, can be evaluated using Sterling's approximation

$$S_0 \simeq k_B[N_p \log N_p + N_s \log N_s - (N_s - N_p)\log(N_s - N_p)]; \tag{5}$$

the validity condition for this result is that $1 \ll N_s \ll N_p$. An important case for which the above approximation is invalid is for $N_p = N_s$; i.e., we have a filling factor of $n=1$, where $S_0=0$. This case corresponds to the unit filling factor result shown in Fig. 2(c) where, as a result of the entropy plateau occurring at $S=0$, only a heating region is observed.

Similar entropy plateaus are observed for greater than unit filling ($N_p > N_s$); e.g., as is seen in Fig. 2(d). For fermions such high filling factors necessarily means that higher bands are occupied, and in general the precise details of these higher plateaus will depend on the particle band structure of the lattice. For example, in the lattice we consider here (1), there are three degenerate first excited bands that contain a total of $3N_s$ single-particle states. Because the first band is fully occupied, only $N_p' = N_p - N_s$ particles are available to occupy the excited band, so that the total number of available states is found according to the ground band result (5), but with the substitutions $N_s \to 3N_s$ and $N_p \to N_p - N_s$. This result is shown as the dashed horizontal in Fig. 2(d) labeled as S_1.

The suppression of the plateaus at specific integer filling factors (e.g., $n=1$ for $S_0 \to 0$ and $n=4$ for $S_1 \to 0$) corresponds to the Fermi energy of the system approaching a band gap. Whenever this occurs it means that all the states below the gap are occupied at $T=0$, and excitations in the system require the promotion of particles into the excited band (above the gap). As all band gaps increase in size with lattice depth, the temperature of the system must increase for the entropy to remain constant. Thus, in regimes wherein the Fermi energy lies at a band gap, the system exhibits heating only with increasing lattice depth [e.g., see Fig. 2(c)].

D. Scaling: Tight-binding limit at low temperatures and filling factors

Here we give limiting results for the entropy-temperature curves.

As discussed in Sec. III C, when $N_p < N_s$ and the temperature is sufficiently low that $S < S_0$, then only single-particle states within the ground band are accessible to the system. In addition, when the tight-binding description is applicable for the initial and final states of an adiabatic process, the initial and final thermodynamic variables are related by a scaling transformation.

In the tight-binding regime, which is a good approximation for $V \gtrsim 4E_R$, the ground band dispersion relation takes the form

$$\epsilon_{\mathrm{TB}}(\mathbf{q}) = -\frac{\epsilon_{\mathrm{BW}}}{6} \sum_{j=\{x,y,z\}} \cos(q_j a), \tag{6}$$

where $a = \pi/\lambda$ is the lattice period, the ground band width ϵ_{BW} has already been introduced (e.g., see Fig. 1), and the wave vector $\mathbf{q}$ is restricted to the first Brillouin zone. We refer the reader to Refs. [26,27] for more details on the tight-binding approximation.

To illustrate the scaling transformation, we consider an initial system in equilibrium with entropy $S < S_0$, in lattice of depth V_i sufficiently large enough for tight-binding expression (6) to provide an accurate description of the ground band energy states. If an adiabatic process is used to take the system to some final state at lattice depth V_f (also in the tight-binding regime) it is easily shown that the macroscopic parameters of the initial and final states are related as

$$X_f = \alpha X_i, \tag{7}$$

where $X = \{E, T, \text{or } \mu\}$, and the scaling parameter $\alpha = (\epsilon_{\mathrm{BW}})_f/(\epsilon_{\mathrm{BW}})_i$ is given by the ratio of the final and initial band widths. The requirement that the initial and final states are in the tight-binding regime is because the single-particle states are then related as $[\epsilon_{\mathrm{TB}}(\mathbf{q})]_f = \alpha[\epsilon_{\mathrm{TB}}(\mathbf{q})]_i$, which is essential for (7) to hold.

This type of scaling suggests that the occupations of the single-particle levels are unchanged during the change in lattice: the products $\beta\epsilon_{\mathrm{TB}}(\mathbf{q})$ and $\beta\mu$ are independent of V, so that the Fermi distribution $f_F(\mathbf{q})=\{\exp[\beta\epsilon_{\mathrm{TB}}(\mathbf{q})-\beta\mu]+1\}^{-1}$ will also be independent of V. This suggests that being adiabatic in this regime will not require redistribution through collisions, and may allow the lattice depth to be changed more rapidly.

To confirm the scaling predictions, in Fig. 4 we plot the ratio of the temperature to ground band width as a function of lattice depth along contours of constant entropy [i.e., how $k_BT/\epsilon_{\mathrm{BW}}$ varies along the process curves labeled A and B in Fig. 2(a)]. In regimes wherein the scaling relationship (7) holds true, the ratio $k_BT/\epsilon_{\mathrm{BW}}$ should be constant (independent of V). In Fig. 4 this is clearly observed for initial entropies less than S_0 and lattice depths $V\gtrsim 5E_R$. For $S>S_0$, single-particle states of higher bands necessarily play an important role in the thermodynamic state of the system, and the scaling transformation clearly does not hold at any lattice depth, as is seen in the dotted curve in Fig. 4. For this case, as the lattice depth increases, the cooling effect of the ground band compression is offset by the f particles in the excited band that are lifted to larger energies as the gap (ϵ_{gap}) grows (see Fig. 1).

E. Adiabaticity

Finally, we note that interactions between particles are essential for establishing equilibrium in the system, and understanding this in detail will be necessary to determine the time scale for adiabatic loading. In general, this requirement is difficult to assess, and in systems where there is an additional external potential, it seems that the adiabaticity requirements will likely be dominated by the process of atom transport within the lattice to keep the chemical potential uniform, although recent proposals have suggested ways of reducing this problem [28] for Bose systems. A study of the effects of interactions or inhomogeneous potentials is beyond the scope of this work; however, it is useful to assess the degree to which nonadiabatic loading would cause heating in the system. We consider lattice loading on a time scale to be fast compared to the typical collision time between atoms, yet slow enough to be quantum mechanically adiabatic with respect to the single-particle states. This latter requirement excludes changing the lattice so quickly that band excitations are induced, and it has been shown that in practice this condition can be satisfied on very short time scales [29]. We will refer to this type of loading as fast lattice loading, to distinguish it from the fully adiabatic loading we have been considering thus far.

To simulate the fast lattice loading, we take the system to be initially in equilibrium at temperature T_i for zero lattice depth. For the final lattice depth we fast-load into, we map the initial single-particle distribution onto the equivalent states in the final lattice, and calculate the total energy for this final nonequilibrium configuration [i.e., we calculate $E=\Sigma_{\mathbf{q}}\,\epsilon_{\mathbf{q}}^{(f)}f_F(\epsilon_{\mathbf{q}}^{(i)},T_i)$, where $\epsilon_{\mathbf{q}}^{(i)}$ and $\epsilon_{\mathbf{q}}^{(f)}$ are the single-particle energies for the initial and final lattice depths, respectively, and f_F is the Fermi distribution function]. This procedure assumes that there has been no collisional redistribution to allow the system to adjust to the lattice potential during the period it is changed. To determine the thermodynamic state the final distribution will relax to, we use the energy of the nonequilibrium distribution as a constraint for finding the equilibrium values of temperature and entropy. In general, the final state properties will depend on the initial temperature, filling factor, and final depth of the lattice. To illustrate typical behavior we show a set of fast-loading process curves in Fig. 5 for two different values of the filling factor.

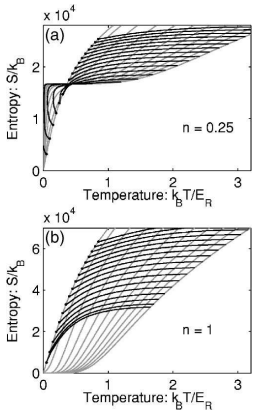

FIG. 5. Fast lattice loading of a $N_s\approx 3\times 10^4$ site cubic lattice, with filling factors of (a) $n=0.25$ and (b) $n=1$. Dark solid lines indicate fast-loading curves (see text). The initial $V=0$ state for each of this curves is indicated with a dot. The lattice depth on these curves can be determined from their intercept with the equilibrium entropy versus temperature curves (gray solid lines), which are described in Figs. 2(a) and 2(c) for $n=0.25$ and $n=1$, respectively.

These curves show, as is expected from standard thermodynamic arguments, that entropy increases for nonadiabatic processes; i.e., all loading curves in Figs. 5(a) and 5(b) bend upwards with increasing lattice depth. For the results with filling factor $n=0.25$ and for initial temperatures deep in the cooling regime (i.e., initial states far below the entropy plateau) a useful degree of temperature reduction can be achieved with fast lattice loading up to certain maximum depth. For example, the second-lowest fast-loading curve in Fig. 5(a) cools with increasing lattice depth up to $V\approx 15E_R$, and then begins to heat for larger final lattice depths. Generally, for low filling factors ($n<1$) where the ground band plays the dominant role in the system behavior at low temperatures, the entropy increase is due mainly to the reshaping of the single-particle energy states that occurs at low lattice depth [30]. This effect can be reduced by taking, as the initial condition for fast-loading, a system in equilibrium at a finite lattice depth for which the dispersion relation is more tight-binding-like. This situation was considered in Ref. [8] in preparing a superfluid Fermi gas using in an optical lattice. Their results, for the case $n=0.5$ and an initial lattice depth of $V\approx 1E_R$, predicted a useful degree of cooling.

As was demonstrated in Fig. 2(c), for filling factor $n=1$, adiabatic lattice loading causes the atoms to heat. This effect

is exacerbated by nonadiabatic loading, as shown in Fig. 5(b). This case also benefits from beginning in a lattice of nonzero depth, since at fixed temperature but increasing lattice depth (hence larger ϵ_{BW}), a smaller number of particles will be found in the excited bands.

IV. CONCLUSION

In this paper we have calculated the entropy-temperature curves for fermions in a 3D optical lattice at various depths and filling factors. We have identified general features of the thermodynamic properties relevant to lattice loading, indicated regimes wherein adiabatically changing the lattice depth will cause heating or cooling of the atomic sample, and have provided limiting results for the behavior of the entropy curves. The results presented in this work suggest optimal regimes (filling factors and temperatures) that will facilitate the suppression of thermal fluctuations in a fermionic gas by lattice loading. These predictions should be easily verifiable with current experiments. We have also shown that for a sample of fermions with a filling factor greater than 1, the cooling regime is accompanied by a significant reduction of the temperature compared to the Fermi temperature. This regime would clearly be desirable for experiments to investigate as an avenue for producing dilute Fermi gases with $T/T_F \ll 1$. We have shown that many of our predictions are robust to nonadiabatic effects.

ACKNOWLEDGMENTS

P. B. B. would like to thank C. W. Clark (NIST) for support during the initial stages of this research.

[1] B. DeMarco and D. S. Jin, Science **285**, 1703 (1999).
[2] F. Schreck, L. Khaykovich, K. L. Corwin, G. Ferrari, T. Bourdel, J. Cubizolles, and C. Salomon, Phys. Rev. Lett. **87**, 080403 (2001).
[3] K. M. O'Hara, S. L. Hemmer, M. E. Gehm, S. R. Granade, and J. E. Thomas, Science **298**, 2179 (2002).
[4] G. Modugno, G. Roati, F. Riboli, F. Ferlaino, R. J. Brecha, and M. Inguscio, Science **297**, 2240 (2002).
[5] S. Gupta, Z. Hadzibabic, M. W. Zwierlein, C. A. Stan, K. Dieckmann, C. H. Schunck, E. G. M. van Kempen, B. J. Verhaar, and W. Ketterle, Science **300**, 1723 (2003).
[6] C. A. Regal, C. Ticknor, J. L. Bohn, and D. S. Jin, Nature (London) **424**, 47 (2003).
[7] J. Cubizolles, T. Bourdel, S. J. J. M. F. Kokkelmans, G. Shlyapnikov, and C. Salomon, Phys. Rev. Lett. **91**, 240401 (2003).
[8] W. Hofstetter, J. I. Cirac, P. Zoller, E. Demler, and M. D. Lukin, Phys. Rev. Lett. **89**, 220407 (2002).
[9] P. Rabl, A. J. Daley, P. O. Fedichev, J. I. Cirac, and P. Zoller, Phys. Rev. Lett. **91**, 110403 (2003).
[10] L. Viverit, C. Menotti, T. Calarco, and A. Smerzi, Phys. Rev. Lett. **93**, 110401 (2004).
[11] L. Santos, M. A. Baranov, J. I. Cirac, H.-U. Everts, H. Fehrmann, and M. Lewenstein, Phys. Rev. Lett. **93**, 030601 (2004).
[12] G. Modugno, F. Ferlaino, R. Heidemann, G. Roati, and M. Inguscio, Phys. Rev. A **68**, 011601(R) (2003).
[13] H. Ott, E. de Mirandes, F. Ferlaino, G. Roati, G. Modugno, and M. Inguscio, Phys. Rev. Lett. **92**, 160601 (2004).
[14] C. Orzel, A. K. Tuchman, M. L. Fenselau, M. Yasuda, and M. A. Kasevich, Science **23**, 2386 (2001).
[15] M. Greiner, O. Mandel, T. W. Hänsch, and I. Bloch, Nature (London) **419**, 51 (2002).
[16] M. Greiner, O. Mandel, T. Esslinger, T. W. Hänsch, and I. Bloch, Nature (London) **415**, 39 (2002).
[17] O. Mandel, M. Greiner, A. Widera, T. Rom, T. Hänsch, and I. Bloch, Phys. Rev. Lett. **91**, 010407 (2003).
[18] T. Rom, T. Best, O. Mandel, A. Widera, M. Greiner, T. W. Hänsch, and I. Bloch, Phys. Rev. Lett. **93**, 073002 (2004).
[19] A. Kastberg, W. D. Phillips, S. L. Rolston, R. J. C. Spreeuw, and P. S. Jessen, Phys. Rev. Lett. **74**, 1542 (1995).
[20] In fact, this study used adiabatic deloading to reduce the temperature of the constituent atoms.
[21] P. B. Blakie and J. V. Porto, Phys. Rev. A **69**, 013603 (2004).
[22] For a discussion of how the quantum numbers of quasimomentum and band index are introduced, we refer the reader to N. W. Ashcroft and N. D. Mermin, *Solid State Physics* (W. B. Saunders, Philadelphia, 1976).
[23] The delay in appearance of the excitation spectrum gap until $V \approx 2E_R$ is a property of the 3D band structure. In a one-dimensional lattice a gap is present for all depths $V > 0$.
[24] This also means that a single-component Fermi gas is quite well described by a noninteracting theory.
[25] The Fermi temperature is given by $T_F = \epsilon_F / k_B$, where ϵ_F (the Fermi energy) is the energy of the highest occupied single-particle state for the system at $T = 0$ K.
[26] D. Jaksch, C. Bruder, J. I. Cirac, C. Gardiner, and P. Zoller, Phys. Rev. Lett. **81**, 3108 (1998).
[27] D. van Oosten, P. van der Straten, and H. T. C. Stoof, Phys. Rev. A **63**, 053601 (2001).
[28] S. E. Sklarz, I. Friedler, D. J. Tannor, Y. B. Band, and C. J. Williams, Phys. Rev. A **66**, 053620 (2002).
[29] J. H. Denschlag, J. E. Simsarian, H. Häffner, C. McKenzie, A. Browaeys, D. Cho, K. Helmerson, S. L. Rolston, and W. D. Phillips, J. Phys. B **35**, 3095 (2002).
[30] As the lattice is ramped up, the free particle dispersion relation $\epsilon(\mathbf{q}) = \hbar^2 \mathbf{q}^2 / 2m$ rapidly changes to a tight-binding form $\epsilon_{\mathrm{TB}}(\mathbf{q})$ [see Eq. (6)]. As the lattice depth increases further, the ground band energy states compress more (i.e., scale), but do not undergo further reshaping.

PHYSICAL REVIEW A **75**, 063609 (2007)

Degenerate Fermi gas in a combined harmonic-lattice potential

P. B. Blakie,[1] A. Bezett,[1] and P. Buonsante[1,2]
[1]*Jack Dodd Centre for Photonics and Ultra-Cold Atoms, Department of Physics, University of Otago, P.O. Box 56, Dunedin, New Zealand*
[2]*Dipartimento di Fisica, Politecnico di Torino, Corso Duca degli Abruzzi 24, I-10129 Torino, Italy*
(Received 27 March 2007; published 11 June 2007)

In this paper we derive an analytic approximation to the density of states for atoms in a combined optical lattice and harmonic trap potential as used in current experiments with quantum degenerate gases. We compare this analytic density of states to numerical solutions and demonstrate its validity regime. Our work explicitly considers the role of higher bands and when they are important in quantitative analysis of this system. Applying our density of states to a degenerate Fermi gas, we consider how adiabatic loading from a harmonic trap into the combined harmonic-lattice potential affects the degeneracy temperature. Our results suggest that occupation of excited bands during loading should lead to more favorable conditions for realizing degenerate Fermi gases in optical lattices.

DOI: 10.1103/PhysRevA.75.063609 PACS number(s): 03.75.Ss, 32.80.Pj, 05.30.−d

I. INTRODUCTION

Tremendous progress has been made in the preparation, control, and manipulation of Fermi gases in the degenerate regime [1–7]. Such systems have many potential applications in the controlled study of fermionic superfluidity and the production of ultracold molecules. Another area of developing theoretical interest is in the physics of fermions in optical lattices [8–12], and experiments have already begun to examine the properties of Fermi gases (prepared as boson-fermion mixtures) in one-dimensional [13,14] and three-dimensional [15–17] optical lattices.

Optical lattices have many features in common with crystals where a periodic lattice is also present, and many of the ideas and techniques from solid-state physics have been applied to this system. A unique property of optical lattices, as realized in experiments, is that the periodic lattice is accompanied by a harmonic confining potential, arising from an external magnetic trap or from effects related to the focused laser beams used to form the lattice. We shall refer to this potential as the *combined harmonic-lattice potential*, which is the main subject of the investigation presented in this paper (see Fig. 1).

While the harmonic potential and *translationally invariant* periodic potential are well characterized individually, their properties when combined are not as well understood. Even though the harmonic trap is often much weaker than the confinement provided by each lattice site, its effect on the spectrum and properties of the system can hardly be considered small: it breaks the translational invariance of the system and changes the nature of the energy states in the deep lattice from compressed bands, to a set of unbounded overlapping bands. Several recent articles have considered aspects of this system [12,18–20]. In the context of a tightbinding model of ultracold bosons, the spectrum of the combined potential appears to have been first considered by Polkovnikov *et al.* [21]. References [18,19] have made detailed studies of the combined potential spectrum (also within a tightbinding description), and closed-form solutions to this problem were recently given by Rey *et al.* [20]. In Refs. [12,22] an ideal gas of fermions in a one-dimensional (1D) combined potential was examined without making the tightbinding approximation. All of these studies have confirmed that, for appropriate parameter regimes, parts of the single particle spectrum will contain localized states. This is in contrast to the translationally invariant system, where interatomic interactions or disorder are needed for localization to occur (e.g., see [23,24]). In the combined potential localization arises solely from single-particle effects. Experiments with ultracold (though noncondensed) bosons [25] have provided evidence for these localized states.

Many of the physical phenomena that are suitable to experimental investigation in optical lattices are sensitive to temperature and it is therefore of great interest to understand how the temperature of a quantum degenerate gas changes with lattice depth. Experimental results by Kastberg *et al.* [26] in 1995 showed that loading laser cooled atoms into a three-dimensional optical lattice caused the atoms to increase their temperature [27]. In previous work we have studied how the depth of a translationally invariant lattice affects the thermodynamic properties of quantum degenerate Bose [28] and Fermi [29] systems (also see [30–33]). The most important predictions of those studies relate to the temperature changes induced by the lattice, in particular that in appropriate regimes increasing the lattice depth could be used to cool the system. For Fermi gases this cooling effect was used to predict that loading into an optical lattice could be used to enhance the conditions for observing the superfluid transition [8]. However, recent work with a tightbinding model has

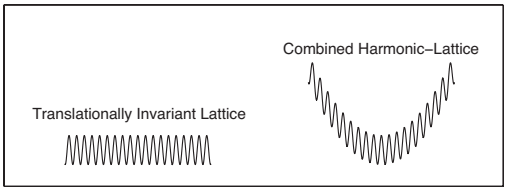

FIG. 1. Schematic diagram comparing the translationally invariant lattice to the combined harmonic lattice considered in this paper.

shown that including the effects of the harmonic potential leads to an increase in the temperature of the system (compared to the Fermi temperature) by a factor of 2 [34], demonstrating the importance of fully treating the combined potential.

In this paper we consider the thermal properties of a Fermi gas in the combined harmonic-lattice potential including the role of higher vibrational states. We derive an analytic approximation to the single-particle density of states and compare this analytic density of states to numerical solutions and determine validity criteria. We give characteristic energy and atom-number scales which can be used to predict when higher band effects will be important. Applying these density of states to a degenerate Fermi gas we consider how adiabatic loading from a harmonic trap into the combined harmonic-lattice potential affects the degeneracy temperature over a wide parameter regime. Our results show that beyond tightbinding effects provide an appreciable correction to the adiabatic loading calculations presented in Ref. [34]. Also, in the regime where higher band states are appreciably occupied, we find that the degeneracy temperature tends to increase to a lesser extent or even reduce during loading, suggesting that this regime might be useful for preparing a strongly degenerate Fermi gas in an optical lattice. Recently molecule production was used to measure the temperature of fermions in an optical lattice [15] and using this (or other approaches [35]) the predictions of our work can be examined in current experiments.

II. FORMALISM

A. Analytic density of states in the inhomogeneous lattice potential

Here we consider the properties of a system described by the single-particle Hamiltonian

$$H = -\frac{\hbar^2}{2m}\nabla^2 + V_c, \tag{1}$$

where the *combined* potential V_c is formed by an optical lattice potential and harmonic trap potential, i.e.,

$$V_c = V_h + V_l, \tag{2}$$

$$V_h = \frac{1}{2}m(\omega_x^2 x^2 + \omega_y^2 y^2 + \omega_z^2 z^2), \tag{3}$$

$$V_l = V_0[\sin^2(kx) + \sin^2(ky) + \sin^2(kz)]. \tag{4}$$

The harmonic trap is taken to be anisotropic, with angular frequencies $\{\omega_x, \omega_y, \omega_z\}$ along the coordinate directions. The lattice is of depth V_0, k is the wave vector of the counterpropagating light fields used to form the lattice, and $a=\pi/k$ is the direct lattice vector. We also use k to define the recoil frequency $\omega_R=\hbar k^2/2m$, and associated recoil energy $E_R=\hbar\omega_R$. The combined harmonic-lattice potential, as defined in Eqs. (2)–(4), has minima (i.e., lattice sites) at positions $\mathbf{r}=n_x a\hat{\mathbf{x}}+n_y a\hat{\mathbf{y}}+n_z a\hat{\mathbf{z}}$, where $\{\hat{\mathbf{x}},\hat{\mathbf{y}},\hat{\mathbf{z}}\}$ are unit vectors, and $\{n_x,n_y,n_z\}$ are integers that are convenient for labeling particular lattice sites. We note that our highly symmetric choice of the lattice potential, having a site coincident with the minimum of the harmonic potential, may be rather difficult to arrange experimentally. However, our primary interest is in the thermodynamic properties of the system which are insensitive to this symmetry.

We are interested in the limit where the lattice dominates the short-length scale properties of the system, and will take $a \ll a_{\mathrm{ho}}$, where $a_{\mathrm{ho}}=\min\{\sqrt{\hbar/m\omega_j}\}_{j=x,y,z}$ is the smallest harmonic oscillator length. This removes our need to consider systems where extremely tight harmonic confinement causes all the atoms to coalesce to a single site.

1. 1D spectrum

Viverit *et al.* [12] have shown for the one-dimensional case of Eq. (1) that when the lattice is sufficiently deep the eigenstates are localized to lattice sites. For our symmetric potential the eigenstate localized at site n will necessarily also localize at site $-n$, so strictly we should not call such states localized. However, this property is fragile to any asymmetry in the system, and has no discernible effect on the energy spectrum (which is of primary interest to us). In this regime, the lattice site index n forms a convenient quantum number for the eigenstates, specifying the site where the state is localized. The respective energy eigenvalue is given by the value of the harmonic potential at that site, i.e.,

$$\epsilon_n^{(0)} = \frac{1}{2}ma^2\omega^2 n^2, \tag{5}$$

where ω is the trap frequency and we have set to zero the zero-point energy associated with the confinement in each lattice site. We will refer to these states as *ground band* states for clarity. The condition for localization is $\Delta E(n) > J_0$, where $\Delta E(n) \equiv \epsilon_{n+1}^{(0)} - \epsilon_n^{(0)}$ is the difference in (harmonic trap) potential energy between lattice site n and $n+1$, and J_0 is the tunneling between sites [36]. This requirement is most difficult to satisfy near the trap potential minimum, where the difference in energy between adjacent sites is least. This validity condition is equivalent to

$$|n| > n_{\mathrm{crit}} \equiv q/8, \tag{6}$$

where n_{crit} is the approximately the index of the closest site to the origin for which the localization condition is satisfied and $q \equiv 8J_0/m\omega^2a^2$ is a dimensionless parameter which we discuss below (originally defined in [20]).

While states satisfying Eq. (5) are valid for sufficiently large values of n, this expression neglects the existence of excited vibrational states, which for the case of a translationally invariant lattice would correspond to the first excited band. The energy scale for the emergence of these excitations is ϵ_{gap}, and an analytic approximation for this quantity is calculated in the Appendix. Like the ground band states, these states will also localize when the difference between potential energy at neighboring sites exceeds the tunneling matrix element for the first excited band, which we denote J_1. Where this condition is satisfied the spectrum of these states will take the analytic form

$$\epsilon_n^{(1)} = \frac{1}{2}ma^2\omega^2 n^2 + \epsilon_{\text{gap}}. \tag{7}$$

For clarity we shall refer to these as the *first excited band* states. This argument could be extended to additional bands of states, in particular, at an energy of roughly $2\epsilon_{\text{gap}}$ the next vibrational states will be accessible. However, the tunneling rate J_m increases with the band index m, making the localization condition more difficult to satisfy, and analytic estimates for the energy gap to higher bands less accurate. Indeed, for single-particle energies large compared to the lattice depth the spectrum will cross over to that of a harmonic oscillator. Additionally, for typical experimental parameters, the first two bands include sufficiently many states, and a large enough energy range to provide an accurate description description of the system. Of course, high temperatures, or large lattice constants would require consideration of additional bands.

2. 3D spectrum and density of states

For more than one spatial dimension the wave-function localization may be broken by neighboring sites which have approximately the same local potential value. However, since Eq. (1) is separable, the 3D ground band spectrum is completely determined by the one-dimensional results (5) and (7), and under the assumption of localized states (see below), the ground and first excited band spectra are given by the expressions

$$\epsilon_{n_x n_y n_z}^{(0)} = \frac{1}{2}ma^2(\omega_x^2 n_x^2 + \omega_y^2 n_y^2 + \omega_z^2 n_z^2), \tag{8}$$

$$\epsilon_{n_x n_y n_z}^{(1)} = \frac{1}{2}ma^2(\omega_x^2 n_x^2 + \omega_y^2 n_y^2 + \omega_z^2 n_z^2) + \epsilon_{\text{gap}}, \tag{9}$$

respectively. Because of the lattice symmetry, there are three equivalent (and completely overlapping) first excited bands. Thus each energy state specified by the quantum numbers $\{n_x, n_y, n_z\}$ in Eq. (9) is threefold degenerate [37]. This degeneracy would be broken if the lattice depth was different in each direction causing the first excited bands to separate in energy, but we do not consider that case here. The separability of the potential means that the validity conditions discussed for the one-dimensional case apply immediately, using the respective trap frequency in each direction, i.e., $n_j > n_{\text{crit}}^{(j)}$, $j=x,y,z$, where $n_{\text{crit}}^{(j)}$ is n_{crit} evaluated according to Eq. (6) using the trap frequency along direction j.

The density of states for the spectra in Eqs. (8) and (9) is given by

$$g_c(\epsilon) = \frac{16}{\pi^2}\left(\frac{\omega_R}{\bar{\omega}}\right)^{3/2}\frac{\epsilon^{1/2}}{(\hbar\bar{\omega})^{3/2}} + \frac{48}{\pi^2}\left(\frac{\omega_R}{\bar{\omega}}\right)^{3/2}\frac{(\epsilon-\epsilon_{\text{gap}})^{1/2}}{(\hbar\bar{\omega})^{3/2}}\theta(\epsilon-\epsilon_{\text{gap}}), \tag{10}$$

where $\theta(x)$ is the unit step function, and $\bar{\omega} \equiv \sqrt[3]{\omega_x\omega_y\omega_z}$. The first term, corresponding to the ground band contribution to the density of states, exhibits a $\sqrt{\epsilon}$ scaling with energy, similar to that of a homogeneous gas of free particles [34]. The second term includes the contribution of the first excited band states that occur at energies $\epsilon > \epsilon_{\text{gap}}$. As was noted in our discussion of the validity conditions of the spectra, additional bands will become accessible at $\epsilon \sim 2\epsilon_{\text{gap}}$, and so Eq. (10) should only be used in situations where $k_B T$ and the Fermi energy are much less than $2\epsilon_{\text{gap}}$.

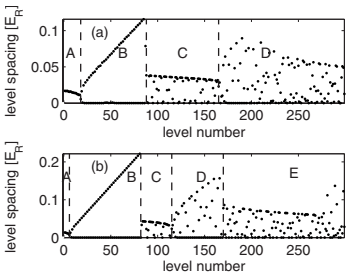

FIG. 2. Energy level spacing for the 1D eigenspectrum relevant to the experimental setup in Ref. [16]. (a) $V_0=5E_R$, $\omega=0.024\omega_R$. (b) $V_0=10E_R$, $\omega=0.033\omega_R$. Parameters derived for ^{40}K with lattice made from counter propagating $\lambda=826$ nm lasers with harmonic confinement arising from the focused lasers (beam waist taken to be 50 μm). Labels $A-E$ explained in text.

B. Numerical results for single-particle spectrum

1. 1D spectrum

Here we show some typical results of the 1D spectrum of the combined potential in Fig. 2. In Refs. [18–21] a detailed analysis of the spectrum has also been made, but in the tight binding (Hubbard) limit where only the vibrational ground state of each lattice site are included. Those studies considered a wide parameter regime of trapping frequencies and lattice depths, however in the tight-binding limit a single parameter describing the ratio of tunneling to harmonic potential is sufficient to characterize the nature of the eigenspectrum. Several choices of parameter are used in the literature, and we follow the choice of Rey *et al.* [20] who define $q \equiv 4J_0/(\frac{1}{2}m\omega^2a^2)$. With the inclusion of higher bands this single parameter by itself is insufficient to characterize the spectrum and both the lattice depth and harmonic confinement parameters are independently important. In Fig. 2 we show the level spacing obtained from numerical diagonalization of the one-dimensional case of Eq. (1). The parameters for this calculation were taken to correspond to those of the experiment [16]. For Fig. 2(a) with $V_0=5E_R$ we find that $q \approx 193$ and for Fig. 2(b) with $V_0=10E_R$ we find that $q \approx 28$. It is useful to compare our results to Fig. 1(b) of Ref. [19] to assess the effects of higher band states on the spectrum. We have segmented our spectrum with vertical dashed lines and indicated the characteristic regions by the letters $A-E$, which we explain: In region A tunneling dominates over the offset between lattice sites and the eigenstates are delocalized [for these states Eq. (5) will be a poor approximation]. In region B localized states emerge which are approximately degenerate in energy (the spacing between every

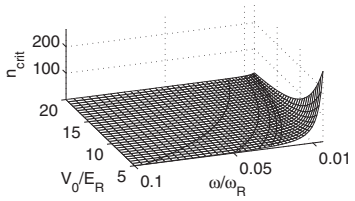

FIG. 3. The critical site number for localization, as defined in Eq. (6), as a function of lattice depth and harmonic trap frequency. Contour lines are shown for $n_{\mathrm{crit}}=1$, 3, 5, and 7.

second eigenvalue is approximately zero). Because of the localizations [and applicability of Eq. (5)], the energy spacing between degenerate pairs increases linearly throughout this region. Regions A and B, as identified in Fig. 2, are equivalent to those in Fig. 1(b) of Ref. [19], and in general we find that the tightbinding description is in good qualitative agreement with our more general analysis. For the next regions (i.e., C, D, etc.) the role of higher bands is essential and cannot be described within a simple tightbinding model. Region C has a similar appearance to region A, and consists of delocalized excited band states. The scatter in level spacing seen in C occurs because ground band states are also available in this energy range. In region D the excited bands state have become localized (similar to what happened in region B to the ground band states). In region E we have reached a sufficiently high energy scale that a third band of states have begun to contribute.

The harmonic confinement used in Fig. 2 originates from the dipole confinement provided by the focused lasers used to make the lattice [38], and as the lattice depth increases so does the strength of harmonic confinement. We note that for Fig. 1(b) of [19], $q \approx 13 \times 10^6$, which is many orders of magnitude away from that found in current experiments [39]. The number of states in region A roughly scales as $\sqrt{q}$ [20] so that in experimentally realized lattices region A is quite small and the majority of ground band states are well localized.

2. Critical site index

In Fig. 3 we present n_{crit} (6) for a wide range of lattice depths and trap frequencies (note that we have used band structure calculations in a translationally invariant lattice to determine J_0 for each value of V_0). We observe that n_{crit} is large for small trap frequencies and shallow lattices so that only neighboring lattice sites quite far from the harmonic trap minimum have a sufficiently large potential difference to tunneling ratio to cause eigenstate localization. In such cases the analytic approximation for the eigenspectra given in Eqs. (8) and (9), and density of states given in Eq. (10) will not be valid, and the result of the full numerical diagonalization will be necessary.

With increasing lattice depth the ground band tunneling matrix element decreases and the potential difference to tunneling ratio increases. Thus we find that n_{crit} decreases with increasing V_0. Similarly, increasing the harmonic trap frequency also leads to a decrease in n_{crit}. The particular value of n_{crit} that justifies the use of our analytic density of states

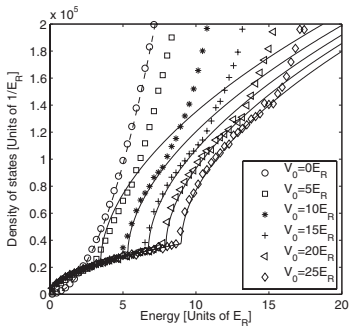

FIG. 4. Density of states for $\bar{\omega}=0.051\omega_R$. Numerical results for the density of states are shown using various markers (as labeled in the figure). The analytic density of states given in Eq. (10) is plotted for the cases with $V \geqslant 5E_R$ (solid line), using the expression $\epsilon_{\mathrm{gap}} = 2\sqrt{V_0 E_R} - E_R$ for the band gap energy. The harmonic oscillator density of states is also shown (dashed line). The averaging interval used for the smoothed density of states is $\Delta\epsilon=0.303E_R$.

(10) depends on the parameters of system under consideration. If the system extends over N_s lattice sites in each direction, then $n_{\mathrm{crit}} \ll N_s$ will be sufficient to ensure that the majority of the occupied states are well described by the localized spectrum.

3. Density of states

Equation (10) for the density of states in the combined potential is one of the central results of this paper. In this section we present numerical results to confirm the validity regime of this expression. To do this we diagonalize Eq. (1) to obtain the single particle eigenspectrum $\{\epsilon_j\}$ for various trap frequencies and lattice depths. For the purposes of comparison to the analytic results, it is useful to construct a smoothed density of states, defined as

$$\bar{g}(\epsilon) = \frac{1}{2\Delta\epsilon} \int_{\epsilon-\Delta\epsilon}^{\epsilon+\Delta\epsilon} \sum_j \delta(\epsilon - \epsilon_j), \tag{11}$$

giving the average number of eigenstates with energy lying within $\Delta\epsilon$ of ϵ.

In Fig. 4 we compare the numerically calculated smoothed density of states against the analytic result $g_c(\epsilon)$ for various lattice depths in an isotropic trap of frequency $\bar{\omega}=0.051\omega_R$. Agreement between the analytic and numerical calculations is seen to improve as the lattice depth increases. We also observe that at energies greater than approximately twice the gap energy the analytic and numerical results begin to differ more significantly as the contribution of additional bands become important (the gap energy in each case is the energy at which the cusp in the analytic density of states occurs).

It is of interest to more closely examine the reliability of the analytic density of states at low energy scales and for weak harmonic traps. In Fig. 5 we show such a comparison for an isotropic trap of frequency $\bar{\omega}=0.01\omega_R$. For $V_0=4E_R$

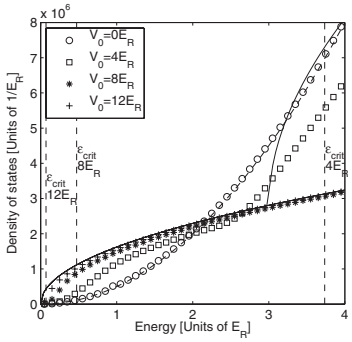

FIG. 5. The density of states for a combined harmonic trap and lattice in the loose trap limit. Isotropic harmonic trap with trap frequency $\bar{\omega}=0.01\omega_R$. The critical energy, given by $\epsilon_{\rm crit}=m\bar{\omega}^2a^2n_{\rm crit}^2/2$, is shown as a dashed vertical line and labeled by its corresponding lattice depth. The averaging interval used for the smoothed density of states is $\Delta\epsilon=0.10E_R$.

the analytic result is in poor agreement with the numerical result, as the low energy states in this case are not localized. For $V_0=8E_R$ and more so $V_0=12E_R$, the analytic result is seen to provide a useful description of the numerical density of states. To quantify the degree of agreement seen in these results it is useful to consider the energy of the (first) localized state at site $n\approx n_{\rm crit}$, i.e., $\epsilon_{\rm crit}=m\bar{\omega}^2a^2n_{\rm crit}^2/2$, indicated as vertical dashed lines in Fig. 5. The quantity $\epsilon_{\rm crit}$ is the energy scale above which the ground band states become localized, and hence the lowest energy at which spectrum (5) is valid. For the case of $V_0=4E_R$, $\epsilon_{\rm crit}$ exceeds $\epsilon_{\rm gap}$ so that no states in the ground band are localized below the energy scale at which excited band states become accessible. For the case of $V_0=8E_R$, $\epsilon_{\rm crit}\simeq 0.5E_R$ and for energies above this better agreement between the analytic and numerical results is observed in Fig. 5. For $V_0=12E_R$ the critical energy is $\epsilon_{\rm crit}\simeq 0.07E_R$ and the analytic density of states furnishes better agreement at much lower energies.

In summary, we make the following observations about our analytic expression for the density of states:

(1) Within its regime of validity, the analytic density of states provides an accurate description at intermediate energy scales, i.e., at energies above $\epsilon_{\rm crit}$ where the spectrum is well localized, yet below $\epsilon\sim 2\epsilon_{\rm gap}$, where additional bands become accessible.

(2) The agreement between the analytic density of states and numerical calculations improves with increasing lattice depth and increasing trap frequency.

III. APPLICATIONS TO FERMI GASES

A. General properties

The Fermi energy in the combined harmonic-lattice potential, $\epsilon_{F,c}$, is determined from the number of particles in the system according to

$$N=\int_0^{\epsilon_{F,c}} d\epsilon g_c(\epsilon). \tag{12}$$

To compute the Fermi energy from our analytic result (10) it is convenient to define the *cusp number* [40] N_c as the number of particles for which $\epsilon_{F,c}=\epsilon_{\rm gap}$. Because the energy gap depends on the lattice depth, so does N_c. Using Eqs. (10) and (12) we obtain

$$N_c=\frac{32}{3\pi^2}\left(\frac{\omega_R}{\bar{\omega}}\right)^{3/2}\left(\frac{\epsilon_{\rm gap}}{\hbar\bar{\omega}}\right)^{3/2}. \tag{13}$$

For $N<N_c$ (i.e., $\epsilon<\epsilon_{\rm gap}$) only the first term in the density of states (10) is nonzero in Eq. (12) and we can invert to obtain the Fermi energy

$$\epsilon_{F,c}=\left(\frac{3\pi^2N}{32}\right)^{2/3}\frac{\hbar\bar{\omega}^2}{\omega_R},\quad N<N_c. \tag{14}$$

For $N>N_c$ excited band states contribute. In this case a general analytic expression for the Fermi energy in terms of N is not available, but for $(N-N_c)\ll N_c$ we make a series expansion of the integral of the density of states about $\epsilon_{\rm gap}$. This expression can then be solved perturbatively to yield the approximate expression

$$\epsilon_{F,c}=\epsilon_{\rm gap}\left\{1+\delta-\frac{2\delta^{3/2}}{1+3\delta^{1/2}}\right\},\quad 0<\delta\ll 1, \tag{15}$$

where $\delta\equiv 2(N-N_c)/3N_c$ is the small parameter.

It is also convenient to define the *cusp depth* V_c, as the lattice depth at which $\epsilon_{F,c}=\epsilon_{\rm gap}$. The cusp depth is a function of the number of particles and harmonic trap frequency, given by

$$V_c=\frac{\hbar\omega_R}{4}\left[\left(\frac{3\pi^2N}{32}\right)^{2/3}\left(\frac{\bar{\omega}}{\omega_R}\right)^2+1\right]^2, \tag{16}$$

where we have made use of the analytic expression relating $\epsilon_{\rm gap}$ to V_0, as derived in the Appendix.

The two cusp parameters characterize the interesting features of the combined harmonic-lattice system and can be interpreted as follows:

(i) N_c: For a system with fixed combined potential (i.e., fixed V_0, $\{\omega_j\}$), N_c is the maximum number of atoms that can be accommodated in the ground band only. For $N>N_c$, the $T=0$ ground state of the system will contain excited band states.

(ii) V_c: For a system with fixed atom number and harmonic trap frequencies, V_c is the smallest lattice depth for which the atoms can be accommodated in the ground band. For $V_0<V_c$, the $T=0$ ground state of the system will contain excited band states.

These parameters motivate us to emphasize the distinctive properties of the energy spectrum in the combined potential as compared to the usual periodic lattice case. In the translationally invariant lattice, there is a fixed number of single-particle states in each band (equal to the number of lattice sites), and for sufficiently deep lattices (typically $V_0\gtrsim 2E_R$) the ground and first excited bands occupy disjoint energy regions separated by a finite energy gap. In contrast, for the combined harmonic-lattice potential, the energy bands are overlapping and can only be differentiated by the local nodal structure of the wave functions at each site, where they have a spatial character approximately given by harmonic oscilla-

tor states (see the Appendix). This local structure of the wave functions is apparent in experiment, and leads to states of different bands (as we have defined them here) residing in distinctive regions of momentum space in expansion images (e.g., see Refs. [16,41]). If it is desirable to restrict the system to access only states of the ground band, so as to realize a system well described by a Hubbard model, then according to our above prescription this necessarily requires $N<N_c$ or equivalently $V_0>V_c$, in addition to having sufficiently low temperature.

B. Sommerfeld analysis of isentropic loading of a degenerate Fermi gas

The properties of a quantum degenerate Fermi gas can be approximated by the Sommerfeld expansion (e.g., see [42]). Of particular interest is the expression for entropy $S=\frac{\pi^2}{3}g(\epsilon_F)k_B^2T$, valid for $T\ll T_F$, where $g(\epsilon_F)$ is the density of states evaluated at the Fermi energy, ϵ_F. For many applications to Fermi gas experiments, the parameter of most interest is the degeneracy parameter $t\equiv k_BT/\epsilon_F$, i.e., the ratio of the temperature to the Fermi temperature, for which the Sommerfeld expression can be written as

$$S=\frac{\pi^2}{3}\epsilon_F g(\epsilon_F)k_B t. \tag{17}$$

Here we consider the change in degeneracy temperature of a Fermi gas as it is slowly loaded from a harmonic trap into the combined harmonic-lattice potential, as is done in experiments. To characterize this temperature change we assume that the loading is *isentropic* so that the initial entropy in the harmonic potential (with initial degeneracy temperature t_i) is the same as the final entropy when the system is in the combined harmonic-lattice potential (with final degeneracy temperature t_f). Within the validity regime of the Sommerfeld relation (17), the ratio of these temperatures is given by

$$\frac{t_f}{t_i}=\frac{\kappa_h(N)}{\kappa_c(N)},\quad t_i,t_f\ll 1, \tag{18}$$

obtained by assuming that S remains constant, where we have introduced the dimensionless extensive parameter $\kappa_x(N)\equiv\epsilon_{F,x}g_x(\epsilon_{F,x})$ $(x=h,c)$, with $g_h(\epsilon)$ and $\epsilon_{F,h}$ the density of states and Fermi energy for a harmonic trap, respectively. We have chosen to express κ as a function of N rather than ϵ_F, since the number of atoms remains constant during the loading procedure, whereas the Fermi energy may change significantly.

For the purely harmonic trap $g_h(\epsilon)=\epsilon^2/(2\hbar^3\bar{\omega}^3)$ and $\epsilon_{F,h}=\hbar\bar{\omega}(6N)^{1/3}$ (e.g., see [43]), which give

$$\kappa_h(N)=3N. \tag{19}$$

For $N<N_c$, the excited band states do not contribute to κ_c and using results (10) and (14) we obtain

$$\kappa_c(N)=\frac{3}{2}N,\quad N<N_c. \tag{20}$$

Thus for $N<N_c$, the ratio of degeneracy temperatures will increase by a factor of 2. Because N_c is a monotonically increasing function of V_0, it might be expected that for sufficiently deep final lattice depth we will always obtain this factor of 2 increase in the degeneracy temperature. However, N_c decreases with increasing $\bar{\omega}$, and since $\bar{\omega}$ may change with lattice depth (e.g., if the lattice is produced by focused lasers) a large final lattice depth may in fact lead to $N>N_c$. We also note that when $N<N_c$ the ratio of the degeneracy temperatures (18) is independent of the harmonic trap frequency, even if this parameter changes during the loading [44]. Similar conclusions to those presented in this section are given in Ref. [34].

C. Numerical results for isentropic loading of the combined harmonic lattice

In this section we numerically examine the temperature of an ideal Fermi gas loaded into a combined harmonic-lattice potential for a range of lattice depths. Our main results are calculated using the energy spectrum found by numerically diagonalizing (1). To determine the temperature under this type of loading we calculate the entropy of a gas of N fermions over a range of temperatures and lattice depths, i.e., $S(T,V_0,\vec{\omega},N)$, where $\vec{\omega}=\{\omega_x,\omega_y,\omega_z\}$. We numerically invert this function to find temperature as a function of the other quantities $T(S,V_0,\vec{\omega},N)$, and by examining the behavior of T for fixed S, we can predict the temperature of the gas as a function of lattice depth.

Our procedure for determining entropy is as follows: The single particle spectrum $\{\epsilon_j\}$ of the lattice is calculated for given values of $\vec{\omega}$ and V_0. We then calculate the partition function $\mathcal{Z}$

$$\ln\mathcal{Z}=\sum_j \ln(1+e^{-\beta(\epsilon_j-\mu)}), \tag{21}$$

where μ is found by ensuring particle conservation. The entropy of the system can then be expressed as

$$S=k_B(\ln\mathcal{Z}+\beta E-\mu\beta N), \tag{22}$$

where $\beta=1/k_BT$, and $E=-\partial\ln\mathcal{Z}/\partial\beta$ is the mean energy.

In Figs. 6(a)–6(f) we show the properties of an isentropically loaded gas for various parameters. In Figs. 6(a) and 6(c) we show the ratio of the final to initial reduced temperatures for $N=50\times10^3$ and $N=250\times10^3$, respectively. In both cases, the reduced temperature is seen to increase as the lattice depth increases. For $N=50\times10^3$ atoms the critical lattice depth is $V_c\approx2.3E_R$. For the lowest initial reduced temperature [i.e., the frontmost curve in Fig. 6(a)] we see that the reduced temperature increases by a factor of 2 by the time that V_0 increases beyond V_c, in agreement with the predictions of Eqs. (18)–(20) (also see Ref. [34]). Similarly, for the case of $N=250\times10^3$ atoms, $V_c\approx12.4E_R$ and for the lowest temperature result in Fig. 6(c), we see that the reduced temperature increases by a factor of 2 as V_0 increases beyond this value of V_c. For higher initial temperatures the Sommerfeld result does not hold. In Figs. 6(a) and 6(c) we see that the warmer systems (larger t_i values) have the contrasting behavior of heating up more or less than the Sommerfeld prediction, respectively. In that regime the degeneracy temperature is dominated by the change in the Fermi energy that

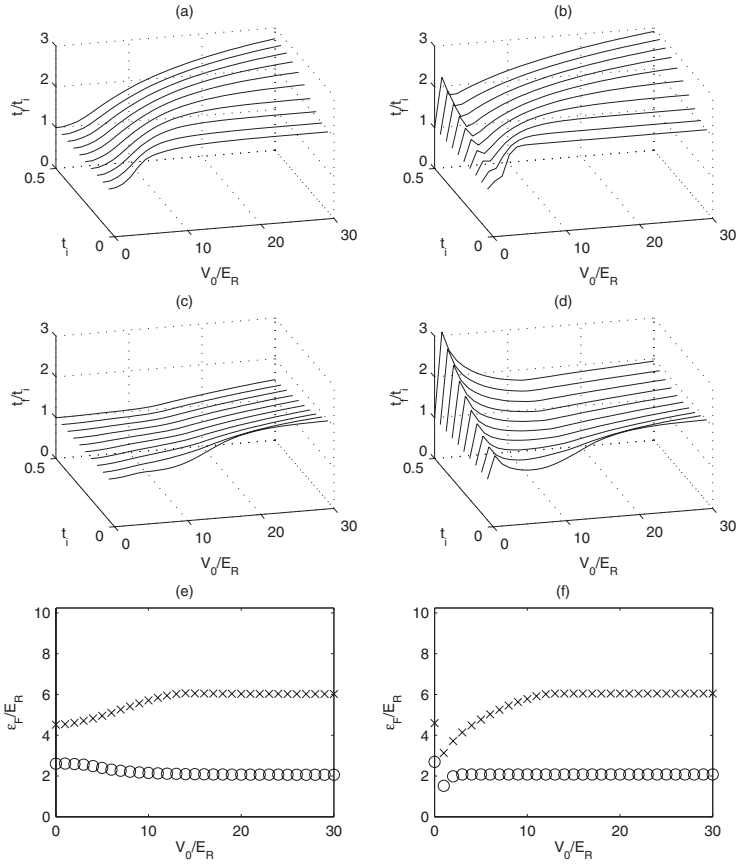

FIG. 6. Temperature of an ideal Fermi gas isentropically loaded into a combined harmonic-lattice potential. The ratio of the final degeneracy temperature (after loading) to the initial degeneracy temperature in the harmonic trap are shown for various initial temperatures and lattice depths for the case (a) $N=50\times10^3$ and (c) $N=250\times10^3$. In (e) the Fermi energy is shown as a function of lattice depth for $N=50\times10^3$ (circles), $N=250\times10^3$ (crosses). (b), (d), and (f) correspond to (a), (c), and (e), respectively, but are calculated using the analytic density of states (10). For all results we have used an isotropic harmonic trap of frequency of $\bar{\omega}=0.04\omega_R$.

occurs during the lattice loading procedure, as shown in Fig. 6(e). That is, for the case in Fig. 6(a) [6(c)] the Fermi energy tends to decrease [increase] with increasing lattice depth.

In Fig. 6(c) [and to a lesser extent in Fig. 6(a)] we see that while excited bands are occupied (i.e., for $V<V_c$) the degeneracy temperature increases by a factor of less than 2. This suggests that having excited bands occupied might provide more favorable conditions for investigating fermionic superfluidity in lattices. Additionally, because the tunneling rate is larger for higher bands it may be more easy to reversibly manipulate the lattice in this regime.

In Figs. 6(b), 6(d), and 6(f) we show the results equivalent to those in Figs. 6(a), 6(c), and 6(e), but calculated using the analytic density of states given in Eq. (10). Qualitatively the agreement between the results is good for $V_0\gtrsim4E_R$. The main discrepancy is observed for small V_0 values where the role of nonlocalized states and higher bands is important.

IV. RELATION TO EXPERIMENTS

It is of interest to compare how important excited band effects might be for current experiments. In Fig. 7 we show N_c for parameters similar to those used in recent experiments by the ETH Zürich group [15,16]. In those experiments up to 10^5 atoms were prepared in each spin state. Because the harmonic confinement increases with lattice depth ($\bar{\omega}\sim\sqrt{V_0E_R}/\hbar$), we find that the Fermi energy will eventually lie in the first excited band, but only for very large lattice depths ($V_0\gtrsim280E_R$). We also consider a longer wavelength lattice made from lasers with $\lambda=1200$ nm with slightly tighter focus (beam waist of 50 μm) for which the recoil energy and the gap to higher bands is smaller. In such a configuration (dashed curve) we see that higher bands would become important for much lower atom numbers.

In Fig. 8 we consider the effect of loading on the degeneracy temperature for parameters relevant to the experiment in Ref. [15]. The results in Fig. 8(a) are for the same parameters considered by Köhl who made a calculation in the tightbinding limit (see Fig. 1 of Ref. [34]). We broadly find agreement with those results, however, make note of several differences. First, at the lowest depths considered ($V_0\sim5E_R$) Köhl observed the reduced temperature to initially decrease with increasing lattice depth. In contrast our results,

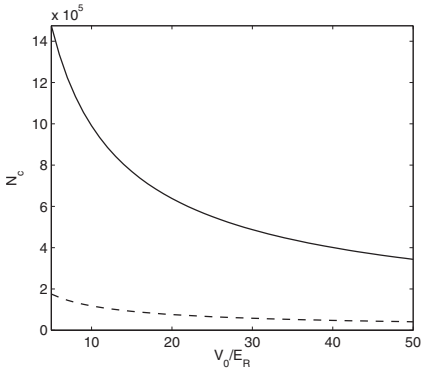

FIG. 7. N_c for the case of ^{40}K in a lattice formed by focused lasers (solid) $\lambda=826$ nm with 70 μm waist, (dashed) $\lambda=1200$ nm with 50 μm waist.

which are valid for all lattice depths, do not exhibit this feature, and instead are seen to smoothly connect with the $V_0=0E_R$ (purely harmonic case). We conclude that in this region the tightbinding approximation and the neglect of higher bands is not valid.

Second, in Köhl's results the reduced temperature is observed to saturate to a value of twice that of the initial harmonic trap when the lattice is sufficiently deep (typically $V_0 \gtrsim 15E_R$). Many of our high temperature curves instead show a slight decrease in reduced temperature as the depth of the lattice increases. We have verified that this behavior is due to higher band states, and that if we neglect them from our calculations our results saturate in agreement with those in [34]. This indicates that even when the deep lattice behavior is dominated by the ground band (i.e., we have $N<N_c$), if a small number of atoms are able to thermally access excited band states they can have a significant effect on the temperature of the system during loading.

In Fig. 8(b) the same parameters are used, except the number of atoms is increased to 750 000. According to Fig. 7 for this number of atoms $V_c \approx 15E_R$. In this case we see that only a small increase in the degeneracy temperature occurs during loading and ultimately for sufficiently large final lattice depth (i.e., $V_0 \gtrsim 20E_R$) the reduced temperature is observed to be approximately the same as in the initial harmonic trap. We note that this result requires the occupation of higher bands and cannot be analyzed using a tightbinding approach.

The discussion in this section shows that while current experiments are likely not strongly affected by higher bands, the parameter regime where they become important is rather close. Experiments could enter this regime by using larger wavelength lattices or tighter harmonic confinement (e.g., more tightly focused lasers to produce the optical lattice).

V. CONCLUSIONS

We have discussed the nature of the spectrum of a Fermi gas in a combined harmonic trap and optical lattice potential.

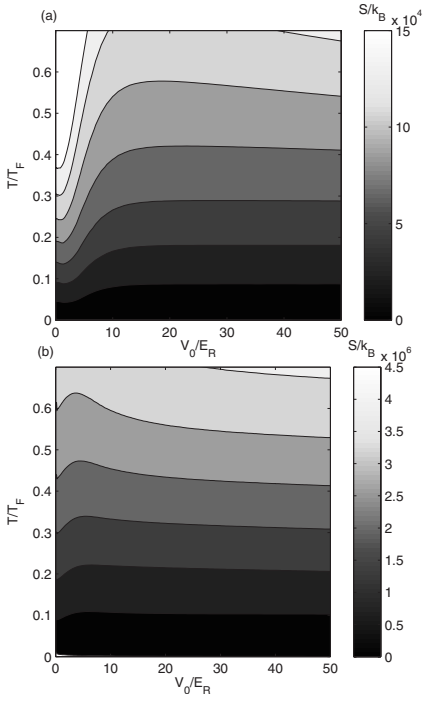

FIG. 8. Degeneracy temperature for isentropic loading of ^{40}K into an optical lattice. (a) $N=50\,000$ and (b) $N=750\,000$. Parameters correspond to solid line in 7. Additional harmonic confinement of frequency $\omega=0.005\omega_R$ is superimposed on the confinement due to the focused beam waist to make the spectrum well behaved as $V_0 \to 0$.

Using this spectrum we have derived an analytic density of states that is relatively accurate for the lattice depths and harmonic confinements used in experiments. We have characterized the validity criteria for this density of states and have used it to characterise a Fermi gas in the combined potential. As an application we have examined how adiabatic loading from a harmonic trap into the combined harmonic-lattice potential affects the degeneracy temperature of an ideal Fermi gas. Our results show that when excited band states are occupied the system is less heated by the lattice loading, and may be less sensitive to nonadiabatic effects, suggesting that this regime is worthy of further investigation in experiments.

ACKNOWLEDGMENTS

P.B.B. would like to acknowledge useful discussions with M. Köhl and support from the Marsden Fund of New Zealand. P.B. acknowledges a grant from the *Lagrange Project*-CRT Foundation and is grateful to the Jack Dodd Centre for the warm hospitality.

APPENDIX: ANALYTIC APPROXIMATION TO BAND-GAP ENERGY

In this section we derive an analytic expression for the band gap in deep lattices. We go beyond the usual harmonic oscillator approximation and obtain results equivalent to those used in Ref. [45].

We will consider the standard harmonic approximation the optical lattice potential, by making a Taylor expansion about the lattice site minimum at $x=0$, i.e.,

$$V_l = \frac{V_0}{2}[1-\cos(bx)] \approx \frac{V_0 b^2}{4}x^2 - \frac{V_0 b^4}{48}x^4, \qquad \text{(A1)}$$

where $b=2k$ is the reciprocal lattice vector.

Casting the harmonic term in the form of a harmonic oscillator potential, $1/2m\omega_{\mathrm{Latt}}^2 x^2$, yields the effective harmonic oscillator frequency of $\omega_{\mathrm{Latt}}=\sqrt{V_0 b^2/2m}$, and the localized states in the optical lattice can be approximated as harmonic oscillator states. This approximation neglects the influence of tunneling between sites that gives a quasimomentum dependence, and predicts that the band gap is equal to $\hbar\omega_{\mathrm{Latt}}$. For our purposes it is desirable to go beyond this approximation and obtain a more accurate analytic expression for the band-gap energy. To do this we use the harmonic oscillator states to treat the quartic term in Eq. (A1) perturbatively. This is most easily done using the normal ladder operators, so that $x^4=\left(\frac{\hbar}{2m\omega_{\mathrm{Latt}}}\right)^2(a^\dagger+a)^4$, which gives the first-order shifts in the oscillator state energies as

$$\Delta E_n = -\frac{E_R}{4}(2n^2+2n+1). \qquad \text{(A2)}$$

Thus the approximate energies of the localized states are given by

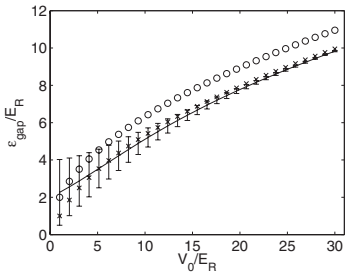

FIG. 9. Comparison between numerically determined energy gap for a 1D sinusoidal lattice (solid), with the upper and lower limits corresponding to the band gap at the center and the edge of the Brillouin Zone. The harmonic approximation, $\hbar\omega_{\mathrm{Latt}}=2\sqrt{V_0 E_R}$ (circles) and the estimate treating the quartic expansion perturbatively, $\epsilon_{\mathrm{gap}}=2\sqrt{V_0 E_R}-E_R$ (crosses).

$$E_n = \left[2\sqrt{\frac{V_0}{E_R}}(n+1/2) - \frac{1}{4}(2n^2+2n+1)\right]E_R. \qquad \text{(A3)}$$

Of most interest is the difference in energy between the $n=0$ and $n=1$ states, which provides an estimate of the energy gap between the ground and first excited bands, i.e.

$$\epsilon_{\mathrm{gap}} = 2\sqrt{V_0 E_R} - E_R. \qquad \text{(A4)}$$

We see that treating the quartic term leads to a 1 recoil suppression of the band gap compared to the harmonic oscillator frequency. In Fig. 9 we compare this analytical expression with the band gap determined numerically by evaluating the full band structure of the $\frac{V_0}{2}[1-\cos(bx)]$ potential. For shallow lattices the band gap is strongly dependent on the value of quasimomenta considered and error bars indicate the range of energy gaps from band center to band edge.

[1] B. DeMarco and D. S. Jin, Science **285**, 1703 (1999).
[2] F. Schreck, L. Khaykovich, K. L. Corwin, G. Ferrari, T. Bourdel, J. Cubizolles, and C. Salomon, Phys. Rev. Lett. **87**, 080403 (2001).
[3] K. M. O'Hara, S. L. Hemmer, M. E. Gehm, S. R. Granade, and J. E. Thomas, Science **298**, 2179 (2002).
[4] G. Modugno, G. Roati, F. Riboli, F. Ferlaino, R. J. Brecha, and M. Inguscio, Science **297**, 2240 (2002).
[5] S. Gupta, Z. Hadzibabic, M. W. Zwierlein, C. A. Stan, K. Dieckmann, C. H. Schunck, E. G. M. van Kempen, B. J. Verhaar, and W. Ketterle, Science **300**, 1723 (2003).
[6] C. A. Regal, C. Ticknor, J. L. Bohn, and D. S. Jin, Nature (London) **424**, 47 (2003).
[7] J. Cubizolles, T. Bourdel, S. J. J. M. F. Kokkelmans, G. V. Shlyapnikov, and C. Salomon, Phys. Rev. Lett. **91**, 240401 (2003).
[8] W. Hofstetter, J. I. Cirac, P. Zoller, E. Demler, and M. D. Lukin, Phys. Rev. Lett. **89**, 220407 (2002).
[9] P. Rabl, A. J. Daley, P. O. Fedichev, J. I. Cirac, and P. Zoller, Phys. Rev. Lett. **91**, 110403 (2003).
[10] L. Santos, M. A. Baranov, J. I. Cirac, H.-U. Everts, H. Fehrmann, and M. Lewenstein, Phys. Rev. Lett. **93**, 030601 (2004).
[11] M. Rigol and A. Muramatsu, Phys. Rev. A **69**, 053612 (2004a).
[12] L. Viverit, C. Menotti, T. Calarco, and A. Smerzi, Phys. Rev. Lett. **93**, 110401 (2004).
[13] G. Modugno, F. Ferlaino, R. Heidemann, G. Roati, and M. Inguscio, Phys. Rev. A **68**, 011601(R) (2003).
[14] H. Ott, E. de Mirandes, F. Ferlaino, G. Roati, G. Modugno, and M. Inguscio, Phys. Rev. Lett. **92**, 160601 (2004).
[15] T. Stöferle, H. Moritz, K. Günter, M. Köhl, and T. Esslinger, Phys. Rev. Lett. **96**, 030401 (2006).
[16] M. Köhl, H. Moritz, T. Stöferle, K. Günter, and T. Esslinger, Phys. Rev. Lett. **94**, 080403 (2005).
[17] S. Ospelkaus, C. Ospelkaus, O. Wille, M. Succo, P. Ernst, K. Sengstock, and K. Bongs, Phys. Rev. Lett. **96**, 180403 (2006).
[18] C. Hooley and J. Quintanilla, Phys. Rev. Lett. **93**, 080404 (2004).
[19] M. Rigol and A. Muramatsu, Phys. Rev. A **70**, 043627 (2004).

[20] A. M. Rey, G. Pupillo, C. W. Clark, and C. J. Williams, Phys. Rev. A **72**, 033616 (2005).
[21] A. Polkovnikov, S. Sachdev, and S. M. Girvin, Phys. Rev. A **66**, 053607 (2002).
[22] V. Ruuska and P. Törmä, New J. Phys. **6**, 59 (2004).
[23] D. Jaksch, C. Bruder, J. I. Cirac, C. W. Gardiner, and P. Zoller, Phys. Rev. Lett. **81**, 3108 (1998).
[24] P. Buonsante, V. Penna, A. Vezzani, and P. Blakie e-print arXiv:cond-mat/0610476 (to be published).
[25] H. Ott, E. de Mirandes, F. Ferlaino, G. Roati, V. Türck, G. Modugno, and M. Inguscio, Phys. Rev. Lett. **93**, 120407 (2004).
[26] A. Kastberg, W. D. Phillips, S. L. Rolston, R. J. C. Spreeuw, and P. S. Jessen, Phys. Rev. Lett. **74**, 1542 (1995).
[27] In fact this study used adiabatic deloading to reduce the temperature of the constituent atoms.
[28] P. B. Blakie and J. V. Porto, Phys. Rev. A **69**, 013603 (2004).
[29] P. B. Blakie and A. Bezett, Phys. Rev. A **71**, 033616 (2005).
[30] F. Werner, O. Parcollet, A. Georges, and S. R. Hassan, Phys. Rev. Lett. **95**, 056401 (2005).
[31] A. M. Rey, G. Pupillo, and J. V. Porto, Phys. Rev. A **73**, 023608 (2006).
[32] T.-L. Ho and Q. Zhou e-print arXiv:cond-mat/0703169 (to be published).
[33] P. B. Blakie, A.-M. Rey, and A. Bezett, Laser Phys. **17**, 198 (2007).
[34] M. Köhl, Phys. Rev. A **73**, 031601(R) (2006).
[35] For example, Bragg and Raman spectroscopy is sensitive to temperature and fluctuation effects for bosons in optical lattices [A.-M. Rey, P. B. Blakie, G. Pupillo, C. J. Williams, and C. W. Clark, Phys. Rev. A **72**, 023407 (2005); P. B. Blakie, New J. Phys. **8**, 157 (2006)]. We expect that generalizations of these probing schemes to fermions will also be useful for measuring temperature.
[36] We determine J_0 using band structure calculations, see P. B. Blakie and C. W. Clark, J. Phys. B **37**, 1391 (2004).
[37] This is in addition to the degeneracy arising from spatially equivalent lattice sites, e.g. for $\{n_x,n_y,n_z\}$ all non-zero there are 8 states of the same energy found by taking $\{\pm n_x,\pm n_y,\pm n_z\}$.
[38] The harmonic frequency is given by $\omega=\sqrt{8V_0/mw^2}$ where w is the beam waist (also see [33]).
[39] We calculate that $q=13\times10^6$ roughly corresponds to a $V_0=4E_R$ deep lattice and harmonic confinement of oscillator frequency 0.8 Hz.
[40] So named, because the corresponding Fermi energy sits at the cusp in the analytic density of states (e.g., see Fig. 4).
[41] J. H. Denschlag, J. E. Simsarian, H. Häffner, C. McKenzie, A. Browaeys, D. Cho, K. Helmerson, S. L. Rolston, and W. D. Phillips, J. Phys. B **35**, 3095 (2002).
[42] K. Huang, *Statistical Mechanics* (Wiley, New york, 1967).
[43] D. A. Butts and D. S. Rokhsar, Phys. Rev. A **55**, 4346 (1997).
[44] However, the absolute temperature does depend on the trap frequency.
[45] I. B. Spielman, P. R. Johnson, J. H. Huckans, C. D. Fertig, S. L. Rolston, W. D. Phillips, and J. V. Porto, Phys. Rev. A **73**, 020702(R) (2006).

Bibliography

[1] M. H. Anderson, J. R. Ensher, M. R. Matthews, C. E. Wieman, and E. A. Cornell. Observation of Bose-Einstein Condensation in a Dilute Atomic Vapor. *Science*, 269:198, 1995.

[2] D. S. Jin, J. R. Ensher, M. R. Matthews, C. E. Wieman, and E. A. Cornell. Collective Excitations of a Bose-Einstein Condensate in a Dilute Gas. *Physical Review Letters*, 77:4984, 1996.

[3] D. S. Jin, M. R. Matthews, J. R. Ensher, C. E. Wieman, and E. A. Cornell. Temperature-Dependent Damping and Frequency Shifts in Collective Excitations of a Dilute Bose-Einstein Condensate. *Physical Review Letters*, 78:764, 1997.

[4] M.-O. Mewes, M. R. Andrews, N. J. van Druten, D. M. Kurn, D. S. Durfee, C. G. Townsend, and W. Ketterle. Collective Excitations of a Bose-Einstein Condensate in a Magnetic Trap. *Physical Review Letters*, 77(6):988, Aug 1996.

[5] D. M. Stamper-Kurn, H. J. Miesner, S. Inouye, M. R. Andrews, and W. Ketterle. Collisionless and Hydrodynamic Excitations of a Bose-Einstein Condensate. *Physical Review Letters*, 81:500, 1998.

[6] Onofrio Marago, Gerald Hechenblaikner, Eleanor Hodby, and Christopher Foot. Temperature Dependence of Damping and Frequency Shifts of the Scissors Mode of a Trapped Bose-Einstein Condensate. *Physical Review Letters*, 86:3938, 2001.

[7] Mark Edwards, P. A. Ruprecht, K. Burnett, R. J. Dodd, and Charles W. Clark. Collective Excitations of Atomic Bose-Einstein Condensates. *Physical Review Letters*, 77:1671, 1996.

[8] A. Griffin. Conserving and gapless approximations for an inhomogeneous Bose gas at finite temperatures. *Physical Review B*, 53:9341, 1996.

[9] S. Stringari. Collective excitations of a trapped Bose-Condensed Gas. *Physical Review Letters*, 77(12):2360, September 1996.

[10] N. P. Proukakis, S. A. Morgan, S. Choi, and K. Burnett. Comparison of gapless mean-field theories for trapped Bose-Einstein condensates. *Physical Review A*, 58(3):2435–2445, Sep 1998.

[11] D. A. W. Hutchinson, R. J. Dodd, and K. Burnett. Gapless Finite-T Theory of Collective Modes of a Trapped Gas. *Physical Review Letters*, 81:2198, 1998.

[12] D. A. W. Hutchinson, K. Burnett, R. J. Dodd, S. A. Morgan, M. Rusch, E. Zaremba, N. P. Proukakis, Mark Edwards, and C. W. Clark. Gapless mean-field theory of Bose-Einstein condensates. *Journal of Physics B: Atomic, Molecular, and Optical Physics*, 33:3825, 2000.

[13] M. Rusch, S. A. Morgan, D. A. W. Hutchinson, and K. Burnett. Second Order Theory of Excitations in Trapped Bose Condensates at Finite Temperatures. *Physical Review Letters*, 85:4844, 2000.

[14] S. A. Morgan, M. Rusch, D. A. W. Hutchinson, and K. Burnett. Quantitative Test of Thermal Field Theory for Bose-Einstein Condensates. *Physical Review Letters*, 91:250403, 2003.

[15] D. A. W. Hutchinson and E. Zaremba. Finite Temperature Excitations of a Trapped Bose Gas. *Physical Review Letters*, 78:1842, 1997.

[16] R. J. Dodd, Mark Edwards, Charles W. Clark, and K. Burnett. Collective excitations of Bose-Einstein-condensed gases at finite temperatures. *Physical Review A*, 57:R32, 1998.

[17] S. A. Morgan. Quantitative test of thermal field theory for Bose-Einstein condensates. II. *Physical Review A*, 72(043609), 2005.

[18] M. J. Bijlsma and H. T. C. Stoof. Collisionless modes of a trapped Bose gas. *Physical Review A*, 60:3973, 1999.

[19] B. Jackson and E. Zaremba. Finite-Temperature Simulations of the Scissors Mode in Bose-Einstein Condensed Gases. *Physical Review Letters*, 87:100404, 2001.

[20] B. Jackson and E. Zaremba. Quadrupole Collective Modes in Trapped Finite-Temperature Bose-Einstein Condensates. *Physical Review Letters*, 88:180402, 2002.

[21] B. Jackson and E. Zaremba. Modeling Bose-Einstein condensed gases at finite temperatures with N-body simulations. *Physical Review A*, 66:033606, 2002.

[22] S. A. Morgan. A gapless theory of Bose-Einstein condensation in dilute gases at finite temperature. *Journal of Physics B*, 33:3847, 2000.

[23] Xia-Ji Liu, Hui Hu, A. Minguzzi, and M. P. Tosi. Collective oscillations of a confined bose gas at finite temperaturein the random-phase approximation. *Physical Review A*, 69(4):043605, Apr 2004.

[24] A.J. Geddes, S.A. Morgan, and D.A.W. Hutchinson. Novel dynamical resonances in finite-temperature Bose-Einstein condensates. *Proceedings of the Royal Society A*, 461(4):3547, 2005.

[25] Nick P. Proukakis and Brian Jackson. Finite-temperature models of Bose-Einstein condensation. *Journal of Physics B*, 41:203002, 2008.

[26] A. Minguzzi and M. P. Tosi. Linear density response in the random-phase approximation for confined Bose vapours at finite temperature. *Journal of Physics: Condensed Matter*, 9:10211, 1997.

[27] H. Shi and W.-M. Zheng. Temperature-dependent frequency shifts in collective excitations of a Bose-Einstein condensate. *Physical Review A*, 59:1562, 1999.

[28] J. Reidl, A. Csordas, R. Graham, and P. Szepfalusy. Shifts and widths of collective excitations in trapped Bose gases determined by the dielectric formalism. *Physical Review A*, 61:043606, 2000.

[29] S Giorgini. Collisionless dynamics of dilute Bose gases: Role of quantum and thermal fluctuations. *Physical Review A*, 61:063615, 2000.

[30] U. Al Khawaja and H. T. C. Stoof. *Physical Review A*, 62(053602):053602, 2000.

[31] P. Storey and M. Olshanii. Closed class of hydrodynamical solutions for the collective excitations of a Bose-Einstein condensate. *Physical Review A*, 62:033604, 1998.

[32] T. Nikuni, E. Zaremba, and A. Griffin. Two-Fluid Dynamics for a Bose-Einstein Condensate out of Local Equilibrium with the Noncondensate. *Physical Review Letters*, 83:10, 1999.

[33] E. Zaremba, A. Griffin, and T. Nikuni. Two-fluid hydrodynamics for a trapped weakly-interacting Bose gas. *Physical Review A*, 57(6):4695, June 1998.

[34] Eugene Zaremba, T. Nikuni, and Allan Griffin. Dynamics of Trapped Bose Gases at Finite Temperatures. *Journal of Low Temperature Physics*, 116(3/4):277, 1999.

[35] S. A. Morgan. Response of bose-einstein condensates to external perturbations at finite temperature. *Physical Review A*, 69(2):023609, Feb 2004.

[36] R. Hanbury Brown and R. Q. Twiss. Correlation between photons in two coherent beams of light. *Nature*, 177:27–29, 1956.

[37] Masami Yasuda and Fujio Shimizu. Observation of Two-Atom Correlation of an Ultracold Neon Atomic Beam. *Physical Review Letters*, 77:3090, 1996.

[38] E. A. Burt, R. W. Ghrist, C. J. Myatt, M. J. Holland, E. A. Cornell, , and C. E. Wieman. Coherence, Correlations, and Collisions: What One Learns about Bose-Einstein Condensates from Their Decay. *Physical Review Letters*, 79:337, 1997.

[39] B. Laburthe Tolra, K. M. O'Hara, J. H. Huckans, W. D. Phillips, S. L. Rolston, and J. V. Porto. Observation of Reduced Three-Body Recombination in a Correlated 1D Degenerate Bose Gas. *Physical Review Letters*, 92:190401, 2004.

[40] E. W. Hagley, L. Deng, M. Kozuma, M. Trippenbach, Y. B. Band, M. Edwards, M. Doery, P. S. Julienne, K. Helmerson, S. L. Rolston, and W. D. Phillips. Measurement of the Coherence of a Bose-Einstein Condensate. *Physical Review Letters*, 83:3112, 1999.

[41] Zoran Hadzibabic, Peter Krüger, Marc Cheneau, Baptiste Battelier, and Jean Dalibard. Berezinskii-Kosterlitz-Thouless crossover in a trapped atomic gas. *Nature*, 441:1118, 2006.

[42] S. Richard, F. Gerbier, J. H. Thywissen, M. Hugbart, P. Bouyer, and A. Aspect. Momentum Spectroscopy of 1D Phase Fluctuations in Bose-Einstein Condensates. *Physical Review Letters*, 91(1):010405, Jul 2003.

[43] D. E. Miller, J. R. Anglin, J. R. Abo-Shaeer, K. Xu, J. K. Chin, and W. Ketterle. High-contrast interference in a thermal cloud of atoms. *Physical Review A*, 71:043615, 2005.

[44] M. Schellekens, R. Hoppeler, A. Perrin, J. Viana Gomes, D. Boiron, A. Aspect, and C. I. Westbrook. Hanbury Brown Twiss Effect for Ultracold Quantum Gases. *Science*, 310(648), 2005.

[45] Anton Ottl, Stephan Ritter, Michael Kohl, and Tilman Esslinger. Correlations and Counting Statistics of an Atom Laser. *Physical Review Letters*, 95(090404), 2005.

[46] T. Jeltes, J. M. McNamara, W. Hogervorst, W. Vassen, V. Krachmalnicoff, M. Schellekens, A. Perrin, H. Chang, D. Boiron, A. Aspect, and C. I. Westbrook. Comparison of the Hanbury Brown-Twiss effect for bosons and fermions. *Nature*, 445:402–405, 2007.

[47] Simon Folling, Fabrice Gerbier, Artur Widera, Olaf Mandel, Tatjana Gericke, and Immanuel Bloch. Spatial quantum noise interferometry in expanding ultracold atom clouds. *Nature*, 434:481–484, 2005.

[48] M. Greiner, C. A. Regal, J. T. Stewart, and D. S. Jin. Probing Pair-Correlated Fermionic Atoms through Correlations in Atom Shot Noise. *Physical Review Letters*, 94:110401, 2005.

[49] T. Rom, Th. Best, D. van Oosten, U. Schneider, S. Foelling, B. Paredes, and I. Bloch. Free fermion antibunching in a degenerate atomic Fermi gas released from an optical lattice. *Nature*, 444:733, 2006.

[50] T. Donner, S. Ritter, T. Bourdel, A. Ottl, M. Kohl, and T. Esslinger. Critical Behavior of a Trapped Interaction Bose Gas. *Science*, 315:1556–1558, 2007.

[51] T. Bourdel, T. Donner, S. Ritter, A. Öttl, M. Köhl, and T. Esslinger. Cavity QED detection of interfering matter waves. *Physical Review A*, 73:043602, 2006.

[52] M. Naraschewski and R. J. Glauber. Spatial coference and density correlations of trapped Bose gases. *Physical Review A*, 59:4595, 1999.

[53] E. V. Goldstein, O. Zobay, and P. Meystre. Coherence of atomic matter-wave fields. *Physical Review A*, 58:2373, 1998.

[54] Ehud Altman, Eugene Demler, and Mikhail D. Lukin. Probing many-body states of ultracold atoms via noise correlations. *Physical Review A*, 70:013603, 2004.

[55] J. Viana Gomes, A. Perrin, M. Schellekens, D. Boiron, C. I. Westbrook, and M. Belsley. Theory for a Hanbury Brown Twiss experiment with a pulsed atomic beam. *Physical Review A*, 74(053607), 2006.

[56] Stephen M. Barnett, Sonja Franke-Arnold, Aidan S. Arnold, and Colin Baxter. Coherence length for a trapped Bose gas. *Journal of Physics B: Atomic, Molecular, and Optical Physics*, 33:4177, 2000.

[57] R. J. Dodd, Charles W. Clark, Mark Edwards, and K. Burnett. Characterizing the coherence of Bose-Einstein condensates and atom lasers. *Optics Express*, 1:284, 1997.

[58] M. Holzmann and Y. Castin. Pair correlation function of an inhomogeneous interacting Bose-Einstein condensate. *The European Physical Journal D*, 7:425–432, 1999.

[59] M. J. Steel, M. K. Olsen, L. I. Plimak, P. D. Drummond, S. M. Tan, M. J. Collett, D. F. Walls, and R. Graham. Dynamical quantum noise in trapped Bose-Einstein condensates. *Physical Review A*, 58:4824, 1998.

[60] Christopher Gies and D. A. W. Hutchinson. Coherence properties of the two-dimensional Bose-Einstein condensate. *Physical Review A*, 70, 2004.

[61] Anna Posazhennikova. Weakly interacting, dilute Bose gases in 2d. *Reviews of Modern Physics*, 78:1111, 2006.

[62] J. A. Lipa, J. A. Nissen, D. A. Stricker, D. R. Swanson, and T. C. P. Chui. Specific heat of liquid helium in zero gravity very near the lambda point. *Physical Review B*, 68:174518, 2003.

[63] H. Kleinert. Critical exponents from seven-loop strong-coupling φ^4 theory in three dimensions. *Physical Review D*, 60:085001, 1999.

[64] M. Campostrini, M. Hasenbusch, A. Pelissetto, P. Rossi, and E. Vicari. Critical of the three dimensional xy universality class. *Physical Review B*, 63:214503, 2001.

[65] E. Burovski, J. Machta, N. Prokof'ev, and B. Svistunov. High-precision measurement of the thermal exponent for the three-dimensional xy universality class. *Physical Review B*, 74:132502, 2006.

[66] M. Schellekens, R. Hoppeler, A. Perrin, J. V. Gomes, D. Boiron, A. Aspect, and C. I. Westbrook. Hanbury Brown Twiss Effect for Ultracold Quantum Gases. *Science*, 310:648, 2005.

[67] Anton Öttl, Stephan Ritter, Michael Köhl, and Tilman Esslinger. Correlations and Counting Statistics of an Atom Laser. *Physical Review Letters*, 95(9):090404, 2005.

[68] T. Jeltes, J. M. McNamara, W. Hogervorst, W. Vassen, V. Krachmalnicoff, M Schellekens, A Perrin, H. Chang, D. Boiron, A. Aspect, and C. I. Westbrook. Comparison of the Hanbury Brown-Twiss effect for bosons and fermions. *Nature*, 445:402, 2006.

[69] S. Fölling, F. Gerbier, A. Widera, O. Mandel, T. Gericke, and I. Bloch. Spatial quantum noise interferometry in expanding ultracold atom clouds. *Nature*, 434:481, 2005.

[70] M. Greiner, C. A. Regal, J. T. Stewart, and D. S. Jin. Probing Pair-Correlated Fermionic Atoms through Correlations in Atom Shot Noise. *Physical Review Letters*, 94(11):110401, 2005.

[71] T. Rom, Th. Best, D. van Oosten, U. Schneider, S. Fölling, B. Paredes, and I. Bloch. Free fermion antibunching in a degenerate atomic Fermi gas released from an optical lattice. *Nature*, 444:733, 2006.

[72] Ehud Altman, Eugene Demler, and Mikhail D. Lukin. Probing many-body states of ultracold atoms via noise correlations. *Physical Review A*, 70:013603, 2004.

[73] Ana Maria Rey, Indubala I. Satija, and Charles W. Clark. Noise Correlations of Hard-core Bosons: Quantum Coherence and Symmetry Breaking. *Journal of Physics B*, 39:S177, 2006.

[74] Ana Maria Rey, Indubala I. Satija, and Charles W. Clark. Quantum coherence of Hard-Core-Bosons and Fermions : Extended, Glassy and Mott Phases. *Physical Review A*, 73:063610, 2006.

[75] Ana Maria Rey, Indubala I. Satija, and Charles W. Clark. Hanbury Brown-Twiss Interferometry for Fractional and Integer Mott Phases. *New Journal of Physics*, 8(8):155, 2006.

[76] S. Ashhab. Interference between a large number of independent Bose-Einstein condensates. *Physical Review A*, 71:063602, 2005.

[77] V. W. Scarola, E. Demler, and S. Das Sarma. Searching for a supersolid in cold-atom optical lattices. *Physical Review A*, 73:051601 R, 2006.

[78] Q. Niu, I. Carusotto, and A. B. Kuklov. Imaging of Critical Correlations in Optical. Lattices and Atomic Traps. *Physical Review Letters*, 73:053604, 2006.

[79] Jing Min Hou. Quantum Phases of Ultracold Bosonic Atoms in a Two-Dimensional Optical Superlattice. *arxiv*, page 0705.1888v3, 2008.

[80] E. Toth, A. M. Rey, and P. B. Blakie. Theory of correlations between ultracold bosons released from an optical lattice. *Physical Review A*, 78(1):013627, 2008.

[81] A. Polkovnikov, E. Altman, and E. Demler. Interference between independent fluctuating condensates. *PNAS*, 103:6125, 2006.

[82] F. M. Gasparini, M. O Kimball, K. P. Mooney, and M. Diaz-Avilla. Finite-size scaling of ^{4}He at the superfluid transition. *Reviews of Modern Physics*, 80:1009, 2008.

[83] M. E. Fisher and M. N. Barber. Scaling Theory for Finite-Size Effects in the Critical Region. *Physical Review Letters*, 28:1516, 1972.

[84] M. E. Fisher. The renormalization group in the theory of critical behavior. *Reviews of Modern Physics*, 46:597, 1974.

[85] K. Damle, T. Senthil, S. N. Majumdar, and S. Sachdev. Phase transition of a Bose gas in a harmonic potential. *Europhysics Letters*, 36(1):7, 1996.

[86] P. B. Blakie, A. S. Bradley, M. J. Davis, R. J. Ballagh, and C. W. Gardiner. Dynamics and statistical mechanics of ultra-cold Bose gases using c-field techniques. *Advances in Physics*, 57:363, 2008.

[87] B. V. Svistunov and G. V. Shlyapnikov. *Journal of the Moscow Physical Society*, 1:373, 1991.

[88] Yu. Kagan, B. V. Svistunov, and G. V. Shlyapnikov. *Zh. Éksp. Teor. Fiz.*, 101:528, 1992. [JETP **75**, 387 (1992)].

[89] Yu. Kagan and B. V. Svistunov. *Zh. Éksp. Teor. Fiz.*, 105:353, 1994. [JETP **75**, 387 (1992)].

[90] Yu. Kagan and B. V. Svistunov. Evolution of Correlation Properties and Appearance of Broken Symmetry in the Process of Bose-Einstein Condensation. *Physical Review Letters*, 79:3331, 1997.

[91] K. Damle, S. N. Majumdar, and S. Sachdev. Phase transition of a Bose gas in a harmonic potential. *Physical Review A*, 54(5037), 1996.

[92] R. J. Marshall, G. H. New, K. Burnett, and S. Choi. Exciting, cooling, and vortex trapping is a Bose-condensated gas. *Physical Review A*, 59:2085, 1999.

[93] M. J. Davis, R. J. Ballagh, and K. Burnett. Dynamics of thermal Bose fields in the classical limit. *Journal of Physics B*, 34:4487, 2001.

[94] Matthew J. Davis and P. Blair Blakie. Critical Temperature of a Trapped Bose Gas: Comparison of Theory and Experiment. *Physical Review Letters*, 96:060404, 2006.

[95] F. Gerbier, J. H. Thywissen, S. Richard, M. Hugbart, P. Bouyer, and A. Aspect. Critical Temperature of a Trapped, Weakly Interacting Bose Gas. *Physical Review Letters*, 92:030405, 2004.

[96] T. P. Simula and P. B. Blakie. Thermal activation of vortex-antivortex pairs in quasi-2D Bose-Einstein condensate. *Physical Review Letters*, 96:020404, 2006.

[97] Sabine Stock, Zoran Hadzibabic, Baptiste Battelier, Marc Cheneau, and Jean Dalibard. Observation of Phase Defects in Quasi-Two-Dimensional Bose-Einstein Condensates. *Physical Review Letters*, 95(190403), 1932.

[98] M. J. Davis and S. A. Morgan. Microcanonical temperature for a classical field: Application to Bose-Einstein condensation. *Physical Review A*, 68:053615, 2003.

[99] A. Bezett, E. Toth, and P. B. Blakie. Two-point correlations of a trapped interacting Bose gas at finite temperature. *Physical Review A*, 77(023602), 2008.

[100] T. P. Simula, M. J. Davis, and P. B. Blakie. Superfluidity of an interacting trapped quasi-two-dimensional Bose gas . *Physical Review A*, 77:023618, 2008.

[101] Chad N. Weiler, Tyler W. Neely, David R. Scherer, Ashton S. Bradley, Matthew J. Davis, and Brian P. Anderson. Spontaneous vortices in the formation of Bose-Einstein condensates. *Nature*, 455:948:951, 2008.

[102] A. A. Norrie, R. J. Ballagh, and C. W. Gardiner. Quantum turbulence in condensate collisions: an application of the classical field method. *Physical Review Letters*, 94:040401, 2005.

[103] A. Bezett and P. B. Blakie. Projected Gross-Pitaevskii equation theory of finite temperature collective modes for a trapped Bose gas. *Physical Review A*, 79:023602, 2009.

[104] A. Bezett and P. B. Blakie. Critical properties of a trapped interacting Bose gas. *Physical Review A*, 79:033611, 2009.

[105] P. Blair Blakie and Matthew J. Davis. The Projected Gross-Pitaevskii Equation for hamonically confined Bose gases at finite temperature. *Physical Review A*, 72:063608, 2005.

[106] K. Huang and C. N. Yang. Quantum-Mechanical Many-Body Problem with Hard Sphere Interaction. *Physical Review*, 105:767, 1957.

[107] Adam Norrie. *Colliding Bose Einstein Condensates*. PhD thesis, 2005.

[108] M. J. Davis, S. A. Morgan, and K. Burnett. Simulations of thermal Bose fields in the classical limit. *Physical Review A*, 66:053618, 2002.

[109] M. J. Davis and P. B. Blakie. Calculation of the microcanonical temperature for the classical Bose field. *Journal of Physics A*, 38:10259, 2005.

[110] C. W. Gardiner, J. R. Anglin, and T. I. A. Fudge. The stochastic Gross-Pitaevskii equation. *Journal of Physics B*, 35:1555, 2002.

[111] C. W. Gardiner and M. J. Davis. The stochastic Gross-Pitaevskii equation:II. *Journal of Physics B*, 36:4731, 2003.

[112] K. Gòral, M. Gajda, and Rzążewski. Multi-mode description of an interacting Bose-Einstein condensate. *Optics Express*, 8:92, 2001.

[113] M. J. Davis, S. A. Morgan, and K. Burnett. Simulations of Bose Fields at Finite Temperature. *Physical Review Letters*, 87:160402, 2001.

[114] Vortex Lattice Formation in Bose-Einstein Condensates. *Physical Review Letters*.

[115] Anatoli Polkovnikov and Daw-Wei Wang. Effect of quantum fluctuations on the dipolar motion of Bose-Einstein condensates in optical lattices. *Physical Review Letters*, 93:070401, 2004.

[116] Classical-Field Method for Time Dependent Bose-Einstein Condensed Gases. *Physical Review Letters*.

[117] A. Sinatra, C. Lobo, and Y. Castin. The truncated Wigner method for Bose-condensed gases: limits of validity and applications. *Journal of Physics B*.

[118] A. S. Bradley, P. B. Blakie, and C. W. Gardiner. Properties of the stochastic Gross-Pitaevskii equation: Projected Ehrenfest relations and the optimal plane wave basis. *Journal of Physics B*, 38:4259, 2005.

[119] P. B. Blakie and M. J. Davis. Projected Gross-Pitaevskii Equation for harmonically confined Bose gases at finite temperature. *Physical Review A*, 72:063608, 2005.

[120] P. Blair Blakie. Numerical method for evolving the projected Gross-Pitaevskii equation. *Physical Review E*, 78:026704, 2008.

[121] Oliver Penrose and Lars Onsager. Bose-Einstein Condensation and Liquid Helium. *Physical Review*, 104:576, 1956.

[122] H. H. Rugh. Dynamical Approach to Temperature. *Physical Review Letters*, 78:772, 1997.

[123] C. W. Gardiner. Particle-number-conserving Bogoliubov method which demonstrates the validity of the time-dependent Gross-Pitaevskii equation for a highly condensed Bose gas. *Physical Review A*, 56:1414, 1997.

[124] C. W. Gardiner and P. Zoller. *Quantum Noise*. Springer, Berlin, third edition, 2004.

[125] D. F. Walls and G. J. Milburn. *Quantum Optics*. Springer-Verlag, Berlin Heidelberg, first edition, 1994.

[126] E. Wigner. On the Quantum Correction for Thermodynamic Equilibrium. *Physical Review*, 40:749, 1932.

[127] C. W. Gardiner. *Handbook of Stochastic Methods*. Springer, Berlin, third edition, 2004.

[128] R. J. Ballagh. Computational methods for nonlinear partial differential equations, www.physics.otago.ac.nz/research/jackdodd/resources.

[129] Ben Caradoc Davies. *Vortex Dynamics in BEC*. PhD thesis, 2000.

[130] William H. Press, Saul A. Teukolsky, William T. Vetterling, and Brian P. Flannery. *Numerical Recipes in C*. Cambridge, 1992.

[131] J. Stenger, S. Inouye, A. P. Chikkatur, D. M. Stamper-Kurn, D. E. Pritchard, and W. Ketterle. Bragg Spectroscopy of a Bose-Einstein Condensate. *Physical Review Letters*, 82:4569, 1999.

[132] John F. Dobson. Harmonic-potential theorem: Implications for approximate many-body theories. *Physical Review Letters*, 73:2244, October 1994.

[133] J. Viana Gomes, A. Perrin, M. Schellekens, D. Boiron, C. I. Westbrook, and M. Belsley. Theory for a Hanbury Brown Twiss experiment with a ballistically expanding cloud of cold atoms. *Physical Review A*, 74:053607, 2006.

[134] S. Giorgini, L. P. Pitaevskii, and S. Stringari. Condensate fraction and critical temperature of a trapped interacting Bose gas. *Physical Review A*, 54:R4633, 1996.

[135] Anthony J. Leggett. Bose-Einstein condensation in the alkali gases: Some fundamental concepts. *Reviews of Modern Physics*, 73:307, 2001.

[136] Guillaume Huyet Sonja Franke-Arnold and Stephen M Barnett. Measures of coherence for trapped matter waves. *Journal of Physics B*, 34(5):945–964, 2001.

[137] V. A. Kashurnikov, N. V. Prokofév, and B. V. Svistunov. Critical Temperature Shift in Weakly Interacting Bose Gas. *Physical Review Letters*, 87:120402, 2001.

[138] N. V. Prokof'ev, O. Ruebenacker, and B.V. Svistunov. Critical point of a weakly interacting two-dimensional Bose gas. *Physical Review Letters*, 87:270402, 2001.

[139] V. V. Kocharovsky, Vl. V. Kocharovsky, M. Holthaus, C. H. Raymond Ooi, A. Svidzinsky, W. Ketterle, and M. O. Scully. Fluctuations in ideal and interacting bose-einstein condensates: From the laser phase transition analogy to squeezed states and bogoliubov quasiparticles. *Advances in Atomic, Molecular, and Optical Physics*, 53:291, 2006.

[140] W. Ketterle, D. S. Durfee, and D. M. Stamper-Kurn. Making, probing and understanding Bose-Einstein condensates. In M. Inguscio, S. Stringari, and C. E. Wieman, editors, *Proceedings of the International School of Physics - Enrico Fermi*, page 67. IOS Press, 1999.

[141] C. N. Weiler, T. W. Neely, D. R. Scherer, A. S. Bradley, M. J. Davis, and B. P. Anderson. Spontaneous vortices in the formation of Bose-Einstein condensates. *Nature*, 455:948, 2008.